WESTERN SYDNEY
UNIVERSITY

Magnetron Sputter Deposition and Nitridation of Ta_3N_5 Thin Films for Photo-electrochemical Water Splitting

By

Sam Macartney

A dissertation submitted in fulfilment of the requirements

for the degree of

Doctor of Philosophy

Supervisors

Dr. Leigh Sheppard

Dr. Richard Wuhrer

Dr. Laurel George

School of Engineering

Western Sydney University

August 2023

Statement of Authentication

The work presented in this thesis is, to the best of my knowledge and belief, original except as acknowledged in the text. I hereby declare that I have not submitted this material, either in full or in part, for a degree at this or any other institution. This report contains no reproduced material written or published by another person without due acknowledgement.

Acknowledgements

First, I would like to express my deepest gratitude to my supervisory panel, Dr. Leigh Sheppard, Dr. Richard Wuhrer, Dr. Laurel George, and Dr. Rong Liu for their support, discussions, and encouragement over the years. Leigh and Ric's broad knowledge of material science and analytical techniques has proven invaluable in the design and execution of this project's experimental and analytical work. There are numerous techniques and concepts they've introduced to me during this project that I would never have encountered or would have been more difficult to learn without their assistance. I would also thank Laurel for joining the project and providing valuable input at the important final stage of thesis preparation. This project also involved many hours on the SIMS, for which I would like to thank Rong for running and maintaining. It has been a privilege to work under this supervisory panel.

Furthermore, I would like to acknowledge the staff and interns who have helped me over the years at the Advanced Materials Characterisation Facility (AMCF) at Western Sydney University. Especially Dr. Timothy Murphy and Dr. Daniel Fanna. Your assistance with equipment access and discussions pertaining to instrumentation operation and data acquisition were very helpful and deeply appreciated.

I would also extend my sincere thanks to Dr. Marie Wintrebert-Fouquet, Alanna Fernandes and everyone at Bluglass for providing access to their facilities and equipment, especially the Hall measurement equipment. I am also very grateful for Marie's insights and suggestions in solving my sample problems.

Additionally, I would like to thank Prof. Chris Sorrell, Dr. Pramod Koshy, Dr. Sajjad Mofarah and Xiaoran Zheng for providing access to their electrochemistry laboratory at UNSW and helping with my experiments. Their help allowed me to complete this thesis. I would also extend thanks to UNSW for facilitating my access during the COVID pandemic.

Finally, I'd like to extend thanks to WSU and the School of Engineering, Design and Built Environment for providing funding for this project, as well as access to the facilities and the WSU staff who helped me along the way.

And thank you to my family and especially Naomi for the patience you've all demonstrated, and the encouragement provided.

Declarations

Financial support for this work was provided by Western Sydney University, via a WSU Postgraduate Scholarship and allocated yearly funding provisions. The author declares no competing financial or academic interests with this work.

Submitted and Published Works

Journal Publications

1. **Macartney, S**, Liu, R, Wuhrer, R & Sheppard, LR, 2022, ‘Preparation of Aluminium Doped Ta_3N_5 Thin Films via Nitridation of Sputtered Tantalum Oxide Films’, Materials Chemistry and Physics, p. 126110.

2. **Macartney, S**, Liu, R, Wuhrer, R & Sheppard, LR 2020, 'Chromium Doping of Ta_3N_5 Thin Films via Thermal Nitridation of Sputtered Tantalum Oxide Films', Materials Chemistry and Physics, p. 123838.

3. Sheppard, LR, Zhang, H, Liu, R, **Macartney, S**, Murphy, T, Wainer, P et al. 2019, 'Reactive sputtered TixNbyN coatings. II. Effect of common deposition parameters', Materials Chemistry and Physics, vol. 224, pp. 320-7.

4. Sheppard, LR, Zhang, H, Liu, R, **Macartney, S**, Murphy, T & Wuhrer, R 2019, 'Reactive sputtered TiXNbYNZ thin films. I. Basic processing relationships', Materials Chemistry and Physics, vol. 224, pp. 308-13.

5. Hou, W, Cortez, P, Wuhrer, R, **Macartney, S**, Bozhilov, KN, Liu, R et al. 2017, 'Oriented epitaxial TiO2 nanowires for water splitting', Nanotechnology, vol. 28, no. 26, p. 265602.

6. Sheppard, LR, Hager, S, Holik, J, Liu, R, **Macartney, S** & Wuhrer, R 2015, 'Tantalum segregation in Ta-Doped TiO2 and the related impact on charge separation during illumination', The Journal of Physical Chemistry C, vol. 119, no. 1, pp. 392-400.

7. Sheppard, LR, Holik, J, Liu, R, **Macartney, S** & Wuhrer, R 2014, 'Tantalum enrichment in tantalum-doped titanium dioxide', Journal of the American Ceramic Society, vol. 97, no. 12, pp. 3793-9.

Conference Papers

1. **Macartney, S**, Wuhrer, R & Sheppard, LR 2018, 'Effect of Oxygen on Sputtered Tantalum Nitride Thin Films for Photoelectrochemical Water Splitting', Microscopy and Microanalysis, vol. 24, no. S1, pp. 1546-7.

2. **Macartney, S**, Sheppard, L & Wuhrer, R 2020, 'Cobalt Doping in Tantalum Nitride Thin Films Prepared by Sputtering', Microscopy and Microanalysis, pp. 1-4, Cambridge Core, Cambridge University Press, DOI 10.1017/S1431927620022862.

Abstract

The reliance of human society on fossil fuels has created significant environmental consequences, as such it is imperative that renewable and sustainable sources of energy generation are developed. Hydrogen generation via solar water splitting is a compelling method of renewable energy production and could form the basis for a future hydrogen economy.

Tantalum nitride (Ta_3N_5) is a compelling solar water splitting material due to its appreciable band gap of 2.1 eV and redox potentials that straddle those of water, which enables Ta_3N_5 to absorb light in the visible spectrum and perform the overall splitting of water into oxygen and hydrogen. However, Ta_3N_5 self-oxidizes under water splitting conditions which suppresses its performance. This can be avoided by separating Ta_3N_5 from H_2O under water splitting conditions, or by performing the reduction of water with Ta_3N_5 instead of the oxidation reaction.

This thesis describes the synthesis and characterisation of Ta_3N_5 thin films via sputter deposition and thermal nitridation, with the aim of developing Ta_3N_5 as a high performance photo-electrode material through the incorporation of chromium and aluminium as acceptor dopants to drive p-type properties. Films are characterised using SEM/EDS, XRD, UV-Vis, and SIMS to determine phase, elemental composition and opto-electric properties. Photo-response and majority carrier concentration were measured using Hall effect apparatus and electrochemical techniques.

In this work, films were synthesized with the goal of directly depositing Ta_3N_5. Several phases within the tantalum nitride phase series were observed, with the metastable TaN group of phases being the most common. Ta_3N_5 was synthesized from sputtered tantalum oxide films and successfully annealed to produce Ta_3N_5. The difficulty in depositing Ta_3N_5 directly is addressed by describing a mechanism for the ammonolysis of Ta_2O_5 to Ta_3N_5. Acceptor doped Ta_3N_5 photo-electrodes were produced and characterised using this method. Chromium doped Ta_3N_5 films exhibited an exsolved chromium nitride phase in XRD results, and a solubility limit for chromium in Ta_3N_5 was determined to be ~6 at. %. For aluminium doped films, no exsolved phase was observed and no solubility limit determined under the conditions presented. Aluminium doped Ta_3N_5 films demonstrated improved photocathode response relative to the standard Ta_3N_5 films.

Table of Contents

Statement of Authentication i
Acknowledgements ii
Declarations iii
Submitted and Published Works iv
Abstract v
Table of Contents vi
Nomenclature ix
Figures x
Tables xvi
Chapter 1: Introduction and Context of this Work 1
1.1 Structure of this Thesis 1
1.2 Living Standards, Energy and Climate Change 1
1.3 Hydrogen as an Alternative Fuel and a Theoretical Hydrogen Economy 3
1.4 How can Hydrogen be Sustainably Obtained? 5
1.5 Project Aims 6
Chapter 2: Principles of Semiconducting Materials 9
2.1 Properties of Semiconductors 9
2.1.1 Intrinsic and Extrinsic Semiconductors 9
2.1.2 Band Theory: Band Gap and Band Bending 9
2.1.3 p-type and n-type Semiconductors 10
2.2 Semiconductors and Photo-electrochemical Cells 12
2.2.1 Semiconductor and Electrolyte Interfaces 12
2.2.2 The Depletion Layer 13
2.2.3 Mott-Schottky Analysis: Flat Band Potential and Carrier Concentration 13
2.2.4 Hall Effect and Van Der Pauw Method 17
2.2.5 Cyclic Voltammetry 19
2.2.6 Air Mass Coefficient (AM 1.5) 20
2.2.7 Defect Disorder in Semiconductors 20
2.2.8 Defects in Transition Metal Nitrides 23
Chapter 3: Solar Driven Water Splitting 25
3.1 Basic Principles of Solar Water Splitting in a Photo-electrochemical Cell 25
3.2 Particulate Systems and Photo-electrodes in Water Splitting 29
Chapter 4: Sputter Deposition 31
4.1 Magnetron Sputtering 31
4.1.1 Total Deposition Pressure and Reactant Gases 36
4.1.2 Substrate Heating 36
4.1.3 DC and RF Power Sources 37
4.1.4 Substrate Bias 37
Chapter 5: The Tantalum Nitride Phase Series 39
5.1 The TaN Phase 41
5.2 The Ta_3N_5 Phase 43
5.3 Ta_3N_5 Synthesis: Mechanism 47

5.3.1 Challenges in Sputtering Ta_3N_5 Thin Films 47
5.3.2 Proposed Mechanism 49

Chapter 6: Literature Review 52

6.1 Ta_3N_5 in the Literature 52
6.2 Ta_3N_5 and its use as a photo-electrode 53
6.2.1 Doped Ta_3N_5 56
6.3 Ta_3N_5 as a photo-electrode rather than as a photo-catalyst 56
6.4 Synthesis of Ta_3N_5 57
6.4.1 Thermal Nitridation 57
6.4.2 Nanostructured Routes 58
6.4.3 Physical Vapour Deposition 59
6.4.4 Chemical Vapour Deposition and Sol-gel Routes 60
6.5 Other Notable Nitride Photo-electrodes 61
6.5.1 Tantalum Oxynitride (TaON) 61
6.5.2 Niobium Nitride (Nb_3N_5) 62
6.5.3 Germanium Nitride (Ge_3N_4) 63
6.5.4 Gallium Nitride and Zinc Oxide (GaN and GaN:ZnO) 63
6.5.5 Lanthanum Titanium Oxynitride ($LaTiO_2N$) 64
6.5.6 Graphitic Carbon Nitride (g-C_3N_4) 65
6.6 Postulation of the Problem 66

Chapter 7: Experimental Method 67

7.1 Film Synthesis 67
7.1.1 Magnetron Sputter Deposition 67
7.1.2 Thin Film Substrates 68
7.1.3 Post Annealing 69
7.2 Sample Characterisation 69
7.2.1 X-Ray Diffraction 70
7.2.2 Scanning Electron Microscopy 71
7.2.3 Energy Dispersive Spectroscopy 72
7.2.4 Secondary Ion Mass Spectrometry 72
7.2.5 UV-Vis Spectrophotometry 73
7.2.6 Photo-electrochemical Performance Assessment 74
7.2.7 Hall and Van Der Pauw Measurements 76

Chapter 8: Results and Discussion 78

8.1 Reactive Sputtering of Tantalum Nitride Films 78
8.1.1 DC Sputtered Films 78
8.1.1.1 Effect of Nitrogen Partial Pressure, $p(N_2)$ 79
8.1.1.2 Effect of Total Deposition Pressure, P_{dep} 85
8.1.1.3 Effect of Substrate Temperature, T_{sub} 92
8.2 DC Reactive sputtering of Tantalum Oxide and Subsequent Annealing in NH_3 98
8.2.1 Tantalum Oxide Films 98
8.2.2 Film Selection for Doping and Conclusions 100
8.3 DC Reactive Sputtering and NH_3 Annealing of Doped TaO Thin Films 100
8.3.1 Dopant Selection 101
8.3.2 Chromium Doped Ta_3N_5 Thin Films 104
8.3.2.1 Hysteresis of Ta and Cr Targets in Argon 104
8.3.2.2 Deposition and Nitridation of Tantalum Chromium Oxide 106
8.3.2.3 Reaction Kinetics of Ta_3N_5 Evolution in Chromium Doped Tantalum Oxide Films 120
8.3.2.4 UV-Vis Characterisation of Cr-Ta_3N_5 126
8.3.3 Aluminium Doped Ta_3N_5 Thin Films 128

8.3.3.1 Hysteresis of Ta and Al Targets in Argon 129
8.3.3.2 Deposition and Nitridation of Tantalum Aluminium Oxide 131
8.3.3.3 Reaction Kinetics of Ta_3N_5 Evolution in Aluminium Doped Tantalum Oxide Films 144
8.3.3.4 UV-Vis Characterisation of Al-Ta_3N_5 149
8.4 Photo-electrochemical and Electronic Assessment 151
8.4.1 Electronic Properties and PEC Performance Ta_3N_5 Films 151
8.4.2 Electronic Properties and PEC Performance of Cr-Ta_3N_5 Films 154
8.4.3 Electronic Properties and PEC Performance of Al-Ta_3N_5 Films 156
9 Conclusions 161
9.1 Conclusions 161
9.2 Future Work and Outlook 163
10 References 164
11 Appendices 184

Nomenclature

AFM	Atomic Force Microscopy
ALD	Atomic Layer Deposition
AM	Air Mass coefficient
CB	Conduction Band
CE	Counter Electrode
CV	Cyclic Voltammetry
CVD	Chemical Vapour Deposition
DC	Direct Current
DRS/DRA	Diffuse Reflectance Spectroscopy/Diffuse Reflectance Accessory
EDS	Energy-Dispersive Spectroscopy
EIS	Electrochemical Impedance Spectroscopy
EV	Electric Vehicle
ICE	Internal Combustion Engine
NHE	Normal Hydrogen Electrode
pAr	Argon Partial Pressure
P_{dep}	Total Deposition Pressure
PEC	Photo-electrochemical Cell
pN_2	Nitrogen Partial Pressure
pO_2	Oxygen Partial Pressure
PVD	Physical Vapour Deposition
RF	Radio Frequency
RHE	Reversible Hydrogen Electrode
Rq	Roughness parameter
SEM	Scanning Electron Microscopy
UV-Vis	Ultraviolet-Visible Spectroscopy
VB	Valence Band
WE	Working Electrode
XRD	X-Ray Diffraction

Figures

Figure 1-1. Global primary energy consumption by source expressed in terawatt-hours (Ritchie & Roser 2020). ... 2

Figure 1-2. Energy densities of various fuels, horizontal scale is density per mass, vertical scale relates density per volume (Dial 2008). ... 4

Figure 1-3. Near-term, mid-term and long-term predictions for the capacity of hydrogen production methods in the US, produced by the US Department of Energy (*Laboratory* 2018). ... 5

Figure 2-1. Hypothetical energy bands in conductors, semiconductors and insulators. ... 10

Figure 2-2. Visual depiction of (a) n-type As doped Si and (b) p-type Al doped Si (Ling, Sanny & Moebs 2016). ... 11

Figure 2-3. Simplified band diagram of p-type and n-type semiconductors, including the shifted fermi level resulting from dopant impurities (Nave 2007). ... 11

Figure 2-4. Depiction of band bending and photo-electrochemical water splitting process at the interface region between a p-type semiconductor electrode and alkaline electrolyte, where E_g is the band gap, SCL is the space charge layer/depletion layer, IHL is the inner Helmholtz layer and OHL is the outer Helmholtz layer (Bayrak Pehlivan et al. 2019). ... 13

Figure 2-5. Mott-Schottky plots of Ta_2O_5 electrodes under various pH conditions, as determined by Chun and colleagues (Chun et al. 2003). This depicts the linear relationship between the reciprocal of capacitance squared and voltage. ... 15

Figure 2-6. Mott-Schottky plot of p-doped $CuNb_3O_8$ in 0.5M Na_2SO_4 electrolyte solution (Joshi & Maggard 2012) ... 15

Figure 2-7. Mott-Schottky plot of Ta_3N_5 electrode, generated at 10-1000Hz frequency range in 0.1M KOH electrolyte solution. ... 16

Figure 2-8. Diagram depicting Van Der Pauw measurement contact placement on a thin film (left) and the current and voltage measurements on a thin film material using Ohm's law to calculate resistance along the vertical and horizontal edges (right) (Rietveld et al. 2003). . 17

Figure 2-9. Typical cyclic voltammogram depicting current vs voltage regions where oxidation and reduction are respectively taking place, where $i_{p,c}$ and $i_{p,a}$ are the peak cathodic and anodic currents and $E_{p,c}$ and $E_{p,a}$ are the peak cathodic and anodic potentials, respectively (Nnamchi & Obayi 2018). ... 19

Figure 2-10. Air mass coefficient demonstrated with respect to zenith angle of 48.2° (Brownson 2020). ... 20

Figure 2-11. Representation of the possible defects within the lattice of a hypothetical solid. ... 21

Figure 2-12. Depiction of Schottky and Frenkel Defects in NaCl crystal structure. ... 23

Figure 3-1. Demonstration of photo-electrochemical water splitting, where VB = valence band and CB = conduction band. Steps are as follows: (I) light adsorption, (II) charge separation,

(III) charge migration, (IV) charge recombination, (V) water oxidation and (VI) water reduction. 25

Figure 3-2. Chart depicting the relative conduction band (CB) and valence band (VB) energy and band gap values of various semiconducting materials used for water splitting, including Ta_3N_5, $SrTiO_3$, TaON, p-GaAs, Ta_2O_5, n-CdS, TiO_2 and p-Si compared to the redox potentials of water. Where NHE = Normal Hydrogen Electrode. 27

Figure 3-3. Figure depicting the process of charge separation following the excitation of an electron from the valence band of a semiconductor. 28

Figure 3-4. Figure showing a simplistic depiction of the process of charge transfer, which involves a photogenerated hole migrating to the electrolyte/semiconductor interface to perform the oxidation of a water molecule. 29

Figure 3-5. Two of the main routes explored for solar water splitting, a) photo-electrochemical water splitting and b) photocatalytic water splitting depicting a photocatalyst in an electrolyte. 30

Figure 4-1. Schematic of Magnetron Sputtering apparatus pertaining to the sputter coater used in this project. 32

Figure 4-2. Cross sectional and top down view of sputtering target. Image on the right shows a target that has been worn down by sputtering, showing 'race track' run into the surface by the plasma. 33

Figure 4-3. The conservation of momentum in a collision between two particles. 33

Figure 4-4. Diagram depicting the basic process of sputtering. A charged ion strikes the lattice of a target material, and atoms are ejected via successive collisions. 34

Figure 4-5. Sputtering chamber schematic indicating the position of the heating elements below the substrate inside the stage. 37

Figure 4-6. Sputtering chamber schematic showing the generation of a plasma over the substrate using a DC bias, and a DC power source attached to the target material. 38

Figure 5-1. Phase diagram depicting the stable structures in the tantalum nitride phase series as a function of the atom chemical potentials, μ_N and μ_{Ta}. The diagram on top shows the phases as calculated, whereas the bottom diagram omits the most stable Ta_5N_6 phase so other phases in the series can be seen (Stampfl & Freeman 2005). 40

Figure 5-2. Phase diagram of DC magnetron sputtered tantalum nitride films (Salamon et al. 2016), where T_a is the annealing temperature and pN_2 refers to the total amount of nitrogen in the sputtering atmosphere (1 = 100%). 41

Figure 5-3. Extended unit cell crystal structures of a) hexagonal TaN (ε-TaN) and b) fcc cubic TaN (δ-TaN), where the blue balls represent the tantalum and the gray balls represent the nitrogen. 42

Figure 5-4. Band structures of Ta_2O_5, TaON and Ta_3N_5 (Chun et al. 2003). 44

Figure 5-5. The extended unit cell orthorhombic crystal structure of Ta_3N_5. Orthorhombic Ta_3N_5 exists in the space group Cmcm and is composed of irregular packing of TaN_6 octahedra. Blue balls represent the tantalum and grey balls represent the nitrogen. 45

Figure 5-6. Ta_3N_5 thin film mounted as an electrode (left) and red Ta_3N_5 powder (right), reacted from Ta_2O_5 powders via thermal annealing in NH_3. 46

Figure 5-7. Routes to Ta_3N_5 phase as detailed in the literature. Initial tantalum oxide films are deposited in mixed Ar/O_2 gas phase. 49

Figure 5-8. Routes to Ta_3N_5 documented in this project. 50

Figure 5-9. Proposed intermediate reaction mechanism for synthesis of Ta_2O_5 to TaON. Progressive substitution of lattice oxygen by nitrogen will eventually result in the formation of Ta_3N_5. 51

Figure 7-1. AJA Orion 5 Magnetron Sputterer used in this project. Located at Western Sydney University, Hawkesbury Campus.......... 68

Figure 7-2. Bragg diffraction, where n is a positive integer called the order of reflection, λ is the wavelength of the incident wave, d is the distance between the crystal planes and θ is the glancing angle. 70

Figure 7-3. Diagram depicting the XRD geometries of Glancing Angle XRD (left) and Bragg-Brentano scanning mode (right), where ω is the angle of incidence. 71

Figure 7-4. Diagram depicting the basic working of SIMS analysis, including the displacement of secondary ions from the sample by the primary ion beam. 73

Figure 7-5. Representation of the path of light in a UV-Vis spectrophotometer. The DRA integrating sphere accessory is included with the spectrophotometer operating in double-reverse mode as opposed to the traditional cuvette double detector mode. 74

Figure 7-6. Photo-electrochemical cell used in this investigation, the UV lamp light intensity is controlled by an aperture and filter (right) before it strikes the electrode in the cell (left). Apparatus located at Hawkesbury Campus, Western Sydney University. 75

Figure 7-7. Ecopia HMS-3000 Hall Measurement System used in this project with accompanying PC and software shown. The sample mount, with mounted sample and magnet, can be seen in the bottom left. 76

Figure 7-8. Ecopia HMS-3000 Hall Measurement System sample cradle with film and silicon substrate mounted. 77

Figure 8-1. Effect of $p(N_2)$ on the discharge voltage of the Ta target. 80

Figure 8-2. Influence of $p(N_2)$ on nitrogen and tantalum atomic %, roughness (R_q) and deposition rate. 82

Figure 8-3. As-deposited TaN based films. P_{Dep} = 0.66 Pa. 83

Figure 8-4. D spacing values of the (111) peak versus $p(N_2)$.......... 84

Figure 8-5. Surface and cross section SEM micrographs of films deposited at $p(N_2)$ = 0.13 (left) and 0.26 (right) Pa. 85

Figure 8-6. Influence of P_{Dep} on nitrogen and tantalum atomic %, roughness (R_q) and deposition rate for $p(N_2)$ = 0.26 Pa. 87

Figure 8-7. As-deposited TaN based films. $p(N_2)$ = 0.26 Pa. 88

Figure 8-8. D spacing values of the (111) peak versus P_{dep}.......... 89

Figure 8-9. As-deposited TaN based films. P_{dep} = 1.33, 2.00 and 2.66 Pa (left to right)....... 89

Figure 8-10. Surface SEM micrographs of films deposited at 0.66, 1.33, 2.00 and 2.66 Pa deposition pressures with a $p(N_2)$ of 0.26 Pa.. 91

Figure 8-11. Cross section SEM micrographs of films deposited at 0.66, 1.33, 2.00 and 2.66 Pa deposition pressures with a $p(N_2)$ of 0.26 Pa. 91

Figure 8-12. Influence of T_{sub} on nitrogen and tantalum atomic %, roughness (R_q) and deposition rate. 93

Figure 8-13. As Deposited TaN films. $p(N_2)$ = 0.26 Pa, P_{Dep} = 1.33 Pa................................ 94

Figure 8-14. D spacing values of the (111) peak for the films deposited at ambient, 523 K, 723 K and 923 K T_{Sub}.. 95

Figure 8-15. Surface SEM micrographs of TaN films deposited at ambient temperature, 523 K, 773 K and 923 K.. 96

Figure 8-16. Cross section SEM micrographs of TaN films deposited at ambient temperature, 523 K, 773 K and 923 K. 96

Figure 8-17. XRD results of TaO film deposited with a deposition pressure of 0.66 Pa and (pO_2) of 10%, before and after nitridation to show the presence of Ta_3N_5. All TaO films deposited converted to Ta_3N_5 with similar peak positions as seen here. 100

Figure 8-18. Hysteresis of Ta and Cr targets in an Ar/O_2 atmosphere. O_2 gas flow rate is adjusted over time to reflect the displayed $p(O_2)$ values, up to a peak $p(O_2)$ value before being ramped down again. 105

Figure 8-19. Flow chart depicting synthetic and analytical procedure used to synthesize doped and undoped Ta_3N_5 films.. 107

Figure 8-20. Cross section SEM micrographs depicting the morphology of TaO and TaCrO films before thermal annealing in NH_3 gas mixture, where a) TaCrO 10% pO_2, b) TaCrO 15% pO_2, c) TaCrO 20% pO_2, d) TaO 10% pO_2, e) TaO 15% pO_2, f) TaO 20% pO_2. 109

Figure 8-21. Cross section SEM micrographs depicting the morphology of TaO and TaCrO films after thermal annealing in NH_3 gas mixture, where a) TaCrO 10% pO_2, b) TaCrO 15% pO_2, c) TaCrO 20% pO_2, d) TaO 10% pO_2, e) TaO 15% pO_2, f) TaO 20% pO_2. 109

Figure 8-22. Top down SEM micrographs depicting the morphology of TaO and TaCrO films before thermal annealing in NH_3 gas mixture, where a) TaCrO 10% pO_2, b) TaCrO 15% pO_2, c) TaCrO 20% pO_2, d) TaO 10% pO_2, e) TaO 15% pO_2, f) TaO 20% pO_2. 110

Figure 8-23. Top down SEM micrographs depicting the morphology of TaO and TaCrO films after thermal annealing in NH_3 gas mixture, where a) TaCrO 10% pO_2, b) TaCrO 15% pO_2, c) TaCrO 20% pO_2, d) TaO 10% pO_2, e) TaO 15% pO_2, f) TaO 20% pO_2. 111

Figure 8-24. XRD diffractograms of TaCrO and TaO thin films where a) 10% pO_2 pre-nitridation, b) 10% pO_2 post-nitridation, c) 15% pO_2 pre-nitridation, d) 15% post-nitridation, e) 20% pO_2 pre-nitridation, f) 20% pO_2 post-nitridation. ♦ denotes the suspected chromium nitride peaks, and * denotes Ta_3N_5 peaks.. 112

Figure 8-25. SIMS depth profiles of TaCrO and TaO thin films before annealing. Silicon is observed earlier in the TaO films as the TaCrO films are thicker...................................... 115

Figure 8-26. SIMS depth profiles of TaCrO and TaO thin films after annealing. 115

Figure 8-27. Surface and cross section SEM micrographs depicting the morphology of TaCrO films after thermal annealing in NH_3 gas mixture, where a) TaCrO, Cr power = 10W, b) TaCrO Cr power = 20W, c) TaCrO Cr power = 30W, d) TaCrO Cr power = 40W, e) TaCrO Cr power = 10W, f) TaCrO Cr power = 20W, g) TaCrO power = 30W, h) TaCrO power = 40W. 117

Figure 8-28. XRD diffractograms of TaCrO and TaO thin films deposited at 10W, 20W, 25W, 30W and 40W, before and after nitridation. The control film was an otherwise identical TaO film deposited without any power on the Cr target. The ♦ symbol denotes the chromium nitride phase. 118

Figure 8-29. SIMS spectra of 10W, 20W, 25W, 30W and 40W TaCrO films after annealing, compared with TaO film deposited with 0W on the Cr target. 119

Figure 8-30. XRD diffractograms of TaCrO and TaO films annealed at 2h, 4h and 8h dwell times, where a) TaCrO 10% pO_2, b) TaO 10% pO_2, c) TaCrO 20% pO_2 and d) TaO 20% pO_2. ♦ denotes the silicon substrate peak, * denotes Ta_3N_5 peaks, Ω denotes $CrTaO_4$ peaks and Σ denotes Ta_2O_5 (tantite) peaks. 121

Figure 8-31. SIMS spectra of 2h, 4h and 8h thermally annealed TaO and TaCrO films deposited with 10% pO_2. 123

Figure 8-32. SIMS spectra of 2h, 4h and 8h thermally annealed TaO and TaCrO films deposited with 20% pO_2. 125

Figure 8-33. UV-Vis diffuse reflectance spectra of Ta_3N_5 standard film contrasted with 10W, 20W, 25W, 30W and 40W chromium doped films, with wavelength (nm) and photon energy (eV) included. Arbitrary units are used for absorbance intensity. 127

Figure 8-34. Hysteresis of Ta and Al targets in an Ar/O_2 atmosphere. O_2 gas flow rate is adjusted over time to reflect the displayed $p(O_2)$ values, up to a peak $p(O_2)$ value before being ramped down again. 130

Figure 8-35. Cross section SEM micrographs depicting the morphology of TaO and TaAlO films before thermal annealing in NH_3 gas mixture. Where a) TaAlO 10% pO_2, b) TaAlO 15% pO_2, c) TaAlO 20% pO_2, d) TaO 10% pO_2, e) TaO 15% pO_2, f) TaO 20% pO_2 132

Figure 8-36. Cross section SEM micrographs depicting the morphology of TaO and TaAlO films after thermal annealing in NH_3 gas mixture, where a) TaAlO 10% pO_2, b) TaAlO 15% pO_2, c) TaAlO 20% pO_2, d) TaO 10% pO_2, e) TaO 15% pO_2 and f) TaO 20% pO_2. 133

Figure 8-37. Surface SEM micrographs depicting the morphology of TaO and TaAlO films before thermal annealing in NH_3 gas mixture, where a) TaAlO 10% pO_2, b) TaAlO 15% pO_2, c) TaAlO 20% pO_2, d) TaO 10% pO_2, e) TaO 15% pO_2, f) TaO 20% pO_2. 134

Figure 8-38. Surface SEM micrographs depicting the morphology of TaO and TaAlO films after thermal annealing in NH_3 gas mixture, where a) TaAlO 10% pO_2, b) TaAlO 15% pO_2, c) TaAlO 20% pO_2, d) TaO 10% pO_2, e) TaO 15% pO_2, and f) TaO 20% pO_2. 135

Figure 8-39. XRD diffractograms of TaAlO and TaO thin films where a) 10% $p(O_2)$ pre-nitridation, b) 10% $p(O_2)$ post-nitridation, c) 15% $p(O_2)$ pre-nitridation, d) 15% $p(O_2)$ post-nitridation, e) 20% $p(O_2)$ pre-nitridation, f) 20% $p(O_2)$ post-nitridation. Where: * denotes Ta_3N_5 peaks. 136

Figure 8-40. SIMS spectra of TaAlO and TaO thin films before annealing. 138

Figure 8-41. SIMS spectra of TaAlO and TaO thin films after annealing. 139

Figure 8-42. SEM cross sections and surface images of annealed films deposited with 10 W, 20 W and 30 W. Where a) 10 W cross section, b) 20 W cross section, c) 30 W cross section, d) 10 W surface image, e) 20 W surface image, f) 30 W surface image. 141

Figure 8-43. XRD diffractograms of TaAlO and TaO thin films deposited at 10W, 20W and 30W, before and after nitridation. Control sample was deposited without power applied to the Al target. 142

Figure 8-44. SIMS depth profile of 10 W, 20 W and 30 W TaAlO films before annealing, compared with the TaO control film deposited without an aluminium plasma. 143

Figure 8-45. SIMS depth profile of 10W, 20W and 30W TaAlO films after annealing, compared with TaO film deposited with 0W on the Al target. 144

Figure 8-46. XRD diffractograms of TaAlO and TaO films annealed at 2, 4 and 8 hour dwell times, where a) TaAlO 10% pO_2, b) TaO 10% pO_2, c) TaAlO 20% pO_2 and d) TaO 20% pO_2. Where * denotes Ta_3N_5 peaks and Σ denotes Ta_2O_5 (tantite) peaks. 145

Figure 8-47. SIMS depth profiles of 2h, 4h and 8h thermally annealed undoped and Al doped films deposited with 10% pO_2. 146

Figure 8-48. SIMS depth profiles of 2h, 4h and 8h thermally annealed undoped and Al doped films deposited with 20% pO_2. 148

Figure 8-49. UV-Vis diffuse reflectance spectra of Ta_3N_5 standard film contrasted with 10W, 20W and 30W aluminium doped films, with wavelength (nm) and photon energy (eV) included. Arbitrary units are used for absorbance intensity. 150

Figure 8-50. CV plots of Ta_3N_5 in 0.1M KOH and 0.5 H_2SO_4 electrolytes performed at 3mV/s and two different potential ranges relative to the electrolyte pH. 152

Figure 8-51. Mott-Schottky plot of Ta_3N_5 electrodes ($p(O_2)$ = 10%) performed in 0.1M KOH electrolyte solution at 100Hz, 250Hz and 1000Hz across an applied potential range of -1V to 1.5V. 153

Figure 8-52. Cyclic Voltammetry scans of Cr-Ta_3N_5 films and Ta_3N_5 standard performed at 10mV/s under 100mW/cm^2 of illumination and in the dark. 155

Figure 8-53. Mott-Schottky plot of Cr-Ta_3N_5 and Ta_3N_5 electrodes performed in 0.1M KOH electrolyte solution at 100Hz, 250Hz and 1000Hz across an applied potential range of -1V to 1.5V. 156

Figure 8-54. Cyclic Voltammetry scans of Al-Ta_3N_5 films and Ta_3N_5 standard performed at 10mV/s under 100mW/cm^2 of illumination and in the dark. 158

Figure 8-55. Mott-Schottky plot of Al-Ta_3N_5 and Ta_3N_5 electrodes performed in 0.1M KOH electrolyte solution at 100Hz, 250Hz and 1000Hz across an applied potential range of -1V to 1.5V. 159

Figure 11-1. Plot showing the linear relationship between the capacitive current and different scan rates for Cr-Ta_3N_5 and Ta_3N_5 films. Scan rates of 5mV/s, 10mV/s, 100mV/s, 250mV/s and 500mV/s are shown for the selected voltage of 0.5V. 184

Figure 11-2. Plot showing the linear relationship between the capacitive current and different scan rates for Al-Ta_3N_5 and Ta_3N_5 films. Scan rates of 5mV/s, 10mV/s, 100mV/s, 250mV/s and 500mV/s are shown for the selected voltage of 0.5V. 185

Tables

Table 1.1. Summary of hydrogen generating technologies (Holladay et al. 2009). 6

Table 4.1. General sputtering rates of different metallic targets. These rates vary depending on variables like the target power, distance to the substrate and gases used. The rates below assume an applied power of approximately 600W/cm^2 and a target to substrate distance of 10cm (*Sputtering Yield Rates* 2019; Wasa 2012). 35

Table 5.1. Reported phases in the tantalum nitride system and their respective space groups (if reported). 39

Table 5.2. Collection of notable papers that report deposition of Ta_3N_5. 47

Table 6.1. A summary of Ta_3N_5 photo-electrode performance records in the published literature, where STH refers to the solar-to-hydrogen efficiency of the electrodes. 54

Table 6.2. List of notable nitrides to the field of water splitting. 63

Table 8.1. Processing parameters for TaN-based films deposited with varying $p(N_2)$, and the resulting film thickness and composition. All films deposited under total deposition pressure of 0.66 Pa. 80

Table 8.2. Processing parameters for TaN-based films deposited with varying P_{Dep}, and the resulting film thickness and composition. 86

Table 8.3. Deposition conditions of films deposited with substrate temperature. 92

Table 8.4. Sputtering parameters and thicknesses of Tantalum Oxide films. 99

Table 8.5. EDS elemental data for Tantalum Oxide films before and after annealing in NH_3. 99

Table 8.7. List of Potential Doping Candidates. 102

Table 8.8. Sputtering parameters and thicknesses of chromium doped and undoped tantalum oxide thin films, before and after NH_3 annealing. 108

Table 8.9. EDS elemental data for TaCrO and TaO thin films prior to and post annealing in NH_3. 113

Table 8.10. Sputtering parameters and thicknesses of 10W, 20W, 25W, 30W and 40W chromium doped films and the 0W control, before and after nitridation. 117

Table 8.11. EDS elemental data for TaCrO and TaO thin films deposited with 0 to 40 W Cr target power, prior to and post annealing in NH_3. 119

Table 8.12. Sputtering parameters and thicknesses of Al doped and undoped tantalum oxide thin films, before and after NH_3 annealing. 131

Table 8.13. EDS elemental data for TaAlO and TaO thin films prior to and post annealing in NH_3. 137

Table 8.14. Sputtering parameters and thicknesses of 10W, 20W and 30W Al doped films and the 0W control, before and after nitridation. 140

Table 8.15. EDS elemental data for TaAlO and TaO thin films prior to and post annealing in NH_3. 140

Table 8.16. Carrier concentration as determined from Hall measurements of Ta_3N_5, deposited with $p(O_2)$ = 10%, 15% and 20%, after nitridation.. 151

Table 8.17. Carrier concentration as determined from Hall measurements of the Ta_3N_5 standards and Cr-Ta_3N_5 films.. 154

Table 8.18. Carrier concentration as determined from Hall measurements of the Ta_3N_5 standards and Al-Ta_3N_5 films. 157

Chapter 1: Introduction and Context of this Work

1.1 Structure of this Thesis

This thesis is the culmination of work spanning several topics relating to materials science and solar-driven water splitting, specifically in the context of the photosensitive material Ta_3N_5. But before providing some background on the topics discussed in the research, it is necessary to contextualise this work and justify why hydrogen generation via solar water splitting and subsequently Ta_3N_5 are compelling research topics. This initial introduction chapter will focus on providing the background to the work, which include climate change, living standards, sustainable hydrogen generation and the future hydrogen economy. It is against this backdrop that the aims of the project will also be defined.

Chapters 1 and 2 contextualise the need for this work and describe the basic properties of semiconductors in addition to synthetic methodology and analytical techniques relevant to this project. Chapter 3 introduces solar driven water splitting, providing an explanation of photo-electrochemical water splitting and photo-electrochemical cells contrasted with particle suspensions for solar driven water splitting. Chapter 4 will explore sputter deposition, specifically magnetron sputtering, before moving on to a brief overview of the tantalum nitride phase spectrum and phases within it that are important to this work in chapter 5.

The literature background on Ta_3N_5 in the realm of water splitting will be explored in chapter 6, including the various synthetic methods and the performance thus far of Ta_3N_5 as a water splitting material, before closing with a brief overview of other compelling water splitting nitrides in the field. The purpose of this chapter is to give the reader a clear idea of the conclusions currently able to be drawn from research in water splitting nitrides, and especially Ta_3N_5, then draw salient questions from the knowledge gaps in the field.

Chapter 7 will cover the techniques and equipment used to synthesise and analyse the films deposited (TaN, TaO and Ta_3N_5). The results and discussion are covered in a combined chapter 8 and are split up in sections corresponding to the timeline over which this project took place; TaN deposition, TaO deposition and ammonia annealing (ammonolysis), and the final characterisation of performance properties in Ta_3N_5 and doped Ta_3N_5 films. The work will close with a review of the outcomes achieved and the avenues available for future work.

1.2 Living Standards, Energy and Climate Change

Since the industrial revolution, society has relied upon fossil fuels as the primary energy source in the pursuit of ever-increasing living standards, which has resulted in a global

economy predicated on this energy source. In this time, rapid progress in science and technology has yielded unprecedented improvements to living standards and people are now living longer, healthier and more prosperous lives (Goklany 2007). More recently, the environmental consequences of our choice of energy source are also being revealed (Solomon 2007). If we are to avoid a collapse of our quality of lives, modern society will need to undergo a fundamental shift from the current methods of energy generation, especially if we are to keep growing our energy consumption at the rates we currently do (Shafiee & Topal 2009).

Our societal energy demands have rapidly increased over the last century; In 1900, the global consumption of energy was 50 exajoules per annum, by 1950 100 exajoules per annum were consumed (Vlachogianni & Valavanidis 2013), and by 2010 550 exajoules per annum were consumed (Soprano 2013). This trend is visualised below in **Figure 1-1** with energy use expressed in terawatt-hours (TWh).

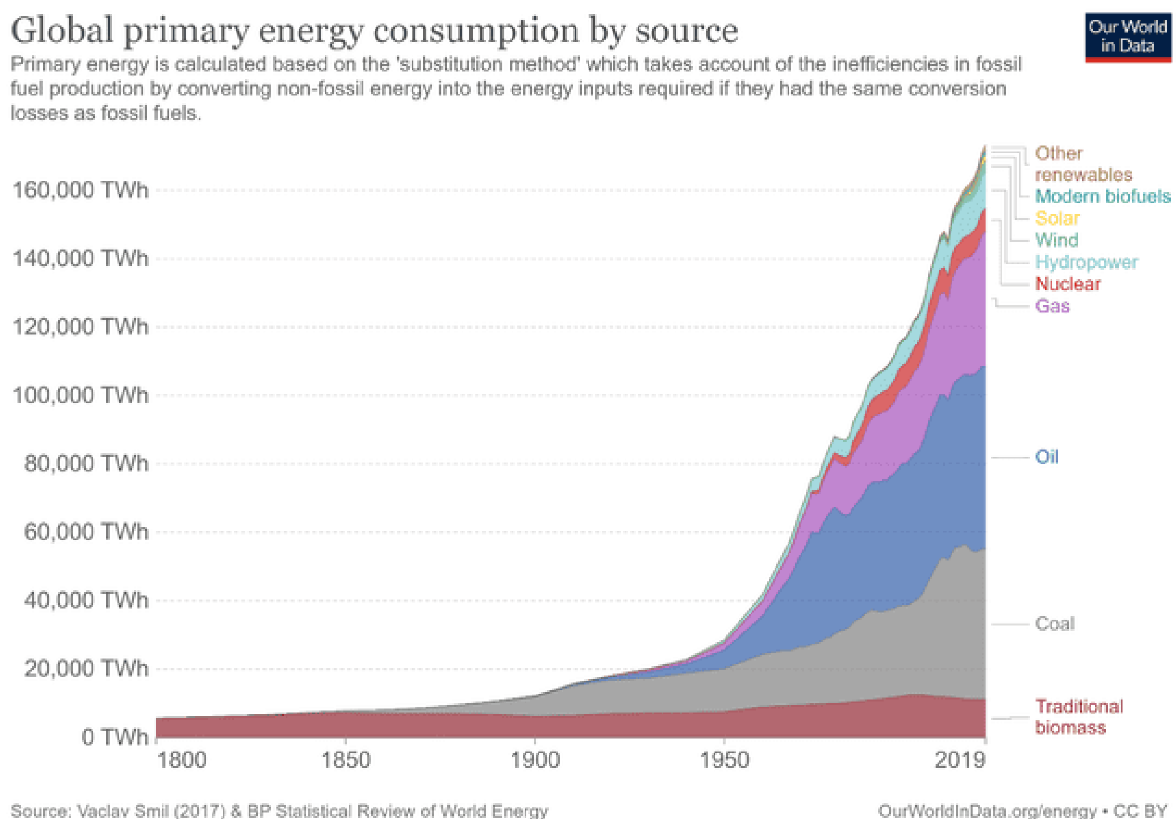

Figure 1-1. Global primary energy consumption by source expressed in terawatt-hours (Ritchie & Roser 2020).

Prior to the industrial revolution, the annual energy consumption by human civilisation was near 10 exajoules/per annum and was primarily ‘muscle’ energy. Throughout the early 2000’s alone, the global consumption of energy was increasing at a yearly rate roughly equal to the

total worldwide consumption in the 1880's (Bithas & Kalimeris 2016). As the global population continues to grow and the pressure to live better lives in as many ways as possible in as many countries as possible also grows, the demand for energy will continue growing exponentially.

This burgeoning growth in energy demand has been primarily met through the burning of biofuels and coal, especially throughout the later portion of the 19th Century through to the mid-20th Century, at which time other fossil fuel sources of oil and natural gas began to make a significant contribution (Bithas & Kalimeris 2016). The burning of these fuels creates significant greenhouse gas emissions, which are known to act as an atmospheric heat shield, impacting the Earth's climate.

At the present time, it is well evidenced that human generated carbon dioxide emissions resulting from the consumption of these fossil fuels are intrinsically linked to the growing CO_2 atmospheric presence (Boden, Marland & Andres 2009), and subsequent change to climate mechanisms (Oreskes 2004). If the growing demand for energy continues to be met by fossil fuels, ecosystems worldwide will suffer extensively, and human society will not be exempt. With a minimum 2 degree increase in global temperatures by 2100 appearing unavoidable at this time (Raftery et al. 2017), it is imperative that the use of greenhouse gas emitting energy sources be curtailed as soon as possible so as to limit the extent of the damage, which includes not only ecological collapse (McCarty 2001) but also major risks to the sustained living standards of western civilisation (Hsiang et al. 2017).

1.3 Hydrogen as an Alternative Fuel and a Theoretical Hydrogen Economy

In the search for alternative energies, hydrogen has been identified as a promising alternative fuel source (Johnston, Mayo & Khare 2005). What makes hydrogen attractive is that it can be utilised in a similar fashion to fossil fuels albeit without the carbon emissions; its use as a combustible fuel produces only water and nitrogen oxides (if burned in air and not pure oxygen) and it can take advantage of already existing natural gas infrastructure without significant upgrade expenditure. Liquid hydrogen also possesses a superior energy density per mass relative to that of most traditional fuels (see **Figure 1-2**). In fuel cells, which do not utilise hydrogen in a combustion reaction, hydrogen and oxygen are consumed to produce water and electrical energy, which can then be stored in a battery and used in an electric motor (Ogden 1999).

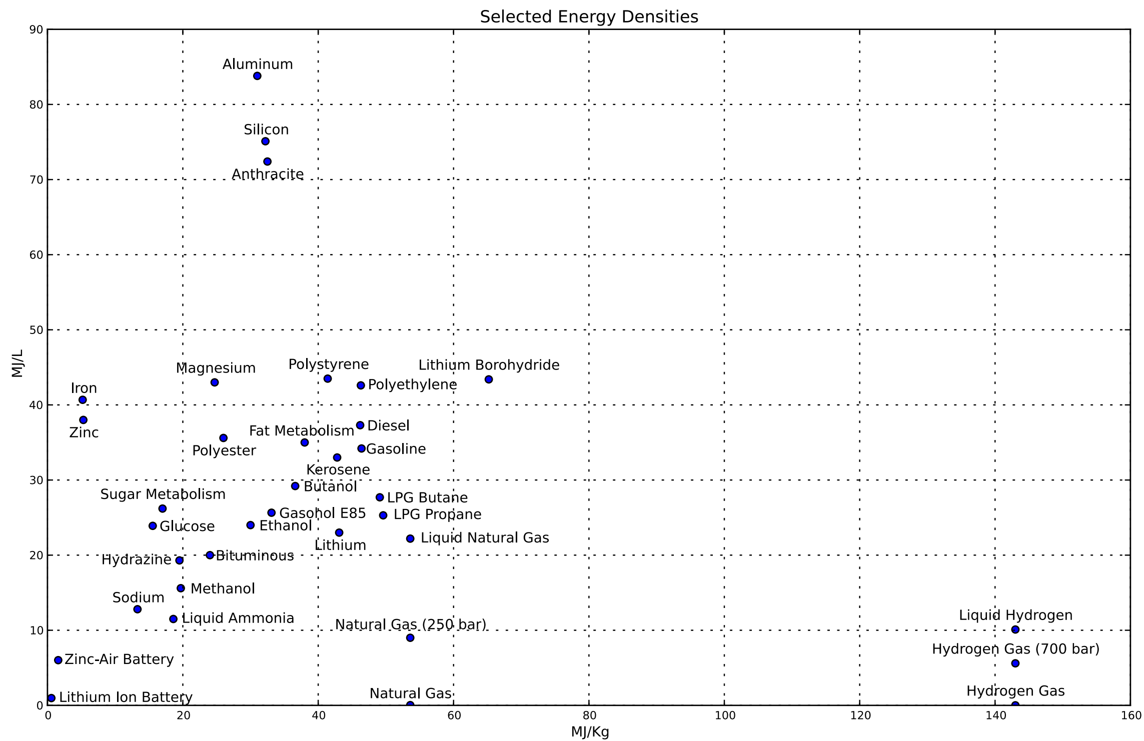

Figure 1-2. Energy densities of various fuels, horizontal scale is density per mass, vertical scale relates density per volume (Dial 2008).

In fact in 1807, before petroleum was properly refined for use in the internal combustion engine (ICE), hydrogen was the fuel used to power the first ICE vehicle concept (Premkartikkumar & Pradeepkumar 2015). Hydrogen as a fuel source represents a compelling alternative for long distance applications, such as in trucking or commuter roles, where the battery storage of electric vehicles (EVs) presents a barrier in the form of limited energy density and charging or refilling time. Additionally, intercontinental goods transport and air travel both represent significant challenges when it comes to renewable alternatives.

Shipping utilises the least refined oil available, which no other industry can feasibly use, and subsequently generates significant pollution, whereas air travel in its current form (especially long-distance flights) requires the use of jet fuel due to high energy requirements and limited storage space. Hydrogen can be used for both of these applications, either in fuel cells on board ships (Farrell, Keith & Corbett 2003) or combusted in jet engines (Khandelwal et al. 2013). The use of hydrogen fuel on a large scale could also offer energy efficiency benefits due to the potential for widespread fuel cell usage for both power generation and transportation, with most combustion engines being between 20-40% practical efficiency, whereas fuel cells can range between 40% and 60% or higher depending on design (Li, X 2007).

Large scale hydrogen reliance would however require significant technical development with respect to improved storage and distribution technologies, and it must also be recognised that on a volume basis, the energy density of hydrogen compares poorly to gasoline or natural gas. While costly, such challenges are not considered insurmountable (Marbán & Valdés-Solís 2007). The clean and sustainable production of hydrogen fuel is the limiting step in the development of a hydrogen economy.

1.4 How can Hydrogen be Sustainably Obtained?

At present, 95% (Ogden 1999) of the world's hydrogen is extracted from petroleum and natural gas via the steam reformation process, with electrolysis and biomass as the alternative routes, although neither comprise a significant portion of hydrogen generation. Hence, hydrogen produced at present is far from carbon emission-free. Hydrogen production methods and future prospects in the US, and the relative amount produced, is displayed below in **Figure 1-3.**

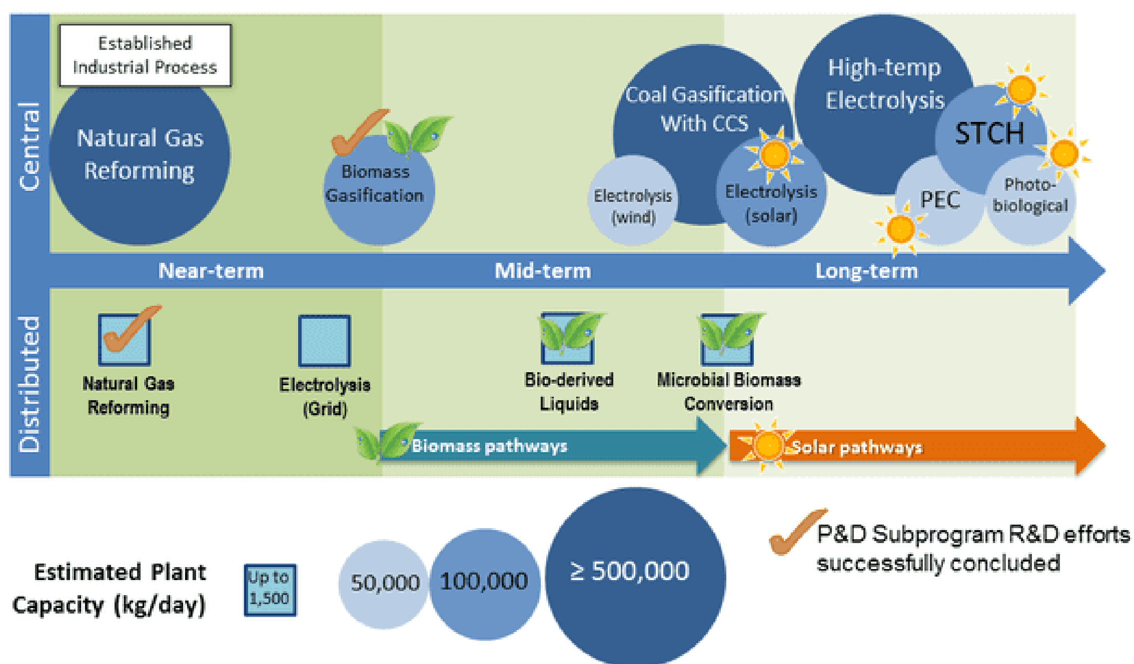

Figure 1-3. Near-term, mid-term and long-term predictions for the capacity of hydrogen production methods in the US, produced by the US Department of Energy (*Laboratory* 2018).

Addressing hydrogen generation via electrolysis first, this method of hydrogen production presents several issues. While the industrial use of electrolysis exhibits system efficiencies of 50-70%, electrolysis is expensive in comparison to the established gas reformation method. It also produces more emissions when using fossil fuel derived electricity (Holladay et al. 2009). This can be somewhat alleviated if hydrogen is produced on site as opposed to being

transported long distances via shipping. It is possible to utilise renewable electricity, be it solar, wind or hydro, to power electrolysis, however from an efficiency point of view it would be preferable to use sunlight to split water directly. This is because generating electricity from renewable methods to then use it to split water is a two-step process, while splitting water directly with sunlight is simpler. There exist numerous methods for hydrogen generation that are currently under active investigation or are even being built on a commercial scale. **Table 1.1**, as compiled by Holladay and colleagues, lists a few of them.

Table 1.1. Summary of hydrogen generating technologies (Holladay et al. 2009).

Technology	Feed stock	Efficiency	Maturity
Steam reformation	Hydrocarbons	70-85%	Commercial
Partial oxidation	Hydrocarbons	60-75%	Commercial
Biomass gasification	Biomass	35-50%	Commercial
Alkaline electrolysis	H_2O + electricity	50-60%	Commercial
Microbial electrolysis cells	Biomass + electricity	78%	Long term
Ammonia reforming	Ammonia	n/a	Near term
Thermochemical water splitting	H_2O + heat	50%	Long term
Photo-electrochemical water splitting	H_2O + sunlight	12.4%	Long term

For hydrogen fuel to be truly carbon-emission free and a viable alternative to established energy sources, a new method of production must be developed that does not generate greenhouse gases in its operation and can be sourced renewably. Additionally, for commercial viability, it must also be able to supply hydrogen at sufficiently low cost to make the price compelling in comparison to fossil fuel-based energy.

These requirements can be met by a technique referred to as solar driven water splitting or photoelectrolysis. This technique requires materials capable of absorbing the energy from sunlight to drive the decomposition of water into H_2 and O_2, some examples of these materials include titanium dioxide (TiO_2), tungsten oxide (WO_3) and tantalum nitride (Ta_3N_5).

1.5 Project Aims

The primary aim of this project is to synthesize Ta_3N_5 via magnetron sputter deposition for use as a photo-electrode material. Secondary to this is to produce a doped Ta_3N_5 material with p-type properties. Several aims have been set to achieve this, indicated below in order of priority:

Project Aim 1: To deposit tantalum nitride (Ta_3N_5) thin films with controlled performance-related properties using sputter deposition. The following objectives are set to achieve this aim:

- Deposit tantalum nitride films in several deposition conditions conducive to the deposition of higher order nitrides through control of sputtering parameters; gas partial pressures (pN_2), total chamber pressure (pDep) and target power.
- Characterise the deposition yield, phase, elemental content, and microstructural properties of deposited films.

This aim seeks to acquire the necessary processing protocols that will enable undoped Ta_3N_5 thin films to be grown in a controlled manner. The development of this synthetic method will enable tailoring of fundamental material properties such as composition, structure, microstructure, surface roughness (Rq), optical properties, and film thickness.

***Sub Aim 1**:* To determine the processing protocols that will enable synthesis of undoped Ta_3N_5 thin films from deposited tantalum oxide (Ta_2O_5) films in a controlled manner.

This sub-aim was incorporated due to the difficulty of directly sputtering Ta_3N_5 thin films. The Ta_3N_5 phase is synthesized via deposition of amorphous tantalum oxide films, which are then thermally annealed in a NH_3/N_2 gas mixture to produce the Ta_3N_5 phase. This is intended to be done in a reproducible manner to produce films with controllable properties as per Project Aim 1.

***Sub Aim 2**:* To provide a mechanism for the reaction of Ta_2O_5 to Ta_3N_5 that accounts for the challenges faced in depositing Ta_3N_5 directly using sputter deposition.

Project Aim 2: To synthesize doped Ta_3N_5 thin films with controlled performance-related properties via sputter deposition.

This aim extends upon Project Aim 1 by introducing acceptor dopant incorporation during the Ta_3N_5 thin film synthetic route with the goal of producing p-type Ta_3N_5. The following objectives were set to meet this aim:

- Select dopant candidates likely to promote p-type semiconductivity and provide mechanisms for dopant incorporation.

- Deposit doped tantalum oxide films and anneal in NH_3 per Sub Aim 1 to achieve a doped Ta_3N_5 film.
- Characterise the electronic and optical properties of the films.
- Prepare doped and undoped Ta_3N_5 films as electrodes and determine electrochemical properties of the films.

Chapter 2: Principles of Semiconducting Materials

A semiconductor is a material that exhibits conductivity in between the relative extremes of an insulator and conductor. Semiconductors are a class of materials that have defined the path of modern technology since silicon-based transistors were first developed and popularized in the early to mid-20th century. Several electronic properties inherent to semiconducting materials had been documented as early as the 19^{h} century, with discoveries such as the thermoelectric effect, the Hall effect and the photoelectric effect (Jenkins 2005) taking place in this time. These phenomena are no less relevant now, and since a few of them stand as fundamental material properties in this project, this chapter is included to provide some background information to appropriately equip the reader for later sections.

2.1 Properties of Semiconductors

While the history of semiconductors stretches nearly three centuries, only the pertinent fundamentals will be covered in this subsection. These include intrinsic and extrinsic semiconductors, the band theory of semiconductors, and the associated concepts of band gap and band bending. Additionally, p and n type semiconductors will be covered briefly. These concepts will then be built upon in the following subsection, where the electronic properties of semiconductors will be covered.

2.1.1 Intrinsic and Extrinsic Semiconductors

There are two types of semiconductors: intrinsic and extrinsic. Intrinsic semiconductors are semiconductors in extremely pure form. They are also known as undoped semiconductors. Examples of such semiconductors include silicon and germanium. Intrinsic semiconductors possess low electrical conductivity at room temperature, which makes them not ideal for use in modern electronics. In contrast, extrinsic semiconductors are semiconductors that contain small amounts of impurity elements, which is referred to as the dopant element. Extrinsic semiconductors are widely used in electronics and will be the focus in this body of work. Extrinsic semiconductors are more conductive relative to intrinsic semiconductors, and as such are widely used in modern electronics due to the control over the electronic properties of the semiconductor afforded by using specific dopants in controlled quantities. Examples of extrinsic semiconductors include boron doped silicon. Extrinsic semiconductors can be further classified as n-type or p-type, which will be described in more detail later in this chapter.

2.1.2 Band Theory: Band Gap and Band Bending

While the application of semiconductor materials was not prevented by the lack of a model to describe their properties, it was however hindered. It wasn't until 1931 that band theory in

semiconductor materials was proposed by Alan Wilson (Wilson 1931). Wilson derived a model to explain the electronic nature of insulators, conductors and semiconductors using quantum mechanics; his model describing the concept of energy 'bands', a conduction band (CB) and a valence band (VB) in a given crystal material. The conduction band describes a region of several empty orbitals through which electrons can move freely, thereby creating a current (and voltage). The valence band is also comprised of several orbitals occupied or partially occupied by electrons, namely the orbital closest to the CB. In non-metals, these bands are separated by a band gap, a range in which no electron energy states can exist. A simple depiction of this is given below in **Figure 2-1**.

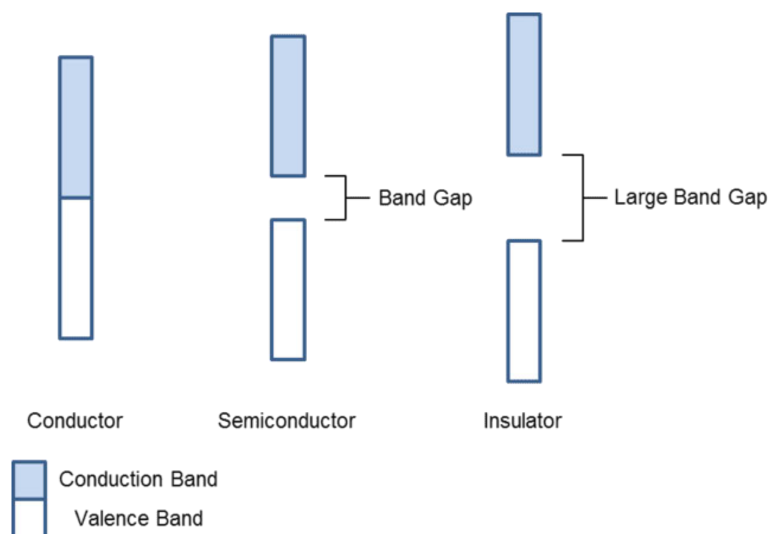

Figure 2-1. Hypothetical energy bands in conductors, semiconductors and insulators.

It was posited by Wilson that conductors possessed very close or overlapping bands, allowing easy electron transfer from the VB to CB, while semiconductors and insulators possessed larger band gaps, insulators especially possessing very large band gaps that impinge the free flow of electrons.

Semiconductor materials will exhibit conductivity when electrons are excited and are able to traverse the band gap from the VB to the CB, leaving a 'hole' in the VB, the implications of which will be elaborated on in the following section. This transfer takes place when the semiconductor material is exposed to energy greater than the band gap energy, typically measured in electron volts (eV). An example of this process is the photoelectric effect, where sunlight provides the energy to excite electrons from the VB to CB.

2.1.3 p-type and n-type Semiconductors

If a small amount of another element is introduced into positions in a hypothesised perfect crystal lattice of a semiconductor material, the conductive properties of the material can be

changed by the relative amount of electrons or electron holes possessed by the impurity element (Cardona & Peter 2005). This is demonstrated with the dopants Arsenic and Aluminium below in **Figure 2-2**.

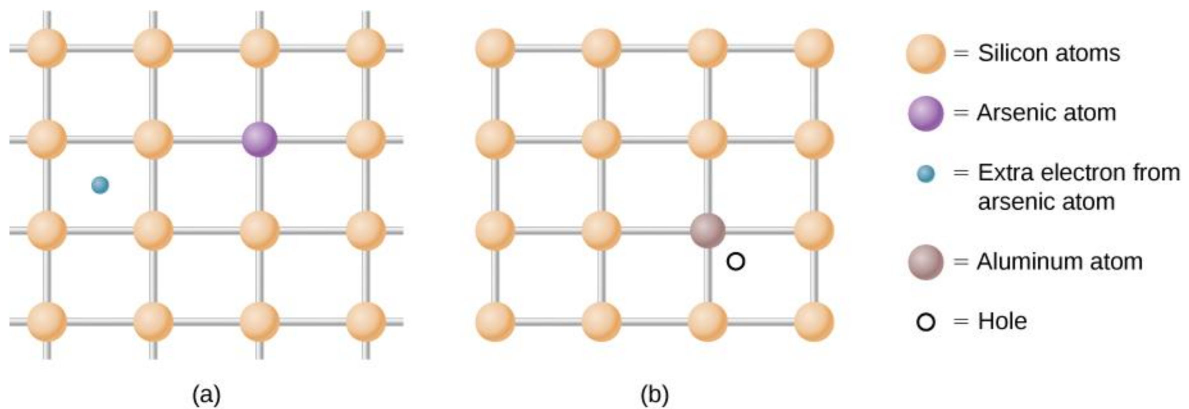

Figure 2-2. Visual depiction of (a) n-type As doped Si and (b) p-type Al doped Si (Ling, Sanny & Moebs 2016).

In this example, arsenic possesses an extra electron compared to the silicon atom it substitutes, and its inclusion at a silicon site as an impurity adds a delocalised electron. Hence the majority charge carriers are electrons and an n-type (or negative type, due to excess electrons) material is produced (Schubert 2015). Conversely, p-type semiconductors possess a dopant element with fewer electrons than the host atoms, resulting in holes acting as the dominant charge carriers in the material. **Figure 2-3** below depicts how the inclusion of dopant impurities alters the band structure in p-type and n-type semiconductors.

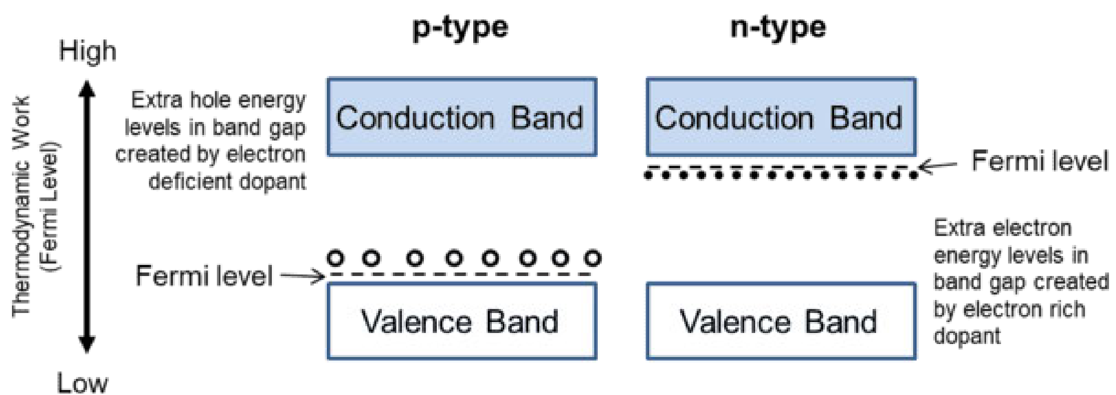

Figure 2-3. Simplified band diagram of p-type and n-type semiconductors, including the shifted fermi level resulting from dopant impurities (Nave 2007).

As can be seen in Figure 2-3, the fermi level of a p-type semiconductor is lower relative to an n-type semiconductor. The fermi level of a solid object can be defined as the thermodynamic work required to add an electron to the system, thus in the case of p-type materials a lower fermi level is observed as there are more holes available and therefore less work to be done.

The converse is true with n-type materials, where there exists an excess of electrons and so more work is required, raising the fermi level of the semiconductor. The properties of p-type and n-type semiconductors can be utilised in a single device, such as a solar cell, when a p-n junction is formed between the two materials (Nelson 2003). This is the basis of photovoltaics, however despite the similarities to photoelectrolysis, it is beyond the scope of this project.

With these fundamental aspects of band theory, band gaps and p-type and n-type semiconductors established, it is now possible to introduce concepts important to the topic of semiconductors in photo-electrochemical water splitting.

2.2 Semiconductors and Photo-electrochemical Cells

The process of solar driven water splitting is predicated on the ability of semiconductor materials to absorb energy from the solar spectrum and convert this energy into a current. While the sequence of this process as it relates to water splitting will be broken down in detail in chapter 3, this section aims to expand on the previously established concepts of band theory as they relate to this process.

2.2.1 Semiconductor and Electrolyte Interfaces

This subsection aims to explain in more detail the background behind topics relating to band bending, band structures, carrier concentration and their relationships and effects on the overall water splitting efficacy of the material in question. Further consideration of these concepts is necessary to help contextualise and aid in understanding the later investigations in the results and discussion which will include Mott-Schottky analysis and Hall effect measurements.

Photo-electrochemical systems are predicated on the junction formed when a solid semiconductor material contacts an electrolyte solution. A junction is formed at the interface between these two materials, and due to the disparity in their respective electron energies, a process of equilibration takes place. This process of equilibration results in a phenomenon referred to as band bending with upwards band bending exhibited at the semiconductor/electrolyte interface, indicative of an n-type electrode (a p-type electrode would instead exhibit downwards bending). The equilibrium between band states at a semiconductor electrode and electrolyte interface is depicted below in **Figure 2-4**.

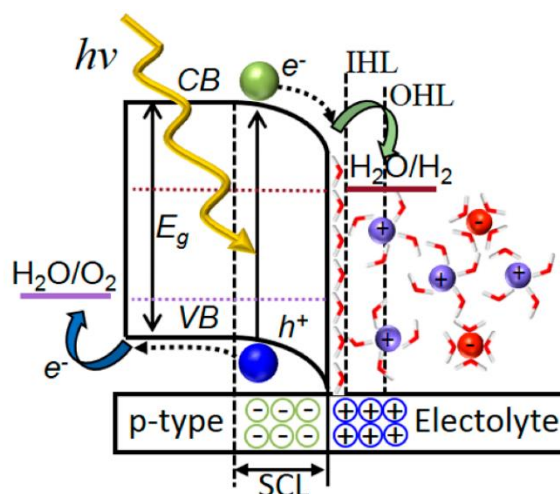

Figure 2-4. Depiction of band bending and photo-electrochemical water splitting process at the interface region between a p-type semiconductor electrode and alkaline electrolyte, where E_g is the band gap, SCL is the space charge layer/depletion layer, IHL is the inner Helmholtz layer and OHL is the outer Helmholtz layer (Bayrak Pehlivan et al. 2019).

The concept of band bending receives a great deal of focus in the fields of electrochemistry and gas sensors due to the way in which it governs the separation of charges in the space charge region and the diffusion of charge carriers, like ions, electrons and holes (Wang, C et al. 2010). It is also important for the same reasons, although receives less direct attention, in the field of solar water splitting.

2.2.2 The Depletion Layer

There exists a region within the doped semiconductor which has been depleted of charge carriers (electrons in n-type materials, holes in p-type materials) from the equilibration process. This region is referred to as the depletion layer and sits as a barrier between the deeper regions in the semiconductor with a neutral charge and the interface. This region is an important component of doped semiconductor electrochemical models, and its characterisation plays a role in the derivation of the Mott-Schottky equation, which is elaborated on in the following section. The depletion layer is also commonly referred to as the space charge layer (or SCL per **Figure 2-4**).

2.2.3 Mott-Schottky Analysis: Flat Band Potential and Carrier Concentration

The potential (V) required to bring the band bending at the semiconductor band edges back to their flat band positions is referred to as the flat band potential (V_{fb}). The V_{fb} can also be described as the potential at which there is no depletion layer at the semiconductor:electrolyte junction. Mott-Schottky analysis is a useful technique for determination of the V_{fb} and carrier concentration. V_f and carrier concentration can be determined from Mott-Schottky plots, which are generated from the reciprocal of the square of capacitance vs voltage. **Equation 1**

provides the Mott-Schottky equation, which is used to calculate V_{fb} and carrier concentration (Gelderman, Lee & Donne 2007). Capacitance is determined via electrochemical impedance measurements, with a certain frequency range applied across several voltage set points.

$$\frac{1}{C^2} = \frac{2}{\varepsilon\varepsilon_0 A^2 e N_D}\left(V - V_{fb} - \frac{k_B T}{e}\right) \qquad \text{(Equation 1)}$$

Where C and A are the electrode/electrolyte interfacial capacitance and electrode area (respectively), ε is the dielectric constant of the semiconductor, ε_0 is the permittivity of free space, N_D the number of dopants (carrier concentration), V the applied voltage, V_{fb} the flat band potential, k_B is Boltzmann's constant, T the absolute temperature and *e* is the elementary charge. The Mott-Schottky equation can be derived from the equation relating the width of the depletion layer given below in **Equation 2**.

$$\omega = \left[\frac{2\epsilon}{e N_D}(V + V_{bi})\right]^{\frac{1}{2}} \qquad \text{(Equation 2)}$$

Where V_{bi} is the built-in potential and ω is the width of the depletion layer. This is related to the capacitance of an electrode of area A by **Equation 3**, which when substituted with Equation 2, the Mott-Schottky equation (Equation 1) can be obtained.

$$C = A\frac{\epsilon}{\omega} \qquad \text{(Equation 3)}$$

The Mott-Schottky equation can be used to relate V with the capacitance such that with the graphed values of $1/C^2$ vs V will yield a straight-line graph. The V_{fb} and the dopant density (N_D) are determined by calculating the slope (**Equation 4**) and extrapolating a straight line from the plotted values to determine the x-intercept (**Equation 5**). Mott-Schottky plots of Ta_2O_5 electrodes are displayed in **Figure 2-5** to provide an example of the plots generated.

$$Slope = \frac{2}{\varepsilon\varepsilon_0 A^2 e N_D} \qquad \text{(Equation 4)}$$

$$V_{fb} + \frac{k_b T}{e} \qquad \text{(Equation 5)}$$

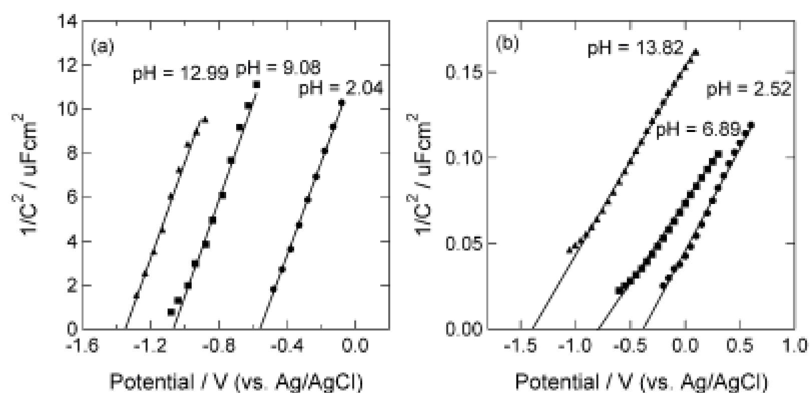

Figure 2-5. Mott-Schottky plots of Ta_2O_5 electrodes under various pH conditions, as determined by Chun and colleagues (Chun et al. 2003). This depicts the linear relationship between the reciprocal of capacitance squared and voltage.

The dopant density is a value that represents the density of dopants in the given material, which is an important metric in evaluating doped semiconductor materials. To contrast the Mott-Schottky plot an n-type semiconductor with a p-type, **Figure 2-6** is provided below.

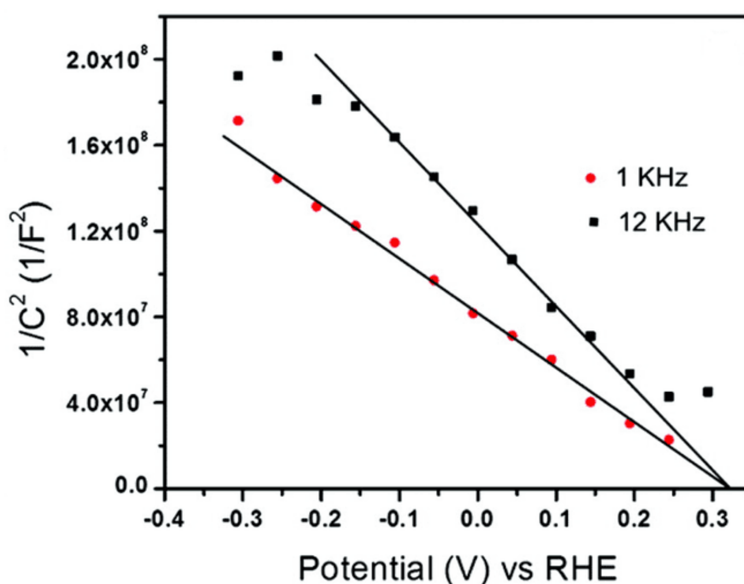

Figure 2-6. Mott-Schottky plot of p-doped $CuNb_3O_8$ in 0.5M Na_2SO_4 electrolyte solution (Joshi & Maggard 2012)

A Mott-Schottky plot of the Ta_3N_5 electrodes developed in this project is provided as an example in **Figure 2-7**.

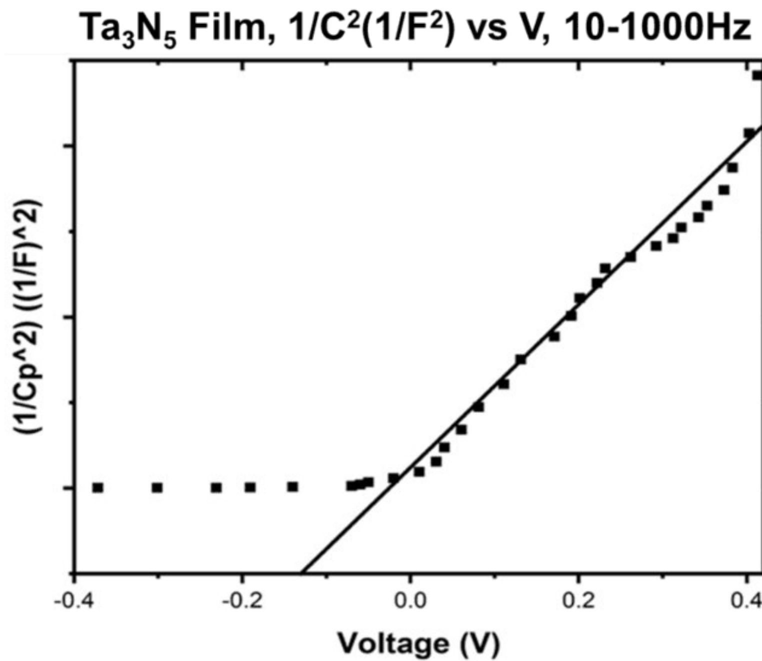

Figure 2-7. Mott-Schottky plot of Ta_3N_5 electrode, generated at 10-1000Hz frequency range in 0.1M KOH electrolyte solution.

As can be seen, a straight line of positive slope is generated in the region of 0-0.4 V, which is indicative of an n-type semiconductor material (Bott 1998). From the generated line, the dopant density can be determined by calculation of the slope and rearrangement of Equation 1, and the flat band potential by extrapolating $1/C^2 = 0$ and obtaining the x intercept. It should however be noted that these values are sensitive to experimental conditions and will change with variation in the applied frequency or electrolyte characteristics (i.e resistance, pH, temperature, sample movement).

Another method used to characterise the dopant properties of semiconductors is the Hall effect, which will be explained more in the following section. Traditionally Hall effect measurements are preferred to Mott-Schottky analysis as the accuracy of Mott-Schottky measurements are heavily reliant on the electrochemical setup used in determining capacitance. Because the Mott-Schottky formula considers many aspects of the electrochemical environment, the results may be prone to error if the experiment is not performed correctly.

Additionally, the values calculated using the Mott-Schottky approach are representative only of the specific electrochemical environment in which they're performed, as can be seen above in Figure 2-5 where different curves are produced with different pH values. This is also true when using different frequencies or voltage ranges.

2.2.4 Hall Effect and Van Der Pauw Method

The Hall effect is an electromagnetic phenomenon first discovered by Edwin Hall in 1879. Essentially, the hall effect describes the generation of a potential difference across an electrical conductor when a magnetic field is applied in a direction perpendicular to the flow of the current across the material in question. This phenomenon is a simple principle and is applied across many fields, from proximity sensors and speed detection technology to material characterisation.

The Van Der Pauw method provides the resistivity of the material using the 4 contact approach displayed below in **Figure 2-8** (Philips'Gloeilampenfabrieken 1958). The method involves the application of conductive contacts to 4 corners of an arbitrary shape (or 4 edges of a circle at equidistant positions). A current is applied in a theoretical x or y axis, (point 1 to 2 or 1 to 4 and vice versa) but not z (point 1 to 3), the latter of which is used to determine the resistivity as displayed above (R_A and R_B).

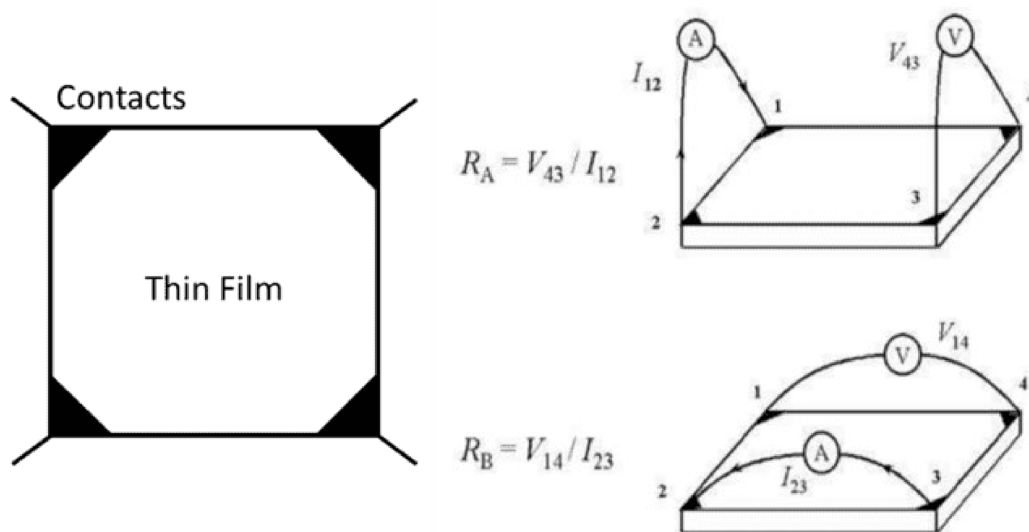

Figure 2-8. Diagram depicting Van Der Pauw measurement contact placement on a thin film (left) and the current and voltage measurements on a thin film material using Ohm's law to calculate resistance along the vertical and horizontal edges (right) (Rietveld et al. 2003).

The Van Der Pauw formula is given below in **Equation 6** as:

$$e^{-\frac{\pi R_A}{R_S}} + e^{-\frac{\pi R_B}{R_S}} = 1 \qquad \textbf{(Equation 6)}$$

Where R_S is the sheet resistance and R_A and R_B are the calculated resistances of two opposing parallel sides. Provided two resistance values R_A and R_B, determined from current and voltage values measured along the vertical and horizontal edges of a given sample (as depicted above in Figure 2-8), the sheet resistance can then be calculated using **Equation 7**:

$$R_S = \frac{\pi R_{AB}}{\ln 2} \qquad \text{(Equation 7)}$$

Hall effect measurements are performed using the same experimental set up, albeit with the addition of a magnet and further formulae. The Hall voltage is defined in **Equation 8** below:

$$V_H = \frac{IB}{qn_s} \qquad \text{(Equation 8)}$$

Where V_H is the hall voltage, I is the current, B is the strength of the magnetic field (Wb/cm^2), q is the elementary charge and n_s is the sheet electron density (the electron density, n, multiplied by the thickness of the film, t). The Hall voltage is determined by the same approach as used in the Van Der Pauw method to determine sheet resistance: voltages are generated between the contacts at each corner of the sample, except a magnet is also moved over the sample such that a perpendicular magnetic field is generated. This is done twice, and the voltages are recorded for these two magnetic fields. The Hall voltage is calculated from the difference between the positive and negative magnetic fields (shown as p-n below), as per **Equation 9**:

$$V_H = \frac{V1_{p-n} + V2_{p-n} + V3_{p-n} + V4_{p-n}}{8} \qquad \text{(Equation 9)}$$

The determination of the Hall voltage then allows the calculation of the sheet electron density. The polarity of the Hall voltage also indicates whether the material is p-type or n-type; a positive polarity indicates p-type, and a negative polarity n-type. Further calculations can provide the charge carrier concentration, which can also be used to determine whether the material is p-type or n-type in the same manner as V_H, and the mobility of the majority carrier. These formulae are given below.

The resistivity (ρ) of a semiconductor is determined using **Equation 10**:

$$\rho = \frac{1}{q(n\mu_n + p\mu_p)} \qquad \text{(Equation 10)}$$

Sheet density can be derived from the alternative formula, given below in **Equation 11**:

$$R_S = \frac{1}{qn_s\mu_m} \qquad \text{(Equation 11)}$$

This can be rearranged to give **Equation 12**:

$$\mu_m = \frac{1}{qn_sR_s} \qquad \text{(Equation 12)}$$

Where ρ = resistivity, q = the elementary charge, μ_n = the mobility of electrons, μ_p = the mobility of holes, R_s = sheet resistivity (resistivity divided by sample thickness), n_s = sheet density and μ_m = mobility of the major carrier.

2.2.5 Cyclic Voltammetry

Cyclic voltammetry (CV) is an electrochemical technique that is often used to characterise the electrochemical nature of semiconductor materials in the field of photoelectrochemistry (Kissinger & Heineman 1983). When a range of voltages are applied to a semiconductor submerged in an electrolyte solution, a corresponding current is generated in the cell when the voltage applied becomes greater than the voltage predicted by the Nernst equation (Feiner & McEvoy 1994).

The technique is performed by cycling the potential of a working electrode (WE), which is compared to the potential of a reference electrode (RE) and connected in a circuit with a counter electrode (CE) and measuring the resulting current. The applied potential is ramped versus time to a maximum point, allowing oxidation to occur at the electrode surface, before being cycled in reverse to produce a negative current and corresponding reduction reaction. A cyclic voltammogram is produced by plotting the current generated versus the potential applied to the working electrode, as seen in **Figure 2-9**.

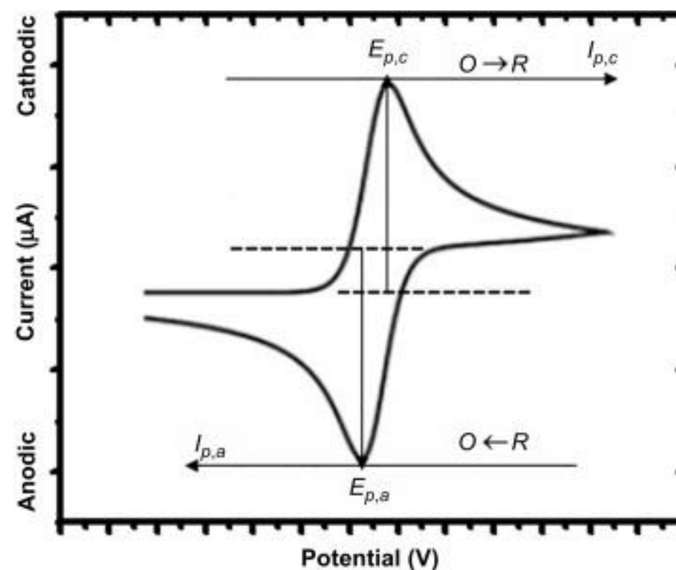

Figure 2-9. Typical cyclic voltammogram depicting current vs voltage regions where oxidation and reduction are respectively taking place, where $i_{p,c}$ and $i_{p,a}$ are the peak cathodic and anodic currents and $E_{p,c}$ and $E_{p,a}$ are the peak cathodic and anodic potentials, respectively (Nnamchi & Obayi 2018).

When performing CV experiments, consideration must be given to variables such as the applied potential range, scan rate and conditions of the electrolyte solution (pH, temperature, etc), as these variables can produce artefacts in the results. CV experiments are useful in

evaluating the water splitting capability of photosensitive materials via testing the stability of materials submerged in electrolyte solutions and direct observation of photocurrents.

2.2.6 Air Mass Coefficient (AM 1.5)

The air mass coefficient defines the direct optical path length of solar radiation through the Earth's atmosphere relative to its path length moving vertically upwards (at the zenith). The AM 1.5 standard was internationally adopted in 1976 (*American Society for Testing Materials* 2003) and is widely for evaluating photovoltaic performance in simulated atmospheric conditions. It should also be noted that the standard carries several specified assumptions about atmospheric conditions, which are provided by the ASTM. **Equation 13**, shown below, is used to determine the ratio:

$$AM = \frac{L}{L_O} \qquad \textbf{(Equation 13)}$$

Where L is the path length through the atmosphere, and L_O is the path length at the zenith at sea level. This is represented below **Figure 2-10**.

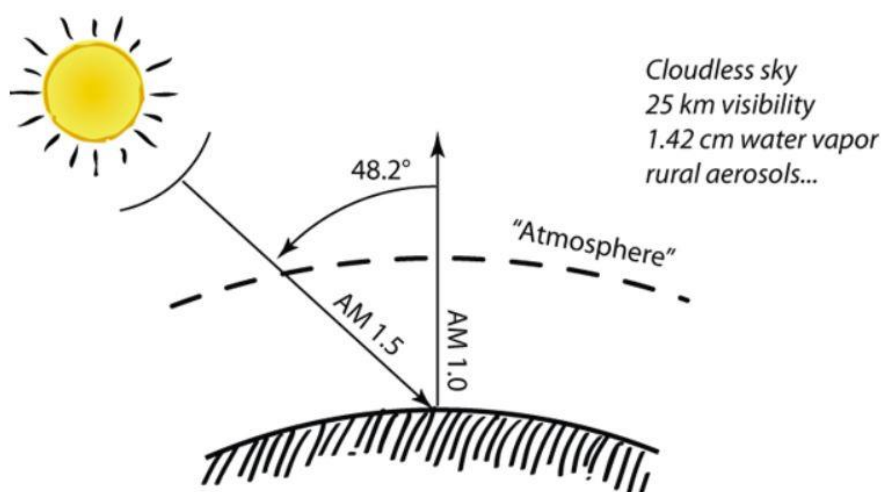

Figure 2-10. Air mass coefficient demonstrated with respect to zenith angle of 48.2° (Brownson 2020).

The AM number will vary with the sun's movement throughout the day, with the highest values in the morning and afternoon and lowest values at midday. The value of AM 1.5 represents a middle point between these two times of the day, corresponding to a zenith angle of 48.2°, where a tilted panel would receive solar radiation equal to ~1000 W/m^2.

2.2.7 Defect Disorder in Semiconductors

Defect disorder, or defect chemistry, is a heavily studied component of modern solid state physics as it relates to semiconductor materials, especially those with inherent non-stoichiometry such as TiO_2 (Nowotny, J et al. 2007; Nowotny, MK et al. 2008). This is because

the properties of semiconductor materials can be drastically impacted by the inclusion of dopant elements, as was explained previously in terms of band gap and fermi level shifts. Therefore, it is important to establish a basis of defect theory, especially as it pertains to the materials and topics covered later in this project, namely nitrides such as Ta_3N_5 and its related nitride phases.

Assuming a repeating solid structure, defects can broadly be introduced to the lattice in 4 ways, as shown below in **Figure 2-11**.

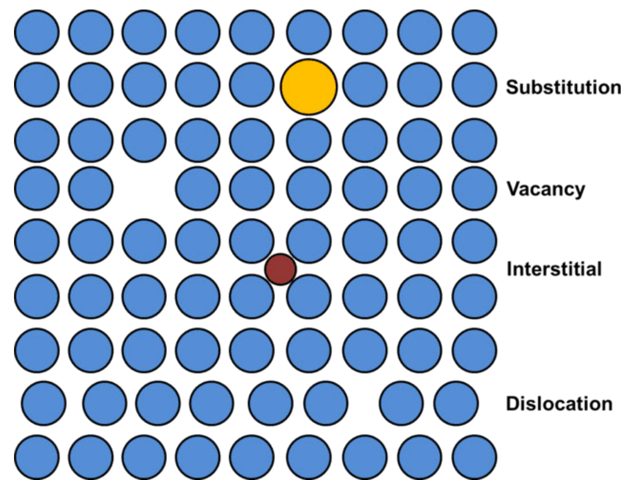

Figure 2-11. Representation of the possible defects within the lattice of a hypothetical solid.

The substitution of a host lattice anion or cation (which are not discriminated in the previous figure for simplicity) refers to the direct substitution of a majority lattice element with another ion possessing similar electronegativity, as in the case of a hypothetical NaCl rocksalt structure where Na^+ and Cl^- could possibly be substituted with Sr^{2+} and O^{-2}, respectively. A lattice vacancy refers to an open position within the crystal lattice, while interstitial defects refer to the positioning of an element between the lattice planes. Dislocation describes a hole in the lattice that is smaller than an outright vacancy and which subsequently creates an incongruity between crystal planes.

Defects can be described using Kroger-Vink notation (Kofstad 1995). Assuming the NaCl crystal structure again, a vacancy on the Na^+ sublattice is shown as:

$$V'_{Na}$$

Whereas a vacancy on the Cl^- sublattice would be depicted as:

$$V^{\bullet}_{Cl}$$

Where the superscript describes effective charge, V' for a negative charge and $V^{\bullet}$ for a positive one. Interstitial positions are notated similarly:

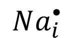

$$Na_i^{\bullet}$$

Which would describe a Na ion lying interstitially.

Every material, regardless of its purity, contains defects. Doped semiconductors are typically treated as perfect structures with intentional impurities (dopants), which confer the altered band states and improved electronic properties described earlier in this chapter. The position occupied in the lattice (i.e interstitial or substitutional) by the incoming dopant, in addition to its charge and size will determine its impact on the lattice.

This work will mostly deal with vacancy defects, specifically Schottky defects, which is a vacancy created in the lattice by simultaneous cation and anion vacancies. In a typical crystal structure denoted as M^-X^+, both a cation and anion site are vacated to maintain the stoichiometric charge in the bulk. There is also what is referred to as the Frenkel defect, which is a defect that occurs when a cation or anion leaves the crystal lattice and occupies an interstitial position in the lattice, creating a defect at this point and leaving a vacancy. These two defect types are illustrated below in **Figure 2-12** in a simple sodium chloride crystal structure.

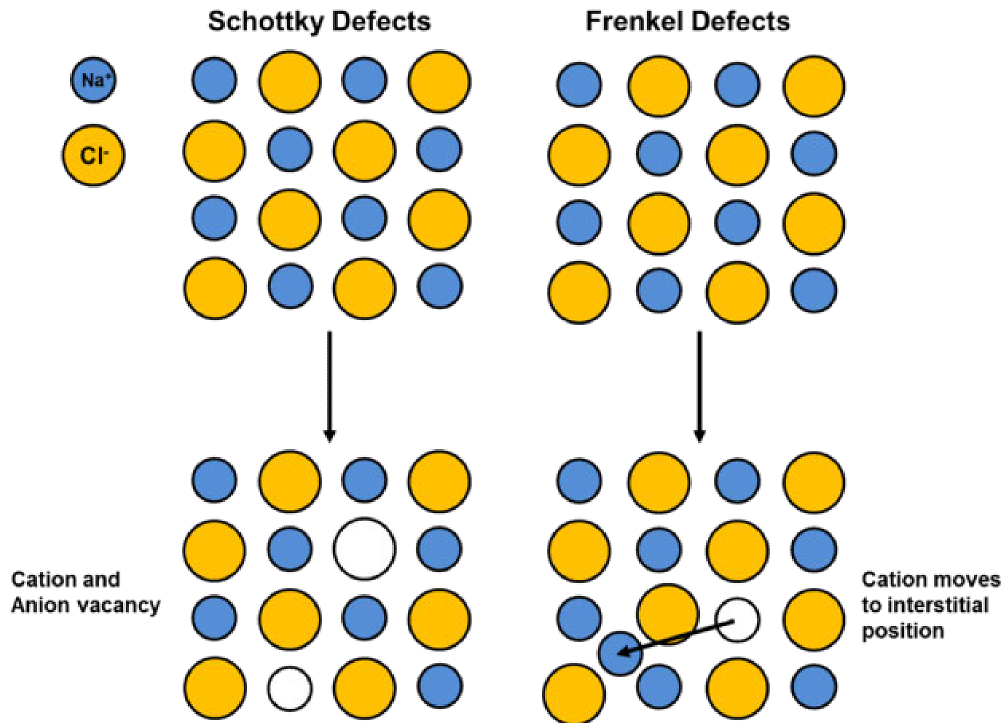

Figure 2-12. Depiction of Schottky and Frenkel Defects in NaCl crystal structure.

Another important defect that will be discussed are antisite defects, which are positions in a lattice occupied by an ion not native to the host lattice. That is, in a doped TiO_2 structure, an antisite defect refers to a dopant (i.e Cr^{2+} or even Ti^{3+}) occupying a position in the lattice where one would typically expect a Ti^{4+}. Doping and the role of these defects play an integral role in the primary phase of interest to this topic (Ta_3N_5) (Paskov & Monemar 2018). Further context regarding the nature of defects in transition metal nitrides similar to Ta_3N_5 will be provided in the following subsection.

2.2.8 Defects in Transition Metal Nitrides

Transition metal nitrides such as TaN, are important functional materials in modern society. These simple nitrides are often used as wear resistant materials in applications such as TiN films deposited on cutting tools (Rebenne & Bhat 1994) or TiN/TaN layers as gate electrode materials for CMOS transistors (Nordin, Larsson & Hogmark 1999). Doped TaN is also employed as a diffusion barrier between copper or other metal layers (Perng, Yeh & Hsu 2008), or as a thin film resistor in plastic electronics (Scandurra et al. 2008). Defects and doping play a key role in governing the electronic properties of semiconducting materials, including Ta_3N_5. The study of defects within the films are relevant to these applications as well as others, due to the inclusion of dopants or because of the position of nitrogen (or lack thereof) in the lattice.

TaN phases exist on a spectrum, which in this case ranges from the metallic tantalum heavy phases to the nitrogen heavy phases. A more in-depth summary of the tantalum nitride phase series will be covered later, in a dedicated chapter. In general, it is demonstrated that the resistivity of TaN increases as nitrogen anti-site (N_{Ta}) defects increase (Kang et al. 2003), with more nitrogen occupying tantalum positions in the lattice. Specifically, most of the electrical, optical and thermoelectric properties are governed by vacancies on the tantalum (V_{Ta}) and nitrogen (V_N) positions, as these defects possess the lowest calculated formation energies relative to other defects studied (i.e nitrogen interstitial defect (N_i), Ta on nitrogen position (N_{Ta})) (Yu, L et al. 2002).

Dopant elements will therefore most likely occupy one of these positions and alter properties of the resulting phase by reducing or increasing the locality or amount of V_{Ta} or V_N defects in the lattice. The nature of defects as it relates to the Ta_3N_5 phase specifically will also be covered in depth in the portion of the literature review dedicated to it.

The nature of defects in the tantalum nitride system has not been explored due to the area of research being relatively new at the time of writing. The way dopant materials are incorporated into the lattice has been evaluated in less than a handful of papers to date, typically with the use of DFT modelling and occasionally with some experimental validation.

Chapter 3: Solar Driven Water Splitting

Solar water splitting describes the process of splitting water utilising just sunlight and photosensitive materials submerged in water. This process can be harnessed using two main engineering approaches. These are photo-electrochemical cells (PEC), or a suspension of photocatalytic materials. The following chapter aims to introduce the concept of solar water splitting, explain the process, and contrast the two primary methods of performing it. There will also be an introduction to the relevant characterisation techniques that were used in this work to determine the electronic and doping properties of the light sensitive materials made.

3.1 Basic Principles of Solar Water Splitting in a Photo-electrochemical Cell

Photo-electrochemical water splitting using a stable TiO_2 electrode absorbing UV light was first reported in 1972 by K. Honda and A. Fujishima (Fujishima & Honda 1972). Hydrogen generation via photo-electrochemical water splitting (**Figure 3-1**) represents a method of hydrogen fuel generation that is both renewable and free of carbon emissions.

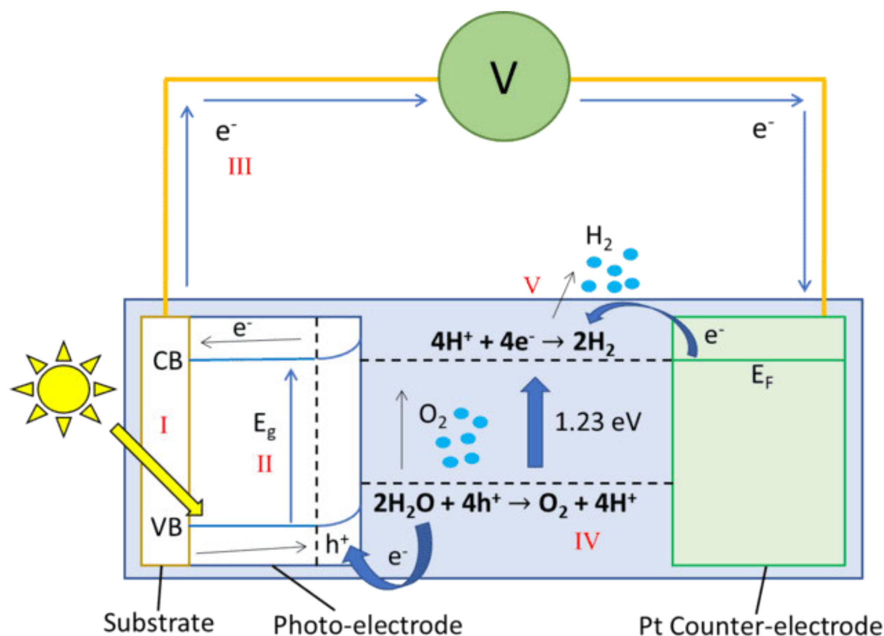

Figure 3-1. Demonstration of photo-electrochemical water splitting, where VB = valence band and CB = conduction band. Steps are as follows: (I) light adsorption, (II) charge separation, (III) charge migration, (IV) charge recombination, (V) water oxidation and (VI) water reduction.

The process takes place in a PEC that consists of either one photo-electrode connected to a counter electrode, or two connected photo-electrodes, submerged in an electrolyte solution. The critical components of the PEC are the photo-electrode(s), where incident sunlight (where

hv > E_g) is absorbed by the photo-electrode, exciting an electron from the valence band to the conduction band and leaving a hole. It is also important that these photo-electrons and photo-holes are able to migrate to their respective reaction sites for water splitting to take place. The full reactions shown in Figure 3-1 are given below in **Equation 14**, **Equation 15** and **Equation 16** (where NHE is Normal Hydrogen Electrode):

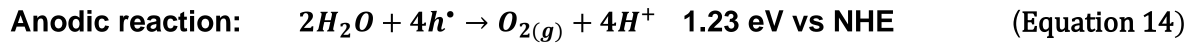

Anodic reaction: $2H_2O + 4h^{\bullet} \rightarrow O_{2(g)} + 4H^{+}$ **1.23 eV vs NHE** (Equation 14)

Cathodic reaction: $4H^{+} + 4e^{-} \rightarrow 2H_{2(g)}$ **0 eV vs NHE** (Equation 15)

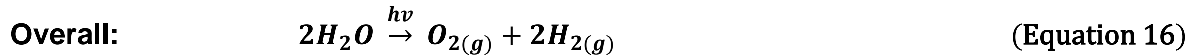

Overall: $2H_2O \overset{hv}{\rightarrow} O_{2(g)} + 2H_{2(g)}$ (Equation 16)

It is regularly assumed that the Schottky Junction will form under conditions of majority-carrier depletion and as such, for an n-type semiconductor, band bending will be upwards, and photo-holes will be directed towards the surface where they will oxidise water and evolve oxygen gas per Equation 14, which describes the photo-anodic reaction.

Conversely, in the instance of a p-type semiconductor, band bending is downwards and photo-electrons are directed towards the photo-electrode surface where they reduce hydrogen ions and hydrogen gas evolves per Equation 15, which describes the photo-cathode reaction. In both instances, the photo-carrier that is directed towards the photo-electrode bulk participates in the alternative reaction at the other electrode so that in all cases both the anodic and cathodic reactions take place concurrently, yielding the overall water splitting reaction described by Equation 16.

The photo-electrodes in a PEC essentially consist of photo-sensitive semiconductor materials whose band gap energy, E_g, dictates the extent of incident light absorption. As described by **Equation 17** and illustrated in Figure 3-1, for photo-electrons and photo-holes to be generated during illumination, the energy of incident photons must exceed the band gap energy of the photo-electrode (where nil refers to default energy level of electrons in the valence band):

$$nil \xrightarrow{hv > E_g} e' + h^{\bullet} \qquad \text{(Equation 17)}$$

Consequently, a material's band gap is an important performance property that relates the minimum wavelength of an incident photon necessary to excite an electron from the valence band to the conduction band. Because the goal is to split water with sunlight, in describing an ideal water splitting material there are two main considerations; one, that a material possess a band gap capable of absorbing light in the visible part of the spectrum, and two, that this material's band gap straddles the water redox potentials which are 0 eV and 1.23 eV at pH = 0 (Tabata et al. 2010). Hence to split water, a material with a band gap exceeding 1.23 eV is necessary. This is illustrated visually in **Figure 3-2** below.

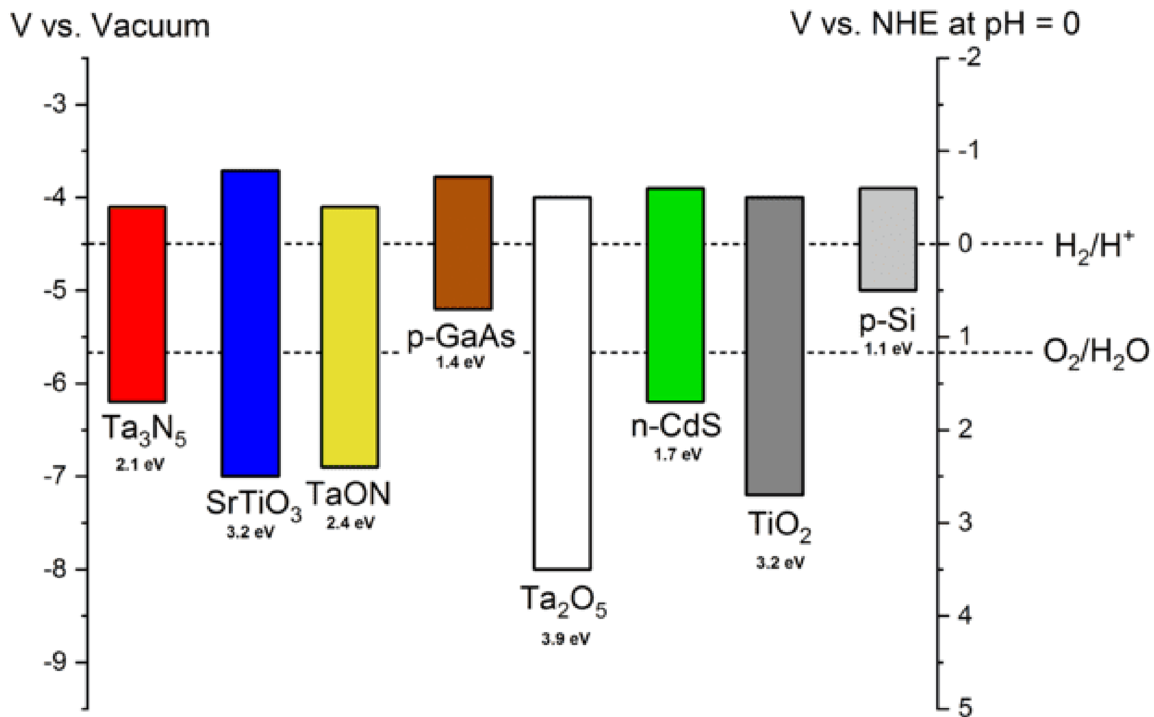

Figure 3-2. Chart depicting the relative conduction band (CB) and valence band (VB) energy and band gap values of various semiconducting materials used for water splitting, including Ta_3N_5, $SrTiO_3$, TaON, p-GaAs, Ta_2O_5, n-CdS, TiO_2 and p-Si compared to the redox potentials of water. Where NHE = Normal Hydrogen Electrode.

Band gap energy (eV) and wavelength (nm) can be related using **Equation 18**:

$$\lambda = \frac{hc}{E_{ph}} \qquad \textbf{(Equation 18)}$$

Where λ = wavelength, h = Planck's constant, c = the speed of light and E_{ph} (the energy of a photon) = eV x 1.602×10^{-19}.

It can be seen in the above figure that the oxide semiconductors Ta_2O_5 and TiO_2 possess large band gap energies of 3.9eV and 3.2eV, hence the minimum wavelength of light absorbed in either case would be 318nm and 388nm, respectively. These wavelengths correspond broadly to that of light in the ultraviolet end of the electromagnetic spectrum (10-400nm). In terms of energy, only a small component of the light that strikes the Earth's surface is in the UV spectrum (3-5%), with visible light (~42-43%) and infrared light (~52-55%) making up the majority of this (Gates 1966). Thus, it is compelling to engineer a material with a band gap capable of absorbing visible light.

Once incident photons of $hv > E_g$ have been absorbed by the photo-electrode, it is imperative that the photo-generated charge carriers remain separated (see **Figure 3-3**) and are

appropriately directed towards the PEC anode or cathode to participate in water oxidation or hydrogen reduction reactions, respectively.

What determines charge separation in this instance is the band bending that occurs within the near-surface region of the photo-electrode in response to the immersion of the semiconductor in the aqueous solution (Zhang, Z & Yates 2012). Specifically, due to a mismatch in the Fermi level of the semiconductor and the chemical potential of electrons in the electrolyte (quasi-Fermi level), a Schottky Junction is formed and a region of band bending results (Léonard & Tersoff 2000). This in turn directs the flow of the photo-electrons and photo-holes in opposite directions, either towards the surface of the photo-electrode, or towards the bulk of the photo-electrode and onwards to the other electrode.

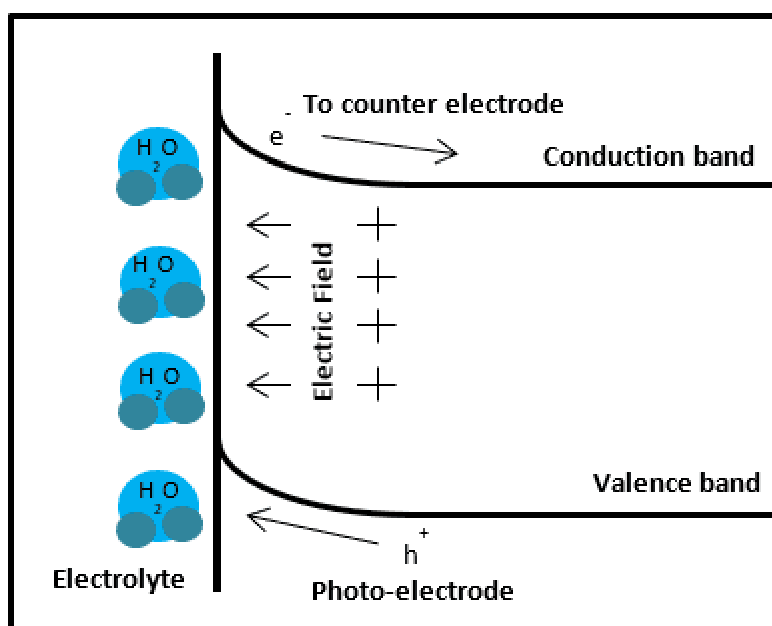

Figure 3-3. Figure depicting the process of charge separation following the excitation of an electron from the valence band of a semiconductor.

For the anodic and cathodic reactions to proceed spontaneously, it is essential that the required charge transfer (see: **Figure 3-4**) at the photo-electrode/electrolyte interface can proceed in an energetically favourable manner. At a minimum, this requires for the conduction band edge of the photo-electrode semiconductor to be energetically negative of the H^+/H_2 redox potential, and the valence band edge to be energetically positive of the O_2/H_2O redox potential. In the case of a PEC based on two photo-electrodes, it is not a requirement that the valence and conduction bands of both photo-electrodes straddle the H^+/H_2 and O_2/H_2O redox potentials, however the condition remains that the valence band edge of the photo-anode is positive of O_2/H_2O and that the conduction band edge of the photo-cathode is negative of H^+/H_2.

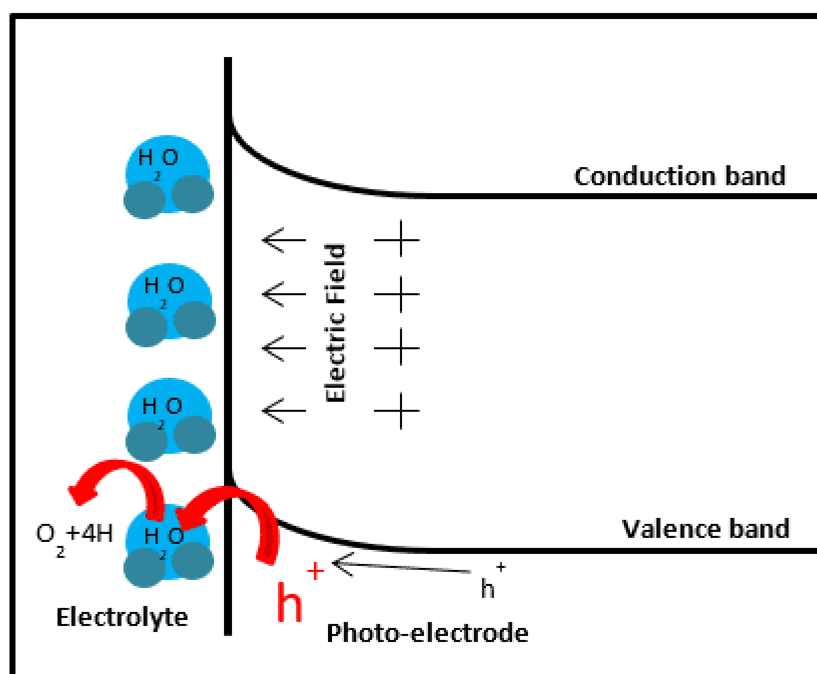

Figure 3-4. Figure showing a simplistic depiction of the process of charge transfer, which involves a photogenerated hole migrating to the electrolyte/semiconductor interface to perform the oxidation of a water molecule.

When the band edge positions are not appropriately located, an external bias must be applied to drive spontaneous charge transfer. The application of external bias will contribute detrimentally to the overall efficiency of the PEC and should be avoided. As a complicating but real point of consideration, the presence of surface states and/or catalysts attached to the surface of the photo-electrode can serve to facilitate spontaneous charge transfer at redox potentials other than near the valence and conduction band edges.

It should be noted that these distinct stages are important to any system designed to split water with sunlight, whether particle or electrode based. However, this project will focus entirely on the photo-electrode method of design. The justification for this, and the broader context of the two design methods, is explored in the following section.

3.2 Particulate Systems and Photo-electrodes in Water Splitting

Solar water splitting is often done via one of two well defined routes: photosensitive particulates (eg. TiO_2) suspended in an electrolyte, or photo-electrochemical cells. Both routes require consideration of the previously outlined fundamental processes of water splitting (light adsorption, charge separation, charge transfer, charge recombination and surface redox reactions), and how the properties of a given material promote or inhibit these processes. These two different approaches are summarised in **Figure 3-5**.

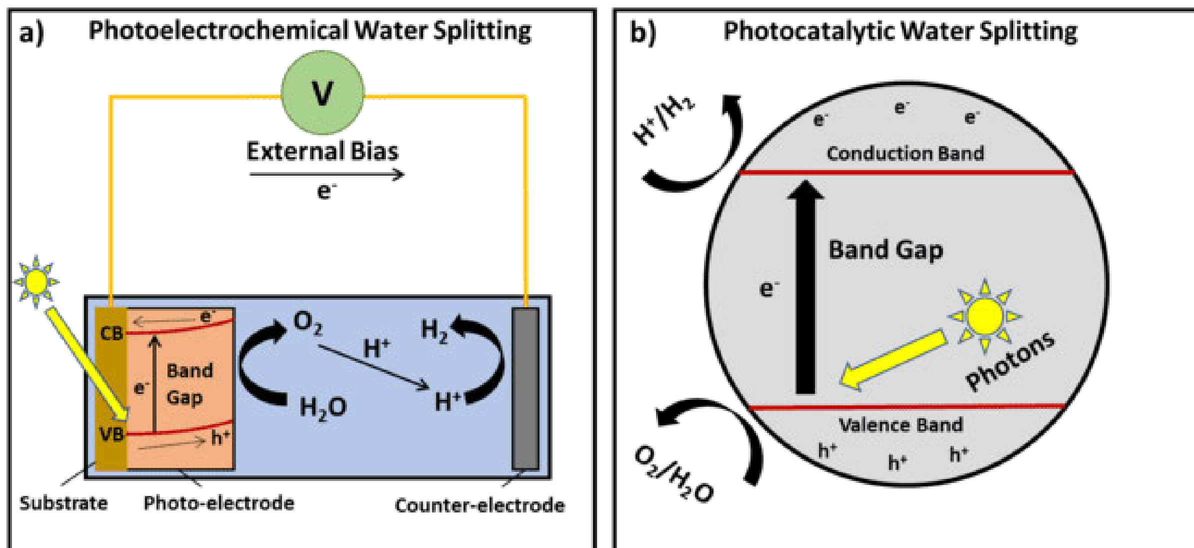

Figure 3-5. Two of the main routes explored for solar water splitting, a) photo-electrochemical water splitting and b) photocatalytic water splitting depicting a photocatalyst in an electrolyte.

A significant focus has been placed on the development of various materials (i.e TiO_2) as photocatalytic particulates. The benefits of performing water splitting at two sites on a single photocatalyst represent a compelling technology, not just for the purpose of hydrogen generation but also as a water purifying technology (Belver et al. 2019) and even oil slick cleaning (Ziolli & Jardim 2002). However, as a method of sustainable hydrogen generation, particulate water splitting routes face key challenges preventing their adoption.

While great strides have been made in producing high performance photocatalytic materials for the role of water purification (Hou et al. 2014; Kibria, MG et al. 2016), engineering challenges still exist when these materials are considered for the role of hydrogen generation, namely the effective separation of H_2 and O_2 as well as the capture of H_2 itself.

Chapter 4: Sputter Deposition

Sputter deposition is a technology used across many industrial and scientific disciplines as a method of depositing thin films of controllable thickness, composition, and morphology onto a desired substrate material. There are many variations of thin film deposition (Guglya & Lyubchenko 2018); however this project will focus almost entirely on a method of physical vapour deposition (PVD). PVD itself is a collection of techniques including sputter deposition, pulsed laser deposition and certain configurations of molecular beam epitaxy. Magnetron sputter deposition offers advantages in options for target materials, film adhesion and uniformity, scalability, automation and competitive build costs and operation (Tudose et al. 2019), as well as various processing controls such as substrate heating and DC/RF power types (Swann 1988).

4.1 Magnetron Sputtering

Sputtering describes the process of applying a voltage across a sputtering chamber such that a cathode and anode are created within the chamber (Gudmundsson & Lundin 2020). The chamber itself is pumped down to a desirable level of vacuum and filled with inert gases (e.g argon, helium). This voltage subsequently generates negatively charged ions from the gases in the chamber, which are attracted through their charge to a given target material. In striking the targets, atoms are ejected from the target material and sputtered onto surfaces within a certain distance of the target, depending on various factors present in the chamber which will be elaborated on later in this section.

The sputtering chamber environment associated with this project is represented below in **Figure 4-1**.

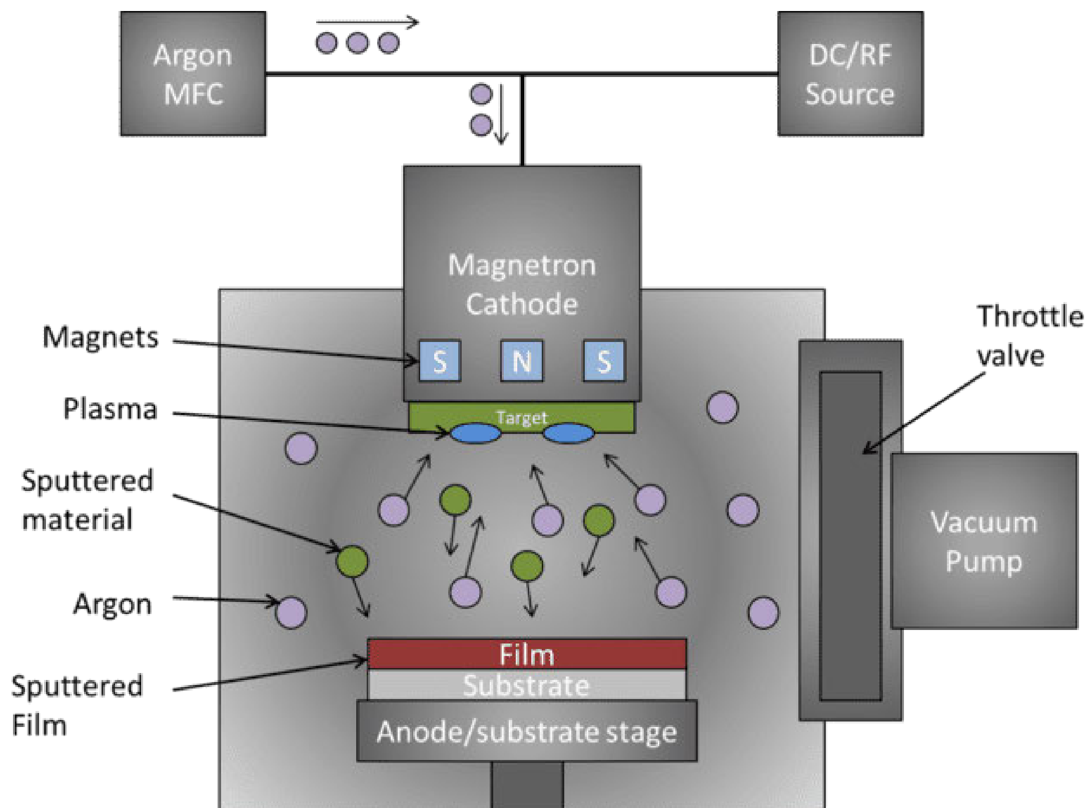

Figure 4-1. Schematic of Magnetron Sputtering apparatus pertaining to the sputter coater used in this project.

Magnetron sputtering itself is a subset of PVD processes that employs the use of magnets situated behind the target material to confine a plasma of charged species to the surface of a target material, as seen below in **Figure 4-2**. As described above, charged species in the plasma strike the target, ejecting atoms that condense on materials situated in the chamber.

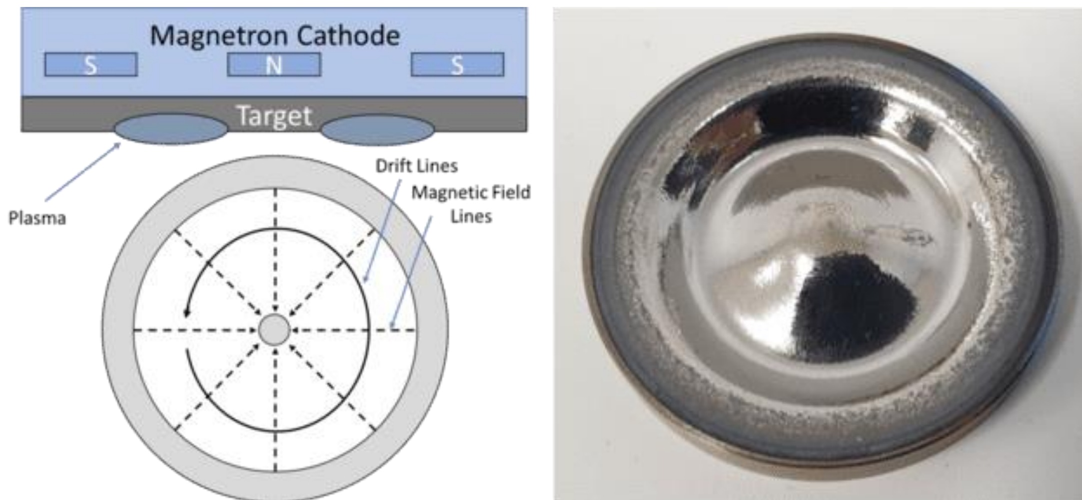

Figure 4-2. Cross sectional and top down view of sputtering target. Image on the right shows a target that has been worn down by sputtering, showing 'race track' run into the surface by the plasma.

Relative to older sputtering methods, which generate the plasma in the gas phase and forgo the use of magnets, magnetron sputtering allows faster deposition rates due to the confinement of the ions near the surface of the target (as opposed to those that must migrate to the target from the gas phase). This carries a higher associated complexity and cost, however the associated benefits have resulted in magnetron sputtering becoming a common deposition technique widely used in industrial and scientific applications (Bräuer et al. 2010).

Sputtering is a physical process and as such, the dynamics of ionic species and sputtered atomic matter obey the principles of conservation of momentum and energy. That is, momentum and kinetic energy are conserved as charged species strike atoms in the target and dislodge them, as shown below in **Figure 4-3** and **Figure 4-4**.

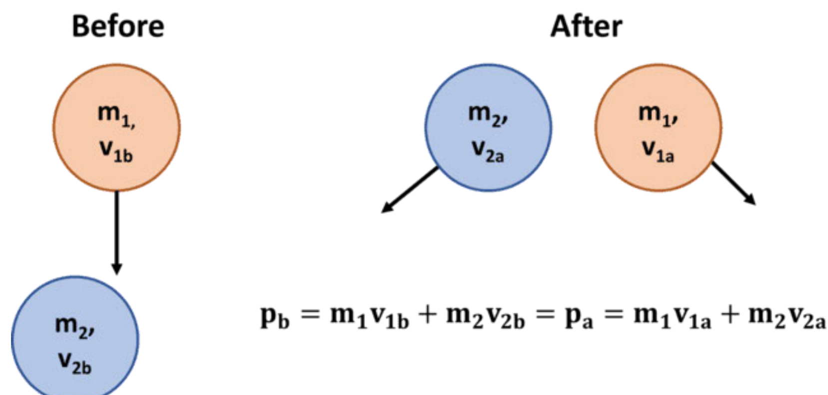

Figure 4-3. The conservation of momentum in a collision between two particles.

Elements like Ar and Kr are typically used for this reason: their high atomic weight (among the halogens) ensures that the maximum transfer of energy takes place. This means that bonding

energies (and other forces at play) are overcome when these high energy ions strike atoms in the lattice, subsequently ejecting them from the target after further collisions.

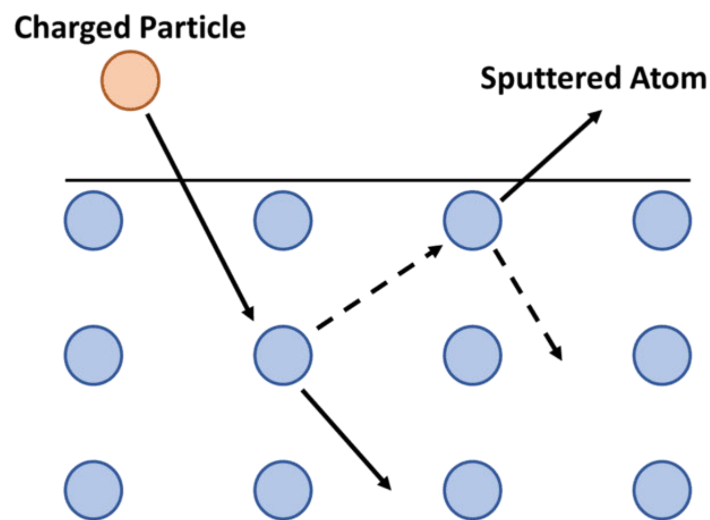

Figure 4-4. Diagram depicting the basic process of sputtering. A charged ion strikes the lattice of a target material, and atoms are ejected via successive collisions.

Once atoms from the target material are ejected, they diffuse through the gas phase, eventually reaching and coating the substrate or chamber walls. The movement of sputtered atoms through the gas phase is a process governed by important variables in the deposition process, namely total deposition pressure and target power (although target voltage can also be used). Another variable to be aware of is the distance from the target to the substrate material itself.

Quantifying the ejection of sputtered atoms is described with sputter yield:

$$Sputter\ Yield = \frac{Number\ of\ Ejected\ Atoms}{Number\ of\ Incident\ Ions}$$

Sputter yield is determined by the relative masses of the ions and atoms, the binding energy of the target material, the types of ions used, the angle of incidence and the energy of the incident ions. The sputtering yield is proportional to the total deposition rate, which is determined more directly through measurement of the film thickness, which can be done with microscopy, profilometry, or indirectly by thickness monitors attached to the sputtering system. The general sputter rates are given for metals of interest to this project, along with the sputtering parameters necessary for them, in **Table 4.1**.

Table 4.1. General sputtering rates of different metallic targets. These rates vary depending on variables like the target power, distance to the substrate and gases used. The rates below assume an applied power of approximately 600W/cm^2 and a target to substrate distance of 10cm (*Sputtering Yield Rates* 2019; Wasa 2012).

Material	Density (g/cm^3)	Sputtering Yield (nm/sec)
Ta	16.6	8.5
Cr	7.1	19
Al	2.7	17
Nb	8.5	8
Ag	10.4	38
Au	19.3	32
Pt	21.4	21

These elements must be considered in any deposition experiment, and in many cases are endemic to individual instrumentation setups; depending on the build, some sputtering systems vary greatly in their substrate to target distances and target sizes, as an example. The total deposition pressure will determine the mean free path of the ejected species; restricting it if too high through multiple successive collisions of the ejected species or failing to sustain a plasma if too low.

Magnetron sputtering was compelling to this project as it afforded great control over the qualities of the final film, and most importantly the ability to introduce dopant elements of controllable quantities homogenously into the film bulk. Additionally, as covered in the literature review chapter, there was already a modest body of work demonstrating that the desired phase of material could be deposited using this technique (Rudolph, M. et al. 2016; Yokoyama et al. 2011).

This system utilised a computer-controlled valve attached to the main chamber, which throttled gas flow in the chamber to obtain a desired pressure value. Mass flow controllers were used to deliver reactive gas species during sputtering, while the chamber pressure was adaptively controlled by opening or closing the valve door to an appropriate position. This is noted in contrast to other systems, such as more traditional sputtering systems, that operate a closed chamber environment whereby reactive gases of appropriate proportions are pumped in prior to deposition, with no changes to them made through external means while sputtering is taking place.

There are many other variables available for controlling the deposition of films, depending on the sputtering system installed. These include (but are not limited to) the total deposition pressure, the respective partial pressures of reactant gases and specific gases, the power applied to the target(s), substrate heating, DC and RF power sources, and substrate bias. The

deposition parameters relevant to this project will be elaborated on in the following subsections.

4.1.1 Total Deposition Pressure and Reactant Gases

The primary means by which the composition of the sputtered film is controlled are the reactant gases, the total deposition pressure and the respective pressures of the reactant gases. This project utilised three gases, argon, nitrogen and oxygen, in pairs of Ar/O_2 or Ar/N_2 and also $Ar/N_2/O_2$. Once the chamber is pumped to a certain level of base pressure, which in this case was $9x10^{-5}$ Pa, the reactive gases are flowed in and a specific value for the total chamber pressure is set via the computer control interface. As above, the total pressure in the chamber is electronically mediated by a single computer-controlled chamber valve which shifts depending on the gas consumption and input.

The chamber pressure is provided as a value in mTorr, and the reactant gases as standard cubic centimetre per minute (or sccm). The respective pressures of each gas are determined by relating the fraction of each gas in sccm to the total deposition pressure. For example, if a pressure of 5 mTorr is set, and 8 sccm of Ar and 2 sccm of N_2 are flowed in, then the pAr is 80% of 5 mTorr, or 4 mTorr, and the pN_2 likewise 20%, or 1 mTorr. Throughout this thesis, these values are provided in pascals and in percentage form for ease of reading.

The deposition pressure relates the gas concentration in the chamber, and with the power applied to the target, determines the sputter yield (Simon 2012). Ejected species will meet a greater number of atoms and scatter more effectively in higher pressure environments, reducing the sputter yield. On the other hand, reactant gas partial pressures determine the elemental composition of the deposited film; metallic films are deposited using just argon, whereas oxide films would require a metal target sputtered in an Ar/O_2 gas environment. Reactant gas partial pressures are also important to control given the tendency of reactive species to 'poison' targets, where reactive species deposit on the surface of the target as well as the substrate, thereby impeding sputtering yield (Depla, Diederik & De Gryse, Roger 2004). In general, higher partial pressures will reflect a greater presence of the respective reactive element in the deposited film.

4.1.2 Substrate Heating

Substrate heating denotes the application of heat to the stage in the sputtering chamber in a controlled and measurable fashion. For this work, substrate heating was practiced using lamps situated under the sample stage (**Figure 4-5**). Substrate heating can assist in promoting the crystallisation of certain material systems in-situ, saving further annealing steps post deposition. In the context used in this work, substrate heating refers to the use of deliberate

heating implements in the deposition process, not the heating resulting from the process of deposition itself.

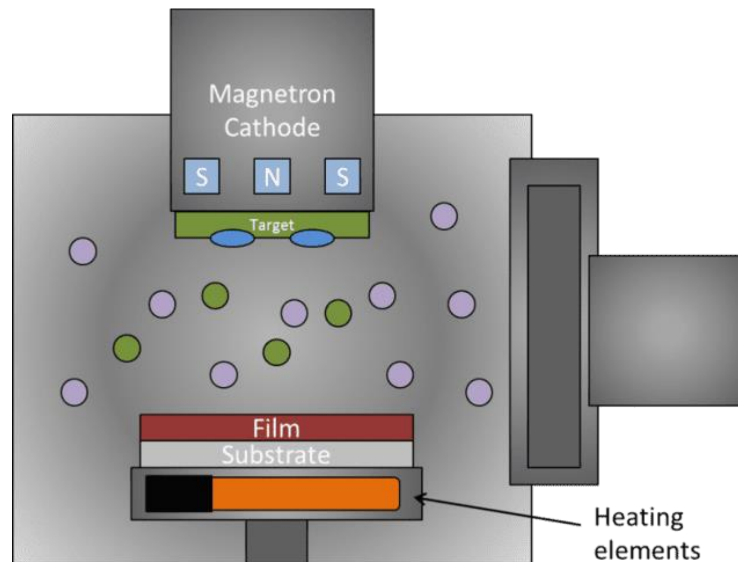

Figure 4-5. Sputtering chamber schematic indicating the position of the heating elements below the substrate inside the stage.

4.1.3 DC and RF Power Sources

In generating a plasma on a target using an applied voltage, there is a choice in the type of power supply delivering power to the target: DC or RF. DC and RF power sources are advantageous for target materials with different conductivity; DC power functions best with conductive target materials, whereas RF power is more conducive to sputtering insulating materials (Morosanu et al. 1997). This is due to the energetics at play during deposition; a DC current produces positive ions from the gas atmosphere that will accumulate on the surface of a target, and in the case of an insulating target, be unable to migrate effectively, slowing deposition yields substantially. However, in the case of an RF power source, the polarity inside the chamber will reverse constantly (as opposed to a DC source, where the target remains the cathode and the stage the anode), which then prompts these accumulated positive ions to leave the target (Muhl et al. 1997).

Energetics in the sputtering chamber can be further controlled with substrate bias, one example of which is increasing DC deposition yields when using targets with insulating properties. This is further elaborated on in the following section.

4.1.4 Substrate Bias

Substrate bias involves the application of a bias voltage to the substrate (see **Figure 4-6**), generating a plasma over the substrate and assisting in the deposition of certain types of materials, or changing the film structure in specific ways. Some deposition systems are

equipped with an additional power source feedthrough to the substrate stage. This power source can be used to apply power to and generate an additional plasma around the sample stage directly. This plasma can be used to increase ion bombardment from the primary plasma generated on the target, which can improve film adhesion, density, smoothness and reactivity (Gudmundsson & Lundin 2020). The additional power source can also be either DC or RF.

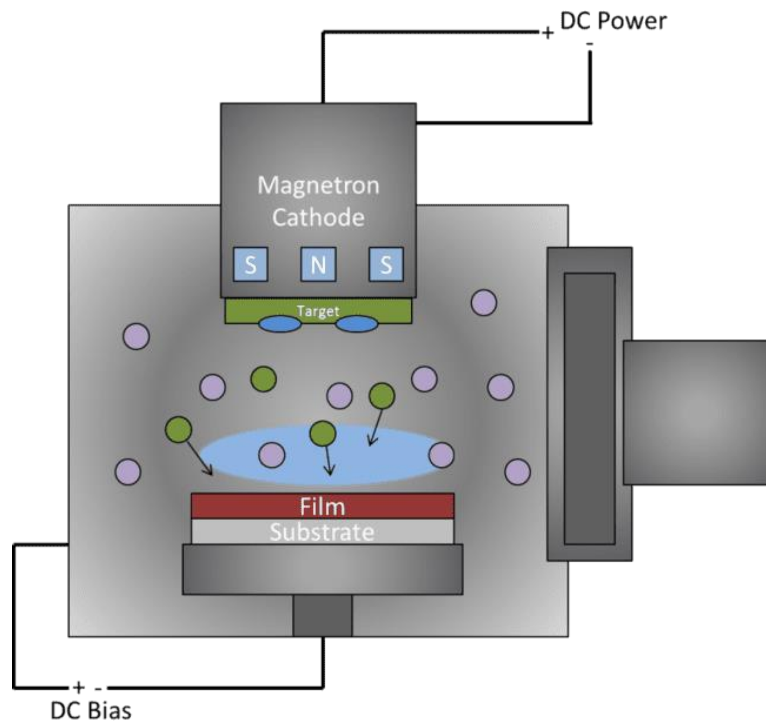

Figure 4-6. Sputtering chamber schematic showing the generation of a plasma over the substrate using a DC bias, and a DC power source attached to the target material.

Substrate bias was investigated experimentally in this work but was not included due to the results being inconclusive. However, substrate bias is mentioned in several referenced research works and is an important component of the deposition environment, as such it is described here for the benefit of the reader.

Chapter 5: The Tantalum Nitride Phase Series

The tantalum nitride phase series consists of several functional materials with various applications depending on the phase in question. Many different metastable structures and preferred orientations of TaN have been reported in the literature (Firouzabadi et al. 2017; Nie et al. 2001). Three stable structures are reported: Ta_2N, Ta_5N_6 and Ta_3N_5, with remaining phases existing as metastable structures (Stampfl & Freeman 2005). Of these, the cubic TaN phase and Ta_3N_5 are of note to this work, being the most oft-observed phase, although Ta_5N_6 and Ta_2N were also observed at points in the project. A table of the common phases in the tantalum nitride phase system, along with their crystal structure and space group, is given below in **Table 5.1**.

Table 5.1. Reported phases in the tantalum nitride system and their respective space groups (if reported).

Phase	Structure	Space Group	Ref
Ta_2N ($TaN_{0.40-0.50}$)	Hexagonal	P31m	(Conroy & Christensen 1977)
ε-TaN	Hexagonal	P62m	(Nobuzo 1971)
ε-TaN	Trigonal	P6/mmm	(Conroy & Christensen 1977)
δ-TaN ($TaN_{0.50-0.90}$)	Hexagonal	Fm3m	(Nobuzo 1971)
β-TaN ($TaN_{0.05}$)	Cubic	P3m1	(Nobuzo 1971)
Ta_4N_5	Tetragonal	I4/m	(Stampfl & Freeman 2005)
Ta_5N_6	Hexagonal	$P6_3$/mcm	(Stampfl & Freeman 2005)
Ta_3N_5	Orthorhombic	CmCm	(Brese et al. 1991)

The structure of the phase synthesized is sensitively attuned to the synthesis conditions and environment in which it's contained. Furthermore, the phase change depends on the activity of tantalum and nitrogen in the synthetic conditions; tantalum deficiency will promote the Ta_3N_5 phase while nitrogen deficiency results in the Ta_2N phase, with middle ground phases such as the stoichiometric TaN phase or Ta_5N_6 phase existing in between the two extremes.

The tantalum nitride phase series was explored both computationally and experimentally by C. Stampfl and colleagues (Stampfl & Freeman 2005), and a phase diagram was determined. This is reproduced below in **Figure 5-1** to assist in visualising the stabilities of tantalum nitride phases as a function of nitrogen and tantalum atomic chemical potentials (expressed as μ_N and μ_{Ta}, respectively). Looking at the top graph in Figure 5-1, it can be seen that several TaN phases are within 0.13 eV free energy of one another at μ_N = -1.5 eV (intersecting lines, where

lower μ_N reflects N-poor conditions). This prediction highlights the importance of carefully controlling the synthetic conditions of tantalum nitride, as small changes to these conditions can result in many different phases, which is reflected by the many phases reported here and in the literature (Borovinskaya 2017).

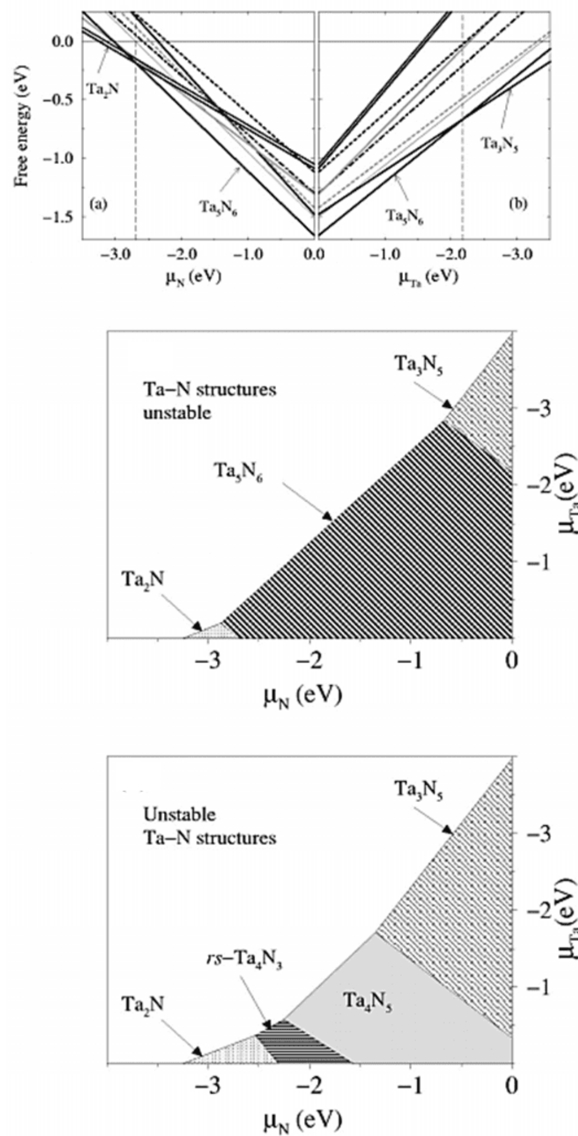

Figure 5-1. Phase diagram depicting the stable structures in the tantalum nitride phase series as a function of the atom chemical potentials, μ_N and μ_{Ta}. The diagram on top shows the phases as calculated, whereas the bottom diagram omits the most stable Ta_5N_6 phase so other phases in the series can be seen (Stampfl & Freeman 2005).

Generally, the stable phases exist in the region where one of the two chemical potentials for tantalum and nitrogen are at odds with the other. That is, Ta_3N_5 exists where tantalum possesses much more energy than nitrogen, whereas Ta_2N reflects the inverse of this relationship. This may reflect the synthetic difficulty in moving one direction down the phase series (nitrogen heavy), versus moving another direction (nitrogen poor).

Another study in 2016 deposited a number of tantalum nitride phases utilising DC magnetron sputtering and post deposition annealing in vacuum to determine a phase diagram (Salamon et al. 2016). This work deposited the phases using just Ar and N_2 and did not report the deposition of the Ta_3N_5 phase, instead describing several of the lesser nitrides in the phase series. A phase diagram was also described in the course of the work and can be seen below in **Figure 5-2**.

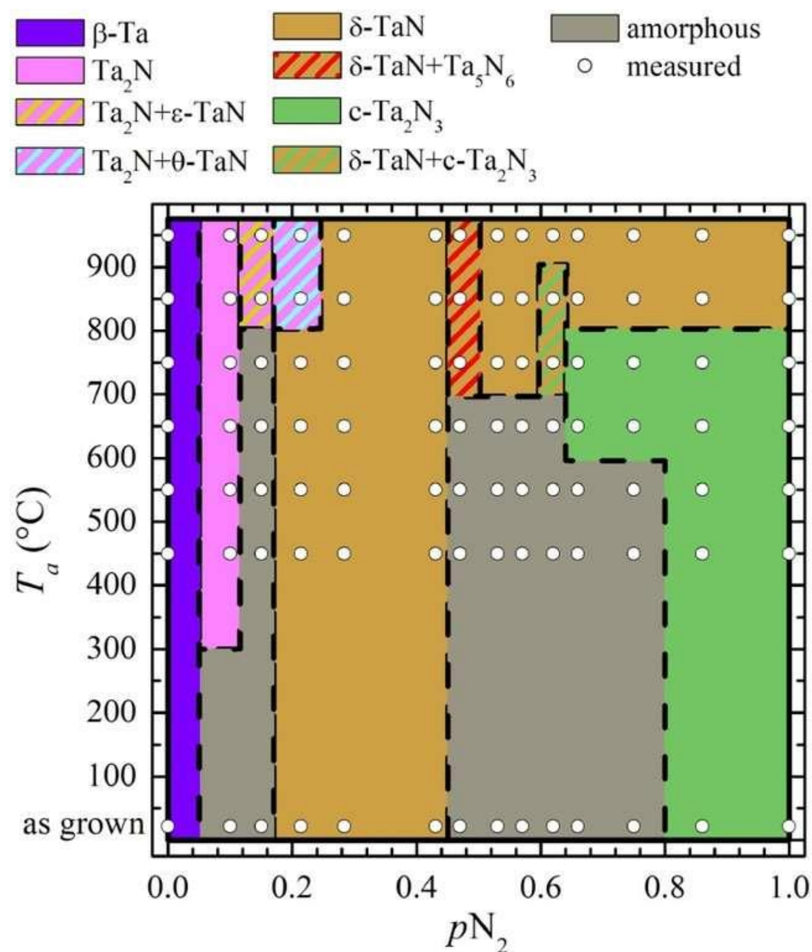

Figure 5-2. Phase diagram of DC magnetron sputtered tantalum nitride films (Salamon et al. 2016), where T_a is the annealing temperature and pN_2 refers to the total amount of nitrogen in the sputtering atmosphere (1 = 100%).

Despite the number of different phases possible, this work will only focus on a few members of the series, specifically members of the TaN phase series and Ta_3N_5, the former because of its tendency to sputter well, and the latter because of its importance to the topic. A brief overview of these structures and their properties will be provided in the following subsections.

5.1 The TaN Phase

The TaN series of phases are heavily studied materials, as structures in the series possess notable electronic and wear properties (An & Zhang 2007; Gladczuk et al. 2005). Among

others, some applications include the use of TaN as a layer electrode in gate transistors (Gladczuk et al. 2005; Min, Chun & Kim 1996; Oku et al. 1996; Riekkinen et al. 2002; Shin, CS et al. 2002), as a diffusion barrier to prevent Cu migration into Si substrates (Oku et al. 1996), and as a functional protective coating on steel (Chauhan et al. 2018).

The TaN phase exists as a metastable series of structures (Arshi et al. 2014; Kim et al. 2020), most commonly existing in either the face centered cubic, or rocksalt structure, expressed as δ-TaN, or the hexagonal structure, which is expressed as ε-TaN (Schonberg et al. 1954). These structures are depicted below in **Figure 5-3**.

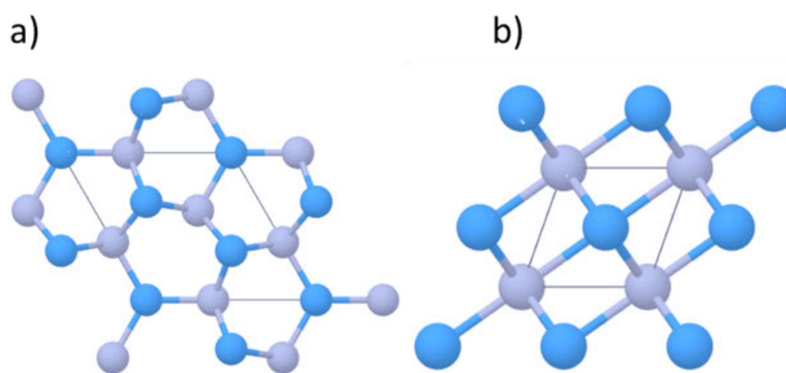

Figure 5-3. Extended unit cell crystal structures of a) hexagonal TaN (ε-TaN) and b) fcc cubic TaN (δ-TaN), where the blue balls represent the tantalum and the gray balls represent the nitrogen.

The desired application of TaN often plays an important role in deciding whether TaN will be deposited with RF (Riekkinen et al. 2002) or DC (Min, Chun & Kim 1996) sputter deposition (Shin, CS et al. 2002), ion beam assisted deposition (Baba & Hatada 1996), chemical vapour deposition (Fix, Gordon & Hoffman 1993) or ammonolysis reactions (Holl et al. 1990).

Of these, physical vapour deposition (PVD) methods, namely sputtering, are particularly common (An & Zhang 2007; Gladczuk et al. 2005; Kim, S & Cha, B 2005; Min, Chun & Kim 1996; Oku et al. 1996; Riekkinen et al. 2002; Shin, CS et al. 2002). However, in the case of PVD as well as other methods, the specific relationships between the applied deposition conditions and the resulting film properties are typically only superficially monitored. Many published works aim to develop the material as a functional material, with the choice of method (i.e. PVD) being largely auxiliary to the investigation of functional properties.

Considering the impact of synthesis method on resulting properties, it is necessary to investigate several deposition regimes if the aim is to produce highly engineered films with

tailored properties. Recent works have explored the deposition parameters and resulting functional properties of sputtered TaN film (Kim, S & Cha, B 2005; Zaman & Meletis 2017), in particular focusing on atmospheric nitrogen values within the 1-30% range. Higher nitrogen pressures, ranging up to pure N_2 sputtering, have been explored in only a few studies (Alishahi et al. 2016; Hieber 1974; Nie et al. 2001).

The relationship between the deposition of these structures and the conditions under which they're deposited has been explored (Noda et al. 2004), however given the complexity of the various sputtering parameters and individual differences in sputtering systems, there still exist gaps in the current body of work. For example, since TaN films are typically investigated for mechanistic, electronic or wear related properties, certain substrates and processing parameters are selected to facilitate this while others are neglected or left unexplored (Borovinskaya 2017). Advancing the research is of growing importance, which is evidenced by much of the contemporary work on this nitride having taken place within the last 10 or 20 years (Firouzabadi et al. 2017; Grosser, Seidel & Schmid 2017).

During the reactive sputtering of TaN, many variables in the sputtering environment can be manipulated and all can affect the exhibited characteristics of the as-deposited film in a range of ways. Therefore, to better employ TaN as a functional material for specific applications, it is important to acquire an understanding of what results can be expected from the imposed fabrication conditions. Those properties of TaN that may be readily affected include fundamental properties such as structure, composition, and microstructure, as well as functional properties, such as electrical conductivity, hardness, or thermal diffusivity. When using reactive magnetron sputtering to prepare TaN with specific performance attributes in mind, success will be determined by how well the available deposition parameters are utilised and exploited.

In general terms, the fcc cubic TaN phase can be easily deposited within a wide range of atmospheric nitrogen values and applied temperature conditions (Shin, CS et al. 2002).

5.2 The Ta_3N_5 Phase

The Ta_3N_5 phase in particular has seen significant research interest in the last few years as a novel water splitting nitride (Hara et al. 2003; Hitoki et al. 2002; Ishikawa et al. 2004; Kim, SK & Cha, BC 2005) after its rediscovery as a potential water splitting material in the early 21st century (Hitoki et al. 2002). Instances of the Ta_3N_5 structure have been reported in the literature using many different synthetic methods (Wang, C et al. 2016), however thin film deposition techniques were of primary interest to this investigation.

Ta_3N_5 is notable as a solar water splitting material for its appreciable band gap of 2.1 eV (Hitoki et al. 2002), which allows it to absorb light in the visible range of the electromagnetic spectrum. Its band edge potentials also straddle the redox potentials of water, which allows both the oxidation and reduction of water ostensibly without any applied bias (Fan et al. 2019). As per **Figure 5-4**, the CB and VB of Ta_3N_5 are primarily characterised by the Ta 5d and N 2p orbitals, respectively (Nurlaela, Ziani & Takanabe 2016).

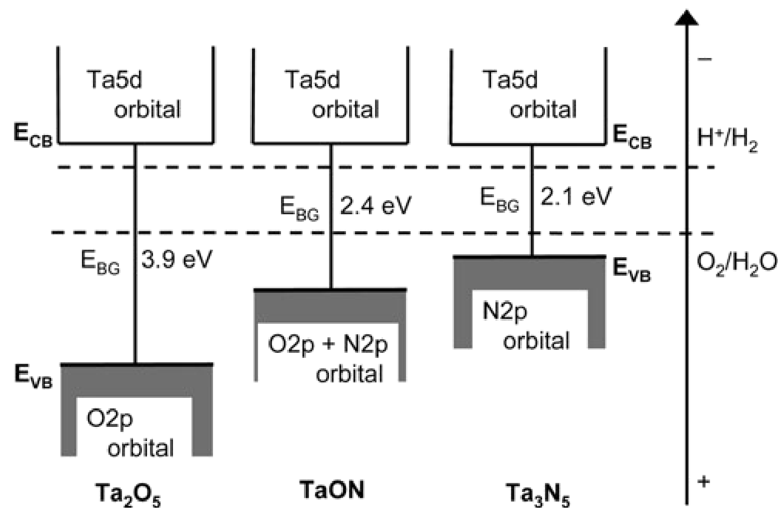

Figure 5-4. Band structures of Ta_2O_5, TaON and Ta_3N_5 (Chun et al. 2003).

Ta_3N_5 is a stable material under ambient conditions, only decaying to lower order tantalum nitride phases (such as Ta_5N_6) when annealed under nitrogen poor atmospheres at high temperatures (Stampfl & Freeman 2005). It is stable in acidic and basic solutions, although it suffers from photocorrosion as a result of surface oxidation under water splitting conditions (Ishikawa et al. 2004). Addressing this remains the major strategy in improving its photo-electrochemical performance and will be covered in more detail in the literature review section.

The Ta_3N_5 structure exists as two distinct crystal phases: monoclinic and orthorhombic, although it is most often synthesized in the orthorhombic conformation. The orthorhombic Ta_3N_5 structure, which will be dealt with predominantly in this work, is shown below in **Figure 5-5**.

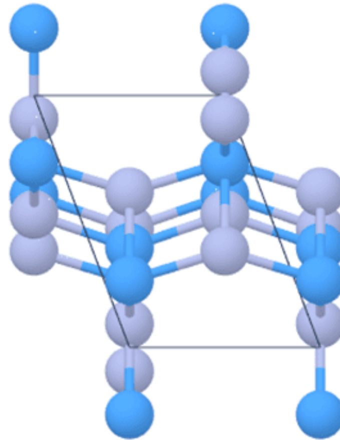

Figure 5-5. The extended unit cell orthorhombic crystal structure of Ta_3N_5. Orthorhombic Ta_3N_5 exists in the space group Cmcm and is composed of irregular packing of TaN_6 octahedra. Blue balls represent the tantalum and grey balls represent the nitrogen.

It is not a biologically hazardous material nor is there any biological concern with using it, its constituents and precursors are economically accessible, and its synthesis is widely documented and well established (Brauer & Weidlein 1965; Hara et al. 2003; Higashi, Domen & Abe 2011). The phase is not known to exist naturally in any significant quantities and is instead synthesized for experimental purposes. This is traditionally done via thermal ammonolysis of the naturally occurring tantalum oxide phase, which is Ta_2O_5 (Brauer & Weidlein 1965). Synthesis via other methods is reported, most commonly deposition methods (Kim, S & Cha, B 2005), however ammonia treatment of the product(s) is often still necessary to achieve desirable crystallinity and phase purity (Zhang, Q & Gao 2004). A more critical review of synthetic methods used in the literature will be covered in the next chapter.

Ta_3N_5 is the most resistive of the phases in the tantalum nitride spectrum, owing to its position in the phase series as the most nitrogen heavy phase. It typically presents as an n-type semiconductor material, although its electronic properties will vary with synthetic methods used (Chun et al. 2003).

Often, Ta_3N_5 will contain oxygen impurities of varying concentrations (Chang et al. 2020), depending on the synthetic method used and the oxygen concentration present, although most published literature does not recognise this. New research has shown the necessity of oxygen in the substitution reaction that produces the Ta_3N_5 phase (Rudolph, M et al. 2019), however it can also create problems that impinge on the water splitting performance of the material, such as increasing the resistivity or reducing charge mobility through the bulk. The mechanism for this lies in the defects produced by oxygen in the host lattice structure, which will be further expounded upon in the literature review section of this work. Ultimately, the

requirement to include oxygen when depositing Ta_3N_5 directly via sputter deposition poses a challenge of necessity; how much oxygen is necessary to produce the phase while not impinging on the performance. Careful consideration must therefore be given to the synthetic method used when synthesizing the phase.

The resulting powders or films typically take on a brilliant reddish hue, indicative of the material's ~2.1eV band gap, which absorbs visible light up to 600nm, leaving just the red end of the spectrum. Examples of Ta_3N_5 in powder and thin films produced during this project can be seen below in **Figure 5-6.** The XRD peaks verifying the presence of Ta_3N_5 in the shown film and powder can be seen in

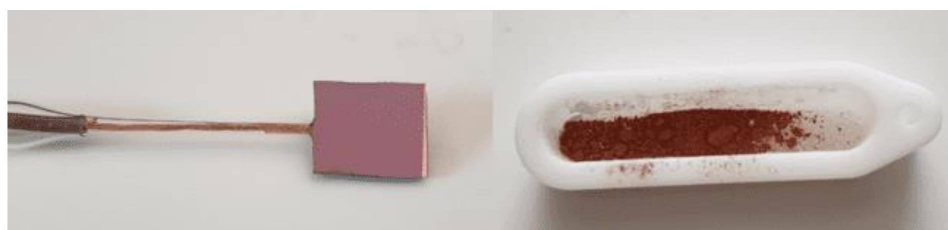

Figure 5-6. Ta_3N_5 thin film mounted as an electrode (left) and red Ta_3N_5 powder (right), reacted from Ta_2O_5 powders via thermal annealing in NH_3.

Finally, while Ta_3N_5 primarily sees interest as a water splitting material, it has also seen investigation for other uses, such as in water purification (Jones et al. 2017) and anti-microbial roles (Cristea et al. 2019), which leverage its properties as an efficient photocatalyst material. A more critical and in-depth discussion of the position of Ta_3N_5 in the literature will be covered in the literature review section.

5.3 Ta_3N_5 Synthesis: Mechanism

The purpose of this chapter is to describe the reaction mechanism behind the nitridation of tantalum oxides (and oxynitrides) as it relates to this work, especially as it relates to the sputter deposition of Ta_3N_5. An overview of the synthetic literature is provided, and the routes used in this project described before the mechanism for the reaction from Ta_2O_5 to Ta_3N_5 is laid out. It is important to address the mechanism in attempting to account for the difficulties presented by attempting to deposit the Ta_3N_5 phase directly and to demonstrate an understanding of the mechanistic processes key to this work.

5.3.1 Challenges in Sputtering Ta_3N_5 Thin Films

Deposition of the Ta_3N_5 phase was initially attempted with a single tantalum target utilising a DC power source, with just argon and nitrogen as the reactive gas mixture. This section of the work was detailed in section 8.1. The Ta_3N_5 phase is the most nitrogen heavy of the phases in the series, as such it was hypothesized that appropriate tuning of the atmospheric nitrogen content would produce higher order tantalum nitrides. However, it was demonstrated that increasing the proportion of atmospheric nitrogen alone does not produce the Ta_3N_5 phase.

Table 5.2. Collection of notable papers that report deposition of Ta_3N_5.

Synthesis Comments	Description	Work
DC magnetron sputtering	Ta_3N_5 deposited at N_2:Ar ratio of 0.3 or higher	(Kim, SK & Cha, BC 2005)
RF magnetron sputtering (with bias)	Ta_3N_5 deposition using Ar/N_2 mix of 1:1	(Scandurra et al. 2008)
RF magnetron sputtering	Deposited Ta_3N_5 using Ar/N_2 mix	(Yang et al. 2011)
RF magnetron sputtering	Deposited Ta_3N_5 using Ar/N_2 mix	(Yang et al. 2012)
DC magnetron sputtering	Deposited Ta_3N_5 with Ar/O_2/N_2 mix	(Rudolph, M. et al. 2016)
DC magnetron sputtering	Deposited mixed Ta_3N_5 with Ar/N_2 mix	(Alishahi et al. 2016)
Unbalanced DC magnetron sputtering	Deposited Ta_3N_5 with Ar/O_2/N_2 mix	(Chang et al. 2020)

Other deposition parameters were examined, with reports in the literature citing their use in deposition of the phase (Scandurra et al. 2008). As Ta_3N_5 is the most resistive phase in the series (Stampfl & Freeman 2005), the use of RF instead of DC power sources represents a viable avenue for future investigations given RF sputtering is preferable when sputtering from non-conductive targets.

It was also speculated that adjusting substrate type and geometry may promote growth of the Ta_3N_5 phase through substrate epitaxy, but these strategies also failed to produce crystalline

Ta_3N_5 structures. It was acknowledged that these results need to be substantiated by looking at the mechanism and discussing the conditions required to sputter Ta_3N_5 when other researchers have reported the phase using the same broad techniques that were utilised in this body of work (Leroy et al. 2012; Rudolph, M. et al. 2016; Rudolph, M et al. 2019; Yokoyama et al. 2011) (as per Table 5.2).

The difficulties faced in synthesizing Ta_3N_5 as it pertains to this project can be simplified to two routes:

1) Sputter deposition of Ta_3N_5 using Ar/N_2 mix with higher atmospheric nitrogen and
2) Sputter deposition of Ta_3N_5 using $Ar/N_2/O_2$ mix, with a very small amount of oxygen (0.1-3%) included to stabilise the formation of the Ta_3N_5 structure

Route 1) will be addressed first. The phases lower in nitrogen cannot be converted directly to Ta_3N_5, as the latter phase is the highest energy state phase in the series. This is due to Ta_3N_5 possessing Ta in the +5 oxidation state, whereas other phases in the series exhibit Ta in the +3 oxidation state, which makes the proposal of incorporating more nitrogen into the metal heavy phases energetically unfavourable.

This work verifies that the incorporation of oxygen in the synthetic process is necessary to synthesize Ta_3N_5 and is even integral in improving various properties of the material, such as the photo-electrochemical potential either in-situ during sputtering or afterwards as part of the annealing process (Rudolph, M. et al. 2016; Rudolph, M et al. 2019). Additionally, as discussed in the doping section of the work, the magnitude of and nature of nitrogen vacancies have been directly implicated in altering the band structure and improving the charge transport in the Ta_3N_5 lattice. Oxygen's role in seeding the Ta_3N_5 phase has been investigated extensively by Rudolph and colleagues and was provided as such: because Ta^{5+} is a high oxidation state for the Ta atom, synthesis of the Ta_3N_5 phase is favourable due to the increased stability when nitrogen positions in the lattice are substituted with oxygen, which is a more electronegative element (Etourneau, Portier & Menil 1992).

As such, in terms of addressing problem 1), it should not be possible to deposit Ta_3N_5 in similar sputtering environments that employ only tantalum targets sputtered under a nitrogen reactive gas, despite literature reports of a crystalline Ta_3N_5 phase resulting from such experiments.

This leaves route 2), which is difficult to address without the use of plasma analysis techniques, which are included in the previously described studies (Chang et al. 2020; Rudolph, M. et al. 2016; Rudolph, M et al. 2019). This presents further problems, because if annealing is necessary to achieve high purity crystalline Ta_3N_5 films from sputter deposition,

there is then a challenge in addressing the complex defect states and microstructural imperfections that arise from the harsh ammonolysis treatment conditions. A conclusion may be that sputter deposition of Ta_3N_5 is inferior to methods such as ALD and other CVD techniques when producing performance-oriented materials.

While Ta_3N_5 could not be deposited directly in this work, others in the field have reported that this is possible. Given the lack of detailed mechanistic reports in current literature and the work covered until this point, it is possible to propose a speculative mechanism whereby tantalum oxide (or TaON) is progressively reacted to Ta_3N_5 in the presence of NH_3 and heat.

5.3.2 Proposed Mechanism

The mechanism by which metal nitrides are created from oxides or the native metals themselves is covered superficially in many works (Dabirian, Spijker & van de Krol 2012; Pinaud, Vailionis & Jaramillo 2014). This is partly due to the scope of the works, which often focus on the performance related effects of the nitridation process, but also because of the difficulty in determining what is taking place at the reaction interface. Pertinent synthetic trajectories described in the literature are shown below in **Figure 5-7** for reference.

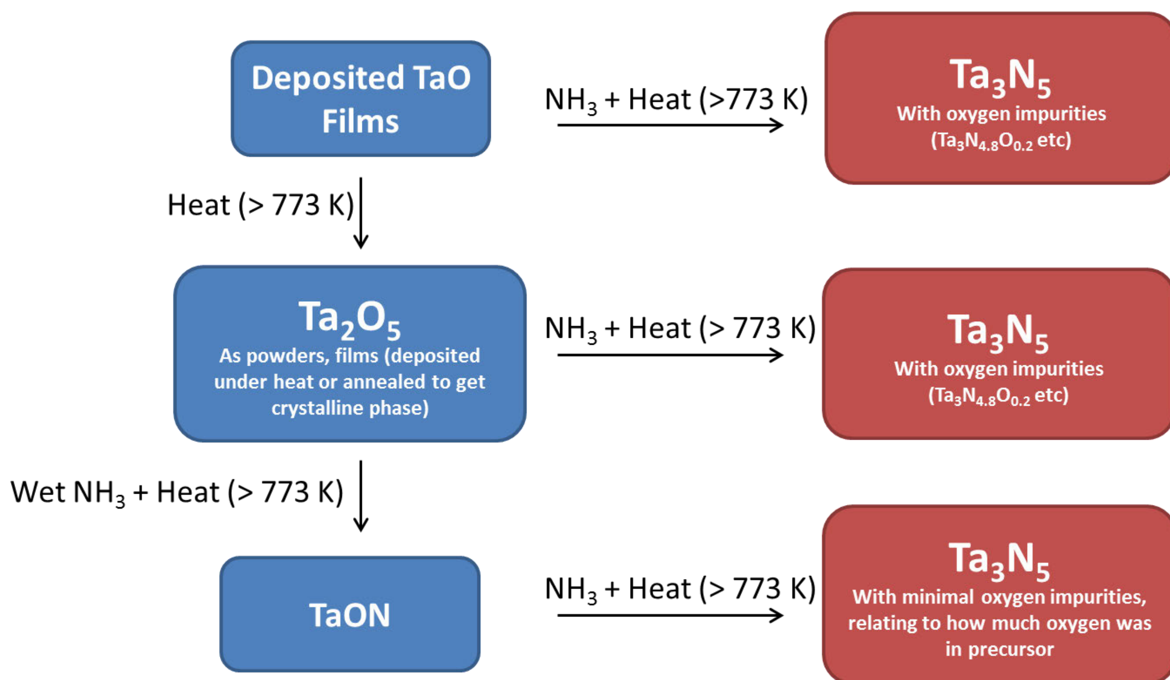

Figure 5-7. Routes to Ta_3N_5 phase as detailed in the literature. Initial tantalum oxide films are deposited in mixed Ar/O_2 gas phase.

As discussed in the literature review section, Ta_3N_5 is historically produced by nitriding the Ta_2O_5 phase. TaON can be derived instead by annealing in 'wet' NH_3 gas phases and can

also be subsequently nitrided to Ta_3N_5 using dry NH_3. This project utilised and tested a number of these routes, the results of which are summarised in **Figure 5-8**.

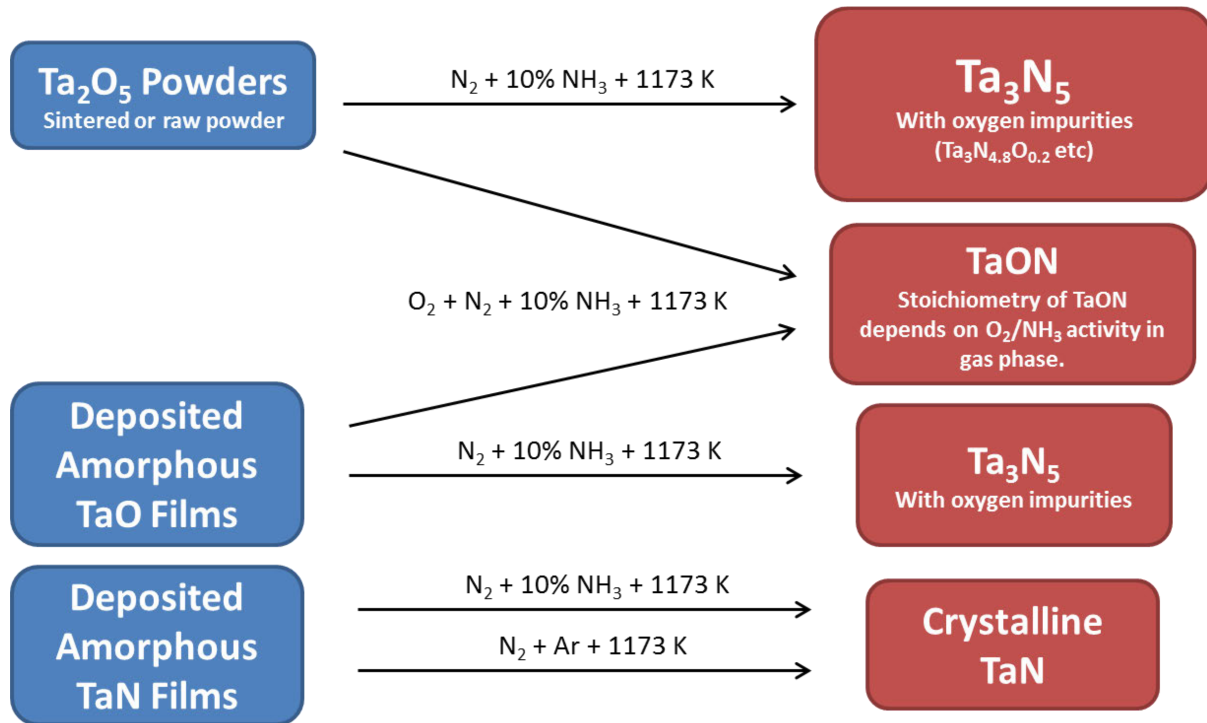

Figure 5-8. Routes to Ta_3N_5 documented in this project.

The routes summarised in Figure 5-7 were tested successfully. TaN films deposited in this work were also annealed in multiple gas phases including N_2/Ar and NH_3, resulting in an amorphous to crystalline phase change in both cases. It is clear from these summaries that the synthesis of Ta_3N_5 requires both oxygen in the reactant species and annealing in NH_3.

This reaction takes place through a process of NH_3 decomposing under heat and driving substitution of oxygen with nitrogen, resulting predominantly with H_2O and Ta_3N_5, as well as other gases (H_2, NH, NH_3, N_2). This approach is speculated to be as follows:

1. NH_3 will begin to undergo decomposition to NH_2 at temperatures within the range of 1023-1423 K (Brauer & Weidlein 1965) and reduce Ta_2O_5 via decomposed H^+ reacting with surface oxygen to form OH.
2. NH_2 and NH_3 will adsorb at the surface of the reduced Ta_2O_5, with NH_3 reacting with a surface O to form additional NH_2 and OH. Surface Ta forms a bond with N in NH_3 as these reactions proceed (Liu, D et al. 2019; Manna et al. 2020; Szaleniec et al. 2013).
3. OH easily reacts with H^+ from decomposed NH_3 to produce H_2O. Dehydroxylation takes place with two H atoms in adsorbed NH_2 taking away surface O, also producing H_2O.

4. As these processes proceed, surface N will diffuse to the bulk, transforming Ta_2O_5 to TaON and finally Ta_3N_5. The overall reaction of tantalum oxide to Ta_3N_5 is shown in **Equation 19** and in **Figure 5-9:**

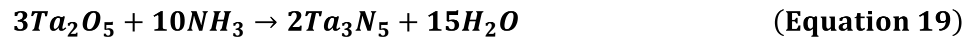

$$3Ta_2O_5 + 10NH_3 \rightarrow 2Ta_3N_5 + 15H_2O \qquad \text{(Equation 19)}$$

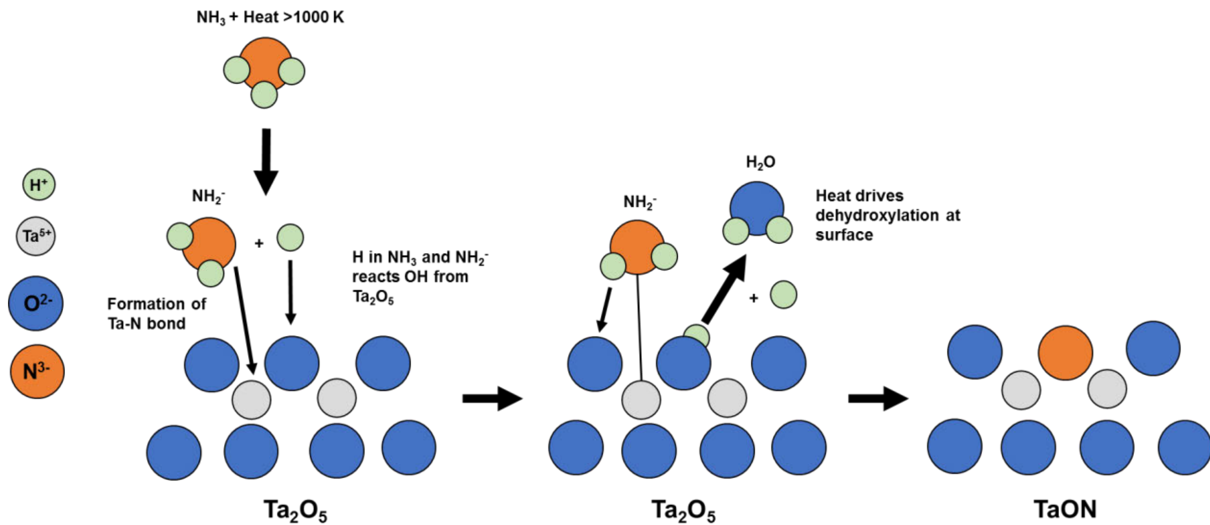

Figure 5-9. Proposed intermediate reaction mechanism for synthesis of Ta_2O_5 to TaON. Progressive substitution of lattice oxygen by nitrogen will eventually result in the formation of Ta_3N_5.

The overall reaction results with Ta_3N_5 with oxygen impurities, outputting H_2O. This process of anion diffusion involves the substitution of three oxygen atoms with two nitrogen atoms to maintain the high oxidation state of the tantalum ion (Ta^{5+}). Maintaining the +5 charge on tantalum is important in catalysing the Ta_3N_5 phase, as Ta_3N_5 is the only nitride phase in the series that possesses Ta in this oxidation state.

If this +5 oxidation state isn't achieved prior to ammonia annealing, a lower order nitride is instead formed, as can be seen with the deposition of TaN in the first section of this work. For these reasons it is also energetically unfavourable for TaN phases to be reacted into Ta_3N_5. The nitridation process is dictated by the flow rate of ammonia, and to a lesser degree the temperature and time. With the absence of oxygen in the sample or the gas phase, NH_3 treatment alone does not convert lower order tantalum nitride phases into higher order phases.

Chapter 6: Literature Review

The focus of this review is placed on developing Ta_3N_5 from a photo-electrochemical perspective, in addition to the use of Ta_3N_5 as a photocatalyst. The development of Ta_3N_5 as a photo-electrode vs photocatalyst will be contrasted. Following this, a brief overview of other notable nitrides and their position in the field is given. Finally, a distillation of the problem that this project aimed to address will conclude the chapter.

6.1 Ta_3N_5 in the Literature

First described theoretically in the mid-20th century, the synthesis of Ta_3N_5 was reported in the literature as early as 1965 (Brauer & Weidlein 1965), as part of the tantalum nitride (TaN, Ta_2N, etc) phase series. Due to its synthetic requirements (thermal nitridation typically requiring dangerous ammonia gas) and lack of known applications, Ta_3N_5 was generally ignored outside of works investigating its electrical properties (Hieber 1974; Swisher & Read 1972).

It was reported in 2002 that Ta_3N_5 was capable of total overall water splitting in the presence of sacrificial reagents (Hitoki et al. 2002). This finding encompassed a recent change in the water splitting field, as research efforts through the late 90's and early 2000's had begun to expand beyond developing traditional oxide materials (Rioult 2015) as water splitting materials.

Several qualities inherent to Ta_3N_5 made it compelling as an effective water splitting material. It maintains a low band gap energy of 2.1eV (Hitoki et al. 2002; Ishikawa et al. 2004; Yokoyama et al. 2011; Zhang, Q & Gao 2004), which is close to the optimum band gap for solar water splitting at 2.0eV (Walter et al. 2010). This corresponds to a wavelength of approximately 600nm, thus allowing the utilisation of light in the visible spectrum (Matsuoka et al. 2007). Traditional metal oxides, such as TiO_2, typically utilise light in the UV spectrum, a small portion of the light striking the Earth's surface.

Additionally, for photoelectrolysis to occur without the application of an external voltage, the conduction band minimum and valence band maximum (E_{CB} and E_{VB}, respectively) of a given material must straddle the redox potentials of oxygen and hydrogen. This is the case with Ta_3N_5, with its band positions straddling the water redox potentials at E_{CB} > 0 V vs RHE and E_{VB} <1.23 V vs RHE (Ma et al. 2012).

DFT modelling has indicated that the conduction band of Ta_3N_5 is primarily composed of Ta5d orbitals, with the valence band composed of N2p orbitals, although these conditions probably do not represent the true nature of the phase, which often contains oxygen purities. As a result of these qualities, Ta_3N_5 has been shown to possess a large theoretical solar-to-hydrogen conversion efficiency of 15.9% (of theoretical ideal 16.8%) when compared to other water splitting materials illuminated by a standard solar source equivalent to AM 1.5 (Murphy et al. 2006).

6.2 Ta_3N_5 and its use as a photo-electrode

In 2002 Hitoki and coauthors reported Ta_3N_5 as a photocatalyst capable of overall water splitting (Hitoki et al. 2002). With light absorption in the visible light range of 600nm, and oxidation reduction potentials straddling those of H_2O, Ta_3N_5 represents a viable material for use in PECs (Chun et al. 2003; Higashi, Domen & Abe 2011). In the following years, Ta_3N_5 received increased attention as both a nanostructured photo-catalyst (Zhang, Q & Gao 2004) and photo-electrode (Feng et al. 2010) material.

Currently, the highest output observed using a Ta_3N_5 photoanode is reported by G. Liu and coauthors at 12.1mA cm^{-2} at 1.23 V vs RHE (Liu, Guiji et al. 2016). This was achieved using a highly engineered approach; a Ta_3N_5 photoanode coupled with a surface $Ni(OH)_x$/ferrihydrite hole storage layer, a TiO_x blocking layer to reduce electron-hole recombination and Co cubane and Ir complex molecular catalysts to assist with water oxidation. To date, the most promising results have incorporated Ta_3N_5 as part of a whole device to compensate for its shortcomings as a photoanode (Pei et al. 2018). A summary of the progress made with Ta_3N_5 photoanodes is given in the **Table 6.1** below.

Table 6.1. A summary of Ta_3N_5 photo-electrode performance records in the published literature, where STH refers to the solar-to-hydrogen efficiency of the electrodes.

Material	STH (%)	Performance ($mA\ cm^{-2}$)	Date (year)	Ref
Theoretical limit for Ta_3N_5	15.9%	-	2010	(Tabata et al. 2010)
CoPi/GaN/Ta_3N_5 film	1.5%	8.5	2017	(Zhong et al. 2017)
Ta_3N_5/Ni(OH)$_x$/ferrhydrite/Co-Ir complex and TiO_x blocking layer	2.5%	12.1	2016	(Liu, Guiji et al. 2016)
Ba doped Ta_3N_5 nanorods	1.5%	6.7	2013	(Li, Y, Zhang, et al. 2013)
Vertically aligned Ta_3N_5 nanorods	<0.5%	3.8	2013	(Li, Y, Takata, et al. 2013)

The major challenges that need to be addressed before employing Ta_3N_5 as an efficient photo-electrode are those of photo-corrosion (Ishikawa et al. 2004), poor electronic properties (Morbec et al. 2014; Ziani et al. 2015) and low photovoltage (Pinaud, Vailionis & Jaramillo 2014). Early papers cited no degradation in efficiency under water splitting conditions, this was due to the use of sacrificial reagents in the PEC setup (Chun et al. 2003; Hitoki et al. 2002). When exposed to water splitting conditions, photo-generated holes prompt oxidation of nitrogen anions at the surface of the Ta_3N_5 electrode, which evolve in the form of gaseous N_2 and leave the oxide, Ta_2O_5 (Su et al. 2015).

As previously outlined, sacrificial reagents quell this reaction (commonly alcohols, ethylene diamine tetraacetic acid (EDTA), lactic acid (Li, Q, Li & Yu 2020)), however this approach is not sustainable (depending on the reagent used (Singh & Dutta 2021)) and does not address the goal of using water exclusively. Research has been directed at applying a layer (or layers) of materials to the Ta_3N_5 electrode in order to delay or prevent photocorrosion through the scavenging of photo-generated holes (Liu, Guiji et al. 2014), which has proven one of the most effective methods in applying Ta_3N_5 as a photo-electrode to date (Wang, L et al. 2015).

As opposed to that of a photo-electrode, a large amount of research has been focused on developing Ta_3N_5 as an effective photocatalytic material (Chen, Shen, et al. 2015; Hitoki et al. 2002; Ma et al. 2012; Zhang, Q & Gao 2004), as the requirements for a viable photocatalytic material are more restrictive than those of a photo-electrode (Nurlaela, Ziani & Takanabe 2016); Ta_3N_5 possesses the ability to perform both the oxidation and reduction of water, a

quality highly appealing for a photocatalytic material as single particles are required to perform the entire reaction. A more critical discussion of these two routes to water splitting will be covered later in this section of the work.

The capability of Ta_3N_5 to perform both the oxidation and reduction of water is also beneficial in the case of photo-electrochemical water splitting, with Ta_3N_5 capable of being used as a photocathode. In the studies that do assess Ta_3N_5 as a photo-electrode in a photoelectrochemical environment, it is typically employed as the photo-anode performing water oxidation. It may be possible to heavily dope Ta_3N_5 to impose p-type behaviour, thereby utilising it as a photo-cathode. By using this approach, the photo-corrosion of the electrode may be avoided as oxidation will not be taking place on the surface of the film. To date, p-type Ta_3N_5 electrodes have not been reported in the literature, although p-type behaviour from certain substrate and layer combinations have been reported (Ziani et al. 2015).

Necessary to a p-type semiconductor is doping, which exists in the literature regarding Ta_3N_5 but remains relatively immature. The alkali metals have been established as efficacious dopant candidates (Ma et al. 2012), able to improve the photocurrent through changes to the defect disorder resulting in suppressed recombination centers (Seo et al. 2015; Xie et al. 2016). These reports focus on the alkali earth metals as dopant candidates, however there does exist some exploration of other metallic dopants, such as Zr (Wang, Yawei, Zhu & Xu 2016) and W (Grigorescu et al. 2015), both of which have seen improvements in Ta_3N_5 electrodes, the former predominantly through the same favourable alteration of the defect disorder as seen in Mg doped Ta_3N_5 (Sun, Q et al. 2017).

Some early reports indicate promising findings regarding doping, including the ability to tune the band gap (Wang, J, Fang, et al. 2014) and shift the conduction band minimum (Wang, J, Ma, et al. 2014). Such works have highlighted the potential of incorporating p-type dopants with codoped oxygen in order to counteract the undesirable electronic properties conferred by inherent oxygen impurities in Ta_3N_5 samples (Wang, J, Fang, et al. 2014). Various reports of Ta_3N_5 doping for use in PEC experiments have seen greater water splitting efficiencies relative to undoped Ta_3N_5 reference electrodes through the various mechanisms outlined above.

Finally, the nature of the synthetic mechanism of Ta_3N_5 has been touched on in some research topics but is not well developed. A phase diagram of the tantalum nitride system has been described recently (Salamon et al. 2016), but is aimed more at describing the conditions that produce the numerous different structures of TaN and other lower order tantalum nitrides. The synthesis of these phases is well described (Noda et al. 2004; Ritala et al. 1999), however

Ta_3N_5, being the most nitrogen rich phase in the series, tends to be more difficult to synthesize in the context of the various synthetic methods used (Rudolph, M. et al. 2016). While tantalum oxides are typically used as precursors, the nature of the reaction series leading to Ta_3N_5 formation has not been thoroughly described, despite having been explored to some degree via sputtering and annealing experiments (Pinaud, Vailionis & Jaramillo 2014; Rudolph, M. et al. 2016). These issues, in addition to shortcomings in water splitting efficacy, should be addressed in preparing Ta_3N_5 for economical use.

6.2.1 Doped Ta_3N_5

At present there are only a few reports available in the literature that describe the synthesis or photo-electrochemical/photo-catalytic performance of doped Ta_3N_5 (Grigorescu et al. 2015; Kado, Hahn, et al. 2012; Kado, Lee, et al. 2012; Macartney et al. 2020; Seo et al. 2015). In all cases performance was improved, albeit through several different mechanisms; improved crystallisation, altering of the band gap, improved conductivity and a lowered onset potential.

Favourable changes to the defect chemistry of Ta_3N_5 have been highlighted as driving these improvements (Seo et al. 2015; Wang, Yawei, Zhu & Xu 2016). The nature of defects within the structure of Ta_3N_5 and how certain dopants play into this relationship has been the topic of a few papers (Wang, Yawei, Zhu & Xu 2016; Xie et al. 2016). These studies have often included DFT studies in evaluating the defect models they describe, as it is difficult to experimentally investigate given the nature of defect chemistry in a material. Despite this, the reduction of nitrogen vacancies and increase in oxygen occupancy in these positions, denoted as $V_N^{\bullet\bullet\bullet}$ and $O_N^{\bullet}$, respectively, in the Ta_3N_5 lattice, were attributed as being the primary factors in improving conductivity and charge transfer in the doped materials. This is due to the tendency of $V_N^{\bullet\bullet\bullet}$ positions to act as charge recombination centres in the material lattice (Wang, Yawei, Zhu & Xu 2016).

As a material for solar energy conversion, the tuning of the electronic structure is vitally important for engineering almost all performance-related properties and doping is one of the most effective ways in which this can be done. For Ta_3N_5 in particular, the scope for acceptor-type doping is especially broad due to the penta-valent nature of Ta. Furthermore, given the relative immaturity of the body of work focusing on Ta_3N_5, any investigations into the doping of Ta_3N_5 will provide a fundamental contribution to the field of solar-driven water splitting.

6.3 Ta_3N_5 as a photo-electrode rather than as a photo-catalyst

The synthesis of Ta_3N_5 is often achieved with nitridation of Ta_2O_5 powders in a stream of NH_3 gas at elevated temperatures. Such powders have subsequently been assessed for their performance as photocatalysts where both the water oxidation and reduction reactions take

place (Jiang et al. 2018). Under such conditions, charge separation during illumination is governed by the relative rates of the respective oxidation (anodic) and reduction (cathodic) reactions and one process may become overwhelmingly rate limiting due to the absence of appropriate reaction sites. This is evidenced by the need to decorate the surface of Ta_3N_5 particles with noble metals such as Ru or Pt in order to promote hydrogen gas evolution (Tabata et al. 2010).

In the alternative and comparatively un-investigated configuration whereby Ta_3N_5 has been processed as thin film and operated as a photo-electrode, charge separation is governed by the presence of a space charge layer and the photo-generated charge carriers are driven apart from each other towards the surface of the two electrodes that principally form the PEC. Under these conditions, the evolution reactions for oxygen and hydrogen gases are not competing for reaction sites, and for the typically n-type Ta_3N_5, hydrogen is evolved exclusively and efficiently at the metallic counter electrode.

Provided that the counter electrode has sufficiently high surface area, this configuration ensures that the evolution of oxygen at the Ta_3N_5 photo-electrode is always rate limiting and therefore simplifies the task of engineering higher water splitting performance. Furthermore, the generation of oxygen and hydrogen at separate locations within the PEC make gas separation easier and prevents the loss of efficiency due to the reverse reaction of hydrogen and oxygen to water.

6.4 Synthesis of Ta_3N_5

This subsection of the literature review will critically evaluate the numerous synthetic methods used in synthesizing Ta_3N_5, whether it is films, nanotubes or powders. The synthetic methods used vary greatly and are important in determining the capability of the material produced. Extra attention will be paid to deposition methods, as these methods underpinned the synthetic routes taken in this project.

6.4.1 Thermal Nitridation

As previously mentioned, the most common method of synthesis of Ta_3N_5 remains the thermal nitridation method, where a precursor material (typically tantalum oxide, but tantalum metal substrates have also been used) is reacted under heat and gaseous ammonia (NH_3) to synthesize the final phase (Hitoki et al. 2002; Swisher & Read 1972). This method was used initially to synthesize a slew of tantalum nitride materials for characterisation purposes during the 60's and 70's (Brauer & Weidlein 1965). It remains a popular synthetic route today given its low cost and ease of setup.

While annealing treatments have advantages, they do not allow fine control over the microstructure of treated materials; with Ta_3N_5 films produced this way typically being multicrystalline, with numerous structural defects as a result of the stressing brought on by the heating (Yokoyama et al. 2011). Grain boundaries in particular are problematic due in part to their tendency to act as charge recombination sites (Shafarman, Siebentritt & Stolt 2011), locally reversing the water splitting reaction. Additionally, defects within the structure of the films appear to negatively influence the electrical properties in a photo-electrochemical environment (Pinaud, Vailionis & Jaramillo 2014), disrupting charge transfer and charge transport properties and driving such charge recombination sites (Fu et al. 2015). These impingements ultimately work to reduce the quantum efficiency of the material (Ma et al. 2012).

Despite these reported drawbacks, thermal nitridation provides a reliable, accessible, and experimentally controllable method by which to synthesize the Ta_3N_5 phase. A variety of synthetic methods have been used to synthesize Ta_3N_5, however given the nature of the reaction mechanism, oxygen impurities tend to remain in the structure; this is especially true of vapour deposition methods (Fu et al. 2015; Rudolph, M. et al. 2016; Xie et al. 2016). As a result, these impurities usually necessitate post-annealing in NH_3 to create high purity Ta_3N_5 products.

6.4.2 Nanostructured Routes

Over the last 30 years, a substantial degree of research has focused on developing nanostructured materials, with numerous products incorporating these advances reaching market and promising vastly superior performance. The field of water splitting is no exception, with nanostructured light sensitive Ta_3N_5 materials and devices seeing an increased frequency of publications since 2001.

Several synthetic routes have been employed in this regard, including hydrothermal processes (Su et al. 2014), particle transfer methods (Seo et al. 2015), anodisation (Kado, Hahn, et al. 2012), atomic layer deposition (Narkeviciute, Chakthranont, Mackus, et al. 2016) and sputtering (Radhakrishnan, Geok Ing & Gopalakrishnan 1999). Physical Vapour Deposition (PVD) and Chemical Vapour Deposition (CVD) synthetic routes will be covered in more detail in subsections 6.4.3 and 6.4.4, respectively.

In terms of nanostructured devices, the core-shell design approach is often utilised to address charge transport limitations in Ta_3N_5 materials (Narkeviciute, Chakthranont, Hahn, et al. 2016; Niu & Xu 2019). Photocatalytic Ta_3N_5 nanoparticles were first reported by Zhang and

associates in 2004, with the nitridation of Ta_2O_5 powders to create Ta_3N_5 nanoparticles (Zhang, Q & Gao 2004); with improved photocatalytic activity reported relative to $TiO_{2-x}N_x$ powders of the same size. In 2012, it was reported that nanostructuring improved the performance of Ta_3N_5 photoanodes nearly four-fold: an output of ~1.4 mA/cm^2 for nanostructured films versus that of ~0.4 mA/cm^2 for dense films (Dang et al. 2012). However; self-oxidation was reported in all films, highlighting the importance of stabilising the electrode against photo-corrosion.

Further improvements were reported in 2016, with one of the highest photocurrents generated using nanostructured Ta_3N_5 electrodes; Wang and associates reported a photocurrent of 4.2 mA cm^{-2} at 1.6 V_{RHE} (Wang, L, Zhou, X, et al. 2016). This result was attributed to drastically improved electron transfer via the back contact, in addition to the incorporation of subnitride layers, upon which Ta_3N_5 nanotubes were grown.

Recent works continue iterating with nanostructured Ta_3N_5 (Narkeviciute & Jaramillo 2017), highlighting the novelty of this synthetic approach. While these routes have led to the creation of Ta_3N_5 electrodes demonstrating the highest observed photocurrent thus far (Wang, L, Mazare, A, et al. 2016), ongoing efforts remain focused on stabilising the electrodes against self-oxidation and improving charge transport properties, usually with the addition of co-catalysts or additional layers.

6.4.3 Physical Vapour Deposition

Physical vapour deposition (PVD) methods represent a desirable synthetic route due to the degree of control afforded by the process. These methods have been utilised to produce thin films of many stable metal nitride phases (Nie et al. 2001), Ta_3N_5 included. Both Radio Frequency (RF) (Yokoyama et al. 2011) and Direct Current (DC) (Kim, SK & Cha, BC 2005) magnetron sputtering have been utilised in these depositions, however most studies employ RF or pulsed DC sputtering (Kerlau et al. 2004; Koller et al. 2018).

Synthesis of Ta_3N_5 thin films via sputtering is difficult, with the TaN phase proving to be more thermodynamically stable and prohibitively difficult or outright impossible to convert to Ta_3N_5 following its deposition. The presence of oxygen is required in most synthetic routes to form Ta_3N_5, and the sputtering process is no exception (Rudolph, M. et al. 2016). A controlled ratio of N_2 to O_2 gases under deposition produce corresponding films; lower partial pressures of N_2 yield TaON films, and lower partial pressures of both reactive gases yields the more metallic phases of Ta_2N and TaN (Kim, SK & Cha, BC 2005; Matsuoka et al. 2007; Radhakrishnan, Geok Ing & Gopalakrishnan 1999; Yokoyama et al. 2011). The individual sputtering

parameters can be controlled to produce thin films of various structures and compositions. In general, deposition of the Ta_3N_5 phase is observed at higher nitrogen partial pressures (approximately 30% N_2 content in the flowing gases), total deposition pressures in the 2 to 5 mTorr range, and substrate temperatures in the 773 K to 1073 K range (Gudmundsson & Lundin 2020; Radhakrishnan, Geok Ing & Gopalakrishnan 1999; Rudolph, M. et al. 2016; Yokoyama et al. 2011). The mechanism of formation of Ta_3N_5 in the sputtering environment has not yet been thoroughly explored, however it has been noted that the Ta target remains largely metallic under regimes that result with the Ta_3N_5 phase (Rudolph, M. et al. 2016).

Like other synthetic approaches, sputtered Ta_3N_5 films have proven effective photo-electrodes (Rudolph, M. et al. 2016), provided the electrode can be stabilised against photo-corrosion. This has been attempted through the inclusion of additional stabilising layers, such as IrO_2 (Yokoyama et al. 2011), though other methods have also been reported. Due to the importance of film morphology in dictating the charge transport and charge recombination properties of Ta_3N_5 thin films (Narkeviciute, Chakthranont, Mackus, et al.), as well as the capability to easily incorporate dopants into the deposited films homogenously, and also the ability to deposit additional layers used to improve the film properties, sputtering confers an important degree of control over the final photoconversion efficiency of Ta_3N_5 films.

6.4.4 Chemical Vapour Deposition and Sol-gel Routes

Chemical vapour deposition (CVD) methods have been employed to deposit Ta_3N_5 thin films (Hieber 1974), namely layered films through atomic layer deposition (ALD). Single phase tantalum nitride thin films deposited via CVD were first reported on in 1974, as well as their electronic properties (Hieber 1974). The advantage of CVD is the ability to deposit controlled layers of materials with desirable electronic properties; modern industry predominantly use CVD techniques to produce the chips used in all modern computers. This is especially useful in the production of efficacious photo-electrode materials, as control over properties that dictate charge recombination and charge transfer is essential. The drawbacks of these methods are the low deposition rate relative to PVD methods, in addition to the expense and complexity of the instrumentation.

As initially mentioned, ALD is a commonly utilised CVD method when discussing the deposition of advanced Ta_3N_5 thin films. This method was used as early as 1999, when a paper reported the deposition of Ta_3N_5 thin films via ALD; amorphous, highly resistive films were observed with deposition temperatures below 673 K, with the inverse being observed in films deposited in excess of 673 K (Ritala et al. 1999). Since then, ALD has been used sparingly in preparing Ta_3N_5 films for water splitting purposes, notable examples of which will be covered here.

One 2016 paper utilizes ALD to side-step issues produced when subjecting transparent conductive oxide (TCO) substrates to ammonolysis (Hamann 2016). High temperatures in NH_3 atmospheres results in nitridation of the TCO substrates, thus precluding their use in such experiments. TaO_xN_y films deposited on TCO substrates were able to be nitrided under more moderate conditions. However, ALD was used to directly deposit Ta_3N_5 thin films on TCO substrates.

ALD has been used to investigate and improve electronic properties of Ta_3N_5 photo-electrode devices. A core-shell approach was utilised by Narkeviciute and associates to examine and address the poor charge transport properties of the Ta_3N_5 phase (Narkeviciute, Chakthranont, Hahn, et al. 2016; Narkeviciute, Chakthranont, Mackus, et al. 2016). Tantalum oxide films were deposited on n-type Si nanostructures and subsequently nitrided to produce Ta_3N_5 thin films tens of nanometers thick (Narkeviciute, Chakthranont, Hahn, et al. 2016), before the introduction of co-catalysts to stabilise the Ta_3N_5 layer against photo-degradation.

Finally, Ta_3N_5 films have been synthesized via sol-gel routes (Mallinson et al. 2013), and kinetically compared to films of the same composition prepared via sputtering (Bard & Fox 1995). However, sol-gel routes have not yet been adequately explored in developing Ta_3N_5 for solar hydrogen generation, possibly due to the wealth of more compelling synthetic methods, which are covered in this work.

6.5 Other Notable Nitride Photo-electrodes

6.5.1 Tantalum Oxynitride (TaON)

Tantalum oxynitride, or TaON, was initially reported as a stable and efficient water oxidation photocatalyst under visible light in 2002 (Hitoki et al. 2002). This activity was observed in the presence of $AgNO_3$ sacrificial reagents. Possessing a band gap of 2.5 eV (corresponding to an adsorption edge at 500nm), TaON represents another promising nitride material for its ability to absorb light in the visible spectrum. With reported conduction band and valence band edges of -0.3 eV and +2.2 eV vs NHE at a pH of 0, TaON has shown to be capable of overall water splitting under visible light (Abe, Higashi & Domen 2010). While high quantum efficiencies are reported for the evolution of O_2, TaON does not efficiently evolve H_2 (Hara et al. 2004), hampering its use as a material employed for overall water splitting.

Like many photoactive nitrides, TaON undergoes self-oxidation in the process of water splitting, curtailing performance as the reaction proceeds. The stability of TaON photoanodes has been improved through the use of various cocatalyst materials, notably IrO_x (Higashi, Domen & Abe 2012), CoO_x (Higashi, Domen & Abe 2012) and IO_3 (Abe et al. 2005). To effectively split water into H_2 and O_2, many of these studies have reported the use of an applied

bias in the range of 0.6 V to 1 V versus the counter electrode (typically platinum) (Abe, Higashi & Domen 2010; Higashi, Domen & Abe 2011, 2012).

6.5.2 Niobium Nitride (Nb_3N_5)

Niobium nitride, in this case referring to the Nb_3N_5 conformation, is a metal nitride postulated to possess similar structural, physical, and electronic properties to Ta_3N_5. Naturally, with the interest Ta_3N_5 continues to receive, this implies a similar degree of novelty for Nb_3N_5.

However, while Ta_3N_5 has enjoyed considerable research interest, Nb_3N_5 is rarely reported in the literature. To date, most of the literature has focused on the study of NbN structures for use as gate electrodes in transistors (Thiede, T et al. 2008; Thiede, TB et al. 2009). Besides the existence of a 2015 patent reporting its synthesis via traditional nitridation methods (Suzuki et al. 2015), a high purity Nb_3N_5 phase is merely speculated on. A band gap of 1.6 eV was reported via this 2015 patent, supporting the idea that Nb_3N_5 could be a similarly efficacious water splitting nitride as Ta_3N_5 is.

The lack of a reported Nb_3N_5 phase could be explained by properties inherent to elemental niobium. While niobium nitride exists as numerous stable phases and structures in a similar fashion to tantalum nitride, including β-NbN, δ-NbN and Nb_2N (Thiede, TB et al. 2009) etc, niobium does not favour the +5 oxidation state in the same way tantalum does, likely resulting in the rarity of the Nb_3N_5 phase (Thiede, TB et al. 2009).

While Nb_3N_5 synthesis has been mentioned in the literature as a by-product in the synthesis of NbN (Van Hoornick et al. 2006), it has not yet been identified as a predominant phase in investigations. A modelling paper published in 2017 predicts that a Nb_3N_5 film, structurally similar to Ta_3N_5, should be stable at a mild nitrogen chemical potential of 0.20 eV/N (Sun, W et al. 2017), but did not explore this prediction experimentally.

In addition to the nitrides already discussed, there exist many nitride materials of interest to the water splitting field with more being reported regularly. Some of the more notable nitride materials, such as TaON (Higashi et al. 2008), g-C_3N_4 (Wang, X et al. 2009), GaN/ZnO systems (Maeda et al. 2005) and perovskite-types (Luo et al. 2014), are discussed in the following sections. A table listing a handful of these materials can be seen below in **Table 6.2**.

Table 6.2. List of notable nitrides to the field of water splitting.

Semiconductor Material	Band gap (eV)	Author/Year
Ta_3N_5	2.1	(Hitoki et al. 2002)
TaON	2.5	(Higashi, Domen & Abe 2012)
$LaTiO_2N$	2.0	(Minegishi et al. 2013)
GaN	3.4	(Wang, D et al. 2011)
Ge_3N_4	3.8	(Sato et al. 2005)
g-C_3N_4	2.75	(Yan et al. 2010)
GaN:ZnO	2.6-2.8	(McDermott et al. 2012)

6.5.3 Germanium Nitride (Ge_3N_4)

Ge_3N_4 is a metal nitride of the d^{10} electronic configuration group, first described as a novel photo-catalytic material in 2005 (Sato et al. 2005). When loaded with RuO_2 nanoparticles, β-Ge_3N_4 was found to perform overall water splitting, it was notable as the first non-oxide material reported capable of doing so. In 2006 (Lee et al. 2006) and 2007 (Maeda et al. 2007), two papers were published exploring the synthetic method of Ge_3N_4 and developing Ge_3N_4 as an effective photo-catalytic material, respectively. However, the former observed the evolution of N_2 during water splitting, suggesting photodecomposition of Ge_3N_4 through the mechanism shown in **Equation 20**:

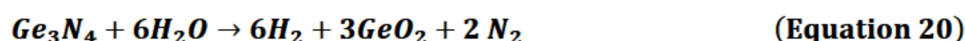

$$Ge_3N_4 + 6H_2O \rightarrow 6H_2 + 3GeO_2 + 2\,N_2 \qquad \textbf{(Equation 20)}$$

Research on the material following these early works has been sparse, largely remaining focused on its use in other electrical applications (Boyko et al. 2013; Rao et al. 2016). In addition to issues with self-oxidation, use of Ge_3N_4 as an effective photo-catalyst is hampered by its prohibitively wide band gap at 3.8 eV, restricting its adsorption to ultraviolet light (Kazuhiko & Kazunari 2016). Recent works in particular have highlighted the use of nanostructuring routes in addressing these issues, particularly increasing the electronic conductivity and tap density (Chanhoon et al. 2017), promoting the use of nanostructured Ge_3N_4 as an effective and scalable battery material.

6.5.4 Gallium Nitride and Zinc Oxide (GaN and GaN:ZnO)

Gallium nitride was one of many early nitride materials, first reported to split water with an applied voltage in 2005 (Katsushi, Takeshi & Kazuhiro 2005). In the years since this initial reporting, it has become apparent that GaN also faces oxidation issues under water splitting conditions in what is presumed to be the reaction given in **Equation 21**:

$$2GaN + 6h^+ \rightarrow 2Ga^{3+} + N_2 \qquad \textbf{(Equation 21)}$$

Where h^+ represents photo-generated holes (Katsushi, Takeshi & Kazuhiro 2005). Additionally, as per Table 6.2, GaN maintains a wide band gap and therefore only utilises light

in the ultraviolent spectrum (Rajaambal, Mapa & Gopinath 2014), similar to traditional oxide materials meticulously studied over the last 40 years. However, in recent years the inclusion of p-type dopants (such as Mg (Kyle et al. 2015) and In (Kibria, M et al. 2014)) have led to improvements in the electronic properties of GaN materials (Kibria, MG et al. 2016; Wang, D et al. 2011).

Improvements in photocurrent resulting from the inclusion of cobalt phosphate co-catalysts have also been highlighted in recent works, with such additions acting to reduce charge recombination effects (Kamimura et al. 2017). More recent works have utilised both doping and nanostructure engineering in order to address the shortcomings of the GaN system (Kibria, MG et al. 2016).

There also exists the GaN:ZnO solid solution which was itself highlighted as a potential overall water splitting photocatalyst material in 2005 (Maeda et al. 2005), however it is important to note the inclusion of a specific cocatalyst, Ru/Cr_2O_3, for best reported results. This system maintains an adjustable band gap of 2.58-2.76 eV (McDermott et al. 2012), is highly stable in photocatalytic conditions, possesses appreciable band edge positions (Huda et al. 2008), and is composed of cheap, safe and abundant elements. So far, the GaN:ZnO system, when combined with specific cocatalysts, has proven among the most active photocatalytic nitride/oxide materials, with a quantum yield of 5.2% under 410nm light (Hisatomi & Kazunari Domen 2009).

6.5.5 Lanthanum Titanium Oxynitride ($LaTiO_2N$)

$LaTiO_2N$ is a compelling oxynitride photocatalyst and photo-electrode material of the perovskite class that possesses a narrow band gap of 2.0 eV (Maeda & Domen 2007) and band edge potentials suitable for total overall water splitting (Minegishi et al. 2013). Additionally, it is composed of naturally abundant materials that are relatively cheap to procure. In 2002, it was reported that $LaTiO_2N$ was capable of oxidizing water into O_2 and reducing H^+ into H_2 under visible light irradiation, through the use of sacrificial reagents in half reactions (Kasahara et al. 2002).

Since these early works, efforts have primarily been focused on improving the photocurrent of the material using novel synthetic techniques. Like many nitrides, $LaTiO_2N$ was at first synthesized via thermal nitridation methods (Kasahara et al. 2002; Kasahara et al. 2003). However, this conferred a low degree of crystallinity and structural defects, both of which promote charge recombination, in turn hampering its efficacy as a water splitting material (Kawashima, Hojamberdiev, Wagata, Yubuta, Oishi, et al. 2015). Flux growth

techniques have been employed to synthesize precursor crystals of La_2TiO_5 (Kawashima, Hojamberdiev, Wagata, Yubuta, Oishi, et al. 2015) and $LaTiO_2N$ directly (Kawashima, Hojamberdiev, Wagata, Yubuta, Vequizo, et al. 2015).

A method deemed the 'particle transfer (PT) method' was reported to produce efficacious $LaTiO_2N$ particles by Minegishi and colleagues in 2013 (Minegishi et al. 2013). In 2016, a material specific record photocurrent of 8.9 mA cm^{-2} at 1.23 V_{RHE} under AM 1.5G simulated sunlight was reported in CoO_x loaded $LaTiO_2N$ particles synthesized via microwave assisted deposition (Akiyama et al. 2016), this value is comparable to that of cutting edge Ta_3N_5 materials and qualifies $LaTiO_2N$ as one of the few nitride materials receiving research attention.

6.5.6 Graphitic Carbon Nitride (g-C_3N_4)

Graphitic carbon nitride is a conjugated polymer material first reported as a potential photocatalyst in 2009 (Wang, X et al. 2009). An environmentally low impact material, g-C_3N_4 has received intense research attention over the last few years on account of its naturally abundant substituents, low toxicity, and promising photocatalytic potential. With a band gap of 2.7, g-C_3N_4 absorbs light in the visible spectrum, and maintains appropriate band edge positions for water splitting (Wang, Yong, Wang & Antonietti 2012). Additionally, on account of its structure, g-C_3N_4 maintains high thermal stability in air and high chemical stability in a variety of solvents (Cao & Yu 2014).

Band engineering has been investigated through the use of metal (Li, Z, Kong & Lu 2015) and non-metal doping routes (Zhu, Ren & Yuan 2015). Currently, g-C_3N_4 performance is limited by electron-hole recombination; efforts to address this have focused on alternative synthetic methods, processing strategies and the incorporation of various dopants (Liu, Gang et al. 2010; Schwinghammer et al. 2014; Zhang, J et al. 2012).

In more recent years, metal-fee nitrogen doped graphene quantum dots have been used to produce efficient g-C_3N_4 hybrid photocatalysts (Zou et al. 2016). In 2017, a z-scheme structural approach consisting of g-C_3N_4 with α-Fe_2O_3 nanosheets was reported to produce the largest H_2 evolution rates and quantum efficiency figures yet reported, at 400 µmol g^{-1} h^{-1} and 44.35% (at 420 nm), respectively (She et al. 2017).

Efforts in recent years have focused on engineering heterogenous structures of TaON and other materials in a z-scheme approach instead of attempting overall water splitting through a single material (Chen, Qi, et al. 2015; Higashi et al. 2008; Hou et al. 2014). These approaches

have met with success, with reports of quantum efficiency values in excess of 6% (Chen, Qi, et al. 2015).

6.6 Postulation of the Problem

It has been shown that the novel material, Ta_3N_5, has favourable properties that enable it to perform as a photo-electrode for solar-driven water splitting with great promise (Hitoki et al. 2002). However, despite a favourable band gap of 2.1 eV (Chun et al. 2003), and band edge positions that adequately straddle the water oxidation and reduction redox potentials (Ishikawa et al. 2004), researchers have as yet been unable to achieve water splitting efficiency levels that approach commercial feasibility. This is due to several key reasons.

Like many nitrides, Ta_3N_5 undergoes varying degrees of self-oxidation under water splitting conditions (Yokoyama et al. 2011). This property necessitates further material engineering measures such as hole storage layers (Liu, Guiji et al. 2014). Low photovoltage (Chun et al. 2003) necessitates the use of a high applied bias in photo-electrochemical cells in order to achieve high water splitting efficiencies.

Traditionally, Ta_3N_5 has been synthesized via methods that typically impose some percentage of oxygen impurities. The use of the Ta_2O_5 precursor is common in most synthetic routes for the evolution of Ta_3N_5 to take place, however the presence of these residual oxide impurities can negatively impact water splitting performance. Additionally, the traditional method of thermal annealing, or ammonolysis, is known to induce defects within Ta_3N_5 electrode materials that promote unfavourable electronic qualities, namely charge recombination (Shafarman, Siebentritt & Stolt 2011).

Chapter 7: Experimental Method

This section details the synthetic methodology used to create thin films for use throughout this project, namely sputter deposition and annealing treatments. In addition to the synthetic methods, analytical methods are also described in detail.

7.1 Film Synthesis

7.1.1 Magnetron Sputter Deposition

All films described in this project were deposited via magnetron sputter deposition using an AJA Orion 5 magnetron sputtering system (AJA International, Scituate, MA). This sputtering system was setup in a top-down sputtering approach, where the substrate is positioned below the sputter sources. The sputtering system was equipped with 5 guns paired to a maximum of 4 power supplies (2 DC, 2 RF) at any one time. It is also equipped with adaptive pressure control via a computer-controlled load lock, substrate bias (RF and DC), substrate heating capability, film thickness monitoring and a charged species analyser, although this final capability was not used during this investigation.

A base pressure of 6×10^{-5} Pa was adhered to prior to all depositions. Films were deposited by a plasma generated on metal targets composed of 99.95% tantalum (AJA International, Scituate MA), with argon used as the carrier gas and nitrogen and oxygen used as reactant gases. All gases were sourced from Coregas and were 99.95% purity grade. Specific experimental details pertaining to the partial pressures, total deposition pressures, target power, substrate temperature, gas flow rates and substrate bias used are tabulated in the relevant sections of the discussion.

Substrate heating was provided by halogen lamps located under the substrate holder in the main chamber, which was also the location of the thermostat. As with the target power supplies, substrate bias was provided by our choice of either an RF power supply source, or a DC supply, both of which were sourced from AJA International. The sputtering instrumentation used is shown below in **Figure 7-1**.

Figure 7-1. AJA Orion 5 Magnetron Sputterer used in this project. Located at Western Sydney University, Hawkesbury Campus.

7.1.2 Thin Film Substrates

Selection of thin film substrates was an important consideration given the known effects of epitaxy on deposited films, in addition to considerations of conductivity and electronic qualities important to photoelectric experiments. For these reasons, we experimented with several substrate types, although predominantly focused on doped single crystal silicon substrates. These substrates included:

P-type and n-type doped silicon substrates with (100) orientation (University Wafer, USA). P-type substrates were the primary substrate used in this project, predominantly because of the heat tolerance of silicon, the low cost of the substrates themselves, and the ease in which they can be processed (e.g. sectioning). Silicon substrates did present issues in certain analyses, namely certain alignments in XRD, higher kV EDS and UV-Vis. These will be noted and addressed where relevant in the discussion. Finally, both p-type and n-type silicon were used in electrical and electrochemical analysis depending on the majority charge carrier in the deposited films. For example, for Hall measurements it is important that the substrate does not possess the same majority charge carrier as the film.

Tantalum (99.9%) sheet metal (Goodfellow, London). Tantalum is a common substrate used in the literature, where it is often oxidized before being nitrided to produce Ta_3N_5. A tantalum sheet of 0.5 mm thickness was sectioned into 1 cm x 1 cm squares prior to being used for deposition. Tantalum substrates were used in some experiments after film properties had been

established using silicon or glass substrates, however silicon substrates comprise the bulk of the results in this work. This was mostly due to the high cost of tantalum sheets as well as the difficulty in sectioning it to create flat substrates, as well as the capability to deposit a thin layer of tantalum directly to aid film adhesion on other substrate materials.

Glass microscope slides (Thermo Fischer Scientific, Australia). These slides were used as a cheap and simple substrate for use in preliminary XRD studies as they only return an amorphous peak at the beginning of the diffractogram when using Bragg-Brentano alignment. However, for samples deposited at higher substrate temperatures or treated in post-deposition annealing processes, these substrates were avoided due to the tendency of the films to delaminate when the film/substrate cooled. This could be remedied with higher quality quartz based substrate materials, however these are disproportionately expensive. Despite this, glass substrates proved useful if just as XRD test bed substrates, and to observe the likelihood of film/substrate bonding and heat tolerance.

7.1.3 Post Annealing

Annealing treatments were carried out using Labec ceramic tube furnaces (Labec, Marrickville, Sydney, Australia). A ramp rate of 5°C/min was used for the heating and cooling stages.

Initial annealing treatments focused on the use of N_2, Ar, O_2 and H_2/Ar mix gases (99.7%, Coregas, Sydney, Australia) at temperatures ranging 773-1273 K with dwell times of 8-12h to treat sputtered TaN films. These treatments did not result in Ta_3N_5, and a gas mixture of 10% NH_3/90% N_2 was acquired (Air Liquide, Sydney, Australia) to create Ta_3N_5 via direct nitridation of tantalum oxides (Ta_2O_5). Films were heated up to 1273 K with dwell times ranging from 8-48 h to react Ta_3N_5 fully, as the reaction is slow. The ammonia was flowed through the tube at a consistent rate of 100 sccm, measured with an ammonia rated flowmeter (Air Liquide, Sydney, Australia). A water filled bubbler system was attached to the end of the process tube to scrub ammonia after it had passed through the tube.

7.2 Sample Characterisation

Sample characterisation techniques comprised a significant component of this project as they were integral in investigating the outcomes of incremental changes to the synthetic methods in the process of synthesizing Ta_3N_5 and other phases thereof. Additionally, the determination of the capability of the films as water splitting devices comprised a major aim of the work. More specifically, SEM was used utilised to image the film surface morphologies, their cross-sectional thickness, and an accompanying EDS detector was used to identify and quantify the elements present. XRD was utilised continuously in determining the phases present in the films as well as the degree of crystallinity or preferred orientation of present phases.

Secondary Ion Mass Spectroscopy (SIMS) was used to determine the composition of the films as a function of depth and to compare the qualitative elemental data to the quantified EDS elemental data, which proved instrumental in lieu of other analytic techniques such as X-ray Photoelectron Spectroscopy (XPS). In the effort to produce Ta_3N_5 films, much work was focused on characterising the effects of the several sputtering parameters on the resulting film structure and quality.

7.2.1 X-Ray Diffraction

X-ray Diffraction is an analytical technique used to characterise and determine the phases present in a crystalline material. It is widely used across numerous scientific disciplines and is well established as a standard qualitative analytical technique, existing as one of the fundamental analytical techniques throughout 20th century science.

Fundamentally, the technique measures the elastic scattering of x-ray photons, which are exhibited when a crystalline material is exposed to an x-ray source. This relationship is explained using Bragg's Law, as displayed below in **Equation 22** and **Figure 7-2**.

$$n\lambda = 2d\sin\theta \qquad \text{(Equation 22)}$$

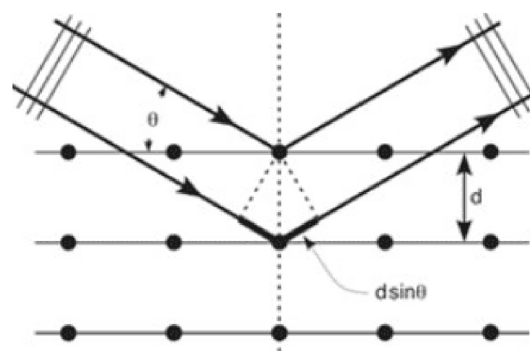

Figure 7-2. Bragg diffraction, where n is a positive integer called the order of reflection, λ is the wavelength of the incident wave, d is the distance between the crystal planes and θ is the glancing angle.

XRD in this project was performed with a Bruker D8 Advance (Bruker, Massachusetts, USA) diffractometer. The diffractometer was setup in Bragg-Brentano (BB) scanning mode or parallel beam glancing angle scanning mode (GAXRD). BB mode was used for powders, sintered pellets and some films depending on thickness, whereas GAXRD was used for the majority of thin film samples due to the intense substrate signal seen with BB geometry. A diagram detailing the setup of Bragg-Brentano XRD and GAXRD is illustrated below in **Figure 7-3**.

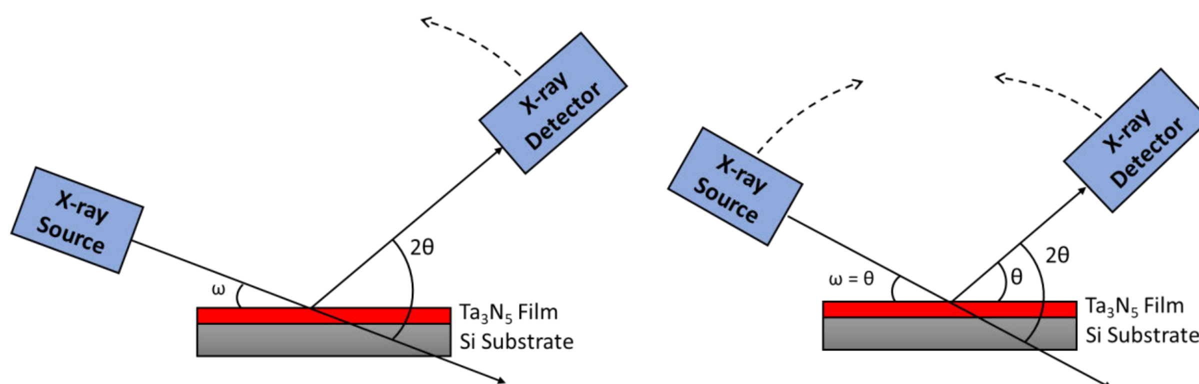

Figure 7-3. Diagram depicting the XRD geometries of Glancing Angle XRD (left) and Bragg-Brentano scanning mode (right), where ω is the angle of incidence.

Bragg-Brentano scans were performed at a range of 10-80° 2θ (unless otherwise noted) with 0.01 degree per second steps, resulting in scans approximately reaching 2 hours (116.6 minutes). For GAXRD scans, 3 scans were performed per sample at an angle of incidence of 0.5°, 1.5° and 3°, with a 2θ range of 10-60° for each. Each scan was performed at 0.01° steps with 1 step per second, totalling 116 minute scans. Additionally, a 0.5 mm slit was inserted in front of the emission source and an equatorial Soller slit attached to the detector. Both scanning modes were carried out using a Cu Kα radiation source with a wavelength of 1.5406 Å.

7.2.2 Scanning Electron Microscopy

Film surface and cross-sectional characterisation was performed using a Zeiss Merlin FEG SEM (Zeiss, Oberkochen, Germany). Surface analysis was important for characterising the changing morphology of the films and to assist in providing a superficial judgement on the quality of the films both before and especially after nitridation. The strongly reducing nature of the NH_3/N_2 atmosphere combined with temperatures more than 873 K can prove detrimental to the film structure, and it was important to verify this visually.

SEM analysis was performed at a range of accelerating voltages depending on the electronic properties and stability of the films; some films charged under the beam, which necessitated low accelerating voltages of 0.25-5 kV or extra sample preparation steps (coating in carbon, chromium or gold depending on the sample), whereas other films could tolerate 10-15 kV without significant charging or damage to the film. Working distance was varied between 3-8 mm, depending on the charging and accelerating voltage in use.

Film cross sections provided direct measurement of the film thickness, which was determined using the ruler function in the SEM software suite. Five points on the film cross section were selected for analysis and the thickness averaged. Cross sections were obtained by scoring the rear of the films before snapping and mounting them vertically, with the snapped edge

facing the electron beam. Values for Rq were determined using SEM software and corroborated using a profilometer and atomic force microscopy (AFM).

7.2.3 Energy Dispersive Spectroscopy

Elemental analysis formed a notable role in this project as a blunt method to determine the elemental presence in the films, especially with regards to doping and tracking the presence of oxygen and nitrogen in the films after annealing. To perform EDS analysis, a Bruker QANTAX XFlash 6 Electron-Dispersive X-ray Spectroscopy detector was used (Bruker, US). This detector was attached to the Zeiss SEM and spectra were taken after surface imagining was performed.

Calibration of the detector was performed using a chromium nitride standard of known 50:50 Cr:N composition, in a pseudo-standardless quantification method. An accelerating voltage of 15kV was used to show the tantalum Lα line at 8.143 eV, and in cases where this resulted in detection of the silicon substrate, we calculated quantification data to account for the presence of the substrate. Prior to analysis the system was calibrated around the nitrogen and chromium peaks of a CrN standard of known 50:50 composition, with quantification performed at 15 kV to verify the 50:50 Cr:N atomic %.

7.2.4 Secondary Ion Mass Spectrometry

Secondary elemental analysis, depth profiling and elemental composition was explored using SIMS. SIMS was especially useful in comparing elemental composition as a function of depth during kinetic experiments. SIMS analysis is an analytical method under the mass spectrometry umbrella of techniques. It operates by milling into a given sample using a primary ion beam, the displaced atoms from the sample (secondary ions) are then passed to a detector as part of a mass spectrometer, which identifies the present elements according to the recorded weights. The basic operation of SIMS is illustrated below in **Figure 7-4**.

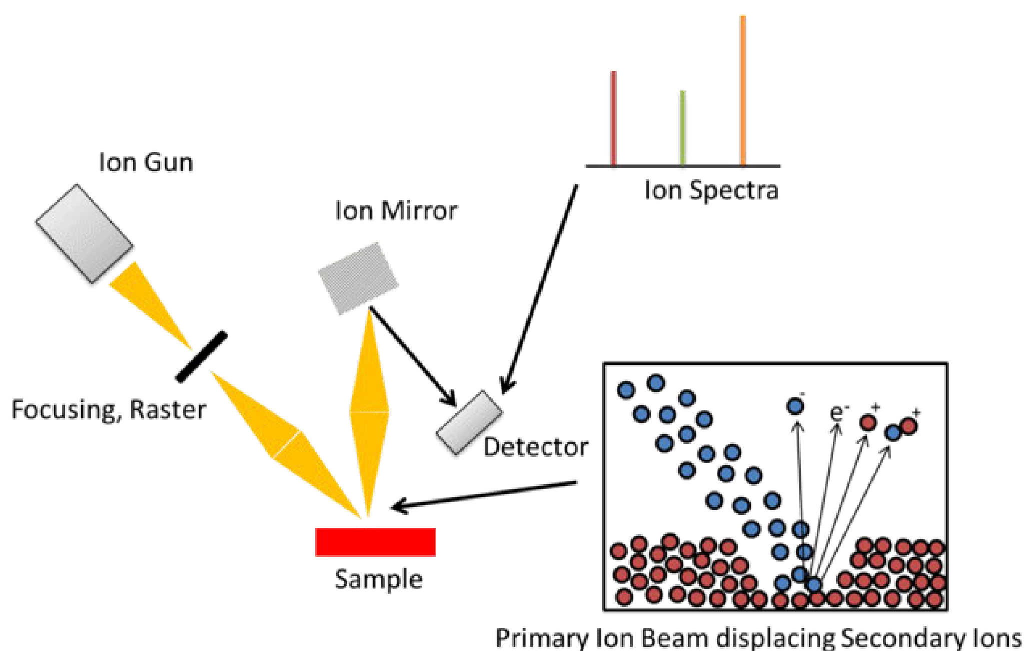

Figure 7-4. Diagram depicting the basic working of SIMS analysis, including the displacement of secondary ions from the sample by the primary ion beam.

While SIMS cannot strictly be used to quantify the elemental presence in the samples, the relative intensity of detected ions can be compared between films sputtered under the same conditions to give an idea of relative elemental content.

SIMS was performed using a Cameca IMS 5fE7 (Cameca, Paris, France). Sample milling was performed with a Cs^+ primary beam operating with a 10.0 kV accelerating voltage and 15 nA current. The raster area was 150 µm x 150 µm, with an analysis area of 8 µm in the center of the crater to avoid crater effects. Secondary ions tracked included $^{52}Cr^+$, $^{14}N^{133}Cs^+$, $^{16}O^{133}Cs^+$, $^{52}Cr^{133}Cs^+$, $^{28}Si^{133}Cs^+$, ^{181}Ta, and $^{181}Ta^{133}Cs^+$. Counts for $^{14}N^{133}Cs^+$ (where relevant), $^{16}O^{133}Cs^+$, $^{52}Cr^{133}Cs^+$ and $^{28}Si^{133}Cs^+$ were normalised against $^{181}Ta^{133}Cs^+$ counts. Crater depth was measured using a KLA Tencor Alpha-Step IQ profilometer (KLA-Tencor, Milpitas, CA).

7.2.5 UV-Vis Spectrophotometry

UV-Vis spectrophotometry was performed using a Varian/Agilent Cary 100 UV-Vis spectrophotometer (Varian (now Cary), USA) configured in diffuse reflectance spectroscopy (DRS) mode with a diffuse reflectance accessory (DRA) for the mounting of solid and powder samples. UV-Vis was a useful technique for verifying the wavelengths being absorbed by the films in question, as Ta_3N_5 is demonstrated to be absorbent in the visible light range (380-600nm), reflecting only red light above this 600nm absorption edge.

After fitting the DRA, the instrument was configured to scan in double-reverse mode. Baseline runs were first performed using a Ba_2SO_4 standard white powder compacted and mounted in

a holder affixed to the integrating sphere. For experimental analysis, films were mounted in the same position, albeit fixed to the sample holder instead of compacted as powder. Scans were performed using the accompanying Cary UV-Vis software and the spectra was generated using the F(R) function to give interpreted absorbance peaks. Scans were run from 800nm to 100nm using both the UV and Visible light sources.

A simple schematic displaying the basic operation of a UV-Vis spectrophotometer utilising a DRA integrating sphere accessory is shown below in **Figure 7-5**.

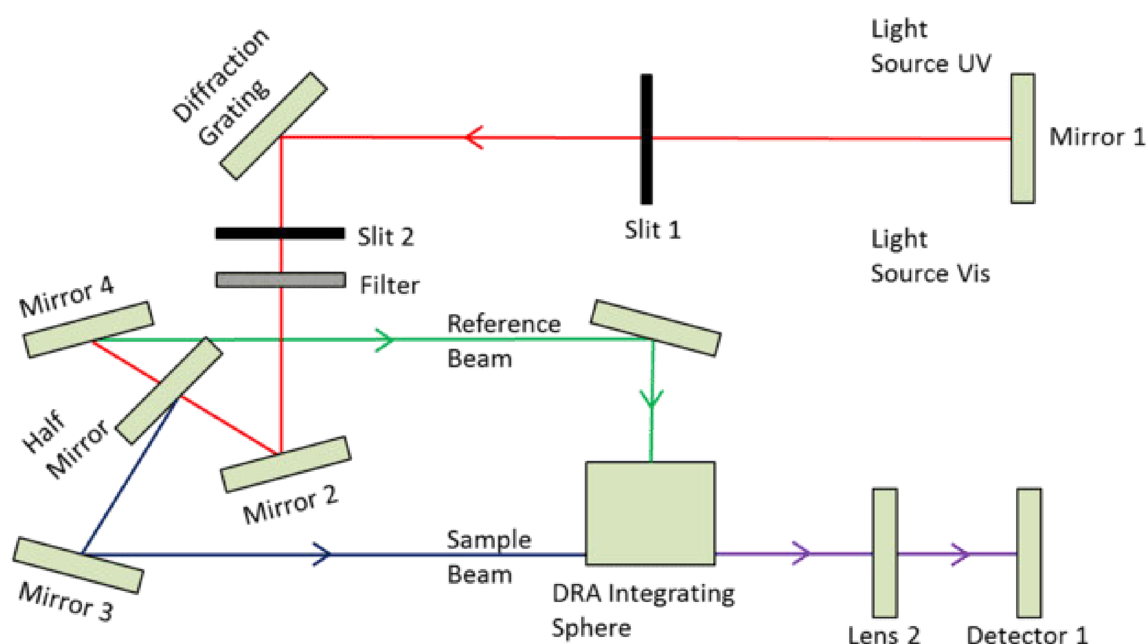

Figure 7-5. Representation of the path of light in a UV-Vis spectrophotometer. The DRA integrating sphere accessory is included with the spectrophotometer operating in double-reverse mode as opposed to the traditional cuvette double detector mode.

7.2.6 Photo-electrochemical Performance Assessment

The water splitting performance of thin film electrodes was assessed using the PEC approach, which utilises two opposing electrodes submerged in an electrolyte solution. Electrodes were constructed by feeding copper wiring to an appropriate length through glass sheathes to protect them from the solution and allow ease of mounting in the cell. The exposed end of the copper wiring was attached to the film substrates or the films themselves using a silver/toluene paste, which was dabbed in such an amount to ensure enough contact without creating an excess which could result in current leakage during voltammetry experiments.

This combination was fixed and allowed to dry before epoxy was applied to the wiring. Epoxy was applied with care such that all exposed reactive surfaces that may react in the cell were covered, then also allowed to dry.

Electrodes were mounted in the cap of the glass cells, opposite a platinum counter electrode and Ag/Cl reference electrode, the design of which is shown visually in **Figure 7-6**. The glass cells were filled with an electrolyte solution consisting of either 0.5M H_2SO_4 or 0.1M KOH (noted where relevant). The electrolyte solution was purged with gaseous N_2 for a period of 30 minutes prior to electrochemical assessment to help remove air from the electrolyte that may create anomalous data.

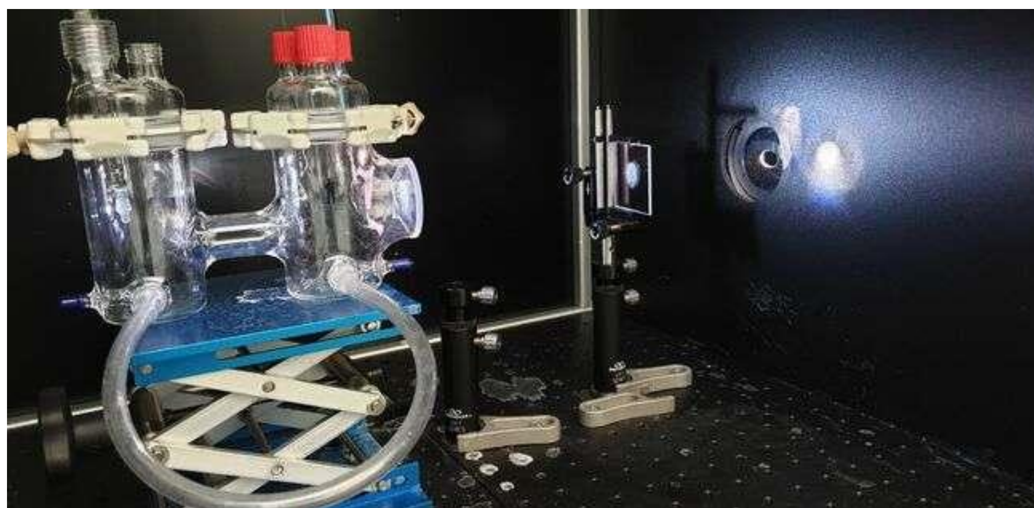

Figure 7-6. Photo-electrochemical cell used in this investigation, the UV lamp light intensity is controlled by an aperture and filter (right) before it strikes the electrode in the cell (left). Apparatus located at Hawkesbury Campus, Western Sydney University.

Simulated sunlight was accomplished using a lamp (Muller Optik GmbH, Germany) with an installed xenon globe. The simulated sunlight was measured at the location of the electrode position outside of the cell using a light meter prior to each experiment to ensure consistency between measurements, especially after a change in the electrolyte, electrodes or cell position. Simulated sunlight was controlled to approximately 100mW/cm^2 (AM 1.5) using 1 lens to filter the intensity of the lamp output.

Once mounted in cells, alligator clips were attached to the electrodes and connected to a Metrohm Autolab PG128N Potentiostat (Metrohm, Netherlands). This potentiostat was paired with a PC running Metrohm Nova software, which was used to run the cyclic voltammetry (CV) tests and impedance testing/frequency response analysis (FRA) scans. CV scans were performed over a range of voltages, with a general scan rate of 10mV/s, with other scan rates noted where used.

The Nova software suite was also used to calculate the reciprocal of capacitance squared, which was derived from FRA impedance scans, and to generate Mott-Schottky plots for the

determination of flat band potential and carrier concentration. FRA scans were performed across a voltage range within the redox potentials of the given electrolyte solution, which would vary with the pH of the given solution. In general, a frequency range of 10Hz to 1000Hz was employed, although the values used will be indicated in the discussion where relevant.

7.2.7 Hall and Van Der Pauw Measurements

Hall and Van Der Pauw measurements were performed with an Ecopia HMS-3000 System paired with a PC running system specific software (**Figure 7-7**). Thin film samples were prepared for analysis by sectioning to approximately 1x1 cm, then placing small indium contacts on the surface in four corners of the sample and pressing the indium balls flat with a tweezer. Before proceeding, contacts were tested for resistivity using a multimeter, to ensure similar resistivities across the four contacts on the sample.

Figure 7-7. Ecopia HMS-3000 Hall Measurement System used in this project with accompanying PC and software shown. The sample mount, with mounted sample and magnet, can be seen in the bottom left.

If this method didn't produce suitable contacts, or the indium contacts failed to adhere fully to the film, a soldering iron was used to solder an indium/tin contact in each corner. This method was also used to solder contacts on top of the previously pressed indium contacts, in the case

contacts were of poor quality. The films with contacts attached were placed on a heating stage set to 340 K for 30 seconds to ensure the indium contacts had appropriately adhered to the film surface.

Samples were then mounted in a cradle with four probes (shown in **Figure 7-8**), placed on each of the four contacts. Before and after mounting, the connections were again checked for resistivity using a multimeter to gauge whether resistance was consistent between each contact. This was done throughout the process as large differences in the resistivity between contacts will cause inaccuracies in the subsequent calculations or may indicate an inconsistent phase or condition within the film.

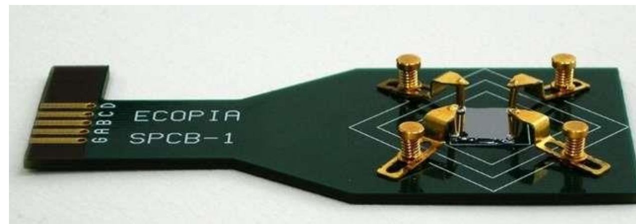

Figure 7-8. Ecopia HMS-3000 Hall Measurement System sample cradle with film and silicon substrate mounted.

The cradle was then slotted into a device mount that allows for convenient use of a magnet. This mount was connected to the current supply system, which itself is connected to and controlled by the computer. Before performing any measurements, a connection check was performed using the computer to ensure contacts were sufficient and working. Then, I/V curves were generated, which displayed resistance vs current and resistance vs voltage plots. The nature of these plots indicated whether the connections were ohmic in nature; voltage and resistance plots must form straight lines that all intersect at a single point, whereas current vs resistance plots should show straight lines that do not intersect.

After this was satisfied, Hall and Van Der Pauw measurements were performed by the computer over a selected current range based on what was used to generate the I/V curves. These currents ranged from nA to µA and will be reported with results as necessary. As part of Hall measurements, a 0.51 Tesla magnet was inserted in the N-S and S-N directions when prompted by the software. Calculations providing the sheet resistance, carrier mobility, Hall voltage and carrier concentration were performed by the PC software.

Chapter 8: Results and Discussion

With the aim to deposit reproducible Ta_3N_5 thin films with appreciable and controlled semiconducting properties, the first step in this project was to investigate the sputtering conditions necessary to do this. While the conditions reported to produce Ta_3N_5 in the literature are discussed in the literature review, it would be significant if the phase were able to be deposited in a controlled fashion without any extra synthetic steps (such as annealing).

In the interest of developing the knowledge of how to deposit this phase and working within the confines of available sputtering equipment, sputtering conditions were selected on a rational basis. That is, Ta_3N_5 is the highest order nitride phase in the tantalum nitride phase series, as such the goal is to incorporate as much nitrogen into the structure as possible. The first three subsections of this section will cover this investigation.

After this, the photo-electrochemical performance of sputtered films will be discussed before a final discussion of the Ta_3N_5 synthetic mechanism as it relates to the work done in this project.

8.1 Reactive Sputtering of Tantalum Nitride Films

The intent in this chapter is to describe the works undertaken in attempting to deposit Ta_3N_5 films directly using only a tantalum target sputtered in a mixture of N_2 and Ar, with no oxygen. Specifically, the impact of N_2 partial pressure (or pN_2), total deposition pressure (or P_{dep}) and substrate temperature (T_{sub}) were investigated, all under the individual DC and RF power types. The influence of other parameters will also be briefly discussed, and a brief conclusion drawn before moving on.

8.1.1 DC Sputtered Films

In this subsection, the effect of deposition parameters $p(N_2)$, P_{dep} and T_{sub} on the deposition of tantalum nitride thin films is discussed. The goal of these investigations is ultimately to characterise these aspects of the high nitrogen activity sputtering environment, given Ta_3N_5 is the highest order nitride phase in the series. To this end, directly and indirectly increasing the $p(N_2)$ and P_{dep} is first investigated. P_{dep} was also evaluated separately in the case that the Ta_3N_5 phase only occurred at certain deposition pressures regardless of nitrogen activity in the reactive gas phase. Substrate temperature is evaluated for similar reasons, as the Ta_3N_5 phase reportedly crystallises at temperatures in excess of 920 K (Pinaud, Vailionis & Jaramillo 2014), given literature cases almost invariably employ some degree of substrate heating. The use of DC power supplies is explored first over RF given the higher yields of DC sputtering when using conductive metallic targets.

8.1.1.1 Effect of Nitrogen Partial Pressure, $p(N_2)$

Atmospheric nitrogen activity is the most important component of the sputtering environment when considering the deposition of a nitride film. Nitrogen present in the gaseous phase will be gettered by ejected Ta ions from the tantalum target and deposit on the substrate, chamber and target. The deposition of a film on the target is referred to as poisoning of the target (Bousquet et al. 2013). This poisoning phenomenon amounts to the formation of a metal nitride layer on the surface of the target and leads to a reduction in the sputtering yield as well as potential changes in the phase evolution and resulting properties of the tantalum nitride film. Due to the absence of an in-situ nitrogen sensor, the activity of nitrogen is approximated to be equal to the nitrogen partial pressure ($p(N_2)$) and is controlled through the variation of N_2 and Ar flow rates in the present investigation.

To assess the tendency for the Ta target to be poisoned under the typical deposition circumstances employed in the present work, a hysteresis experiment was undertaken. Specifically, the $p(N_2)$ during deposition was incrementally increased from 0 Pa to 0.5 Pa at a fixed rate with the corresponding target discharge voltage recorded. After reaching 0.5 Pa, the $p(N_2)$ was returned abruptly to 0 Pa to identify any permanent change on the target associated with nitrogen poisoning. The obtained hysteresis plot detailing the nitrogen activity contrasted with the discharge voltage of the power source can be seen below in **Figure 8-1**. Discharge voltage is observed to increase sharply at 0.06 Pa, indicating nitrogen poisoning of the Ta target. However, this effect does not appear to penetrate deeply into the target, as discharge power steps down predictably with the $p(N_2)$.

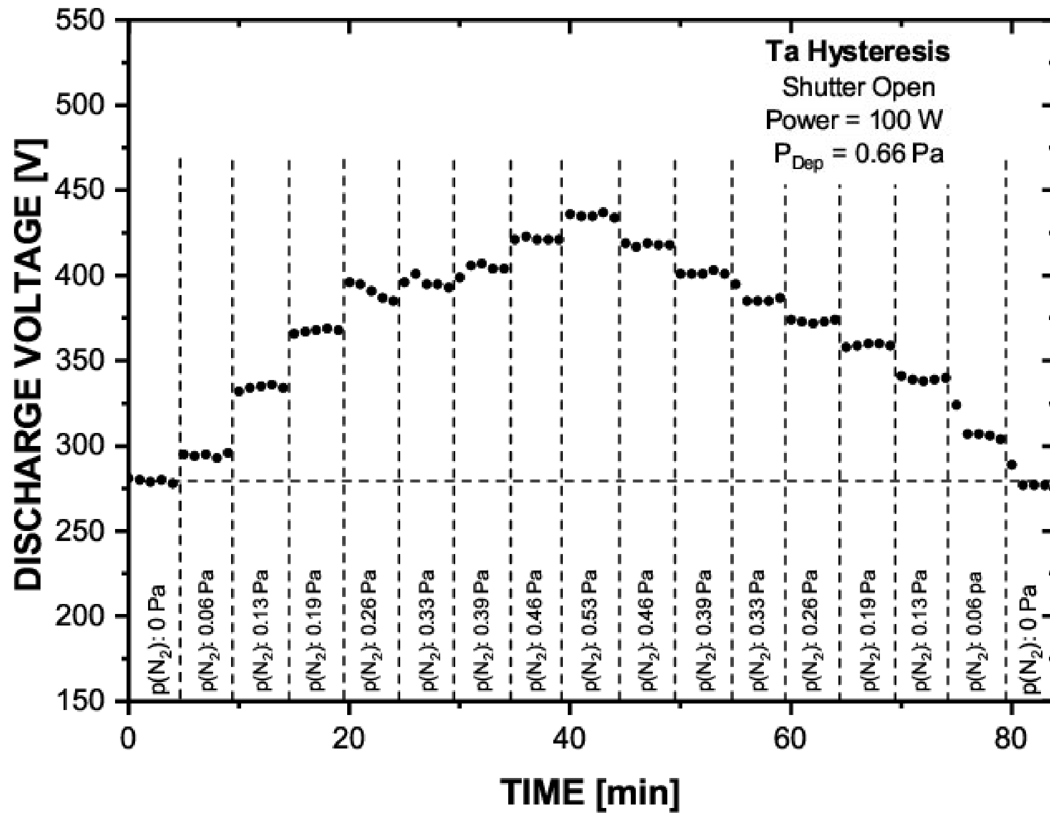

Figure 8-1. Effect of p(N_2) on the discharge voltage of the Ta target.

Due to the clear influence of p(N_2) over the composition of TaN-based films, it is important to explore how the nitrogen content varies with changes in nitrogen activity during deposition. Hence, in the present investigation, the influence of p(N_2) on TaN film properties was examined through the deposition of a series of films, the conditions of which are summarised below in **Table 8.1**. Other variables (deposition pressure, target power, substrate temperature, substrate bias, and deposition time) were fixed.

Table 8.1. Processing parameters for TaN-based films deposited with varying p(N_2), and the resulting film thickness and composition. All films deposited under total deposition pressure of 0.66 Pa.

p(N_2) (Pa)	p(Ar) (Pa)	Film Thickness (nm)	Dep. Rate (nm/min)	R_q (nm)	[N] (at. %)	[Ta] (at. %)
0.06	0.60	680	5.7	7.5	52	48
0.13	0.53	464	3.9	2.3	59	41
0.26	0.40	431	3.6	3.5	59	41
0.47	0.18	244	2.0	4.1	61	39

The effect of p(N_2) on the composition and deposition rate of the TaN films is summarised in **Figure 8-2**. As seen (in Figure 8-1), the extent of nitrogen incorporated into the films generally increases with p(N_2) as would be expected. Conversely, the [Ta] value in the films generally

decreases relative to increases in the value of [N]. However, there are two details of importance to note. Firstly, the most significant change in composition takes place when $p(N_2)$ is altered from 0.06 Pa to 0.13 Pa. From Figure 8-1, this coincides with a substantial increase in target discharge voltage which is indicative of the onset of target poisoning by nitrogen. At this point, the sputtering yield of Ta is likely reduced and accordingly, the opportunity for nitrogen incorporation into the films increased. Secondly, over the studied range, the [N] is always more than the [Ta], which indicates that for the growth of stoichiometric TaN, the $p(N_2)$ should be reduced to less than 0.06 Pa or <10% P_{Dep}.

Surface roughness was observed to decline sharply with the change from 0.06 to 0.13 Pa, before climbing steadily as the nitrogen partial pressure increased to 0.26 and 0.47 Pa. This effect corresponds to film thickness; thicker films predictably produce greater surface roughness resulting from improved grain growth conditions (Ottone et al. 2014).

The effect of $p(N_2)$ on the deposition rate is also displayed in Figure 8-2. Error bars, where displayed in the following figures, were produced by calculating the standard deviation of the respective data sets. This was done for atomic %, d spacing and roughness values. Like the effect of $p(N_2)$ on the [Ta] content, the deposition rate is also observed to fall with increased $p(N_2)$. This reflects the effect of poisoning of the Ta target during deposition and the resulting decrease in Ta sputtering yield.

The decrease in roughness with increasing nitrogen partial pressures could be attributed to the progression of cubic TaN films to amorphous TaN films, further compounded by nitrogen poisoning reducing the deposition rate.

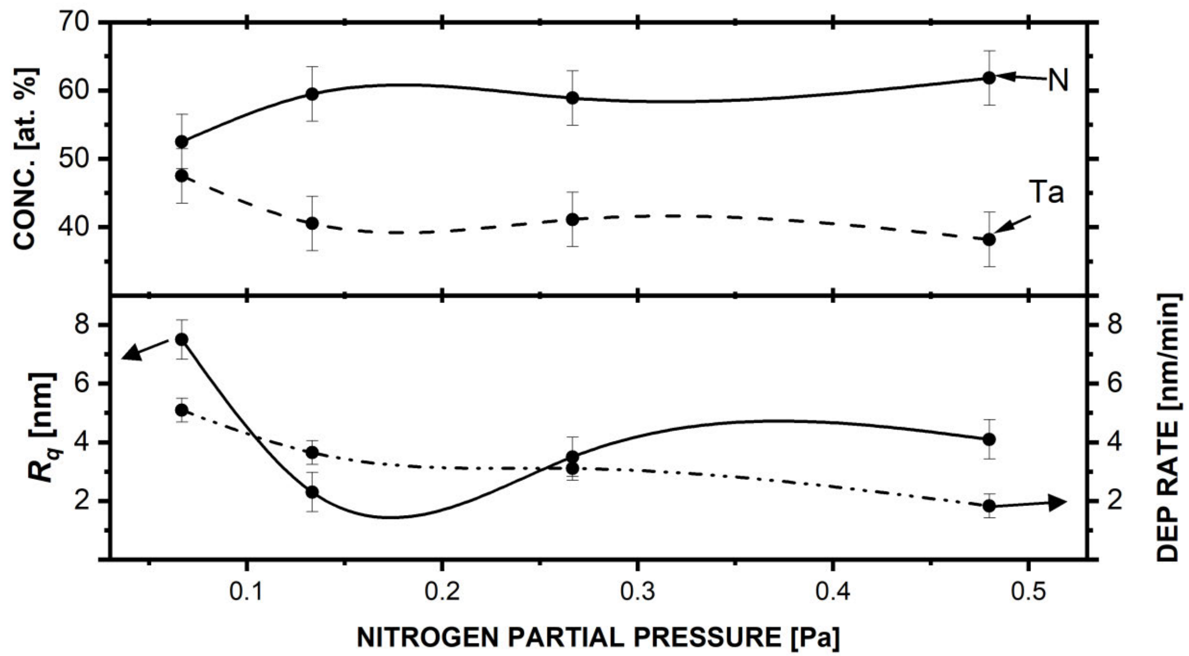

Figure 8-2. Influence of p(N_2) on nitrogen and tantalum atomic %, roughness (R_q) and deposition rate.

Qualitative analysis of the influence of p(N_2) on the structure of as-deposited TaN films was carried out using XRD. A comparison of the resulting patterns can be seen in **Figure 8-3**.

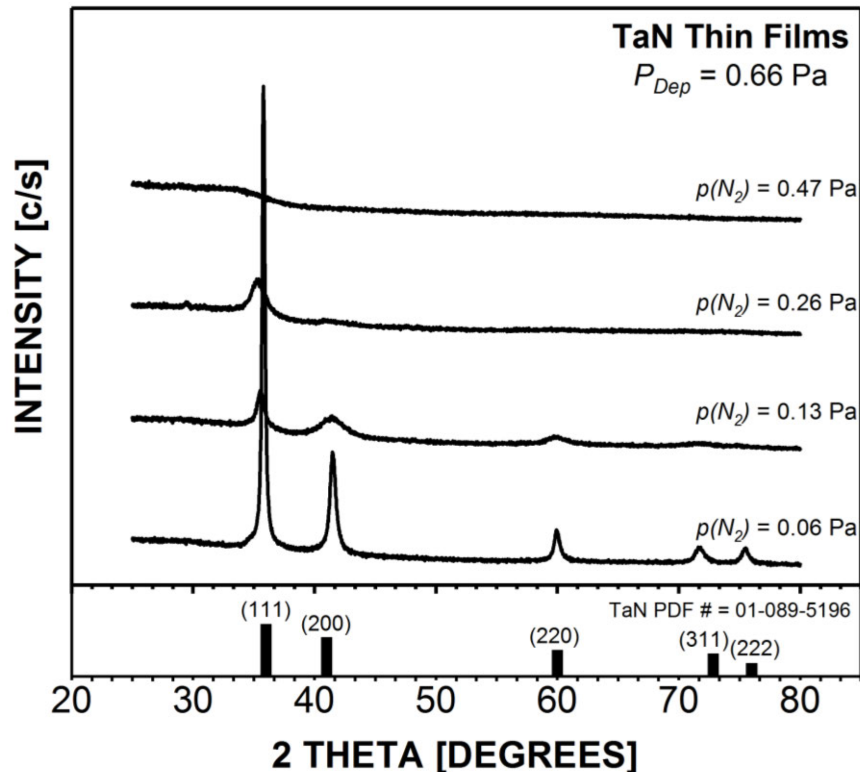

Figure 8-3. As-deposited TaN based films. P_{Dep} = 0.66 Pa.

From this figure it is immediately evident that altering $p(N_2)$ has a strong influence over the structural evolution of reactively sputtered TaN films, in particular the extent of crystallinity and preferred orientation. From Figure 8-3, at the two extremes of $p(N_2)$ studied in this investigation, it is seen that at the lower extreme ($p(N_2)$ equal to 0.06 Pa), the deposited film is clearly crystalline and is a close match for TaN (ICDD card # 01-089-5196). At the alternate extreme ($p(N_2)$ = 0.47 Pa), the deposited film is nearly entirely amorphous and between the two circumstances, the as-deposited films demonstrate degrees of crystallinity that are consistent with this trend. The film deposited under $p(N_2)$ = 0.06 Pa is sufficiently crystalline to match with TaN (ICDD card # 01-089-5196) but this is not the case when the $p(N_2)$ was shifted to the highest value at 0.47 Pa. The pattern is indicative of an amorphous TaN film.

As illustrated in Figure 8-2 and already discussed, the slight increase in $p(N_2)$ from 0.06 Pa to 0.13 Pa is clearly accompanied by a substantial shift in the conditions of deposition as reflected in the extent to which crystallinity is lost (Figure 8-3). Additionally, peak shifting is observed in the $p(N_2)$/Ar = 0.19 Pa film on the (111) TaN peak, possibly indicating the presence of preferentially arranged ε-TaN, which maintains a (100) reflection at 34.6°. Consistent with the behaviour observed in Figure 8-2 and Figure 8-1, this is further evidence for the poisoning of the Ta target by the nitrogen process gas during deposition and indicates that in order to

achieve crystalline TaN films, $p(N_2)$ must be limited to no greater than 0.06 Pa under the conditions presented in this section.

The graph displayed in **Figure 8-4** shows the changing d spacing values of the (111) peak. The shift is difficult to observe in Figure 8-3 but clear when the values themselves are graphed. The shift was consistent across all peaks, given the nature of the phase as a cubic structure.

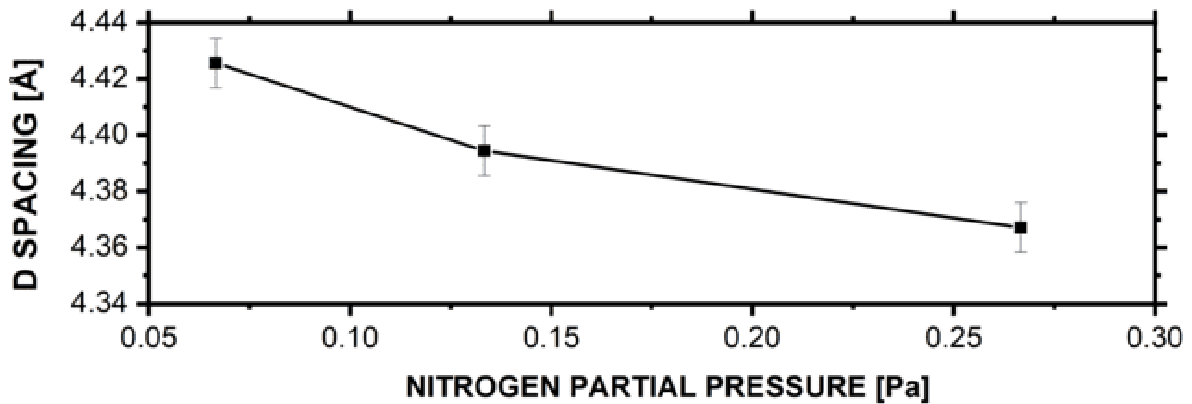

Figure 8-4. D spacing values of the (111) peak versus $p(N_2)$.

SEM micrographs of the as-deposited films, along with cross section images, can be seen in **Figure 8-5**. These indicate a greater degree of conductivity in the $p(N_2)$ = 0.13 Pa film relative to the other films in this series. This can be deduced from the excessive charging evident in micrographs of the $p(N_2)$ = 0.26 film, a result of more nitrogen in the film reducing conductivity. Individual grains could only be observed at magnifications more than 50,000x, and grain sizes across all films appeared consistently in the order of tens of nanometers.

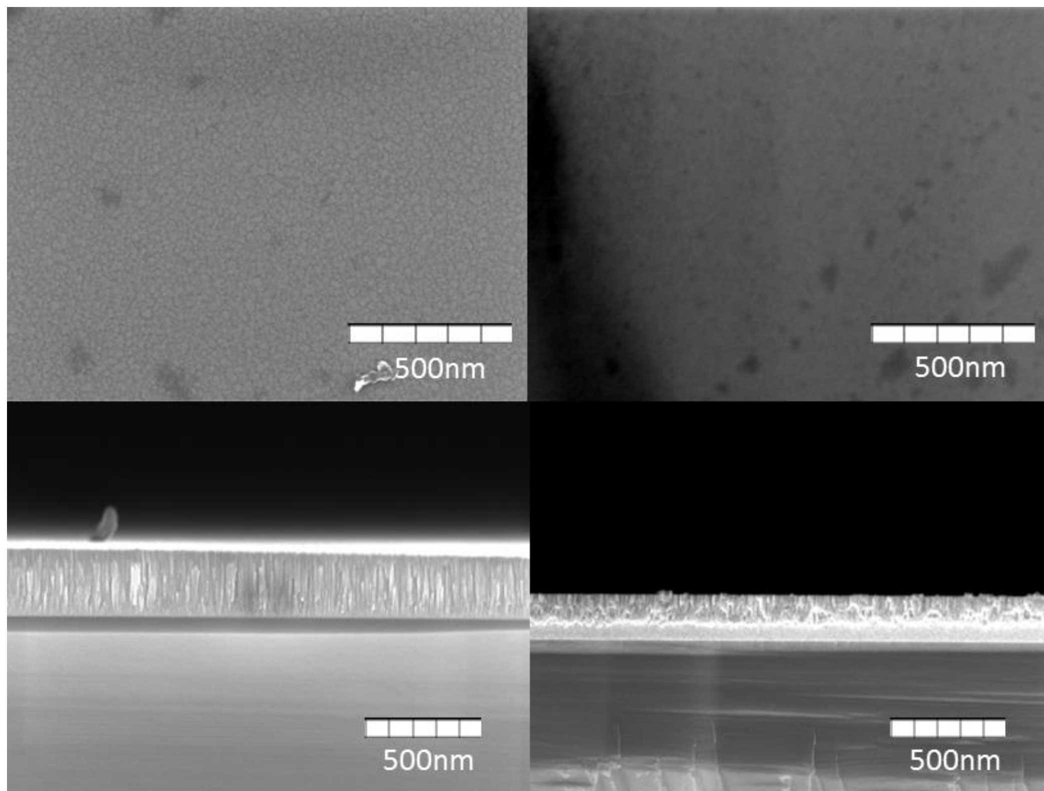

Figure 8-5. Surface and cross section SEM micrographs of films deposited at $p(N_2)$ = 0.13 (left) and 0.26 (right) Pa.

In summary, changes to the nitrogen partial pressure, $p(N_2)$, elicited changes in the crystal orientation, specifically a decline in the crystallinity of films was observed with increasing nitrogen activity. This, in addition to the falling deposition rate, was attributed to the increased posioning of the tantalum target, which was discussed with Figure 8-1. There also appears to be an increase in conductivity in $p(N_2)$ = 0.13 Pa, however this was not substantiated quantitatively. Finally, nitrogen atomic content correlated with the nitrogen activity in the gas phase, but did not produce the Ta_3N_5 phase, instead nitrogen heavy amorphous TaN films were observed with increasing $p(N_2)$.

8.1.1.2 Effect of Total Deposition Pressure, P_{dep}

In expanding the understanding of the relationship between $p(N_2)$ and thin film properties detailed in the previous section, the effect of total deposition pressure (or P_{Dep}) was not explored; P_{Dep} was intentionally held at a consistent value of 0.66 Pa across all films. Total deposition pressure is known to contribute to the formation of preferred orientation crystalline films, as well as amorphous phases of TaN and hexagonal Ta_2N (Nie et al. 2001). As such, the function of deposition pressure was thoroughly explored with a further series of films. To investigate the effect of deposition pressure on film morphology, 9 films were deposited under 3 nitrogen partial pressures of 0.26, 0.53 and 0.79 Pa and at 3 deposition pressures: 1.33,

2.00 and 2.66 Pa. Deposition conditions and associated results for this series are summarised below in **Table 8.2**.

Table 8.2. Processing parameters for TaN-based films deposited with varying P_{Dep}, and the resulting film thickness and composition.

Deposition Pressure (Pa)	$p(N_2)$ (Pa)	Thickness (nm)	Dep. Rate (nm/min)	R_q (nm)	[N] (at. %)	[Ta] (at. %)
0.66	0.26	431	3.5	3.53	59	41
1.33	0.26	494	4.1	6.27	59	41
1.33	0.53	490	4.0	6.15	61	39
1.33	0.80	215	1.7	5.66	64	36
2.00	0.26	816	6.8	9.82	55	45
2.00	0.53	489	4.0	5.02	55	45
2.00	0.80	333	2.7	13.9	63	37
2.66	0.26	948	7.9	16.1	49	51
2.66	0.53	656	5.4	10.7	55	45
2.66	0.80	431	3.5	13.6	56	44

For each of the deposition pressures, an increase in the $p(N_2)$ was associated with a reduced deposition rate, an affect attributed to increased target poisoning and gas phase scattering. In general, films deposited at a total deposition pressure of 2.66 Pa were thicker than those deposited at 1.33 and 2.00 Pa, with the 1.33 Pa film series exhibiting the thinnest films. While higher deposition pressures reduce the mean free path of nuclei ejected from the plasma (Chaoumead, Sung & Kwak 2012), nitrogen activity is lower relative to the nitrogen activity of the lower deposition pressures. More argon etching of the target is taking place as a result, thereby resulting in the deposition of thicker and more metallic films. This is further evidenced by the increasing [Ta] content.

The elemental at. %, surface roughness values and the trend in deposition rate can be seen in **Figure 8-6.** High deposition pressures appear to produce a more stoichiometric TaN film, as [Ta] and [N] both trend towards 50% at. % with a deposition pressure of 2.66 Pa and $p(N_2)$ of 0.26 Pa. Surface roughness and deposition rate both increase with rising deposition pressures; as thicker films are deposited, surface features become more pronounced.

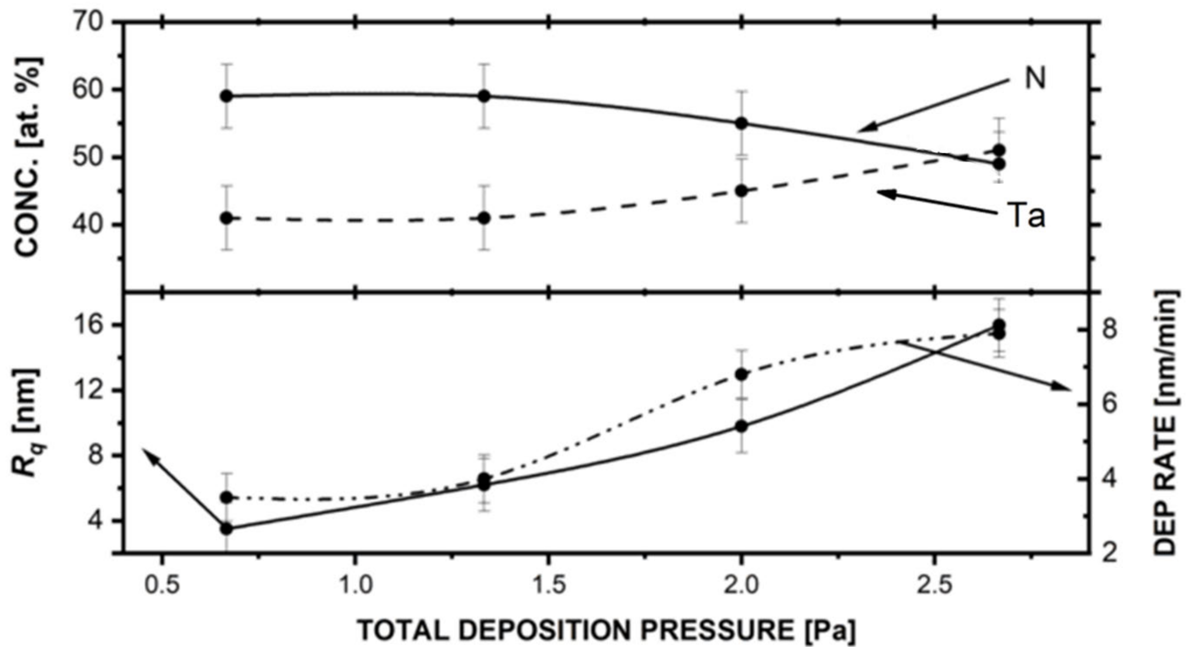

Figure 8-6. Influence of P_{Dep} on nitrogen and tantalum atomic %, roughness (R_q) and deposition rate for $p(N_2)$ = 0.26 Pa.

The effect of total deposition pressure on film structural properties is shown below in **Figure 8-7**. Shifts in the preferred orientation were observed across all deposition pressures when controlling for $p(N_2)$, as per Figure 8-7. All films exhibited peaks matching the δ-TaN database file or possessed at least one of the major peaks, which are located at 35, 41.3 and 60.1 degrees respectively. At 0.66 Pa, only the 35 degrees peak was apparent, indicating the presence of an amorphous TaN structure (Salamon et al. 2016). This peak is observed again under 1.33 and 2.00 Pa, before receding at 2.66 Pa, indicating again the presence of an amorphous TaN phase at high P_{Dep}. At 1.33 and 2.00 Pa, both the (200) and (311) peaks are apparent. Between 1.33 and 2.00 Pa, the (111) and (200) peaks were observed to switch in relative intensity, with the 2.00 Pa film exhibiting intensity values mirroring the matching source file. However, the greatest intensity peaks and therefore largest crystallite size was observed at 1.33 Pa.

This shift in the preferred orientation of cubic metal nitrides with increasing pN_2 is also reported in the literature (Hu et al. 2019). This result was attributed to the higher energy state of the metal ion clusters when sputtered using Ar, which subsequently results in faster grain growth and closer packing, which are two features that drive the preference of the (111) plane.

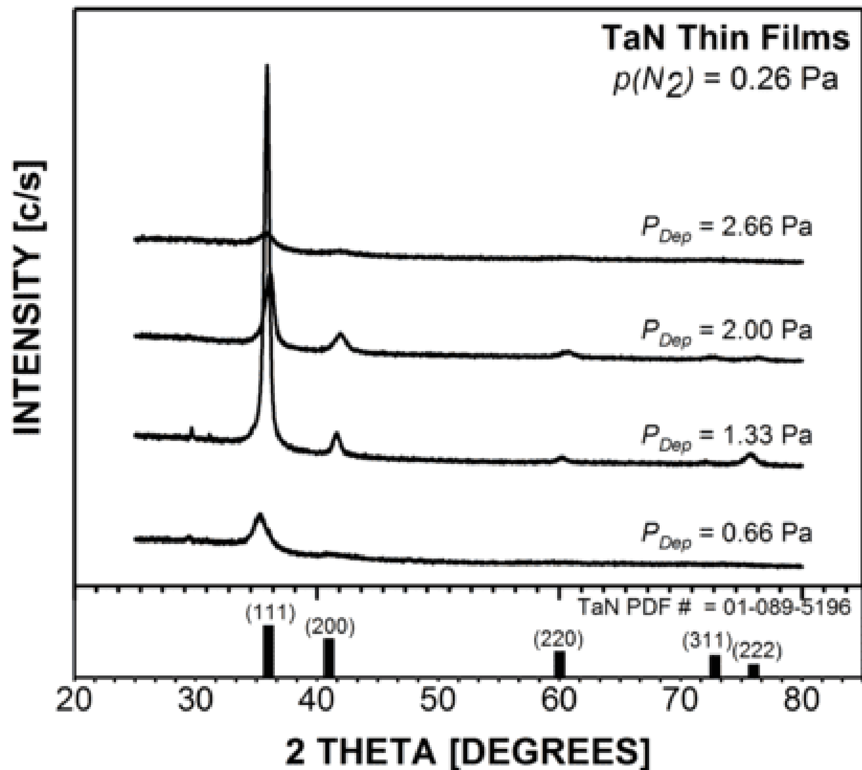

Figure 8-7. As-deposited TaN based films. p(N_2) = 0.26 Pa.

This data further highlights the importance of nitrogen activity in the sputtering atmosphere. It was previously observed in chapter 8.1.1.1 that nitrogen atmospheric content be kept at or below 10% of the total atmospheric content to produce crystalline TaN films; however, while investigating deposition pressure the most crystalline film was produced at 1.33 Pa, with a nitrogen presence of 20% of the total atmosphere. Nitrogen partial pressures below 10% were undesirable considering the aim of depositing the highest order tantalum nitride phase. Ultimately, increasing the nitrogen activity and total deposition pressure did not produce the Ta_3N_5 phase in the conditions studied.

The d spacing values for the (111) orientated peak are plotted against the P_{dep} below in **Figure 8-8.** As can be seen in Figure 8-7, less peak shifting is occurring although there remains a small amount. This is also seen in the small variance of the values in Figure 8-8.

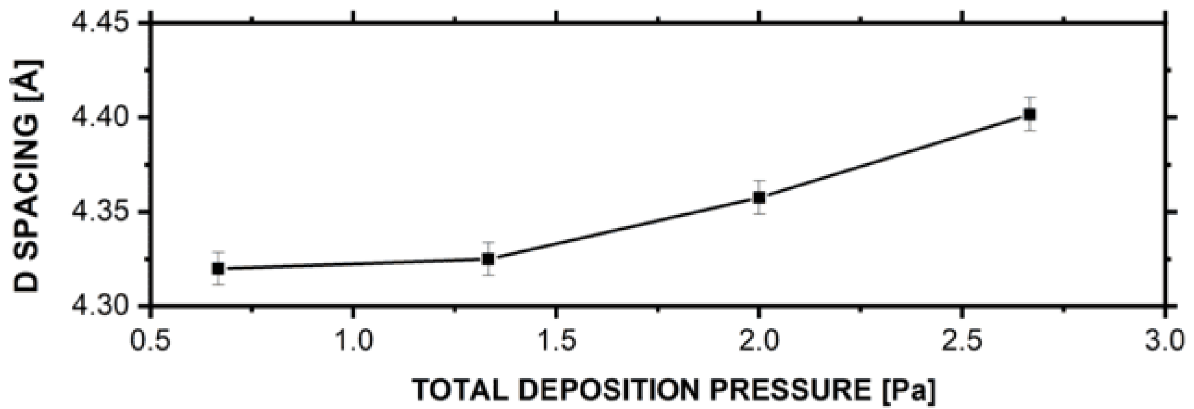

Figure 8-8. D spacing values of the (111) peak versus P_{dep}.

Further exploration of the effect of P_{Dep} elucidated the relationship between nitrogen activity, total deposition pressure and microstructural properties. To compare the effect of P_{Dep} values in a method independent of $p(N_2)$, 3 specific values of $p(N_2)$ were selected and fixed for deposition across the 1.33, 2.00 and 2.66 Pa P_{Dep} ranges. This data is summarised with the XRD patterns in **Figure 8-9**. For each of the different pressure series, a marked drop in crystallinity is observed with the increase in nitrogen activity. Indeed, a clear trend towards the deposition of amorphous films is observed as P_{Dep} is increased from 1.33 to 2.66 Pa. Thin films were still observed in cross sectional analysis, and films appeared largely transparent and without colour to the naked eye. This suggests the deposition of amorphous TaN films as $p(N_2)$:p(Ar) is adjusted to regimes that had a greater nitrogen presence in the sputtering atmosphere.

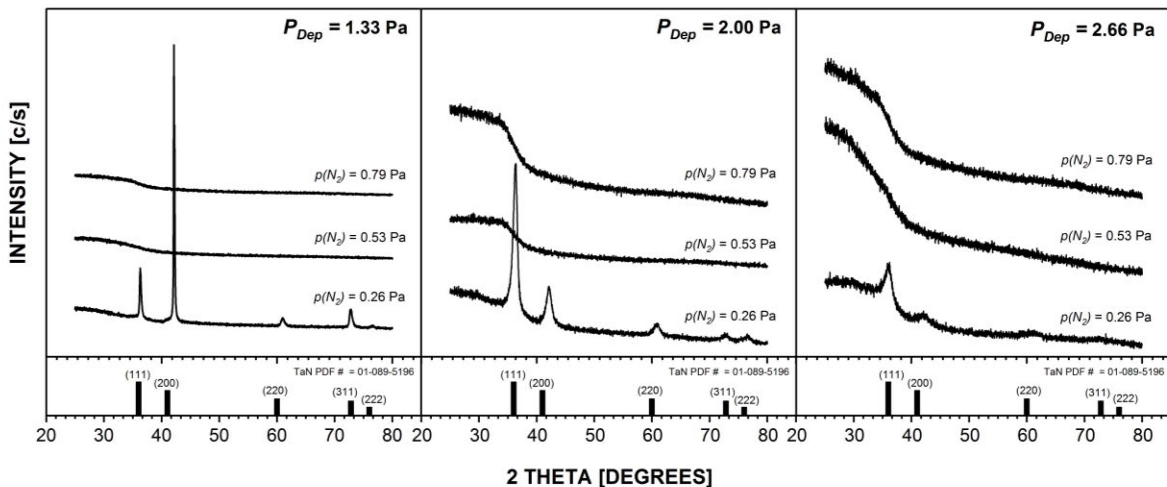

Figure 8-9. As-deposited TaN based films. P_{dep} = 1.33, 2.00 and 2.66 Pa (left to right).

It is speculated that this is the result of reduced nuclei energy; as P_{Dep} is increased, more of the nuclei ejected from the plasma are being scattered by the increasingly dense atmosphere, reducing the energy of those that do deposit on the substrate. Without another source of

energy, such as substrate heating or substrate bias, an amorphous TaN film is instead deposited. Another case of preferred orientation is also observed between the 1.33 Pa series and the 2.00 Pa series, with the (111) and (200) peaks once again changing in relative intensities. This effect was consistently observed, hinting at a relationship between sputtering conditions and preferred orientation that we have not observed in the literature.

SEM images of surface features and cross sections can be seen in **Figure 8-10** and **Figure 8-11.** A clear trend is seen with increasing P_{Dep} values; grain size shares a proportional relationship with increasing P_{Dep}. This result agrees with the recorded roughness values, as per Figure 8-6. This is likely due to the increasing thickness of the films promoting grain evolution.

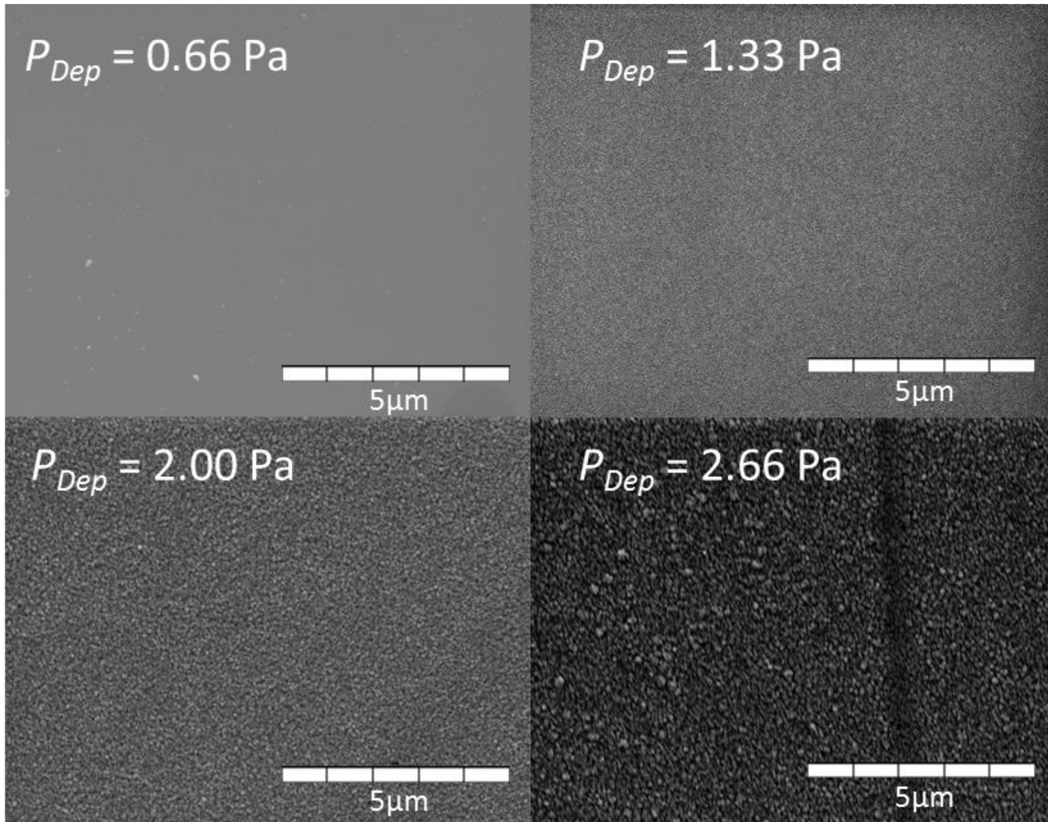

Figure 8-10. Surface SEM micrographs of films deposited at 0.66, 1.33, 2.00 and 2.66 Pa deposition pressures with a p(N_2) of 0.26 Pa.

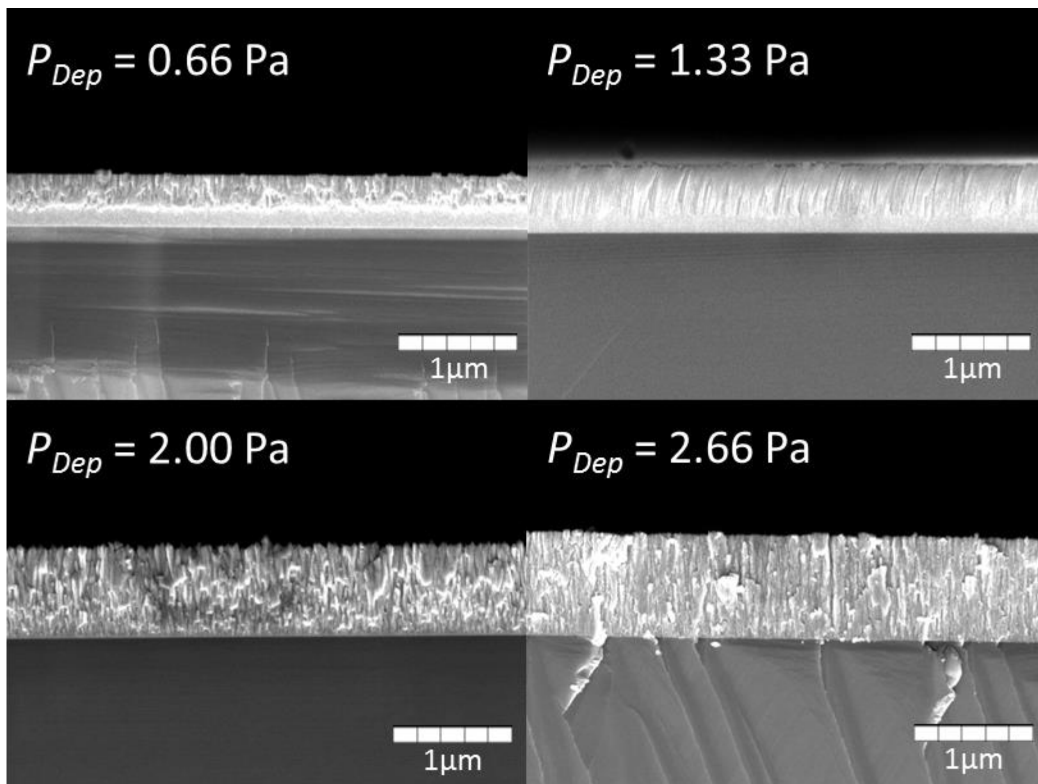

Figure 8-11. Cross section SEM micrographs of films deposited at 0.66, 1.33, 2.00 and 2.66 Pa deposition pressures with a p(N_2) of 0.26 Pa.

In summary, P_{Dep} also has a strong effect on the crystallinity, nitrogen content, thickness and surface morphologies of the films. Higher values of P_{Dep} produce thicker films with higher [Ta] content when sputtering is performed with $p(N_2)$ values equal to 10% of the sputtering atmosphere, as this value rises subsequent yield falls on account of the nitrogen poisoning and increased scattering. Surface roughness increases with P_{Dep} irrespective of nitrogen activity, and amorphous TaN films are produced, whereas lower P_{Dep} values result in films that match crystalline TaN patterns. Higher P_{Dep} values also produced a shift in the preferred orientation from the (200) to (111) plane, which was attributed to Ta depositing in a higher energy state in an Ar discharge relative to a nitrogen dominant plasma. In regards to the aims of this work however, the desired Ta_3N_5 phase was not observed in the conditions studied thus far.

8.1.1.3 Effect of Substrate Temperature, T_{sub}

Substrate temperature (T_{sub}) was investigated for its noted importance in the deposition of specific structures of TaN films (Stampfl & Freeman 2005). In previous sections T_{Sub} was not investigated and was thus left at ambient temperatures. The effect of substrate temperature on film morphologies was investigated with 4 films deposited at the temperatures of ambient, 523 K, 773 K and 923 K. The sputtering conditions for these films are listed in **Table 8.3**. Other aspects of the sputtering environment were controlled for. A deposition pressure of 1.33 Pa and Ar:N_2 ratio of 12:3 sccm (0.26 Pa $p(N_2)$) was selected, as these values provided crystalline films in previous depositions.

Table 8.3. Deposition conditions of films deposited with substrate temperature.

Substrate Temperature (K)	$p(N_2)$ (Pa)	P_{Dep} (Pa)	Film Thickness (nm)	Dep. Rate (nm/min)	R_q (nm)	[N] (at. %)	[Ta] (at. %)
Ambient	0.26	1.33	494	4.1	6.2	59	41
523	0.26	1.33	567	4.2	10.4	55	45
773	0.26	1.33	441	3.7	15.6	55	45
923	0.26	1.33	642	5.3	19.2	54	46

Elemental content did not change significantly, with a 5% difference in [N] at. % between films deposited at ambient temperatures and 923 K; this can be attributed to the anticipated loss of nitrogen due to heating (Goldschmidt 1967). The relationship between the at. % of [Ta] and [N] was inversely proportional relative to the substrate heating. This can be seen in addition to deposition rate and roughness values in **Figure 8-12** below.

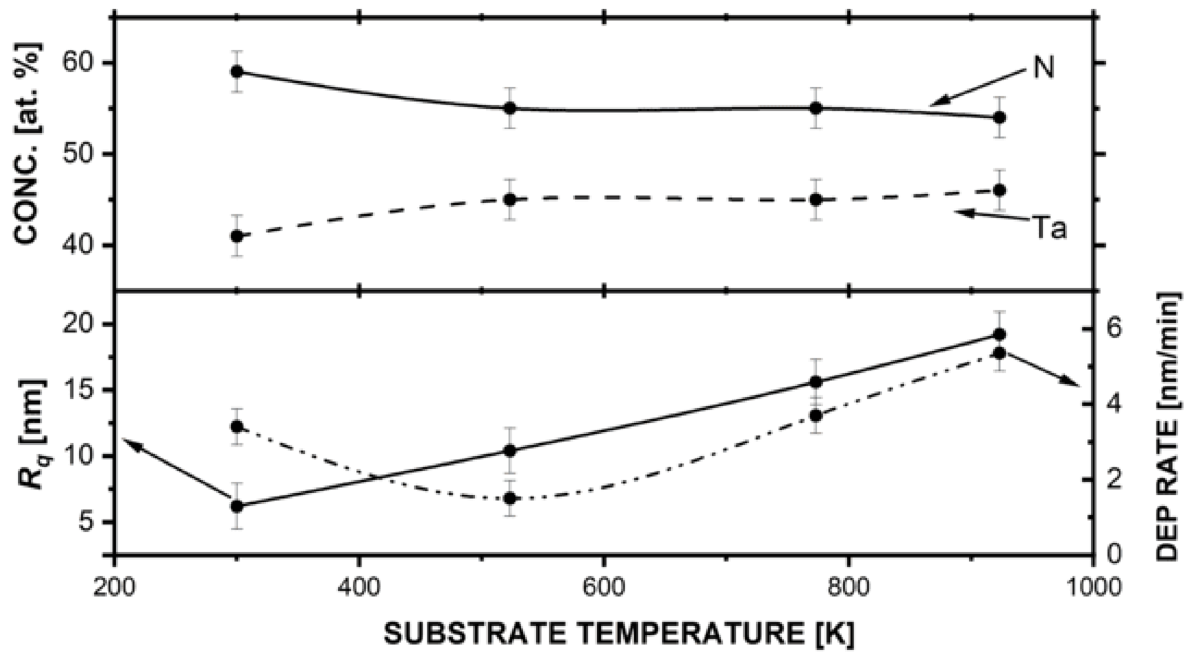

Figure 8-12. Influence of T_{sub} on nitrogen and tantalum atomic %, roughness (R_q) and deposition rate.

The elemental content of the films did not appear to change dramatically, with nitrogen atomic % dropping from 59% to 54% at ambient temperature and 923 K, respectively. The only significant change in nitrogen content took place between ambient temperatures and 523 K, with a drop of 5% nitrogen content. This loss could be attributable to the heating of the films promoting evolution of nitrogen from the films in the form of N_2 (Stampfl & Freeman 2005).

Surface roughness increased with substrate temperature, which is atypical. This could be attributed to residual stress produced by a lattice mismatch between the TaN film and Si substrate, which with increasing temperature drives unstable film growth and increasing roughness (Liu, Z & Shen 2005).

Deposition rate increased from 3.5 to 4.2 nm/min with the temperature increase from ambient levels to 523 K, before a decrease to 3.7 and final jump to 5.35 nm/min in films deposited at 773 K and 923 K, respectively. Film thickness was expected to decrease with temperature due to densification of the films, however this was not observed, with the film deposited at the highest temperature possessing the greatest thickness but also larger grains and porosity. XRD results for the films can be seen in **Figure 8-13**.

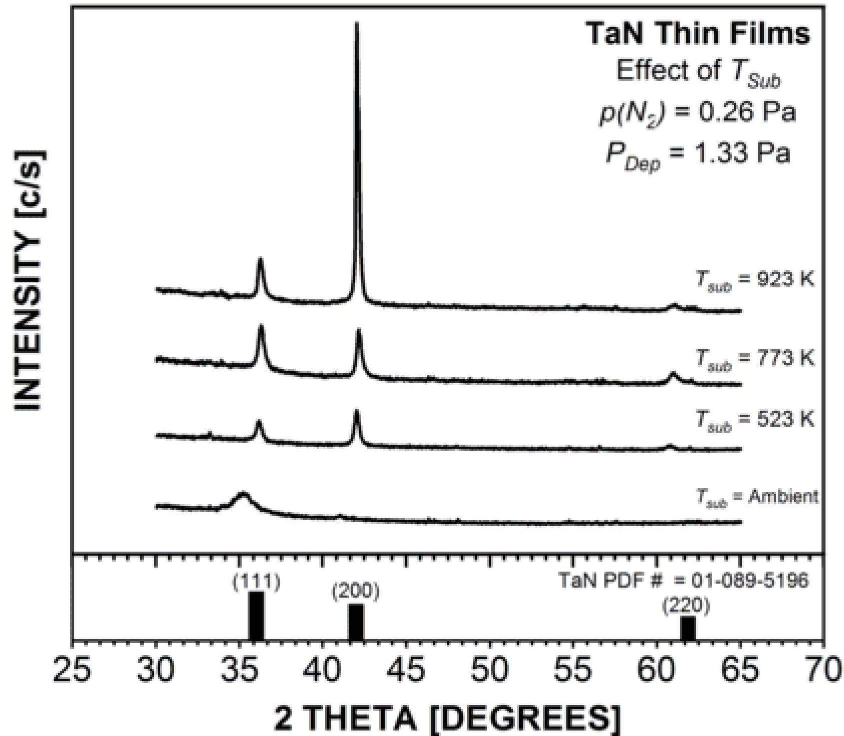

Figure 8-13. As Deposited TaN films. $p(N_2)$ = 0.26 Pa, P_{Dep} = 1.33 Pa.

The film deposited at ambient temperatures returned a pattern indicative of TaN as the primary phase, albeit with low intensity 42° and 61° peaks, indicating the presence of an amorphous structure. As temperature was increased to 523 K and 723 K, an increase in the intensity of the 36° (111) peak was observed, in addition to the appearance of the 42° (200) peak. The final film, deposited with a substrate temperature of 923 K, returned the strongest match for cubic TaN, with a preferred orientation in the (200) plane.

The evolution from an amorphous film to a densified crystalline film is expected with the increase in temperature. It is also apparent that substrate heating has a profound effect on the preferred orientation of the TaN films, although the resulting phases are consistent with what is shown in Figure 5-2.

A shift in the position of the peaks was also observed with the increasing temperature. The changing d spacing values for the (111) peak are plotted in **Figure 8-14** to better show this, although it is apparent in **Figure 8-13**.

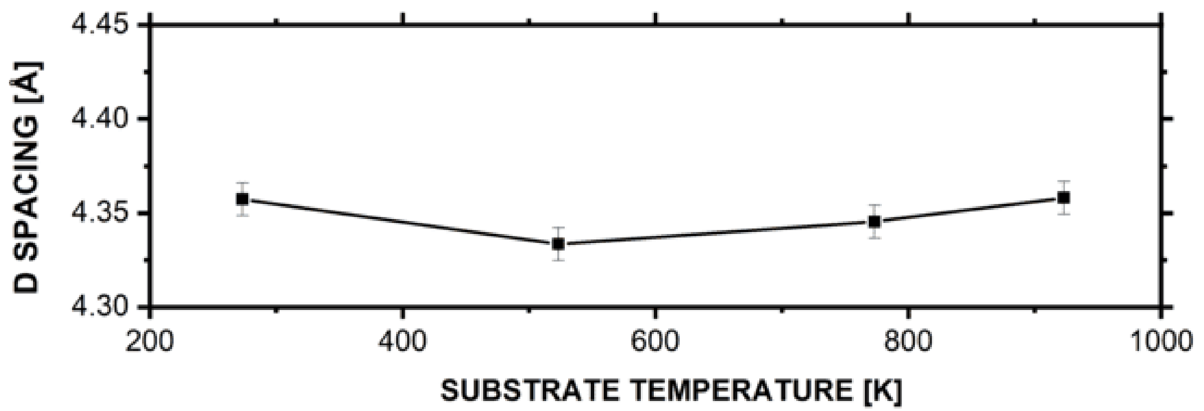

Figure 8-14. D spacing values of the (111) peak for the films deposited at ambient, 523 K, 723 K and 923 K T_{Sub}.

Finally, SEM imaging of the surface features of the films showed significant changes to the morphology as heat was increased. SEM micrographs of the film surface and cross section morphology can be seen below in **Figure 8-15** and **Figure 8-16**.

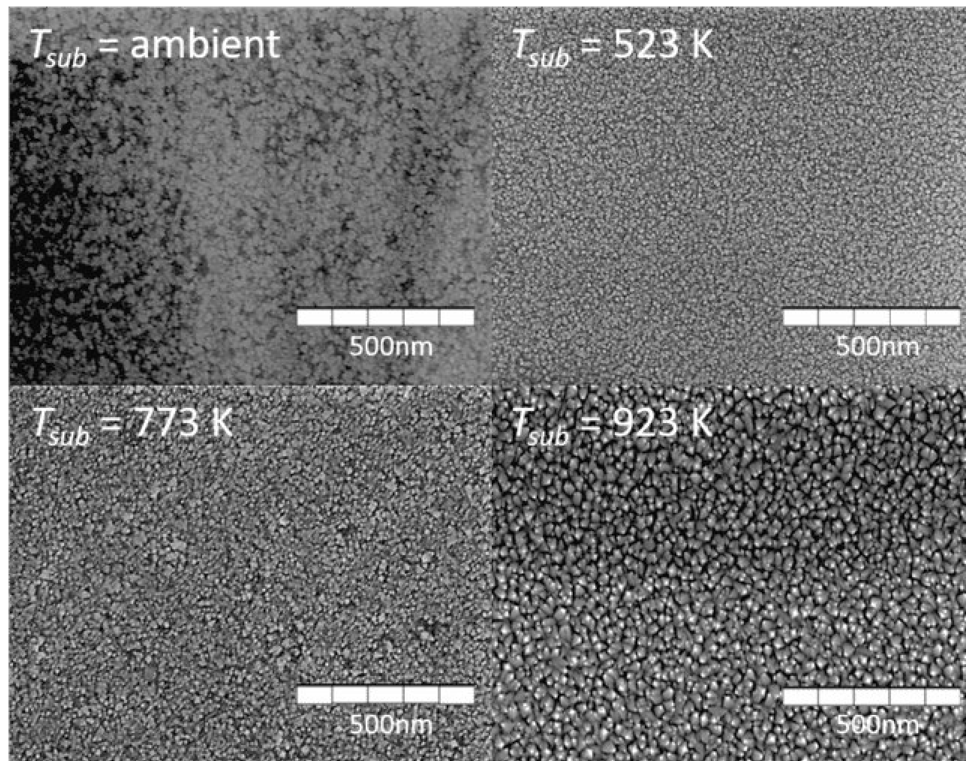

Figure 8-15. Surface SEM micrographs of TaN films deposited at ambient temperature, 523 K, 773 K and 923 K.

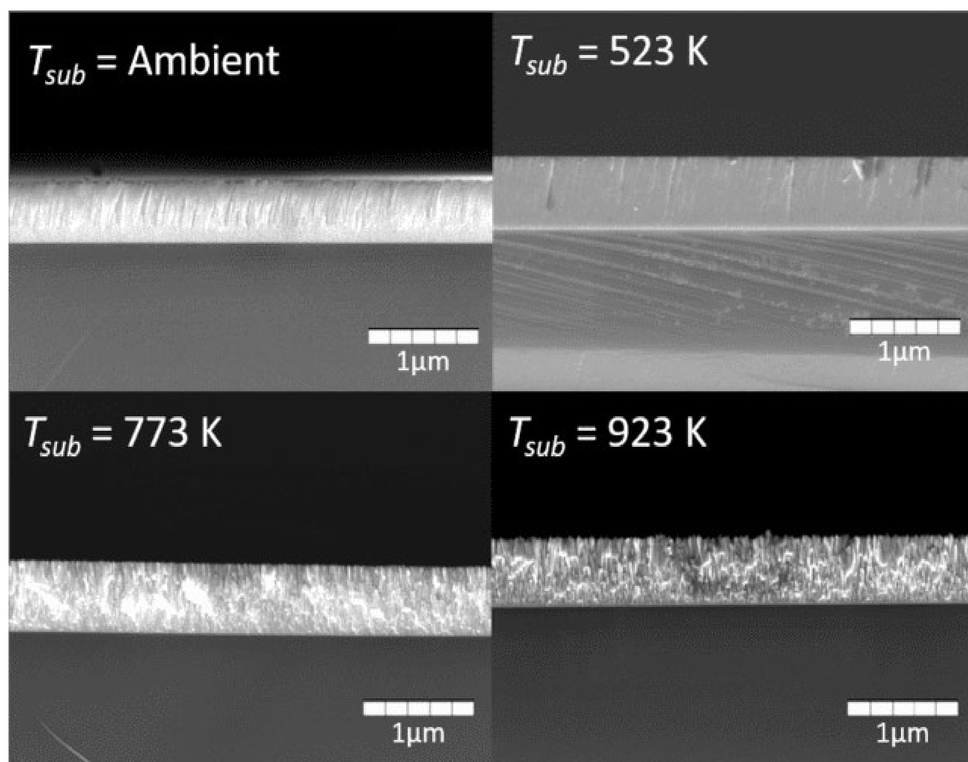

Figure 8-16. Cross section SEM micrographs of TaN films deposited at ambient temperature, 523 K, 773 K and 923 K.

Figure 8-15 and Figure 8-16 depicts a clear trend with the increasing temperature. As more heat was applied to the substrate, a steady increase in grain growth was observed as the film

evolves from a largely flat surface characterised by extremely small, nanometer sized grains to a rough surface punctuated with grains ~20 nm in size as per Figure 8-15.

In conclusion, substrate heating (T_{Sub}) had a direct impact on film structure, predictably driving crystallisation, and the dominant plane shifting from (111) at ambient temperatures to (200) at the highest temperature of 923 K. Surface features became rougher with heat (due to the formation of porous microstructures) and thickness increased, which resulted from increased porosity as seen in Figure 8-16. Nitrogen losses of approximately 5 at. % are also observed. Peak shifting was observed and hypothesized to be a result of the strain brought on by heating, but this is not definitively explored. While films exhibited greater crystallinity after heating, no other phase, including Ta_3N_5, could be observed.

8.2 DC Reactive sputtering of Tantalum Oxide and Subsequent Annealing in NH_3

Up to this point in the investigation, the Ta_3N_5 phase was not able to be synthesized using sputtering, which presented the challenge of explaining this phenomenon. These parameters, explored in depth in previous sections, included a variety of deposition pressures, gas mixtures, substrate temperatures, target power types and wattage settings. This result called for a different approach. Despite original aims to sputter Ta_3N_5 directly using just argon and nitrogen (later, oxygen), it had become clear that the inclusion of gaseous ammonia (NH_3) may be necessary to catalyse the desired phase, as ammonia is reported to be necessary in catalysing the formation of the Ta_3N_5 structure (Rudolph, M et al. 2019).

This section of the discussion will document the results pertaining to films that were deposited using oxygen (as-deposited Ta_xO_y films) before and after annealing in nitrogen and ammonia mixture to achieve the final Ta_3N_5 (or $Ta_3N_xO_y$) phase. Additionally, the substrates used for film deposition and their subsequent effects on the films will be briefly examined.

The sputtering conditions for the films are provided and will be discussed briefly before moving on to the topic of dopants, which will form the subject for the next section. Analytical techniques XRD, SEM/EDS and SIMS are primarily for this section of the work. SIMS analysis is introduced in this section to provide context to EDS data, as SIMS is more sensitive than EDS despite being a qualitative analysis method.

8.2.1 Tantalum Oxide Films

With the adjusted aim of first depositing films, then nitriding them, tantalum oxide (TaO or Ta_2O_5) films were explored first for their predictable and widely studied properties (Chaneliere et al. 1998; Chun et al. 2003). The Ta_2O_5 phase is the most common tantalum oxide structure and can easily be synthesized with appropriate oxygen concentrations in the sputtering atmosphere (Chaneliere et al. 1998), although this typically results in its amorphous form. Temperatures greater than 775 K are required to achieve the crystalline Ta_2O_5 structure, either while sputtering or as part of an annealing treatment.

These films were deposited using a plasma generated on a tantalum target under an argon and oxygen atmosphere. **Table 8.4** below shows the deposition parameters used.

Table 8.4. Sputtering parameters and thicknesses of Tantalum Oxide films.

Deposition Pressure (Pa)	pO_2/Total Atmospheric Oxygen (Pa/%)	Ta Power (W)	Substrate Temperature (K)	Thickness As Deposited (nm)	Thickness Post-NH_3 (nm)
0.66	0.03/5	100	573	510	683
0.66	0.06/10	100	573	471	650
0.66	0.09/15	100	573	426	580
0.66	0.13/20	100	573	402	459

Sputtering conditions selected primarily varied the atmospheric oxygen presence (pO_2), in a range from 5% to 20% of the total atmospheric pressure. EDS data for these films before and after annealing is shown below. Annealing resulted in thicker films. **Table 8.5** lists the EDS results for the amorphous TaO films before and after annealing in NH_3.

Table 8.5. EDS elemental data for Tantalum Oxide films before and after annealing in NH_3.

		As Deposited		Post Annealing		
Film Type	pO_2/Total Atmospheric Oxygen (Pa/%)	[Ta] (at. %)	[O] (at. %)	[Ta] (at. %)	[O] (at. %)	[N] (at. %)
TaO	0.03/5	36	64	31	6	63
TaO	0.06/10	30	70	25	4	71
TaO	0.09/15	22	78	26	8	66
TaO	0.13/20	18	81	25	11	64

Annealing predictably resulted in a significant drop in oxygen and increase in nitrogen presence, corresponding to the nitrogen content in Ta_3N_5 (66%). Of these films, the pO_2 = 10% and 15% contained at. % nitrogen values consistent with those in Ta_3N_5, however all films contained oxygen impurities even after annealing.

These films were subsequently used as standard films for comparison in the doped investigations that are discussed in later chapters of this work. The XRD results showing the presence of Ta_3N_5 in these films is shown in **Figure 8-17**.

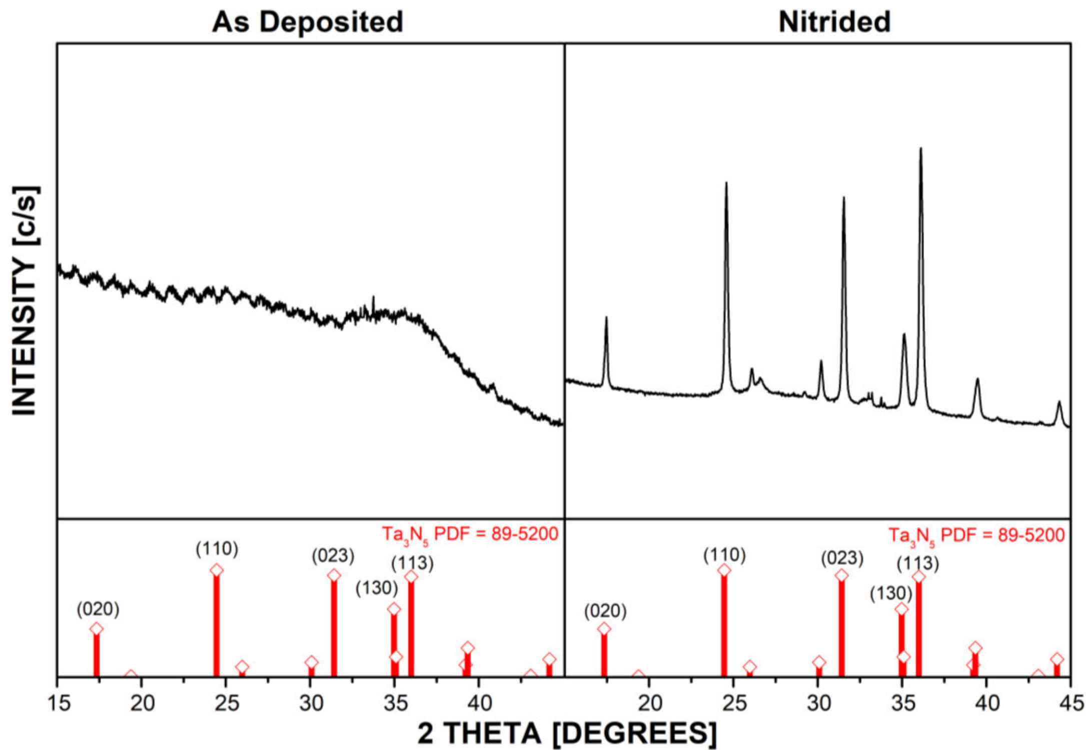

Figure 8-17. XRD results of TaO film deposited with a deposition pressure of 0.66 Pa and (pO_2) of 10%, before and after nitridation to show the presence of Ta_3N_5. All TaO films deposited converted to Ta_3N_5 with similar peak positions as seen here.

8.2.2 Film Selection for Doping and Conclusions

In this section, the multi-step synthesis of Ta_3N_5 films is described; films were first deposited as amorphous tantalum oxide prior to annealing in NH_3, which prompted the transformation to the desired Ta_3N_5 phase. When considering which system to proceed with between a tantalum oxide or mixed tantalum oxynitride film, it was important to consider how dopants would interact with each respective system as well as the nitriding process.

As demonstrated, the TaO system could be deposited in a controlled fashion and readily reacted into crystalline Ta_3N_5 films after annealing. The inclusion of dopants was also considered to be more simplistic in a pure oxide system relative to a mixed oxynitride system. Additionally, from a processing perspective, the inclusion of a third gas in nitrogen presented more complexity in the form of additional arrangements of processing parameters as well as its subsequent impact on the films. For these reasons, the tantalum oxide system was selected as a standard upon which to perform further investigations using sputtered dopant metals, the results of which will be presented and discussed in section 8.3.

8.3 DC Reactive Sputtering and NH_3 Annealing of Doped TaO Thin Films

This section of the work will explore the role of dopants in the sputtered TaO thin films detailed in the previous section. Dopant selection will be discussed, justifying the selection of Cr and

Al as dopant candidates, and their hypothetical incorporation into the films. Prior to deposition of the doped films, a partial hysteresis was performed to determine where in the sputtering regime the dopant candidates sputter best.

The sputtering conditions for the films are provided and will be discussed in the context of the undoped TaO films, which will be used as a standard series. Analytical techniques XRD, SEM/EDS and SIMS are primarily used to characterise the films discussed in this section. SIMS analysis is used to provide context to EDS data, as SIMS is more sensitive than EDS despite being a qualitative analysis method. Additionally, an investigation into the kinetics of the doped films was performed, for which SIMS analysis was of assistance.

8.3.1 Dopant Selection

Compared to other photo-electrode materials such as TiO_2 (Ahmad et al. 2015; Matsuoka et al. 2007; Ni et al. 2007) the body of literature regarding doped Ta_3N_5 is relatively immature (Hitoki et al. 2002; Nurlaela, Ziani & Takanabe 2016). Of these, several notable investigations have been published, including the reporting of Ta_3N_5 as a water splitting material (Hitoki et al. 2002), notable characterisation works identifying key electrochemical properties (Chun et al. 2003) and record photocurrents approaching the theoretical photocurrent limit of the material (Liu, Guiji et al. 2016). The literature has focused primarily on separating the Ta_3N_5 electrode from the electrolyte solution, as Ta_3N_5 has been demonstrated to self-oxidise under water splitting conditions (He et al. 2016).

Several papers have explored the role of dopants for improving Ta_3N_5 for water splitting purposes (Seo et al. 2015; Xie et al. 2016). Early papers focused on the alkali metals (Na, Mg, Ca, Sr, Ba, Be) as dopant candidates, which were experimentally demonstrated to improve water splitting properties of Ta_3N_5 (Kado, Lee, et al. 2012; Ma et al. 2012; Seo et al. 2015). From density functional theory (DFT) modelling, the performance improvement has been attributed to an increase in the number of oxygen defects ($O_N^{\bullet}$) and decrease in the number of nitrogen vacancies ($V_N^{\bullet\bullet\bullet}$) (Wang, Yawei, Zhu & Xu 2016). The latter of which are known to act as recombination centres (Wang, Yawei, Zhu & Xu 2016), as such inhibit water splitting performance.

Despite it being established that these dopants represent viable doping candidates, the effects of other cation dopants in the same role are still largely unknown. Zirconium doping of Ta_3N_5 has been examined (Seo et al. 2015), and has been noted to improve the photocurrent of Ta_3N_5 photoanodes and photocatalysts through the replacement of nitrogen vacancies with oxygen as speculated to occur when doping with alkali elements. In the case of Zr, it is unreasonable to consider that Zr is predominantly incorporating interstitially on the basis of relative ionic radii (Ta^{+5} = 0.64 Å versus Zr^{+4} = 72 Å (Shannon 1976)) which supports the

conclusion that substitutional incorporation of an acceptor can be beneficial to water splitting even if electrical conductivity would likely be reduced as a result (Yin et al. 2010).

Below is a list of potential candidates (**Table 8.6**) considered in this project as potential dopants in the Ta_3N_5 system. With the aim being to induce p-type properties, this called for elements possessing common charge states of 3+ or 4+ with comparable ionic radii to Ta^{5+}. Additional 5+ species are included for reference (including tantalum and niobium).

Table 8.6. List of Potential Doping Candidates.

Cation	Ionic Radii (Å)	Cation	Ionic Radii (Å)
Co^{2+}	0.65	Ti^{4+}	0.61
Fe^{2+}	0.70	Hf^{4+}	0.71
Cr^{3+}	0.62	Nb^{4+}	0.68
Al^{3+}	0.54	Sn^{4+}	0.69
Fe^{3+}	0.55	Ge^{4+}	0.53
Ga^{3+}	0.62	W^{4+}	0.66
Co^{3+}	0.60	Mo^{4+}	0.65
Mo^{3+}	0.69	Nb^{5+}	0.64
Ti^{3+}	0.67	Ta^{5+}	0.64
Nb^{3+}	0.72	W^{5+}	0.62

By extension, this result suggests that nitrogen vacancies are particularly inhibiting to electron mobility, or alternatively, that incorporated oxygen is especially favourable to electron mobility due to the creation of delocalised shallow donor states in the vicinity of the conduction band minimum (Xie et al. 2016). Such scenarios require investigation through solid-state conductivity measurements.

Chromium has seen wide use as a dopant in various fields, including solar water splitting photo-electrode materials like $SrTiO_3$ (Liu, J et al. 2006), $Cu_2V_2O_7$ (Cardenas-Morcoso et al. 2017) and TiO_2 (Sharifi et al. 2018). Cr doping is associated with improved visible light absorption in wide band gap materials such as TiO_2 and $SrTiO_3$. Cr doping has been examined as a means of stimulating visible light sensitivity (Peng, Huang & Huang 2012; Yu, H et al. 2012). In these cases, Cr is an acceptor dopant which introduces defect states into the band gap of the host oxide which facilitate absorption of sub band gap photons.

In terms of developing a p-type Ta_3N_5 photo-electrode, Cr doping is attractive for several reasons. Firstly, as a tri-valent cation (most common oxidation state) Cr^{3+} substitution for Ta^{5+} has strong potential to increase the hole concentration when incorporated under conditions of low oxygen activity (electronic compensation, **Equation 24**). The expectation of such incorporation is reasonable when considering both the similar radii of Cr^{3+} and Ta^{5+} (0.61

Å (Shannon 1976) and Ta^{+5} = 0.64 Å respectively) combined with the use of ammonolysis during materials synthesis.

$$3Cr_2O_3 + 10NH_3 \xrightarrow{Ta_3N_5} 6Cr''_{Ta} + 10N_N^x + 9H_2O + 6H_2 + 12h^{\bullet} \qquad \text{(Equation 24)}$$

The alternative scenario of Cr^{3+} incorporation under conditions favouring ionic compensation, as described by **Equation 25**, occur under conditions of higher oxygen activity. This condition is considered unlikely to be achievable during ammonolysis. However the resulting products reflect the defect states attributed to favourable water splitting performance during doping with alkali earth dopants (Ma et al. 2012) and Zr (Seo et al. 2015; Wang, Yawei, Zhu & Xu 2016).

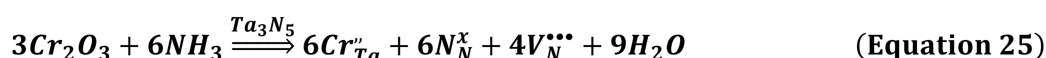

$$3Cr_2O_3 + 6NH_3 \xrightarrow{Ta_3N_5} 6Cr''_{Ta} + 6N_N^x + 4V_N^{\bullet\bullet\bullet} + 9H_2O \qquad \text{(Equation 25)}$$

The development of a p-type Ta_3N_5 material would be compelling for its potential ability to avoid the oxidative stress experienced by an anode when performing the oxidation step of the water splitting reaction (He et al. 2016). In addition to avoiding or at least minimising photo-corrosion, a p-Ta_3N_5 photo-cathode would also avoid the kinetically challenging oxidation of water, and instead only need to drive the relatively simple reduction of H^+. Coupled with a suitable photo-anode material, the development of such a photo-cathode would eliminate the need for a Pt cathode and consequently reduce the applied expense of a future photo-electrochemical cell for hydrogen production.

Another dopant that was selected for investigation was aluminium. In a similar case to chromium, aluminium typically exists as a +3 donor element. Aluminium is an oft-employed dopant candidate (Kelly, Zhou & Postill 2003), known for inducing p-type behaviour in silicon semiconductors. In the solar water splitting field, aluminium has seen regular use as a dopant in many oxide systems used for water splitting, such as ZnO (Shet et al. 2011), $SrTiO_3$ (Shin, C-J, Yoo & Lee 2007) and TiO_2 (Shirley, Kraft & Inderwildi 2010). Aluminium has proven to be an efficacious dopant candidate in these examples, assisting in band gap tuning (Shet et al. 2011) or increasing the photocurrent density of photo-electrochemical films through improved electrical conductivity relative to undoped counterparts (Li, W et al. 2015).

Like chromium, aluminium is an attractive dopant candidate for a few reasons. As with chromium, the trivalent cation of Al^{3+}, when substituted for Ta^{5+}, has a strong potential to increase the hole concentration when incorporated under conditions of low oxygen activity (electronic compensation, **Equation 26**). However, the atomic radii of aluminium is notably dissimilar to that of tantalum such that substitution may not be favourable (Al^{3+} = 0.53

Å (Shannon 1976) and Ta^{+5} = 0.64 Å, respectively), and instead a second phase may be generated.

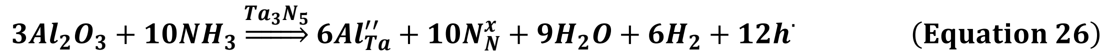

$$3Al_2O_3 + 10NH_3 \xrightarrow{Ta_3N_5} 6Al''_{Ta} + 10N_N^x + 9H_2O + 6H_2 + 12h^{\cdot} \qquad \text{(Equation 26)}$$

Like chromium, the hypothetical alternative scenario of Al^{3+} incorporation under conditions favouring ionic compensation, as described by **Equation 27**, occur under conditions of higher oxygen activity.

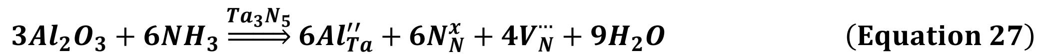

$$3Al_2O_3 + 6NH_3 \xrightarrow{Ta_3N_5} 6Al''_{Ta} + 6N_N^x + 4V_N^{\cdot\cdot\cdot} + 9H_2O \qquad \text{(Equation 27)}$$

8.3.2 Chromium Doped Ta_3N_5 Thin Films

This subsection will detail the experimental results and discussion pertaining to chromium doped Ta_2O_5 films, which were subsequently annealed in NH_3 to achieve the Ta_3N_5 phase, ideally with a proportion of chromium doping. The primary aim was to produce chromium doped Ta_3N_5 films, and subsequently reproduce these films with fine control over the dopant content. The reaction kinetics were also explored in some detail, as the ammonolysis reaction is the most important step of the synthetic process and understanding what is happening to chromium, tantalum, oxygen and nitrogen in this process is of high interest. Prior to beginning the investigation of chromium doping, an investigation into the oxygen poisoning that takes place in tantalum and chromium targets in the presence of a plasma was performed, in a similar fashion to what was done initially when evaluating TaN films.

8.3.2.1 Hysteresis of Ta and Cr Targets in Argon

The use of a reactive process gas (oxygen) during the sputtering of metallic targets can lead to the surface of the targets becoming oxidised during deposition. Known as poisoning, this frequently leads to a reduced sputter yield and weaker deposition energetics. When planned for, this may not necessarily lead to undesired growth conditions, but the tendency for target poisoning to occur abruptly upon a possibly small increase in $p(O_2)$ can make film growth unreliable when not expected. Furthermore, when the rate of oxide removal (unpoisoning) is also relatively rapid upon a small decrease in $p(O_2)$, a region of film growth instability can also be encountered. Hence, it is an important task to assess the sputter dynamics of metallic targets over a broad range of $p(O_2)$ to select $p(O_2)$ values that support stable film growth characteristics.

In the current scenario two metallic targets will be co-sputtered at times to achieve Cr-doped Ta_3N_5. Under these circumstances the dynamics of the combination is important to assess as the dynamics may be different if assessed independently.

The effect of target poisoning can be observed indirectly via the measurement of discharge voltage during deposition. Specifically, any change in the sputter yield through poisoning will manifest as an altered discharge current. Under conditions where power is fixed, any alteration to discharge current will result in a simultaneous change in discharge voltage.

This target poisoning assessment was performed over 45 minutes, beginning with a $p(O_2)$ of 0 Pa which was increased to 0.26 Pa in 0.06 Pa increments after a hold period of 5 minutes. The discharge voltage was recorded every 30 seconds. The results of this assessment are displayed below in **Figure 8-18**.

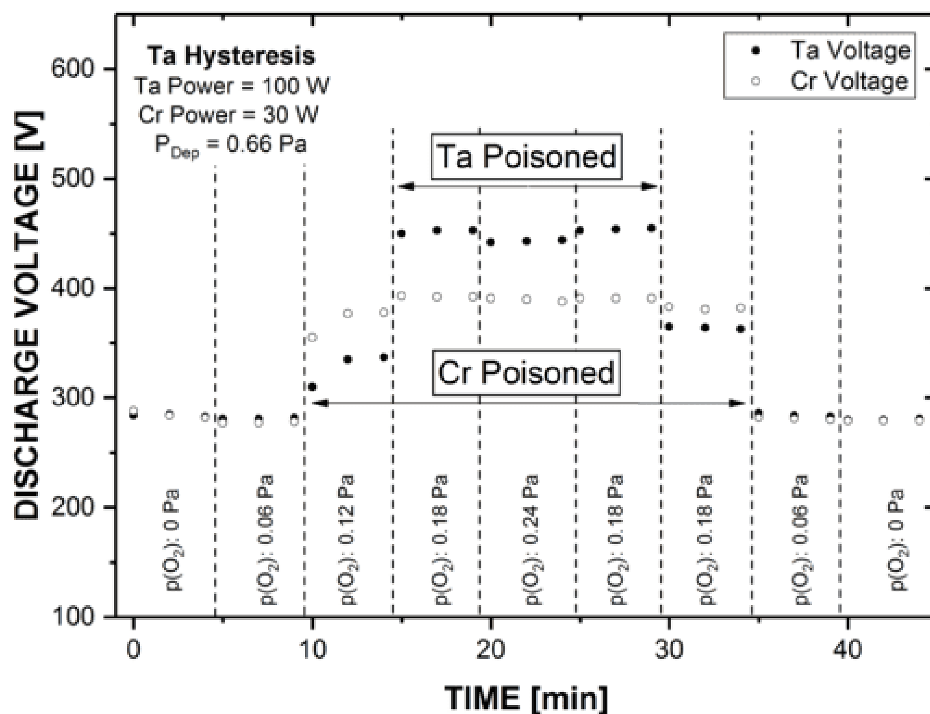

Figure 8-18. Hysteresis of Ta and Cr targets in an Ar/O_2 atmosphere. O_2 gas flow rate is adjusted over time to reflect the displayed $p(O_2)$ values, up to a peak $p(O_2)$ value before being ramped down again.

As seen in Figure 8-18, both metal targets maintained a stable discharge voltage until $p(O_2)$ reached 0.12 Pa and began to increase. At this point, the Cr target displayed a stronger response to $p(O_2)$ than the Ta target. However, upon increasing $p(O_2)$ further to 0.18 Pa, this changed, and the discharge voltage of the Cr target remained almost unresponsive in contrast to the Ta target whose discharge voltage increased abruptly to ~450 V where it became effectively unresponsive to further $p(O_2)$ increases.

These observations indicate that both targets begin to poison (form an oxide species at the target surface) to some extent when $p(O_2)$ is 0.12 Pa. For the Cr target the extent of poisoning that is achieved after 5 minutes at $p(O_2)$ is almost complete, as reflected by the lack of response to further $p(O_2)$ increase. The Ta target however is different. At $p(O_2)$ equal to 0.12

Pa poisoning is taking place but it is not complete after 5 min. For the Ta target complete poisoning appears to require $p(O_2)$ equal to 0.18 Pa. This may reflect slow oxidation kinetics under the applied circumstances, or more likely, that the poisoning process for Ta involves the formation of more than one oxide species. Determining the precise reason is beyond the scope of this investigation. For the purposes of selecting the appropriate $p(O_2)$ range to conduct this study, it is sufficient to conclude that Ta does not reach a fully poisoned condition until $p(O_2)$ reaches 0.18 Pa and that the extent of poisoning encountered at 0.12 Pa is marginal compared with the completely poisoned state.

Upon decreasing $p(O_2)$ from the 0.24 Pa maximum to 0 Pa, both targets followed similar trajectories to when $p(O_2)$ was increased although the rate of increase in discharge voltage is generally faster than the rate of discharge. This is not unexpected as the process of ion etching of an oxide surface is typically more difficult than for a metallic surface. The important aspect relating to the restoration of the unpoisoned surface is that it can be achieved readily. This ensures that the condition of the targets can be returned to a relatively standard condition (metallic) in short time during the setup of the sputtering apparatus immediately prior to a deposition.

While several issues may be investigated from the data displayed in Figure 8-18, the key objective to be reached is the identification of an appropriate range of $p(O_2)$ to apply during this investigation. For the purposes of controlling the extent of Cr doping, a $p(O_2)$ should be applied that supports a wide range of applied Cr target power without depositing Cr at excessive levels. This points toward a poisoned Cr target, complimented by an unpoisoned Ta target that is depositing Ta strongly. From consideration of the results in Figure 8-18, the selection of $p(O_2)$ in the range of 0.06 Pa to 0.12 Pa is expected to achieve this outcome. $p(O_2)$ less than 0.06 Pa will ensure that both targets deposit strongly and reduce fine control over the Cr dopant loading. $p(O_2)$ above 0.12 Pa is likely to reduce the deposition rate of Ta and lead to a similar challenge of Cr loading control. Relative to the deposition pressure, these values correspond to ~10 – 20% O_2.

8.3.2.2 Deposition and Nitridation of Tantalum Chromium Oxide

Cr-Ta-O films were deposited under conditions reflected in the initial hysteresis experiment in the previous section. Ta-O films were sputtered separately, and their discussion is detailed in the earlier section of this work. Ta-O films were sputtered without any power on the chromium target and included as a control series. The methodology used in depositing the doped films was lengthy, with multiple synthetic and analytical steps involved. As such the below figure is provided to visually demonstrate the synthetic steps involved and analysis performed. The

synthetic process used to synthesize the Cr-Ta_3N_5 films in this section is shown below in **Figure 8-19**.

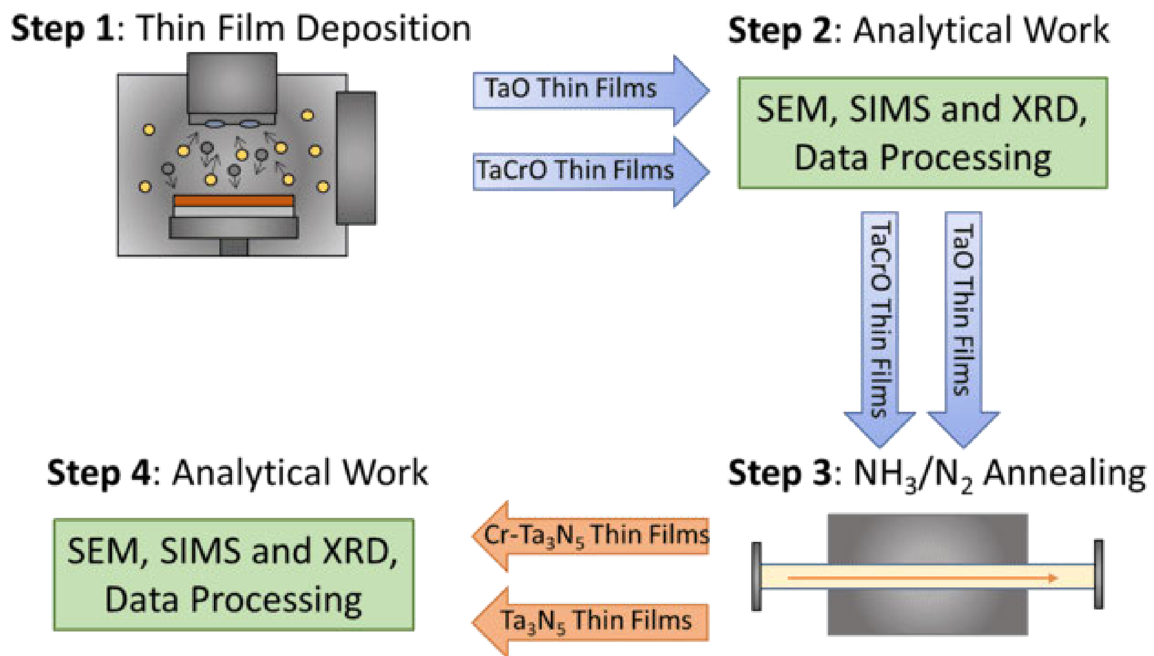

Figure 8-19. Flow chart depicting synthetic and analytical procedure used to synthesize doped and undoped Ta_3N_5 films.

All other parameters were kept consistent between these 'doped' and 'undoped' film series. Amorphous chromium tantalum oxide films were deposited under the conditions summarised in **Table 8.7** below. Similarly, amorphous undoped tantalum oxide films were also deposited according to Table 8.7. All films were assessed for thickness after deposition, and again after nitriding in ammonia gas phase using SEM imaging of film cross-sections. These images are displayed as **Figure 8-20** relating to as-deposited films, and **Figure 8-21** relating to the films achieved post-nitriding in ammonia. The resulting thicknesses are summarised in Table 8.7. All films were deposited at a substrate temperature of 575 K.

Table 8.7. Sputtering parameters and thicknesses of chromium doped and undoped tantalum oxide thin films, before and after NH_3 annealing.

	Deposition Pressure (Pa)	pO_2/Total Atmospheric Oxygen (Pa / %)	Ta:Cr Power (W)	Thickness As Deposited (nm)	Thickness Post-NH_3 (nm)	Thickness Change Post-NH_3 (%)
UNDOPED	0.66	0.06/10	100:0	471	650	38.0
	0.66	0.09/15	100:0	426	580	36.1
	0.66	0.13/20	100:0	402	459	14.1
DOPED	0.66	0.06/10	100:30	804	738	-8.2
	0.66	0.09/15	100:30	1080	732	-32.2
	0.66	0.13/20	100:30	651	584	-10.2

As seen in Table 8.7, the addition of Cr sputtering resulted in the deposition of a thicker film in all circumstances which is consistent with expectation. As the $p(O_2)$ is increased the thickness of the undoped tantalum oxide films tended to decrease. This is in line with the previous observations of the oxygen poisoning behaviour of the Ta target.

The thickness of the Cr doped tantalum oxide films displays an overall tendency to decrease in thickness with increased $p(O_2)$ but a maxima is clearly observed. Explaining this observation is made difficult by the fact that film thickness is the result of both target sputtering yield as well as film density. Potentially, the film deposited at $p(O_2)$ equal to 0.06 Pa is relatively dense compared to all other films due to the higher deposition energetics associated with a reduced extent of target poisoning.

Precisely determining the density of the deposited films is not essential to this investigation. All films were achieved at deposition rates of 8 to 22 nm/min, and displayed a silvery metallic lustre immediately after deposition. After nitriding it was observed that all Cr-doped tantalum nitride films displayed a reduction in film thickness whereas all undoped tantalum nitride films displayed an increase in film thickness. If all films consist of the same phase post-nitriding, this result points towards a significant difference in the film density of the as-deposited Cr-doped and undoped tantalum oxide films as already suggested.

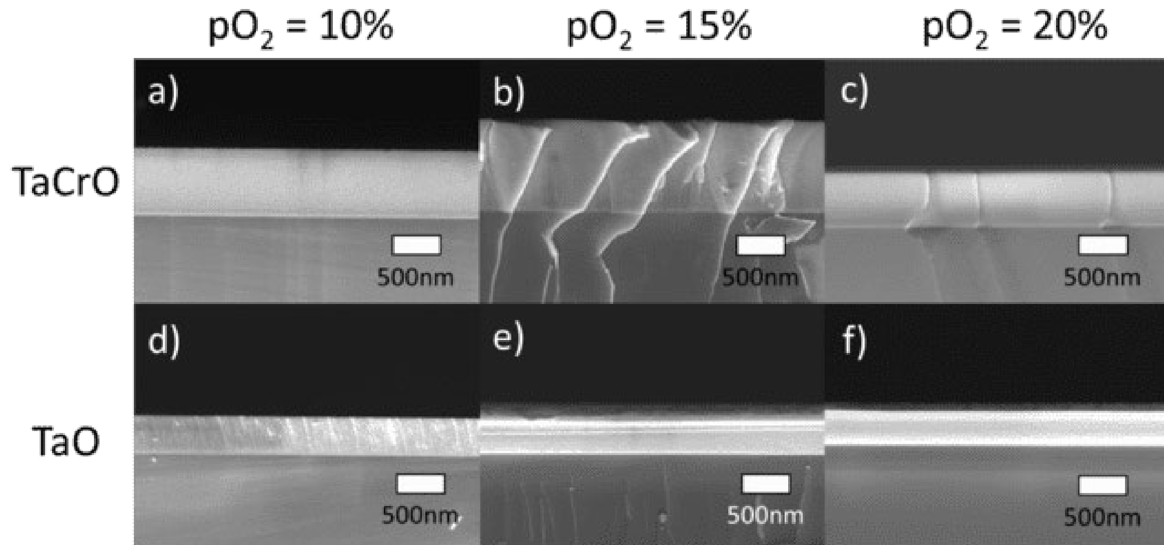

Figure 8-20. Cross section SEM micrographs depicting the morphology of TaO and TaCrO films before thermal annealing in NH_3 gas mixture, where a) TaCrO 10% pO_2, b) TaCrO 15% pO_2, c) TaCrO 20% pO_2, d) TaO 10% pO_2, e) TaO 15% pO_2, f) TaO 20% pO_2.

From Figure 8-20, all as-deposited films lack distinct microstructures, consistent with amorphous films. In contrast, the films seen in Figure 8-21 show microstructures indicative of crystallinity. However, upon comparing the undoped films to the Cr-doped films, the undoped films contain substantially more porosity, this is especially the case at low $p(O_2)$. In fact, it appears that the extent of porosity in the undoped films tends to decrease as $p(O_2)$ increases whereas the Cr-doped films appear to be close to fully dense irrespective of $p(O_2)$.

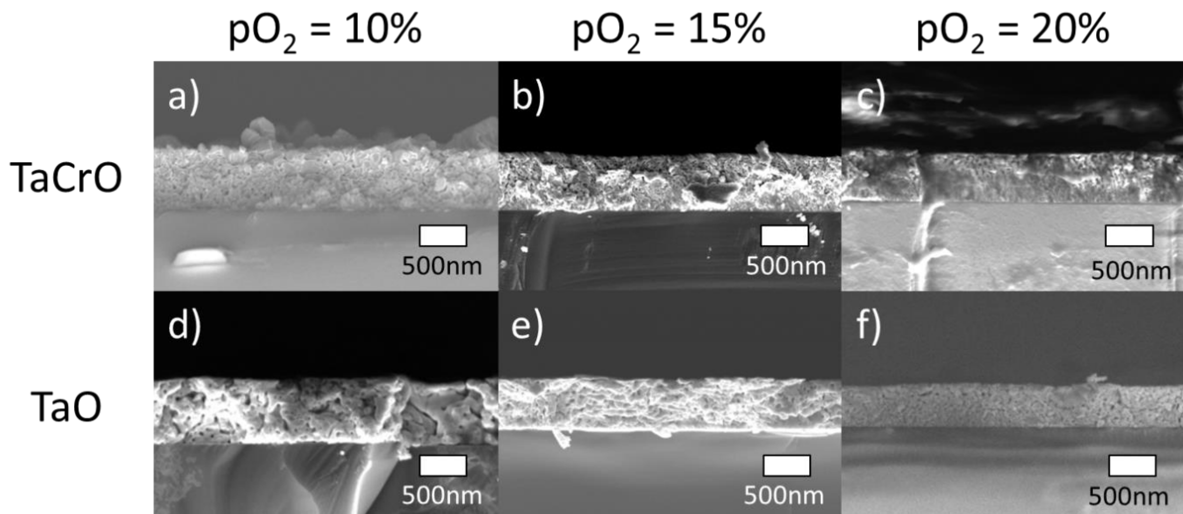

Figure 8-21. Cross section SEM micrographs depicting the morphology of TaO and TaCrO films after thermal annealing in NH_3 gas mixture, where a) TaCrO 10% pO_2, b) TaCrO 15% pO_2, c) TaCrO 20% pO_2, d) TaO 10% pO_2, e) TaO 15% pO_2, f) TaO 20% pO_2.

These observations are consistent with the thickness results reported in Table 8.7. Specifically, the thickness of the undoped films increases upon annealing in ammonia with the

largest gain in thickness at low p(O_2) and the least gain at high p(O_2). For the all Cr-doped films, the thickness decreases for all cases of p(O_2).

Figure 8-22 and **Figure 8-23** respectively display the surface microstructure of the as-deposited and as-annealed films. From Figure 8-22, all films display a high level of grain uniformity with Cr-doped films possessing larger grain size in general. Additionally, the Cr-doped films display a tendency for decreased grain size with increased p(O_2). This trend is not observable for the undoped films and at p(O_2) equal to 20%, the microstructures for both Cr-doped and undoped films are near identical.

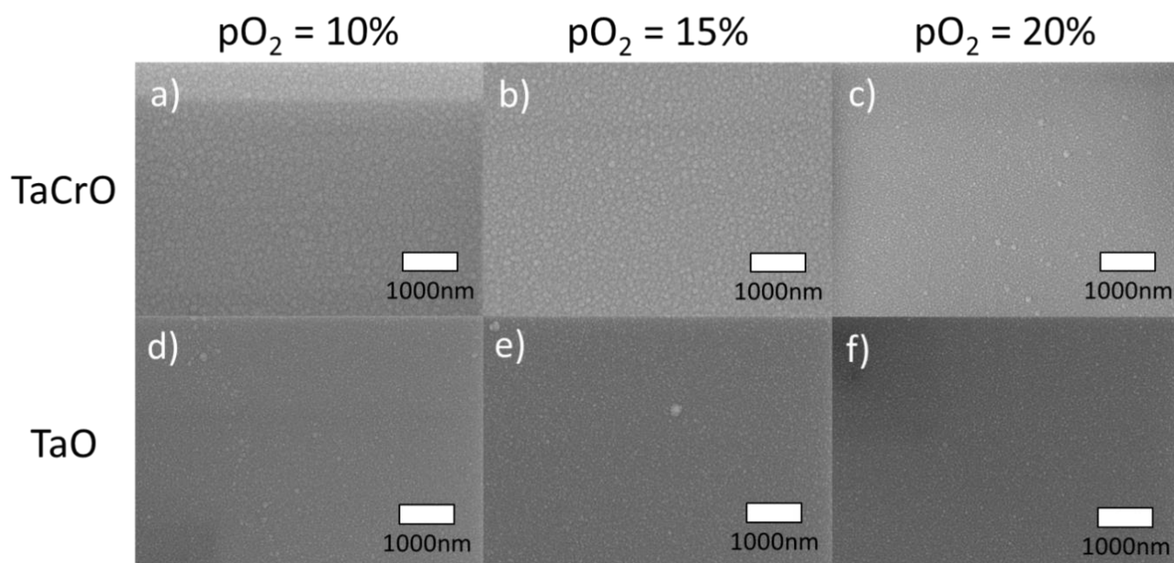

Figure 8-22. Top down SEM micrographs depicting the morphology of TaO and TaCrO films before thermal annealing in NH_3 gas mixture, where a) TaCrO 10% pO_2, b) TaCrO 15% pO_2, c) TaCrO 20% pO_2, d) TaO 10% pO_2, e) TaO 15% pO_2, f) TaO 20% pO_2.

Additionally, the Cr-doped films appear to display a tendency for decreased grain size with increased p(O_2). This trend is not observable for the undoped films and at p(O_2) equal to 20%, the microstructures for both Cr-doped and undoped films are near identical. This tendency for the Cr-doped films to respond to p(O_2) is further observed in Figure 8-23 where the grain size observed at p(O_2) equal to 10% (~200 nm) is much larger than at p(O_2) equal to 15% or 20% (~100 nm). In the case of the undoped films, the grain size does not appear to observe any trend with p(O_2) although the microstructures are dominated by agglomerations rather than distinct grains. Arguably the agglomerations at low p(O_2) are smaller than at high p(O_2).

These microstructural observations suggest that the presence of the Cr dopant favours grain growth and the overall densification of the films as they transform from amorphous oxides to crystalline nitrides. This is similar to behaviour reported in the literature for Mg-Ta_3N_5 films, where grain growth was promoted with the incorporation of an Mg dopant species (Xie et al.

2016). To consider the mass transport behaviour of the films more closely, the structure of each film have been verified using XRD. The resulting diffractograms are summarised in **Figure 8-24**.

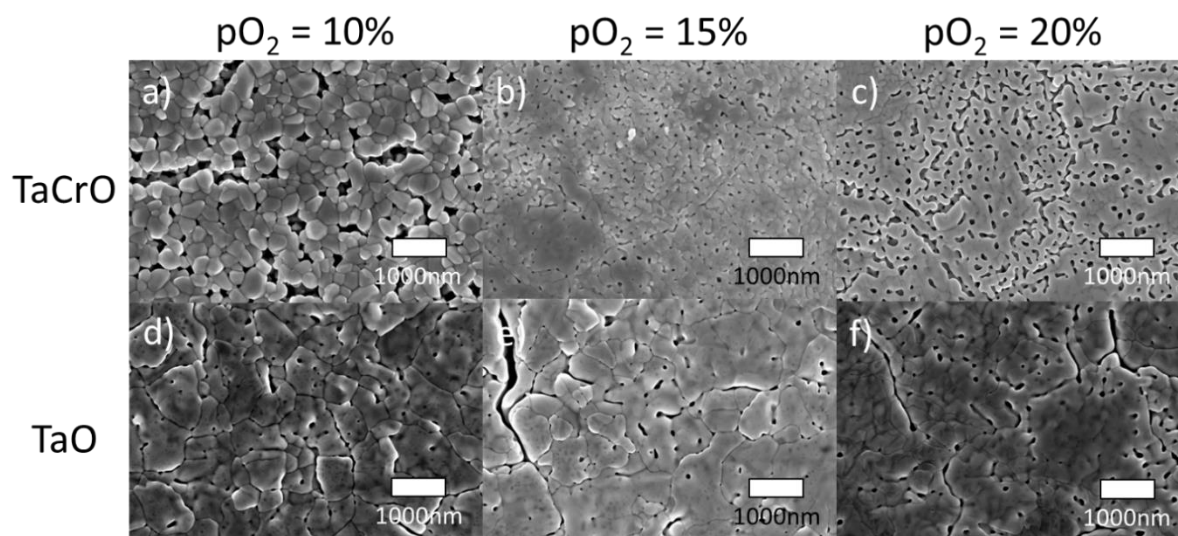

Figure 8-23. Top down SEM micrographs depicting the morphology of TaO and TaCrO films after thermal annealing in NH_3 gas mixture, where a) TaCrO 10% pO_2, b) TaCrO 15% pO_2, c) TaCrO 20% pO_2, d) TaO 10% pO_2, e) TaO 15% pO_2, f) TaO 20% pO_2.

As seen in Figure 8-24a, c and e, all films were confirmed to be amorphous immediately subsequent to deposition. In these patterns the only peak observed relates to the Si substrate. However as seen in Figure 8-24b, d and f, the effect of nitriding in ammonia has clearly induced crystallisation. For the undoped films, the observed patterns in all cases of $p(O_2)$ is consistent with the orthorhombic Ta_3N_5 phase (PDF 89-5200, space group cmcm) and no evidence for the existence of second phases is present. For the Cr-doped films, Ta_3N_5 is also observed as the dominant phase however the distribution of peak intensities appears to respond to $p(O_2)$. At $p(O_2)$ equal to 20%, the distribution of crystal orientations the Cr-doped and undoped films are similar, however at $p(O_2)$ equal to 10% and 15% the specific distribution of orientations between the film types is quite different.

This is consistent with the observed differences in microstructures. Also observed at $p(O_2)$ equal to 10% is an unidentified peak at ~38^0 2-theta. It is possible that this peak represents the formation of an exsolved Cr-based phase, which is identified here to be a Cr_2N phase (PDF = 033-0803, β-Cr_2N plane). However, it is noted that several chromium nitride phases possess peak positions with similar intensities at the observed 2-theta. To assess the nature of this phase better, EDS has been used to determine the composition of the films and the Cr-loading.

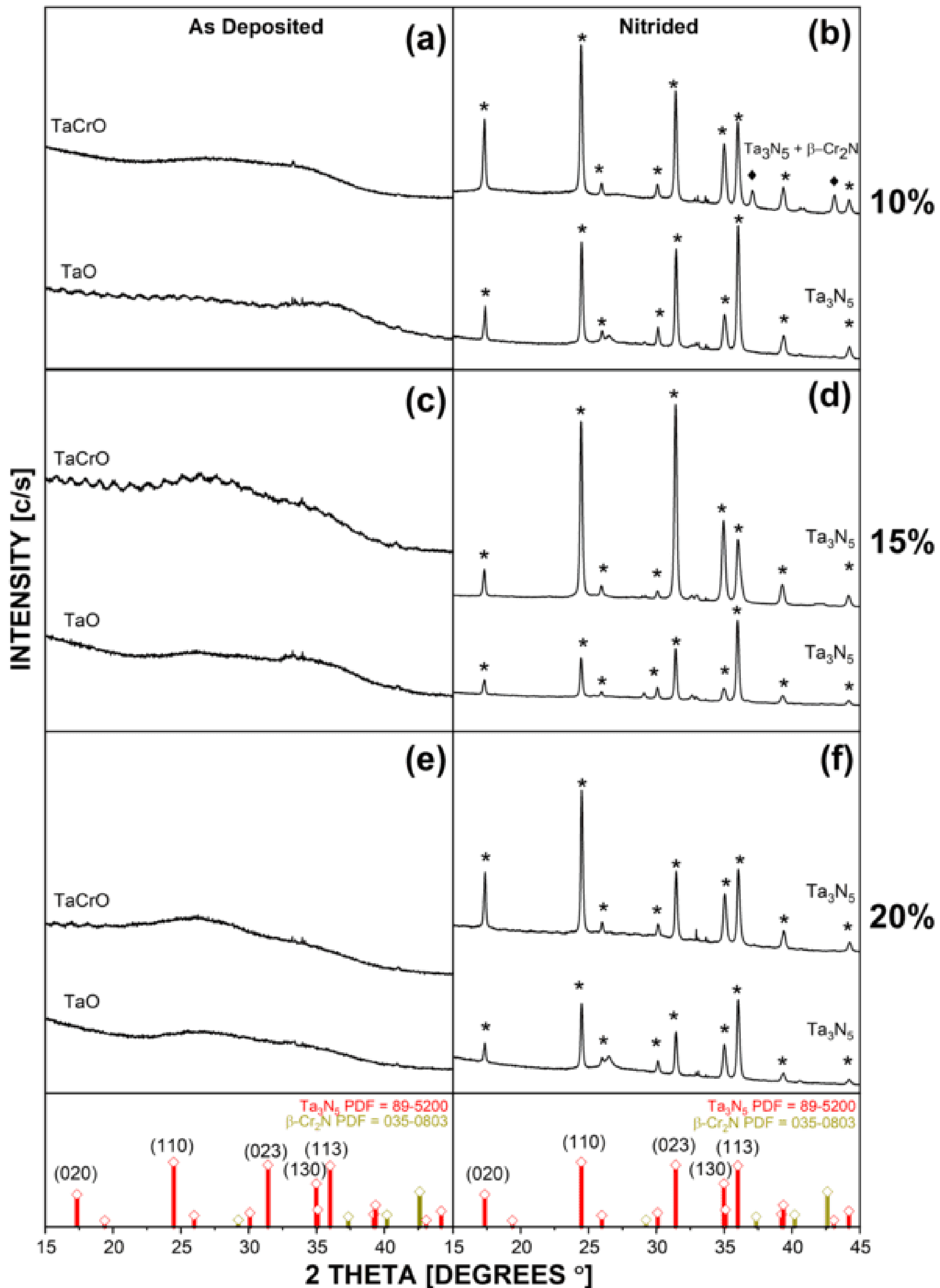

Figure 8-24. XRD diffractograms of TaCrO and TaO thin films where a) 10% pO_2 pre-nitridation, b) 10% pO_2 post-nitridation, c) 15% pO_2 pre-nitridation, d) 15% post-nitridation, e) 20% pO_2 pre-nitridation, f) 20% pO_2 post-nitridation. ♦ denotes the suspected chromium nitride peaks, and * denotes Ta_3N_5 peaks.

As summarised in **Table 8.8**, the composition of each film has been determined at both stages of processing; as-deposited and post ammonia annealing. EDS was used to determine the

presence of Cr and in this regard, Cr was only detected in one film. Specifically, the Cr-doped film deposited at $p(O_2)$ equal to 10%.

Table 8.8. EDS elemental data for TaCrO and TaO thin films prior to and post annealing in NH_3.

		As Deposited			Post Annealing			
Film Type	pO_2/Total Atmospheric Oxygen (Pa/%)	[Ta] (at. %)	[O] (at. %)	[Cr] (at. %)	[Ta] (at. %)	[O] (at. %)	[Cr] (at. %)	[N] (at. %)
TaCrO	0.06/10	29	52	19	23	6	13	68
TaO	0.06/10	30	70	<1	25	4	<1	71
TaCrO	0.09/15	28	72	<1	32	8	<1	60
TaO	0.09/15	22	78	<1	26	8	<1	66
TaCrO	0.13/20	22	78	<1	23	12	<1	65
TaO	0.13/20	18	81	<1	25	11	<1	64

With respect to the EDS determined concentration values for Ta, O and N, it is observed that all films contain a small to moderate level of oxygen contamination post-annealing. As expected, the concentration of O post-annealing is dramatically less than that detected in the as-deposited state and increases with the increased $p(O_2)$ used during deposition. While this level of oxygen contamination has not resulted in the formation of a second phase according to the obtained XRD results, it is nonetheless a contaminant and will impact upon the semiconducting properties of the films. Its residual presence my indicate that additional time is required for completing the nitriding process or that using less oxygen in the sputtering atmosphere (>10%) is needed. This residual presence of oxygen in Ta_3N_5 films is well reported when reacting Ta_3N_5 films from the oxide precursor (Fu et al. 2015; Rudolph, M. et al. 2016; Xie et al. 2016).

At this relatively low level of $p(O_2)$ the condition of the target during deposited is clearly non-poisoned (see Figure 8-18) whereas at higher $p(O_2)$ it can only be assumed that the Cr target was poisoned by oxygen and that the resulting sputter yield was particularly low. Formation of the common chromium oxide phase (Cr_2O_3) on the target surface, which reportedly possesses excellent wear resistant properties (Hones, Diserens & Lévy 1999) would slow chromium sputtering substantially. This phase is reported to result from high $p(O_2)$ sputtering environments (Contoux et al. 1997) such as those in the present investigation. This has

resulted in a Cr loading that is below the detection limit of EDS (~1 at. %). To confirm this result, SIMS has been used to detect Cr at much lower detection limits (ppm to ppb (Schwarz 2001)).

The resulting SIMS results are displayed in **Figure 8-25** and **Figure 8-26**, all elemental traces were normalised against tantalum as tantalum is the host lattice element expected to be stable between phase transitions. With respect to the detection of Cr in the as-deposited Cr-doped films, it is observed that Cr is clearly detected for the Cr-doped film deposited in p(O_2) equal to 10%, but for the two samples deposited at p(O_2) equal to 15% and 20%, Cr is detected at equivalent levels to that found in the undoped films i.e. background. The observed accumulation of Cr at the interface between the deposited films and their substrate confirms that Cr was indeed deposited during the deposition, albeit at exceptionally low levels.

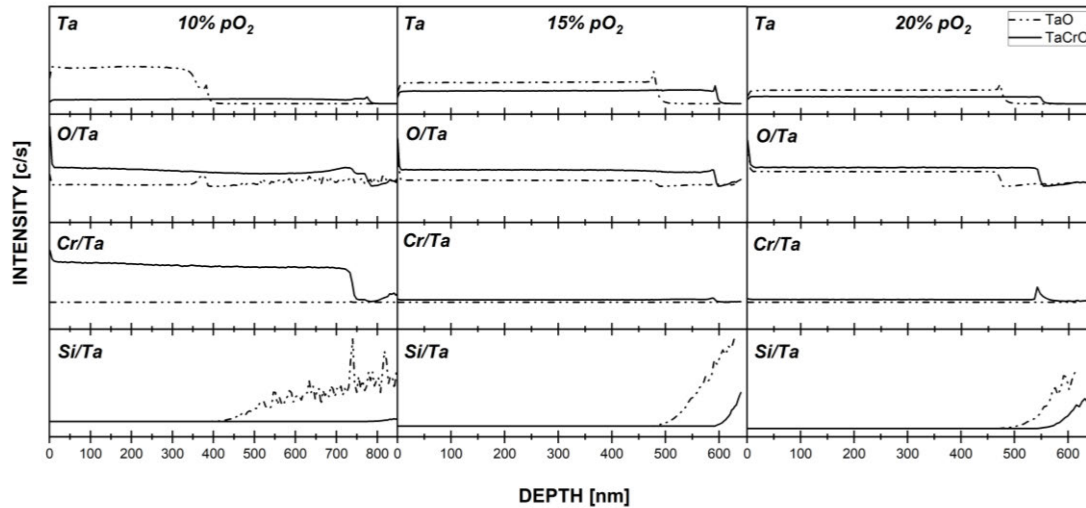

Figure 8-25. SIMS depth profiles of TaCrO and TaO thin films before annealing. Silicon is observed earlier in the TaO films as the TaCrO films are thicker.

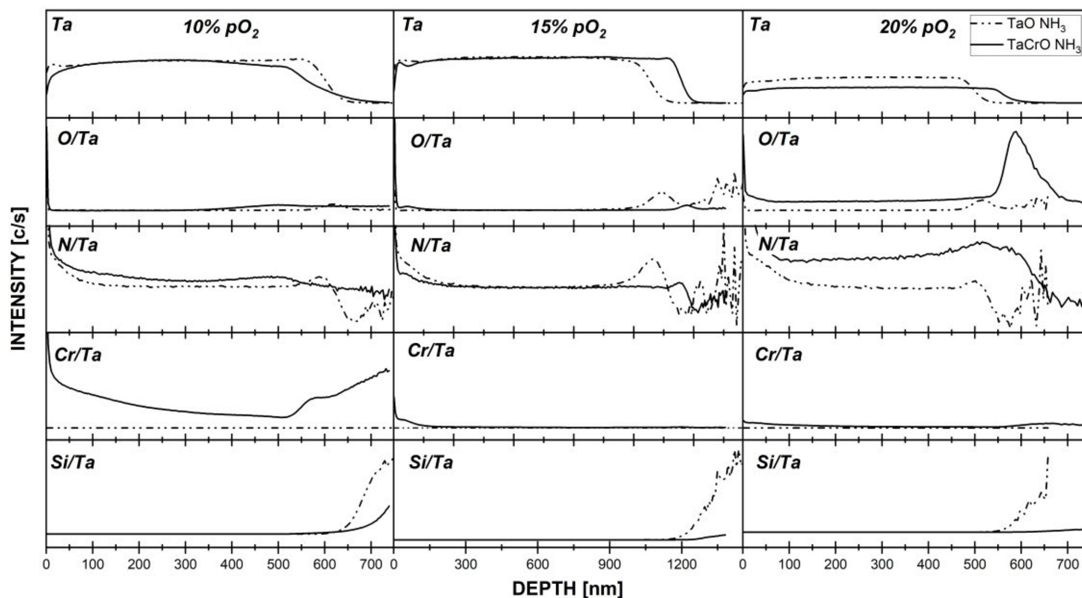

Figure 8-26. SIMS depth profiles of TaCrO and TaO thin films after annealing.

Referring to Figure 8-25, Cr is found to be especially mobile and has demonstrated a strong tendency to segregate towards the surface of the Cr-doped film deposited at $p(O_2)$ equal to 10% and only minimally accumulates at the film/substrate interface. In confirmation of the results displayed in Figure 8-25, at the higher $p(O_2)$ conditions Cr is observed at background levels only. With respect to the EDS determined concentration values for Ta, O and N, it is observed that all films contain a small to moderate level of oxygen contamination post-annealing.

As expected, the concentration of O post-annealing is dramatically less than that detected in the as-deposited state and increases with the increased $p(O_2)$ used during deposition. While

this level of oxygen contamination has not resulted in the formation of a second phase according to the obtained XRD results, it is nonetheless a contaminant and will impact upon the semiconducting properties of the films. Its residual presence may indicate that additional annealing time is required for completing the nitriding process or that using less oxygen in the sputtering atmosphere (<10%) is needed. This residual presence of oxygen in Ta_3N_5 films is nonetheless well reported and expected when reacting Ta_3N_5 films from an oxide precursor (Fu et al. 2015; Rudolph, M. et al. 2016; Xie et al. 2016).

Concerning the detection of Ta, O and N from SIMS (Figure 8-25 and Figure 8-26) there is general agreement between the EDS and SIMS results. Focusing on the post annealed analysis specifically, it is observed that detected O is at low levels which are likely to be reaching background detection limits based on the O yield obtained when analysis had continued into the underlying Si substrate. On the other hand, N yields are very clear and display a tendency to be higher in the immediate vicinity of the film surface which is expected. In all cases the detected level of N plateaus throughout the bulk of the film before occasionally displaying a minor tendency to accumulate at the film/substrate interface before dropping to background levels. Importantly, the relative stability of the N yield combined with the low O yield indicate that the films are single phase in confirmation of the obtained XRD results.

Due to the successful achievement of only one Cr-doped Ta_3N_5 film, the scope of investigation was broadened to explore the processing of Cr-doped Ta_3N_5 at $p(O_2)$ equal to 10%. Specifically, additional samples were deposited at a broader range of Cr target power to facilitate greater range in Cr –dopant loading. These additional target powers ranged from 10 W to 40 W, as summarised in **Table 8.9**, but were otherwise deposited in identical fashion to all other films in this section of the work. Combined surface and cross section images of 10W, 20W and 40W films are shown below in **Figure 8-27**.

Surface images shown in **Figure 8-27** display the cracking that results from the harsh conditions imposed by ammonolysis on the films, particularly in f) and g). As the nitridation reaction takes place at the film surface and oxygen is leeched from the film bulk in concert with ongoing densification, the result of this strain on the film is the porosity seen in surface images. The presence of chromium in the films appears to drive this porosity, which could imply the presence of a chromium phase migrating to or forming at grain boundaries.

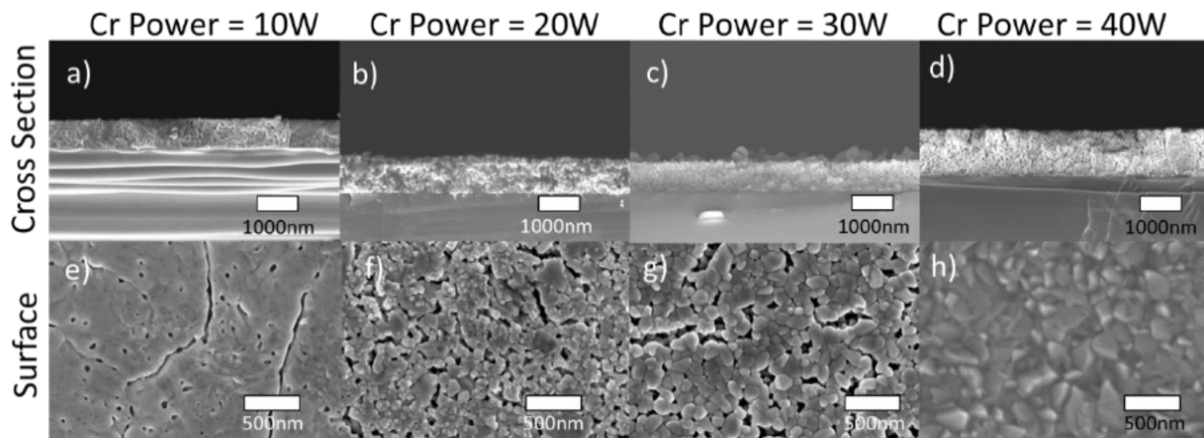

Figure 8-27. Surface and cross section SEM micrographs depicting the morphology of TaCrO films after thermal annealing in NH_3 gas mixture, where a) TaCrO, Cr power = 10W, b) TaCrO Cr power = 20W, c) TaCrO Cr power = 30W, d) TaCrO Cr power = 40W, e) TaCrO Cr power = 10W, f) TaCrO Cr power = 20W, g) TaCrO power = 30W, h) TaCrO power = 40W.

Consistent with the thickness trends observed in Table 8.7 but observed in greater detail, the thickness of these new films demonstrates the same densification behaviour. Specifically, the change in film thickness due to annealing in ammonia changes from a 38% expansion for 0 W of Cr target power, to 4% expansion at 10 W Cr target power, and through to 12% contraction when Cr target power reaches 40 W. The presence of Cr is facilitating the densification of the amorphous films upon crystallisation, however the precise mechanism behind this was not determined and would present an avenue for future research.

Table 8.9. Sputtering parameters and thicknesses of 10W, 20W, 25W, 30W and 40W chromium doped films and the 0W control, before and after nitridation.

Deposition Pressure (Pa)	pO_2/Total Atmospheric Oxygen (Pa/%)	Ta:Cr Power (W)	Thickness As Deposited (nm)	Thickness Post-NH_3 (nm)	Thickness Change Post-NH_3 (%)
0.66	0.06/10	100:0	471	650	27.5
0.66	0.06/10	100:10	754	785	2.6
0.66	0.06/10	100:20	843	817	-3.1
0.66	0.06/10	100:25	826	793	-4.1
0.66	0.06/10	100:30	804	738	-8.9
0.66	0.06/10	100:40	942	827	-13.9

The XRD results for these additional Cr-doped films are displayed in **Figure 8-28**. As seen, the as-deposited films remained amorphous in all cases, consistent with the previously observed results (Figure 8-24). What is observed in greater detail post-ammonia annealing

however is that 1) the same Ta_3N_5 phase is observed and 2) second phase peaks emerge when Cr target power is increased to 20 W and beyond.

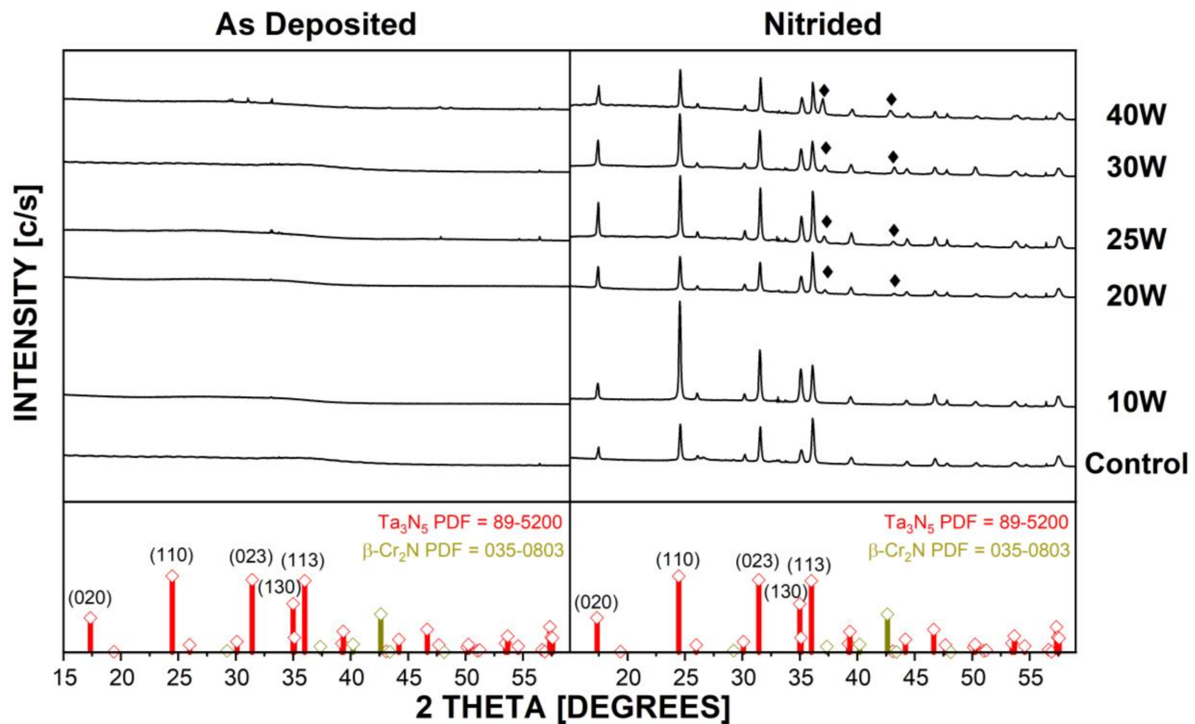

Figure 8-28. XRD diffractograms of TaCrO and TaO thin films deposited at 10W, 20W, 25W, 30W and 40W, before and after nitridation. The control film was an otherwise identical TaO film deposited without any power on the Cr target. The ♦ symbol denotes the chromium nitride phase.

These second phase peaks typically gain intensity as Cr target power is increased with strongly suggests that the Cr solubility limit has been reached and exceeded as earlier suggested.

To estimate the solubility limit, EDS has been used to assess the composition of each of these films. As summarised in **Table 8.10**, Cr is present at detectable limits from 20 W of Cr target power and above. Focusing on the [Cr] achieved after post-annealing in ammonia, it has been determined that Cr is present at levels ranging from 6 – 16 at. %. Referring to Table 8.10 and the first observation of second phase Cr_2N peaks it would appear that the solubility limit of Cr in Ta_3N_5 films is slightly below 6 at. %. However, it is also possible that some chromium is present in the form of an amorphous oxide located at grain boundaries. This is suggested by the observed residual O contamination that persists at the level of ~5 at.% for nearly all films. In this case, the Cr solubility may be substantially lower than 6 at. %. Verification of the grain boundary phase is required and will be undertaken in a future investigation.

Table 8.10. EDS elemental data for TaCrO and TaO thin films deposited with 0 to 40 W Cr target power, prior to and post annealing in NH_3.

		As Deposited			Post Annealing			
Film Type	**Ta:Cr Power (W)**	**[Ta] (at. %)**	**[O] (at. %)**	**[Cr] (at. %)**	**[Ta] (at. %)**	**[O] (at. %)**	**[Cr] (at. %)**	**[N] (at. %)**
TaO	100:0	30	70	<1	25	4	<1	71
TaCrO	100:10	39	61	<1	24	5	<1	71
TaCrO	100:20	23	75	2	27	0	6	67
TaCrO	100:25	19	75	6	22	6	8	64
TaCrO	100:30	29	52	19	20	6	12	62
TaCrO	100:40	23	56	21	19	5	16	60

SIMS was used once again to confirm the presence of Cr and its spatial uniformity within each ammonia annealed film (see **Figure 8-29**). Cr traces were normalised against the tantalum traces since tantalum was observed to have a consistent presence throughout the film. This is expected from a matrix element. From this it is evident that Cr is present in all Cr doped films and displays a strong tendency to accumulate within the near-surface region of each film, particularly in the films deposited with lower amounts of Cr. The Cr SIMS elemental traces, along with the drop in Cr presence after nitridation, indicate that Cr is migrating strongly to the surface region of the films during ammonolysis.

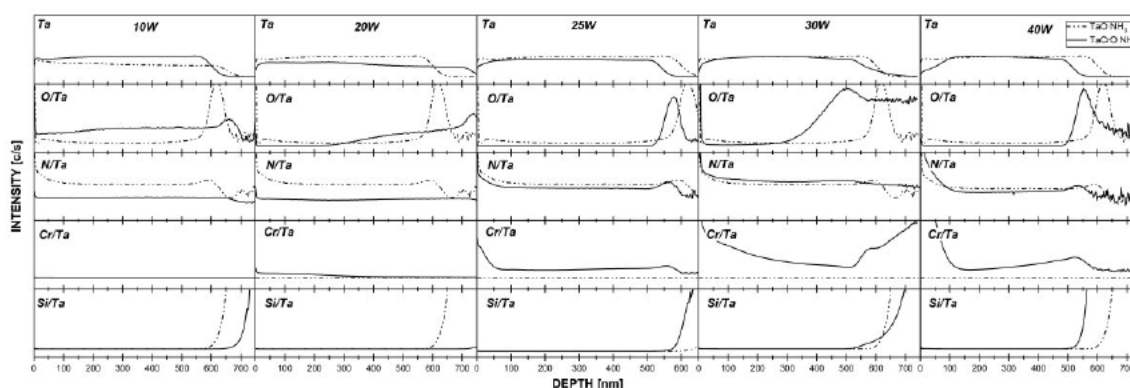

Figure 8-29. SIMS spectra of 10W, 20W, 25W, 30W and 40W TaCrO films after annealing, compared with TaO film deposited with 0W on the Cr target.

8.3.2.3 Reaction Kinetics of Ta_3N_5 Evolution in Chromium Doped Tantalum Oxide Films

As seen in Figure 8-24, the high temperature application of ammonia to the as-deposited films for 8 h was clearly sufficient to achieve highly crystalline Ta_3N_5 films. However, the EDS and SIMS results indicate that oxygen has remained as a contaminant in all cases. While this oxygen may be dissolved within the structure of the Ta_3N_5 phase, it is possible that some of this oxygen may be associated with the presence of Ta_2O_5 or TaON that can form during the annealing process.

Moreover, there are several different phases possessing various levels of nitrogen doping that can exist between the amorphous tantalum oxide starting phase and the final Ta_3N_5 product. These have been discussed in the literature with regards to the tantalum oxynitride phase specifically (Dabirian, Spijker & van de Krol 2012). It is generally cited that to generate TaON phases, the presence of oxygen in the annealing atmosphere is necessary (Chun et al. 2003). However, these phases are also expected to appear as intermediate phases between Ta_2O_5 and Ta_3N_5 as nitrogen progressively substitutes oxygen in the oxide host lattice.

In an attempt to identify additional structural trajectories present under the current experimental circumstances, two more annealing periods were performed at 2 h and 4 h (in addition to the 0 h as deposited films and the films subjected to 8 h of annealing). These extra treatments were carried out for films deposited at $p(O_2)$ equal to 10% and 20%, which were the lowest and highest of the initially selected $p(O_2)$ ranges. Using XRD, these films have been assessed for structure and combined with the existing diffraction results. These XRD results have been summarised in **Figure 8-30**.

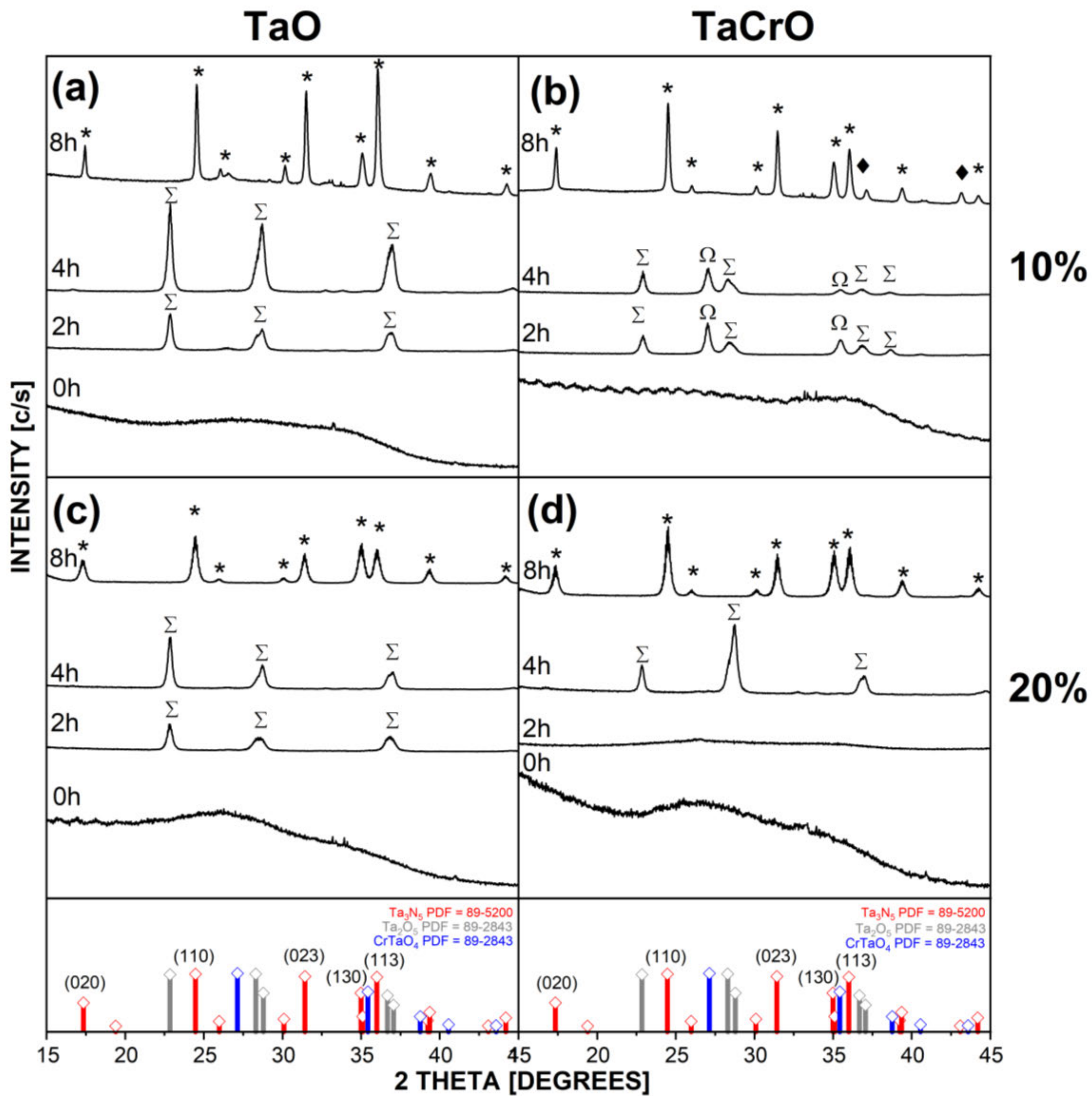

Figure 8-30. XRD diffractograms of TaCrO and TaO films annealed at 2h, 4h and 8h dwell times, where a) TaCrO 10% pO_2, b) TaO 10% pO_2, c) TaCrO 20% pO_2 and d) TaO 20% pO_2. ♦ denotes the silicon substrate peak, * denotes Ta_3N_5 peaks, Ω denotes $CrTaO_4$ peaks and Σ denotes Ta_2O_5 (tantite) peaks.

Considering the undoped circumstance first, at $p(O_2)$ equal to 10%, 2 and 4 h of annealing yields Ta_2O_5 as the transition phase between the as-deposited amorphous phase and the Ta_3N_5 final phase. This was also the case when the $p(O_2)$ during deposition was higher at 20%. These observations indicate that the crystallisation of amorphous tantalum oxide is relatively rapid and complete within 2 h, and any nitrogen rich phase is lower in concentration than can be detected.

Annealing for additional time (to 4 h) serves to achieve grain growth only as indicated by the increase in peak sharpness for both conditions of $p(O_2)$. Further annealing for a total of 8 h yields the Ta_3N_5 phase as was previously shown, without any evidence of residual Ta_2O_5 or TaON as an additional transition phase (despite oxygen impurities as previously elaborated on). This is supported by reports in the literature that the evolution of Ta_3N_5 from Ta_2O_5 is a

quick process that is thermodynamically expedient next to the conversion of Ta_2O_5 to just TaON (Dabirian, Spijker & van de Krol 2012).

Now considering the Cr doped films displayed in Figure 8-30 (b) and (d), a different phase progression is observed. In the $p(O_2)$ = 10% TaCrO film, an additional $CrTaO_4$ phase appears after 2 h, and remains at 4 h, before completing transformation to a chromium nitride phase at 8 h (β-Cr_2N).

Chromium at this concentration is not being incorporated into the dominant tantalum sub-lattice at any point of the nitridation reaction, instead forming as an exsolved phase early in the process. It may be the case that the chromium solubility limit is reached with the formation of the Ta_2O_5 phase prior to evolution of the Ta_3N_5 phase; this represents a novel future investigation topic as Cr doped Ta_2O_5 and Ta_3N_5 films are not thoroughly discussed in the current literature.

The doped films deposited at $p(O_2)$ = 20% proceed similarly to the undoped films, with exception of the 2 h doped film which showed no presence of crystalline structures. The very low Cr deposition would not be expected to produce a result this different to the control, as such further investigation would be necessary to resolve this.

SIMS analysis was performed once again to gather further information on the elemental composition of the films as a function of depth, given no significant amount of the nitrogen rich phases (i.e Ta_3N_5 or TaON) were observed in the XRD patterns at 2 h and 4 h, despite expectations. The SIMS spectra for the $p(O_2)$ = 10% films are displayed in **Figure 8-31**.

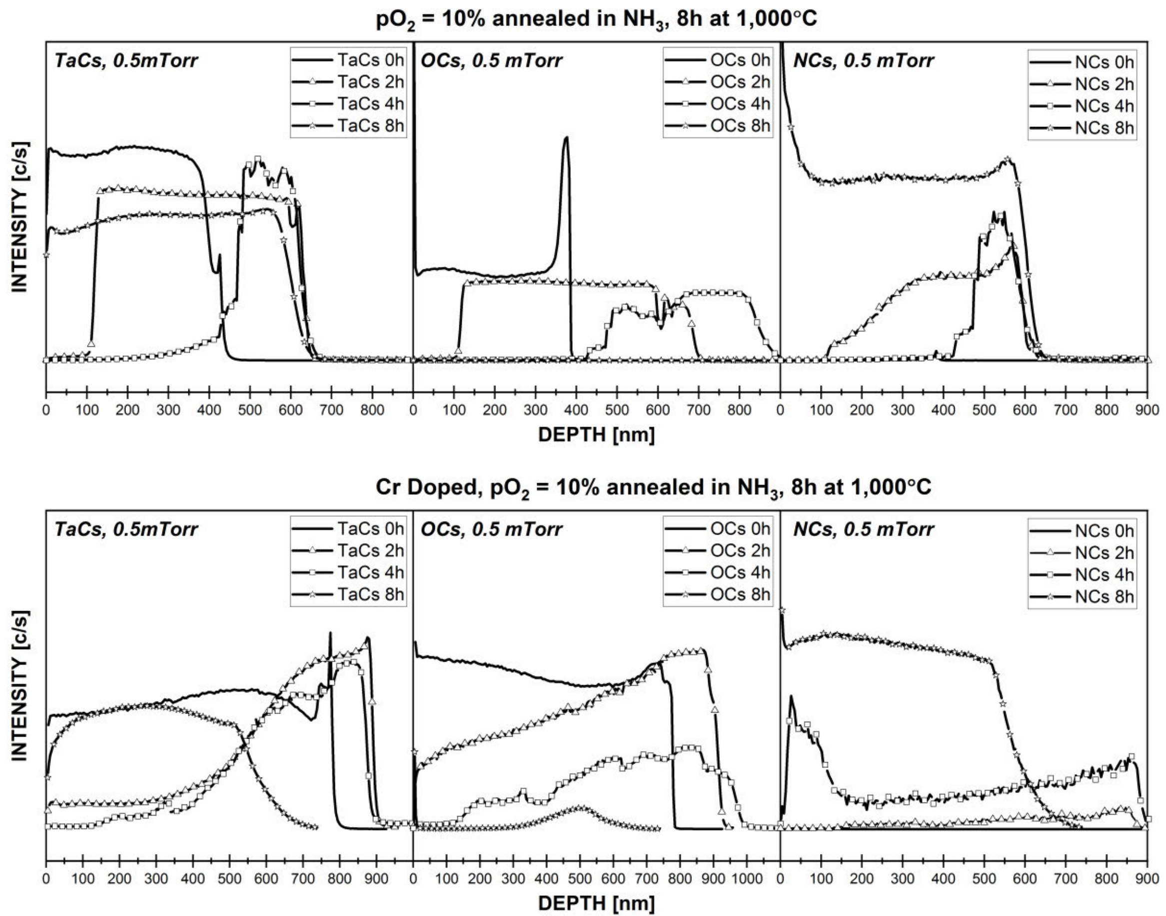

Figure 8-31. SIMS spectra of 2h, 4h and 8h thermally annealed TaO and TaCrO films deposited with 10% pO_2.

The Ta yield varies substantially as annealing time proceeds and reveals several interesting features. Firstly, the expansion in film thickness is observed to have taken place entirely within the first 2 h of annealing. Specifically, at $p(O_2)$ equal to 10 %, the film thickness at 0 h is ~400 nm whereas after 2 h the film thickness has increased to ~650 nm. At 4 h and 8 h, the film remains 600-650 nm thick. This observation indicates that the crystallisation to Ta_2O_5 is responsible for this thickness expansion which supports earlier results.

Secondly, the Ta yield at 2 h displays an abrupt step at ~100 nm below the film surface. At 4 h a step is observed at 400 – 450 nm. Presumably these steps are related to the transitionary interface between the amorphous precursor phase and crystalline Ta_2O_5. The relative absence of Ta signal observed prior to the step (phase closest to the surface) can be attributed to poor electrical conductivity and the resulting weak Ta signal. This is consistent with Ta_2O_5 (Balachandran & Eror 1982).

The O yield after 0 h displays a sharp peak immediately prior to an abrupt drop observed at a depth of close to 400 nm. This coincides with the drop in the Ta yield and reliably indicates the location of the film/substrate interface. The peak in O yield suggests that either the surface

of the Si substrate was oxidised or that O is otherwise accumulated at this interface. The O yield after 2 h and 4 h are also like the respective Ta yields and confirms the previously discussed phase interface, but in both cases the O yield appears to continue past the clear cut off in the Ta signal at ~650 nm. Specifically, after 2 h the O yield cuts off at ~ 700 nm, and at 4 h it continues until ~800 nm. This suggests that oxygen is accumulating in the film/interface region as the annealing proceeds. It is also seen that the O yield is low in the vicinity of the surface, as per the Ta yield. While a low O yield would ordinarily indicate a low O presence, in combination with a low Ta yield, it is more suggestive of poor electrical conductivity and low secondary ion yield as a consequence. This provides additional confirmation for the presence of a low conductivity oxide such as Ta_2O_5.

The N yields for $p(O_2)$ = 10% displays results that complement the observed O yields. Specifically, no N is detected in the precursor (0 h) film as expected, but after 2 h the N yield displays an onset at ~ 100 nm which closely matches that of the Ta and O yields. Similarly, after 4 h of annealing, the N yield displays an onset at ~400 nm consistent with the O and Ta yields yet again. After 8 h of annealing, the N yield is high and mostly stable until reaching the film/substrate interface where the N yield rapidly drops to background levels. What is notable is that in the vicinity of the film/substrate interface, the N yield closely resembles that of the Ta yield and not the O yield. Specifically, there is no evidence to suggest that nitrogen is accumulating at the film/substrate interface or diffusing into the Si substrate. Due to the low electrical conductivity of Ta_2O_5, it is unfortunately not possible to observe the N yield in the Ta_2O_5 region after 2 h or 4 h. However, what is observed is that the N yield becomes higher in the residual precursor phase as annealing time is increased.

When the $p(O_2)$ is increased to 20%, as seen in **Figure 8-32**, the same trends in Ta, O, and N yields are generally observed as per $p(O_2)$ equal to 10%. At 0 h, the precursor film appears to be almost 500 nm thick and, in this instance, displays a slight accumulation of Ta at the interface instead of O. This observation points towards some inconsistency in the deposition process, where potentially the initial deposition may have been Ta-rich until reaching steady state. The 2 h and 4 h annealed films are respectively ~600 nm and ~525 nm thick as indicated by the Ta and N yields. As observed previously, the O yields once again extend beyond these depths to suggest some diffusion into the Si substrate. After 8 h of annealing, the films appear to be ~550 nm thick according to the Ta and N yields, however the O yield confirms this observation by indicating a clear accumulation of oxygen at ~550 nm. Additionally, the O yield after 8 h of annealing also indicates that there is a reasonable degree of residual oxygen in this film.

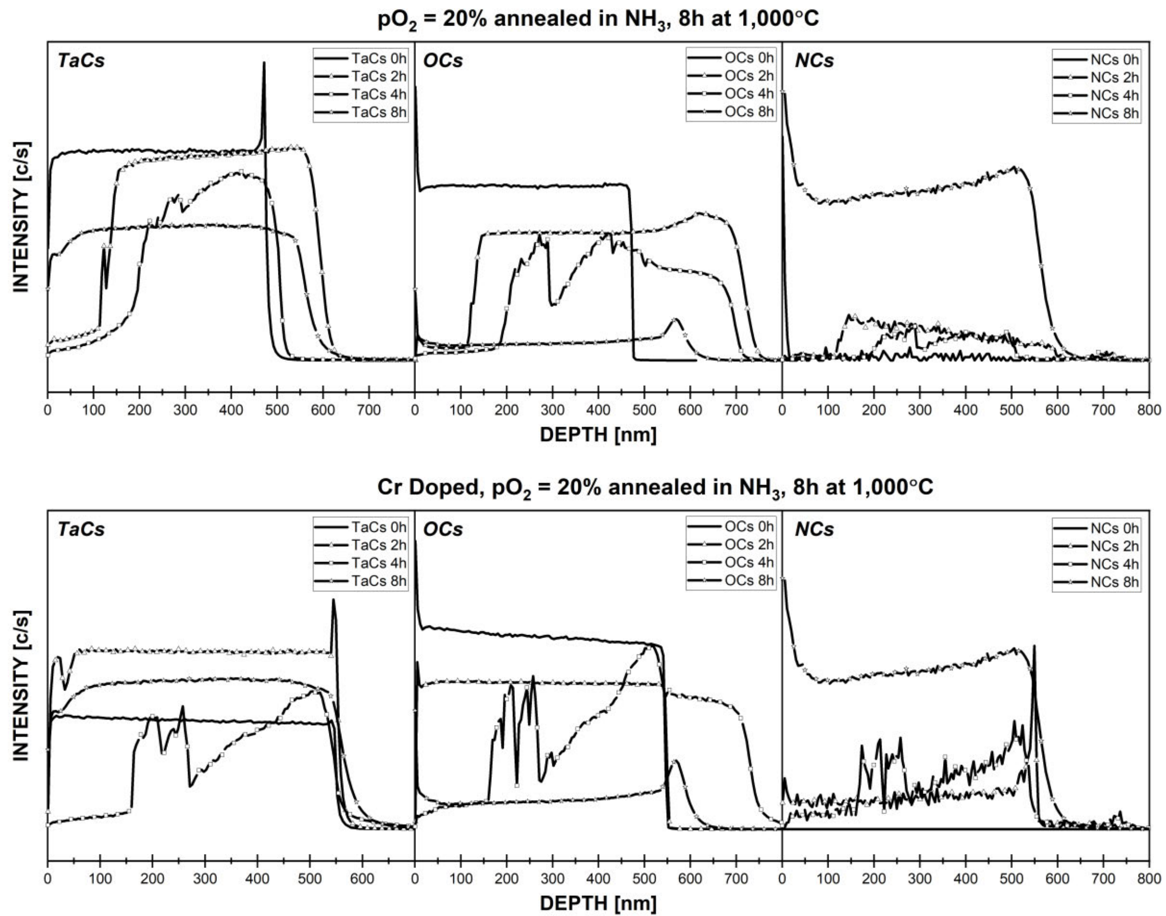

Figure 8-32. SIMS spectra of 2h, 4h and 8h thermally annealed TaO and TaCrO films deposited with 20% pO_2.

From this series of experiments, it is possible to conclude that the evolution of undoped Ta_3N_5 involves a somewhat slow process of crystallisation of the amorphous Ta-O precursor to Ta_2O_5 followed by relatively rapid transformation to Ta_3N_5. It was expected that the obtained SIMS results would identify the presence of mixed phases, but this has been limited to the evolution of Ta_2O_5 from the amorphous precursor phase. Additionally, it appears that the Ta_3N_5 phase evolves rapidly (potentially spontaneously) sometime after 4 h of ammonia annealing.

Unfortunately, neither the obtained XRD or SIMS results can provide much detail concerning the structural evolution of Ta_3N_5 from the TaO precursor. What has instead been identified is the tendency for oxygen to become accumulated at the interface between the film and substrate. As annealing time proceeds, the extent of oxygen accumulation appears to reach a maximum after 4 h but is reduced substantially once 8 h is reached. Clearly further investigations are required to better understand the dynamics of oxygen and nitrogen in the vicinity of the Si substrate.

8.3.2.4 UV-Vis Characterisation of Cr-Ta_3N_5

Previous subsections have described the processing and structural properties of the films, but until this point the optoelectric properties had not been investigated or discussed. It is pertinent to determine the light absorption characteristics of the films in question given the goal of improving the solar water splitting performance of Ta_3N_5. To this end UV-Vis setup with a Diffuse Reflectance Accessory (DRA) was utilised to determine the absorption edge in the films and verify the expected light absorption, prior to mounting the films as electrodes and investigating electrochemical properties.

A Ta_3N_5 standard film of ~800nm thickness was used as the standard of comparison for Cr-Ta_3N_5 films. This film was synthesized with the same methods as the doped films, by first depositing a tantalum oxide film before annealing in NH_3. The standard film exhibited a red lustre after annealing, indicative of the Ta_3N_5 phase absorbing visible light up to the red end of the spectrum (~650nm). In contrast, Cr-Ta_3N_5 films possessed a dark silver lustre with no distinguishable colour. The UV Vis spectra of the Ta_3N_5 and doped films can be seen below in **Figure 8-33**.

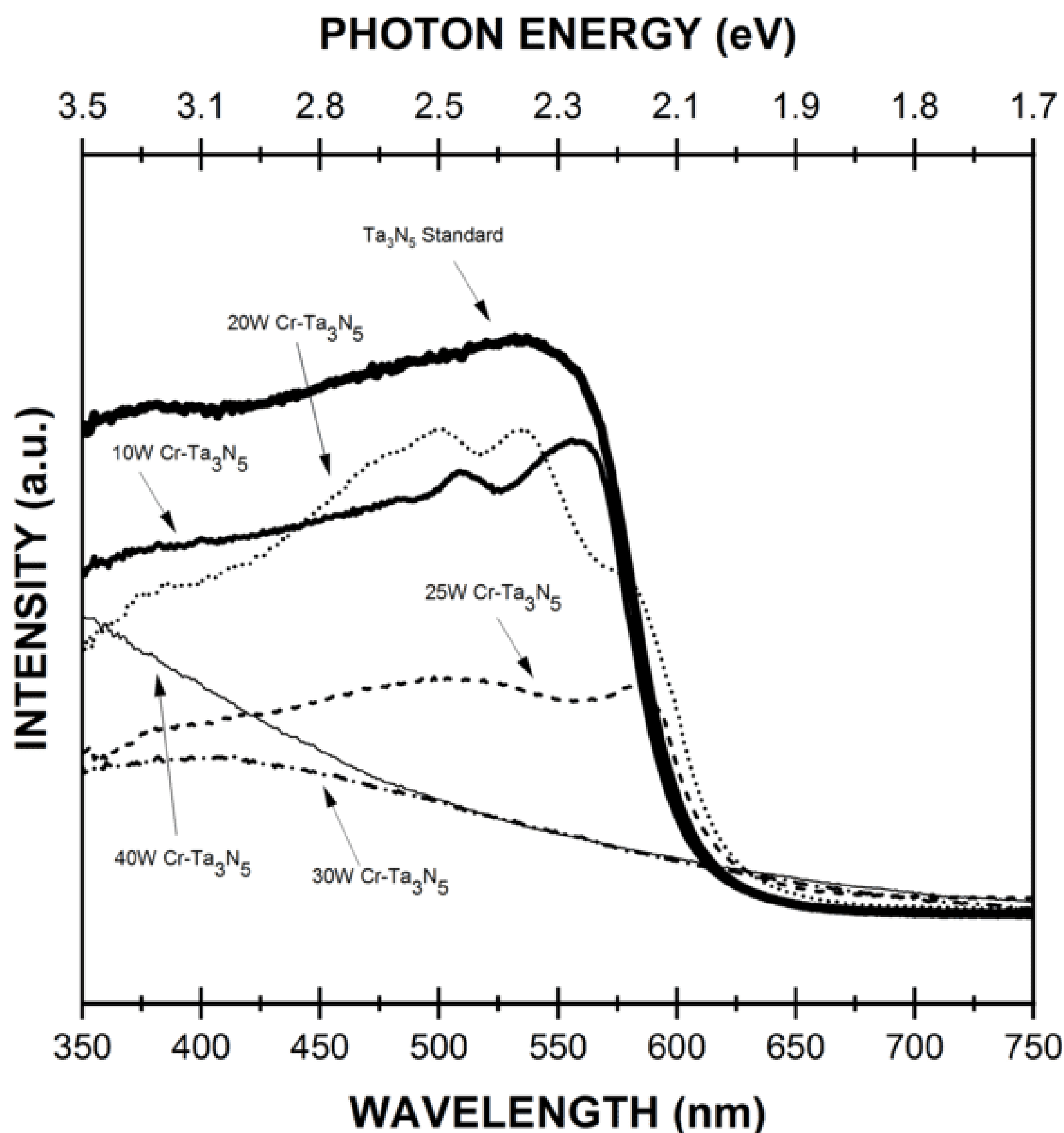

Figure 8-33. UV-Vis diffuse reflectance spectra of Ta_3N_5 standard film contrasted with 10W, 20W, 25W, 30W and 40W chromium doped films, with wavelength (nm) and photon energy (eV) included. Arbitrary units are used for absorbance intensity.

As can be seen in Figure 8-33, the Ta_3N_5 standard showed an absorption edge at approximately 550nm (or a 2.1eV band gap), which is corroborated by literature reports (Chun et al. 2003; Fang et al. 2001; Feng et al. 2010; Hitoki et al. 2002; Ishikawa et al. 2004). The band gap for Ta_3N_5 is largely due to the Ta 5d and N 2p orbitals, which comprise the majority of the valence and conduction bands of the material (Fang et al. 2001). As some chromium is introduced to the film (10W on Cr target), the absorption intensity decreases relative to the Ta_3N_5 standard despite the thickness of the 10W Cr film being greater (as per Table 8.9). This trend continues with the 20W and 25W Cr films, until no absorption peak can be seen in the mostly strongly doped 30W and 40W films. Both the 10W and 20W Cr films show an earlier onset of the main absorption edge. These films also possessed the chromium nitride

secondary phase noted in the previously discussed XRD results (Figure 8-24 and Figure 8-28). Chromium nitride is a metal nitride with a band gap of 70meV and receives interest for its hardness and electrical conductivity properties (Constantin et al. 2004), and may contribute negatively to the optoelectric properties of Ta_3N_5. This can be seen in Figure 8-33, with a slight reduction in the band gap for the 10W Cr doped film, until Cr doping is increased to 20W and higher.

In conclusion, chromium doped Ta_3N_5 films were successfully synthesized after defining a multi-step synthetic process. The precursor tantalum oxide films (doped and undoped) were deposited and characterised after an oxygen partial pressure range was selected using a partial hysteresis experiment. These films were successfully converted to Ta_3N_5 using ammonia annealing and subsequently characterised.

The amount of chromium in the films was effectively controlled using target power during the sputter deposition of the precursor films. XRD analysis of films with low amounts of chromium showed the expected Ta_3N_5 with oxygen impurities, while films with higher amounts of chromium exhibited an exsolved phase that was concluded to be a chromium nitride, which suppressed the band gap of the highly doped films. While EDS analysis quantified a chromium presence in films deposited at 20 W and above, only SIMS analysis detected the chromium presence in all films (sans quantification). This contributed to the identification of a basic trajectory for the evolution of Cr-Ta_3N_5. It was observed that the Ta_3N_5 phase evolved rapidly between 4 and 8 hours of annealing.

Assuming chromium is adopted into the Ta_3N_5 structure as per Equation 24, the chromium solubility limit in Ta_3N_5 was concluded to be less than 6 at. %. There is potential that the limit of Cr solubility in Ta_3N_5 is in fact pre-determined by the Cr limit in Ta_2O_5 due to the specific approach applied in this investigation. This introduces the possibility of a practical limitation for achieving high Cr dopant levels in Cr-Ta_3N_5. It is also noted that chromium may exist in grain boundaries as a stable amorphous oxide phase which nitrides to the Cr_2N second phase observed when Cr exceeds 6 at. %. Resolving the structure and composition of the grain boundary phase will be important for understanding the potential for Ta_3N_5 to be highly doped with Cr but is outside the scope of the present investigation.

8.3.3 Aluminium Doped Ta_3N_5 Thin Films

The second dopant evaluated was aluminium, which will be covered in this subsection. The process of evaluating aluminium will reflect the steps taken with chromium. This means opening with an investigation into the poisoning of behaviour of tantalum and aluminium targets under oxygen, before moving on to evaluating the doped films against the undoped

controls, and finally finishing with another investigation of the kinetics involved when annealing aluminium doped Ta_2O_5 films benchmarked against the Ta_2O_5 controls.

8.3.3.1 Hysteresis of Ta and Al Targets in Argon

Prior to depositing experimental TaAlO films, a brief investigation was first performed to determine the oxygen partial pressure ($p(O_2)$) range in which aluminium and tantalum deposition is appreciable. This was necessary as an indicative test of how much oxygen would be required for the aluminium target to reach a poisoned state, as a result reducing its sputter yield and subsequent presence in the films. The discharge voltage (DV) exhibited by the power supply corresponds broadly to such poisoning taking place; as oxygen presence is increased, the DV will shift in a manner specific to the element being sputtered. When this value changes sharply and plateaus, this generally indicates poisoning of the target material. It was desirable to explore the gap between a metallic sputtering regime and a poisoned one in the effort to control the aluminium yield.

For the hysteresis, a power of 100 W was applied to the tantalum target and 30W to the aluminium target, as tantalum sputters at a slower rate relative to aluminium. An atmosphere composed of argon and oxygen was used, with a total deposition pressure of 0.66 Pa. The hysteresis was performed over 45 minutes, beginning with a $p(O_2)$ of 0 Pa which was graduated in increments to a pO_2 of 0.26 Pa, before returning to a value of 0 Pa. Every 5 minutes, the values of the argon and oxygen flow rates were adjusted in such a way to affect an increase of 0.03 Pa in the pO_2 value. Discharge voltage (DV) readings were recorded every 30 seconds, with 3 values taken for every 5 period at which a $p(O_2)$ value was held; one 30 seconds after the change in value, one halfway through the given period, and one prior to changing the value to the next in series. The results of this hysteresis are shown below in **Figure 8-34**.

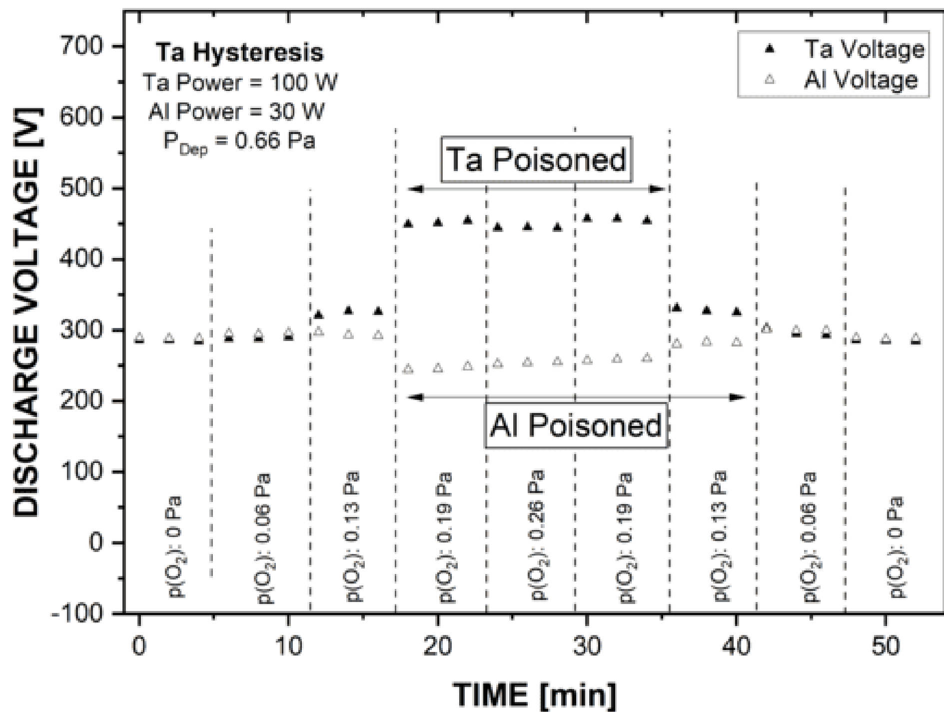

Figure 8-34. Hysteresis of Ta and Al targets in an Ar/O_2 atmosphere. O_2 gas flow rate is adjusted over time to reflect the displayed p(O_2) values, up to a peak p(O_2) value before being ramped down again.

Both aluminium and tantalum showed consistent DV values at the beginning of the hysteresis, showing no evidence of etching from previous runs. This presumed metallic baseline at ~290 V is held until the p(O_2) is stepped up to 0.13 Pa (20% of total atmosphere). After this pO_2 value, aluminium reaches a poisoned state rapidly, and remains poisoned until the p(O_2) is once again reduced. A metallic state on the target appears to be reacquired when the p(O_2) is cycled back to 0.13 Pa.

In comparison, the tantalum target reaches a poisoned state in a similar manner as the p(O_2) increases, increasing in a poisoned state before eventually stabilising around 0.19 Pa pO_2 (~30% of total atmosphere). The tantalum target DV also returns to its baseline quickly after the p(O_2) is reduced from 0.19 Pa through 0.06 Pa. As both targets began to transition from unpoisoned to poisoned and back to unpoisoned over this p(O_2) range, values between 0.06 Pa and 0.19 Pa were selected for investigation in the subsequent depositions of both undoped and doped films.

Oxygen was first investigated as a variable for controlling the aluminium yield over power due to the target's sensitivity to poisoning when sputtering at input power values below 30W. This is especially true in the case of a soft, easily oxidized metal like aluminium.

8.3.3.2 Deposition and Nitridation of Tantalum Aluminium Oxide

With the preferred oxygen range selected, three regimes within this range were then chosen for sputtering films. These corresponded to an atmospheric oxygen presence of $p(O_2)$ = 10% (0.06 Pa), 15% (0.09 Pa) and 20% (0.13 Pa), with the remaining gas presence comprised of argon. Films were deposited at each of these $p(O_2)$ values with power on both Ta and Al targets, and power on just the Ta target as a control. A constant substrate temperature of 573 K was observed across all films. A 0.66 Pa total deposition pressure was carried on from the poisoning investigation.

The detailed sputtering parameters for these films can be seen below in **Table 8.11**.

Table 8.11. Sputtering parameters and thicknesses of Al doped and undoped tantalum oxide thin films, before and after NH_3 annealing.

	Deposition Pressure (Pa)	$p(O_2)$/Total Atmospheric Oxygen (Pa/%)	Ta:Al Power (W)	Thickness As Deposited (nm)	Thickness Post-NH_3 (nm)	Thickness Change Post-NH_3 (%)
UNDOPED	0.66	0.06/10	100:0	471	650	38.0
	0.66	0.09/15	100:0	426	580	36.1
	0.66	0.13/20	100:0	402	459	14.1
DOPED	0.66	0.06/10	100:30	580	718	23.7
	0.66	0.09/15	100:30	493	633	32.3
	0.66	0.13/20	100:30	361	507	40.4

Referring to the thickness values of the doped and undoped films prior to annealing, thicknesses were observed to linearly decrease as $p(O_2)$ was increased, which is expected with the increased poisoning taking place on the targets (per Figure 8-34). After nitridation, the films all increased in thickness, which was unexpected based upon similar experiments undertaken recently for Cr-doped Ta_3N_5 8.3.2). In that case, nitridation resulted in a reduction in thickness and was simply attributed to a densification process.

The present result for Al-doping could instead indicate an increase in film porosity from the nitrogen-oxygen substitution reaction. The as-deposited doped films were thicker than the undoped films at the $p(O_2)$ values of 10% and 15%, but not 20%. This could be attributed to the inclusion of aluminium in the case of the lower $p(O_2)$ values, but for the 20% film, it may be the case that the aluminium target excessively poisoned from the high $p(O_2)$ content, resulting in a film with a similar thickness to the undoped counterpart.

In contrast to previous work evaluating the role of chromium as a dopant, aluminium doped films became thicker instead of losing thickness after the nitridation process. Determining the reason for this would require a thorough evaluation of the nitridation kinetics in the Cr and Al doped films, which is beyond the scope of the present work. However, $CrTaO_4$ and Cr_xN phases were both noted in previous works and could account for the difference in thickness after nitridation between the two dopants. After nitridation, films were snapped and imaged using SEM instrumentation to observe the thickness and morphology. The cross section images from this can be seen below in **Figure 8-35** and **Figure 8-36**.

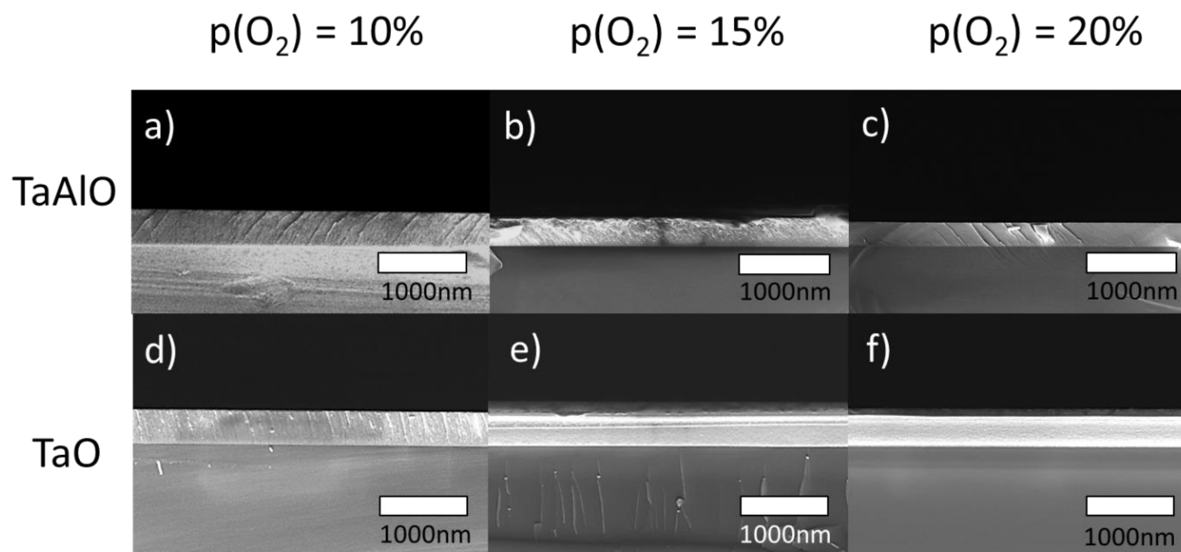

Figure 8-35. Cross section SEM micrographs depicting the morphology of TaO and TaAlO films before thermal annealing in NH_3 gas mixture. Where a) TaAlO 10% pO_2, b) TaAlO 15% pO_2, c) TaAlO 20% pO_2, d) TaO 10% pO_2, e) TaO 15% pO_2, f) TaO 20% pO_2

In terms of microstructure, all films prior to annealing exhibited generally uniform, amorphous looking microstructures. The film cross sections post annealing, depicted in Figure 8-36, show a clear increase in thickness, with microstructures showing clear crystallinity. Also observed is a substantial degree of porosity, which may account for the increase in thicknesses seen after annealing as suggested above. The increased thickness of the nitride films relative to the as deposited films may be a result of gas expansion as oxygen is substituted with nitrogen via the ammonolysis reaction.

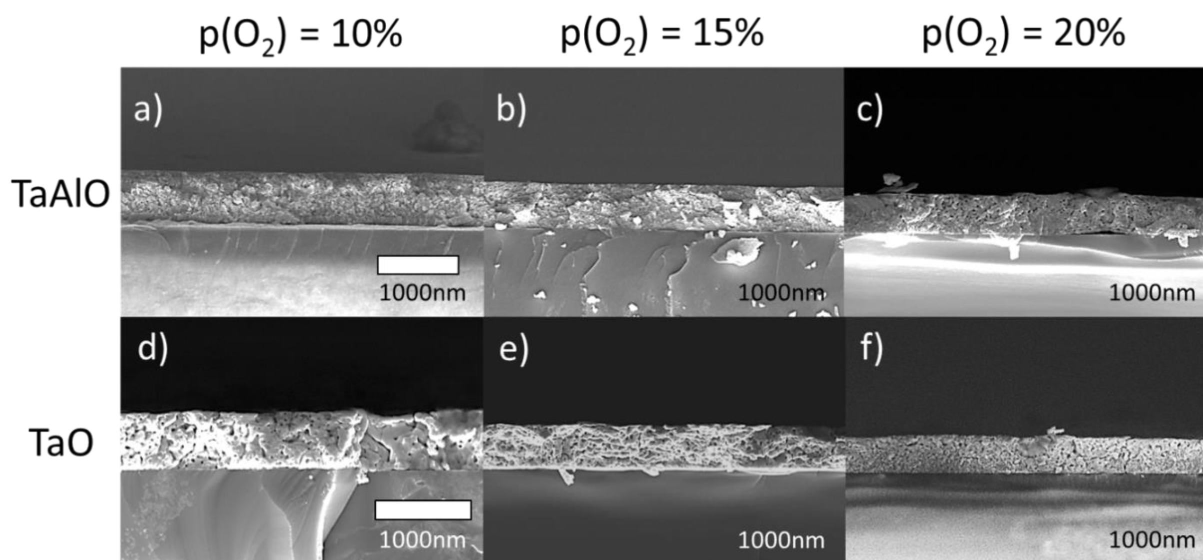

Figure 8-36. Cross section SEM micrographs depicting the morphology of TaO and TaAlO films after thermal annealing in NH_3 gas mixture, where a) TaAlO 10% pO_2, b) TaAlO 15% pO_2, c) TaAlO 20% pO_2, d) TaO 10% pO_2, e) TaO 15% pO_2 and f) TaO 20% pO_2.

Surface images of the films can be seen in **Figure 8-37** and **Figure 8-38**. There were few observable differences in the surface features of the as-deposited films. The aluminium doped films, especially the $p(O_2)$ = 15% film, appeared rougher than the corresponding undoped films. As seen in Figure 8-37, grain sizes varied in the range of 30nm to 50nm for the Al-doped films and 10nm to 30nm for the undoped films. Whether this was due to the aluminium content is unclear, however the dissimilarity to the $p(O_2)$ = 10% film, which was expected to possess more aluminium on account of less oxygen poisoning, is evidence against this. The surface morphology of the films after annealing is shown in Figure 8-38.

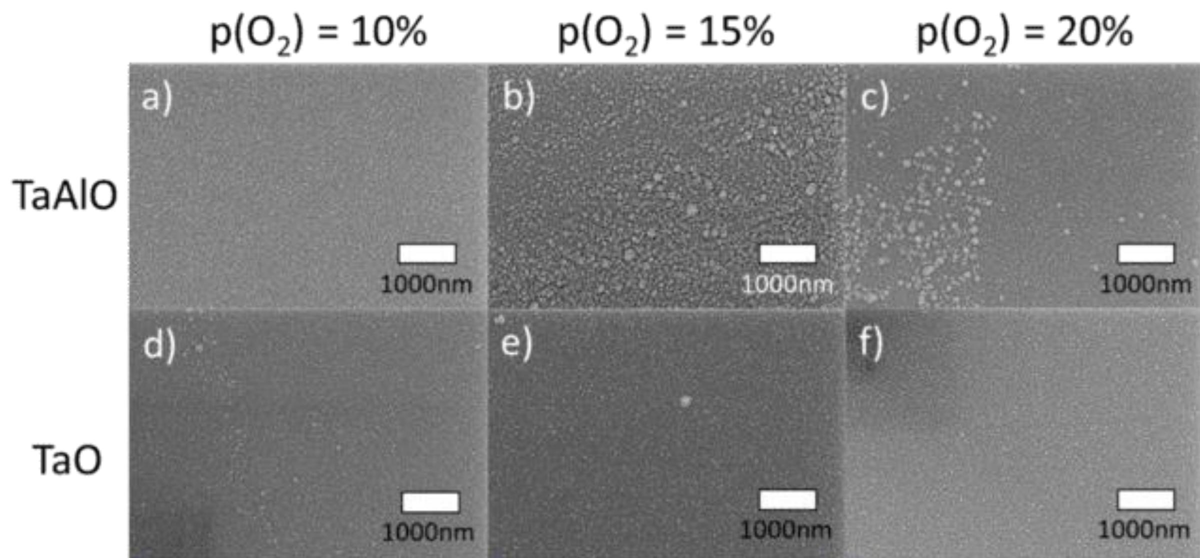

Figure 8-37. Surface SEM micrographs depicting the morphology of TaO and TaAlO films before thermal annealing in NH_3 gas mixture, where a) TaAlO 10% pO_2, b) TaAlO 15% pO_2, c) TaAlO 20% pO_2, d) TaO 10% pO_2, e) TaO 15% pO_2, f) TaO 20% pO_2.

After annealing, the surface morphology of the films changed drastically, as seen in Figure 8-38. Referring to the undoped control films (Figure 8-38 d-f), substantial and consistent grain growth is observed across all 3 films. Looking at the doped films, the two films deposited under $p(O_2)$ = 10% and 20% exhibited significant grain growth similar to that of the undoped films, however the $p(O_2)$ = 15% film showed much smaller grains, closer to those seen in the as-deposited films. It is unlikely that this was due to aluminium content given the $p(O_2)$ = 10% doped film was more likely to possess significant aluminium. Finally, a clear difference in porosity and grain boundary sizes can be seen between the doped and undoped films, with the undoped films possessing expressed grain features and porosity in the surface features.

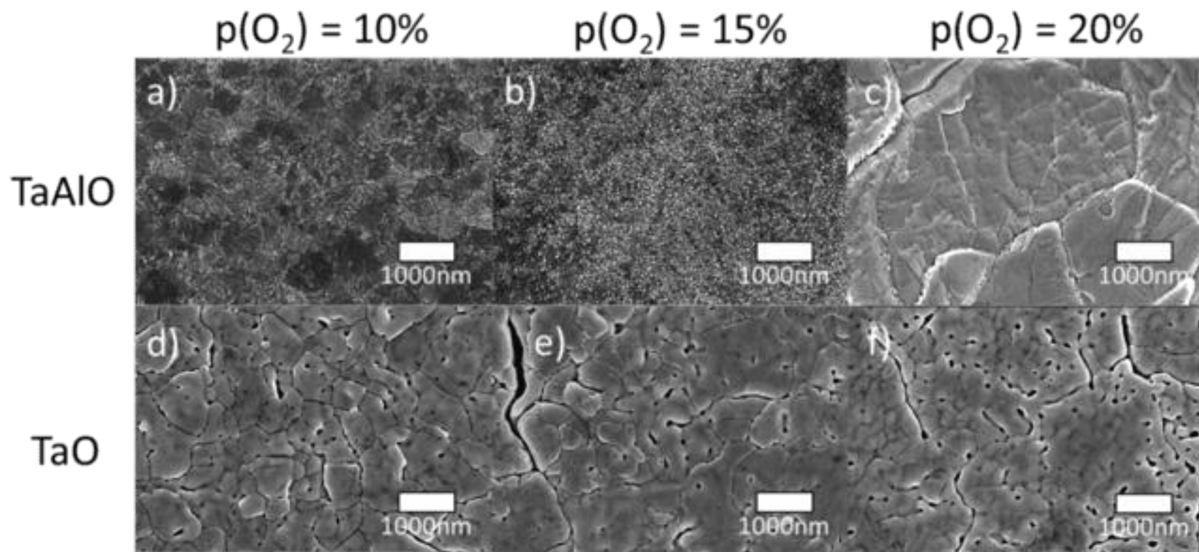

Figure 8-38. Surface SEM micrographs depicting the morphology of TaO and TaAlO films after thermal annealing in NH_3 gas mixture, where a) TaAlO 10% pO_2, b) TaAlO 15% pO_2, c) TaAlO 20% pO_2, d) TaO 10% pO_2, e) TaO 15% pO_2, and f) TaO 20% pO_2.

Phase analysis was performed via XRD, the patterns for which can be seen in **Figure 8-39** below. As-deposited films all exhibited patterns indicating the presence of amorphous structures, verifying the conclusions drawn from SEM images.

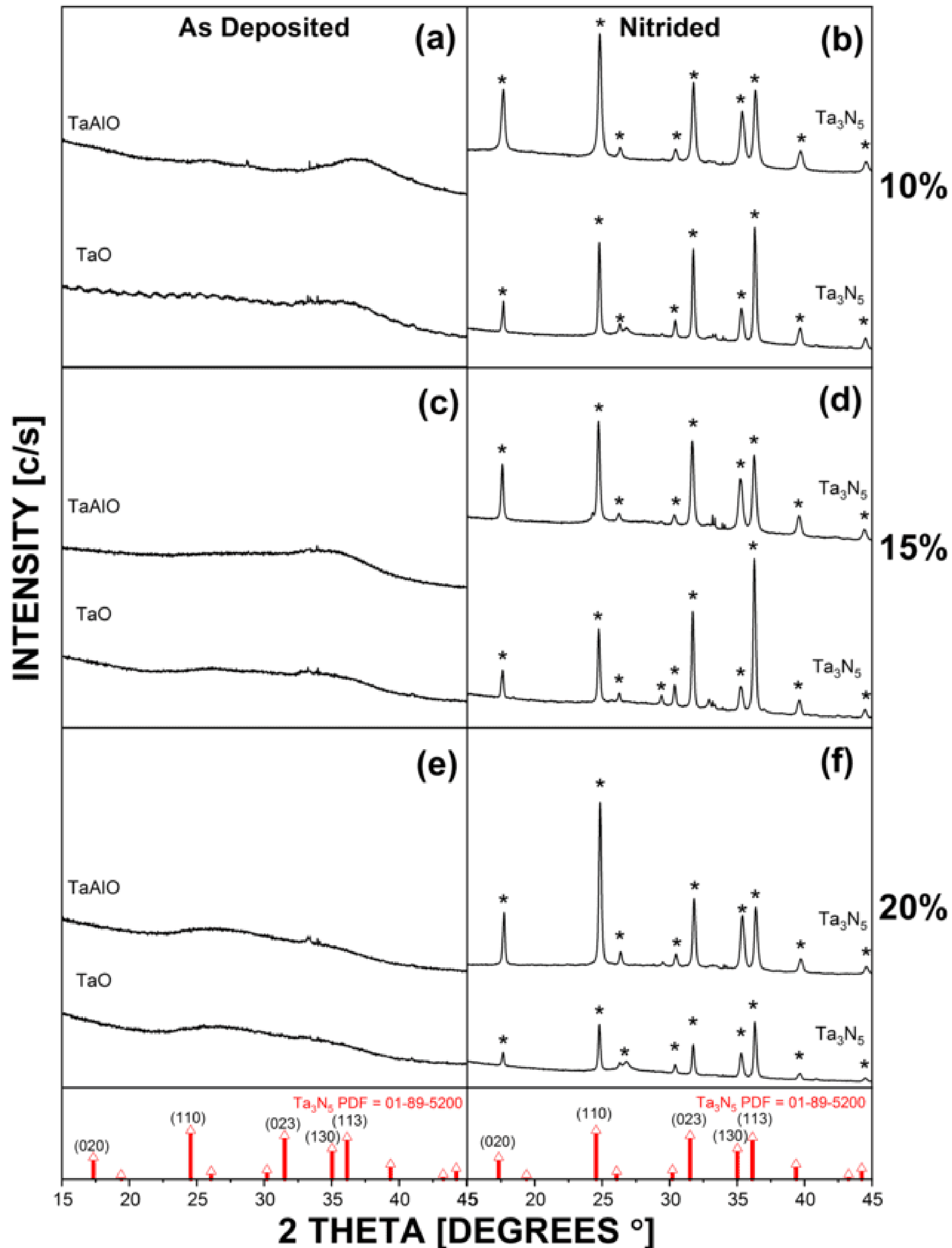

Figure 8-39. XRD diffractograms of TaAlO and TaO thin films where a) 10% p(O_2) pre-nitridation, b) 10% p(O_2) post-nitridation, c) 15% p(O_2) pre-nitridation, d) 15% p(O_2) post-nitridation, e) 20% p(O_2) pre-nitridation, f) 20% p(O_2) post-nitridation. Where: * denotes Ta_3N_5 peaks.

After annealing, all films exhibited a dominant orthorhombic Ta_3N_5 phase (PDF 01-89-5200, monoclinic, space group C2/m) with no detectable TaON or Ta_2O_5 second phases observed. Additionally, no exsolved aluminium oxide or nitride phases could be seen, nor were there any significant unidentified peaks. Furthermore, all XRD patterns were highly resolved and displayed clear peaks which is indicative of high crystallinity. When contrasted with XRD

results in Figure 8-30, the lack of a secondary dopant phase is notable given the formation of a CrN phase in the work with Cr-Ta_3N_5 films. No aluminium nitride phase is seen at any $p(O_2)$ value.

Referring to graphs in Figure 8-39(b) and (d), intense Ta_3N_5 peaks are observed in the aluminium doped films, relative to the undoped nitride films, implying a change in crystallographic orientation. The peak located at ~36°, indicative of the (113) plane, varies significantly in intensity between the undoped films, especially as $p(O_2)$ is increased to 20%, however consistent peak intensities were observed across other planes in the doped films. Preferred orientations may be a result of varying crystallite distributions produced by higher $p(O_2)$ but is otherwise not of interest to this work.

To provide confirmation that aluminium was incorporated into the films at all, EDS analysis was utilised. The results of this analysis can be seen below in **Table 8.12**.

Table 8.12. EDS elemental data for TaAlO and TaO thin films prior to and post annealing in NH_3.

		As Deposited			Post Annealing			
	$p(O_2)$/Total Atmospheric Oxygen (Pa/%)	[Ta] (at. %)	[O] (at. %)	[Al] (at. %)	[Ta] (at. %)	[O] (at. %)	[Al] (at. %)	[N] (at. %)
UNDOPED	0.06/10	30	70	<1	25	4	<1	71
UNDOPED	0.09/15	22	78	<1	26	8	<1	66
UNDOPED	0.13/20	18	81	<1	25	5	<1	70
DOPED	0.06/10	27	57	16	36	7	11	46
DOPED	0.09/15	24	76	<1	30	3	<1	67
DOPED	0.13/20	20	80	<1	30	5	<1	65

As seen in Table 8.12 undoped films showed the presence of tantalum and oxygen prior to annealing, an aluminium presence was detected in the $p(O_2)$ = 10% doped film, before and after annealing. There was a drop in aluminium presence after annealing, which was also observed with chromium (section 8.3.2). Aluminium content at first appears to displace oxygen in the as-deposited film, but after annealing correlated with higher tantalum and lower oxygen presence relative to reduced nitrogen at. %. Aluminium values <1 at. % are presented as undetected levels of aluminium utilising the EDS method for this investigation.

This perhaps indicates a tantalum-aluminium-oxide or Al_2O_3 presence after annealing, in addition to a Ta_3N_5 phase. An oxygen presence was consistent across all films, confirming the presence of inherent oxygen impurities in the Ta_3N_5 structure as shown in Figure 8-39, a phenomenon which is also reported in the literature (Rudolph, M. et al. 2016; Rudolph, M et al. 2019; Xie et al. 2016).

It was possible that aluminium content was below the detection limits of or within the margin of error of EDS analysis. SIMS analysis was therefore performed to assist in resolving this question, and to provide information on the diffusion of the aluminium through the films. The SIMS depth profile for the as-deposited films and annealed films can be seen below in **Figure 8-40** and **Figure 8-41**, respectively.

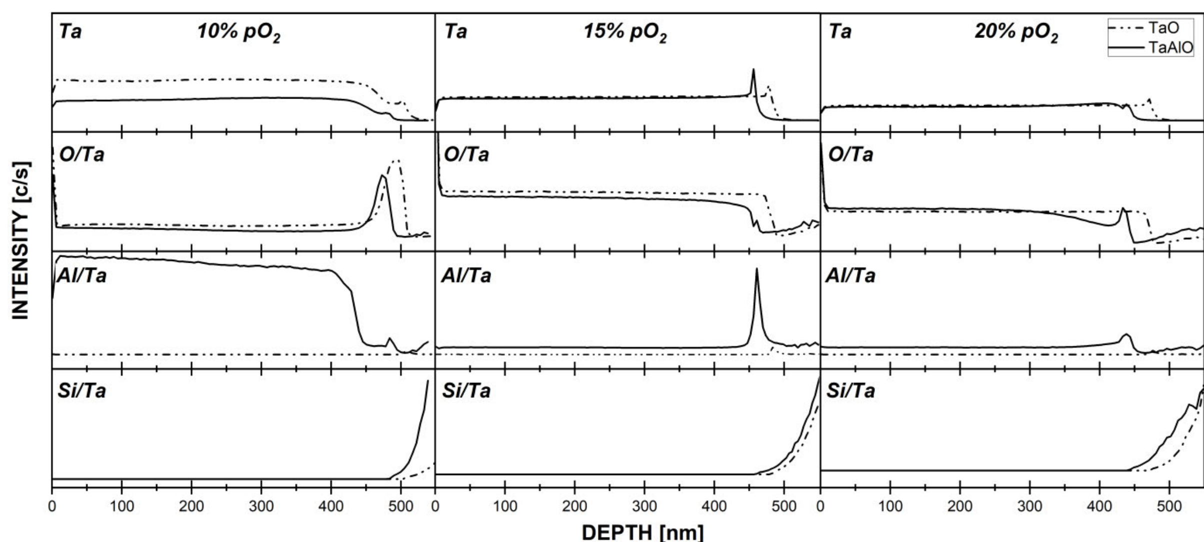

Figure 8-40. SIMS spectra of TaAlO and TaO thin films before annealing.

Firstly, referring to the $p(O_2) = 10\%$ films, tantalum maintains a consistent presence throughout the film however the oxygen spikes at the film/substrate interface, in both the doped and undoped films. While a consistent tantalum presence was expected, oxygen migration to the film/substrate interface may imply the presence of a SiO_2 (or similar) phase, possibly formed during deposition of the films. While not of pressing interest to this investigation, such a phase could present problems in charge migration or other electronic challenges. Otherwise, aluminium intensity was significantly higher relative to the undoped film, confirming EDS results.

The SIMS depth profile for the $p(O_2) = 15\%$ and 20% films both exhibited similar ion intensities relative to the $p(O_2) = 10\%$ film with exception of aluminium, which was significantly lower in relative intensity but nonetheless present in the films above baseline (undoped aluminium trace). It is therefore clear that aluminium exists in the films below the detection limits of EDS, and likely not at any concentration that could significantly alter electronic or phase properties.

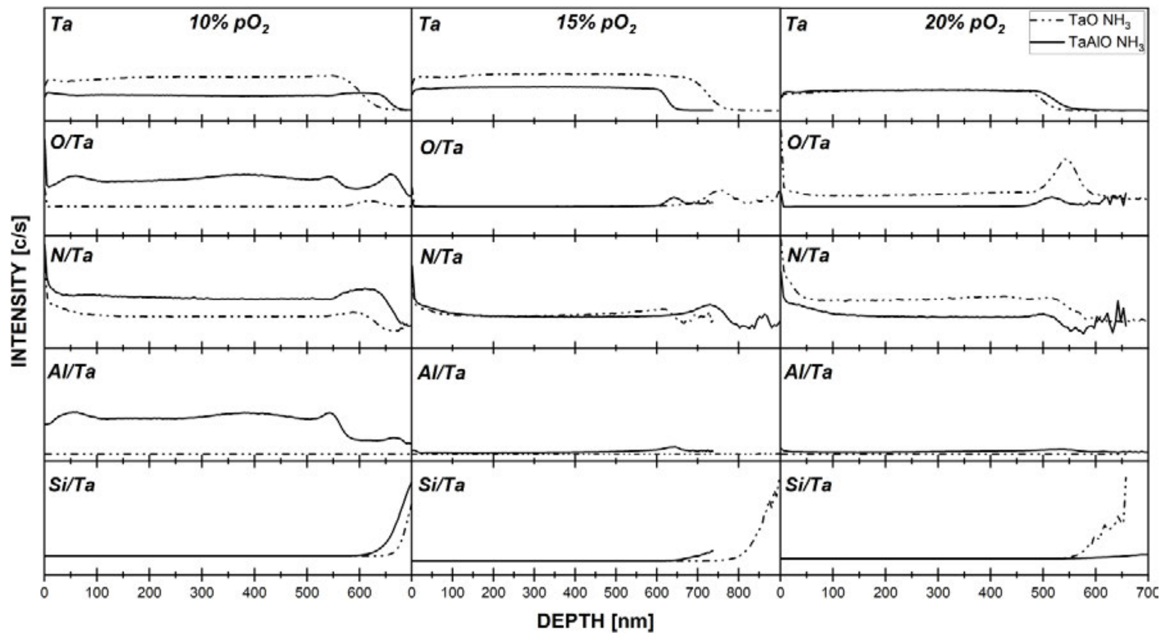

Figure 8-41. SIMS spectra of TaAlO and TaO thin films after annealing.

An aluminium presence remained in the films after nitridation, although much less in the 15% and 20% p(O_2) films relative to the 10% p(O_2) film. Referring to the p(O_2) = 10% film, aluminium migration appears to have taken place in the direction of both interfaces: the film/substrate interface and film/gas interface. The aluminium presence also appeared to accompany a greater oxygen presence, relative to the pO_2 = 15% and 20% films, however no oxide phase is observed per Figure 8-39. Aluminium oxide species may instead exist as amorphous structures or be present at low quantities in grain boundaries, as was speculated in the previous Cr-Ta_3N_5 study (section 8.3.2).

The tantalum presence in all 3 films was consistent after annealing, as was the nitrogen presence, although lower nitrogen counts in the bulk relative to the interfaces was also evident. SIMS analysis confirmed that while aluminium was present in all doped films, it was below EDS detection limits in the p(O_2) = 15% and 20% films as was previously speculated. It can be concluded from this that the use of oxygen partial pressure as a method of controlling the aluminium sputter rate was suppressed.

More films were deposited with varying power applied to the aluminium target. The aim was to improve control over the aluminium content in the deposited tantalum oxide films. These additional films were deposited with 10 W and 20 W applied to the aluminium target with a p(O_2) of 10%, as it was previously established that significant aluminium sputtering takes place at this p(O_2) value. The full deposition parameters for these films are given below in **Table 8.13**. Additionally, the EDS elemental data for these films is provided in **Table 8.14**.

Table 8.13. Sputtering parameters and thicknesses of 10W, 20W and 30W Al doped films and the 0W control, before and after nitridation.

Deposition Pressure (Pa)	pO_2/Total Atmospheric Oxygen (Pa/%)	Ta:Al Power (W)	Thickness As Deposited (nm)	Thickness Post-NH_3 (nm)	Thickness Change Post-NH_3 (%)
0.66	0.06/10	100:0	471	650	38.0
0.66	0.06/10	100:10	562	753	31.9
0.66	0.06/10	100:20	576	747	29.6
0.66	0.06/10	100:30	580	718	23.7

Table 8.14. EDS elemental data for TaAlO and TaO thin films prior to and post annealing in NH_3.

		As Deposited			Post Annealing			
Film Type	Ta:Al Power (W)	[Ta] (at. %)	[O] (at. %)	[Al] (at. %)	[Ta] (at. %)	[O] (at. %)	[Al] (at. %)	[N] (at. %)
TaO	100:0	30	70	<1	25	4	<1	71
TaAlO	100:10	20	74	6	36	4	2	58
TaAlO	100:20	22	66	12	24	6	9	61
TaAlO	100:30	27	57	16	36	7	11	46

Considering the as-deposited thicknesses of the additional films, a linear trend in film thickness with aluminium power is observed, with thickness increasing from 471nm before aluminium sputtering, to 562nm at 10 W, 576nm at 20 W and finally 580nm at 30 W. The increase in thickness is consistent with additional aluminium content depositing with the films. After annealing, the trend instead decreased with higher power on the aluminium target, possibly indicating excess aluminium evolving from the film to the NH_3/N_2 gas phase during annealing.

Aluminium content clearly varied with the power applied to the target, with 10 W, 20 W and 30 W corresponding to 6 at. %, 12 at. % and 16 at. % after annealing respectively. The previous trend in atomic % loss after annealing was also observed, with a drop in aluminium content to 2 at. %, 9 at. % and 11 at. %, likely for the same reasons as were previously discussed. This is very close to the margin of error for the standardless analysis (±5 at. %) method used. Cross sections and surface images show internal morphology indicative of polycrystalline structures, with increasing grain sizes and thicknesses of the 10 W, 20 W and 30 W films after annealing in **Figure 8-42**.

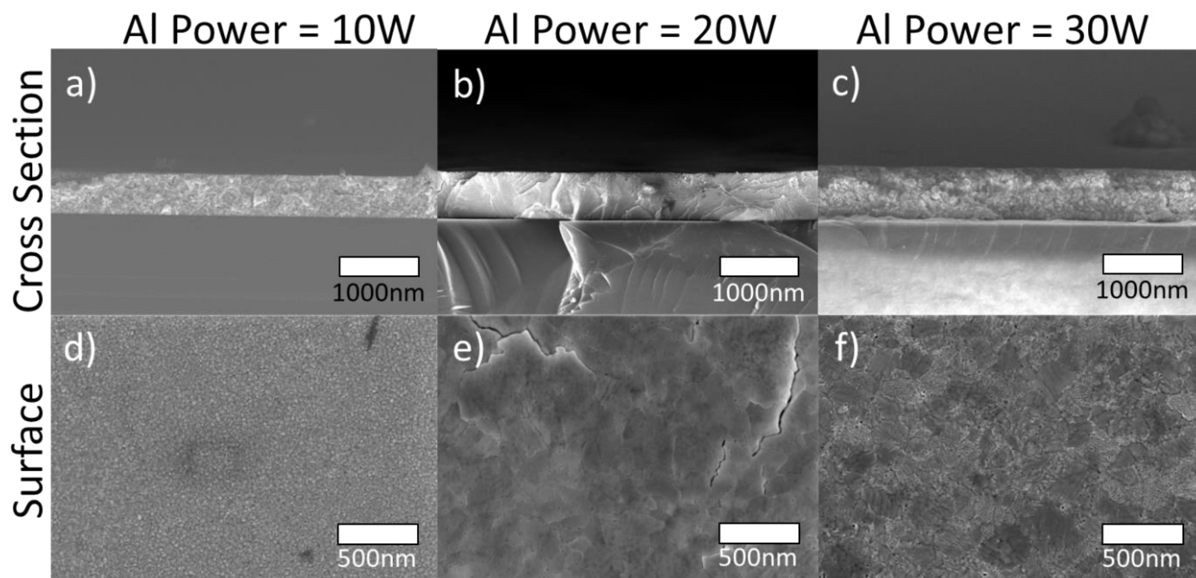

Figure 8-42. SEM cross sections and surface images of annealed films deposited with 10 W, 20 W and 30 W. Where a) 10 W cross section, b) 20 W cross section, c) 30 W cross section, d) 10 W surface image, e) 20 W surface image, f) 30 W surface image.

The XRD diffractograms for the films deposited with lower aluminium target power can be seen in **Figure 8-43**. Both 10 W and 20 W films presented amorphous structures prior to annealing and crystalline Ta_3N_5 after annealing, albeit relative to the control and 30 W films broader peaks were exhibited, indicating poorer crystallinity. Again, no secondary aluminium phases were apparent, despite this not being the case in the previous chromium study.

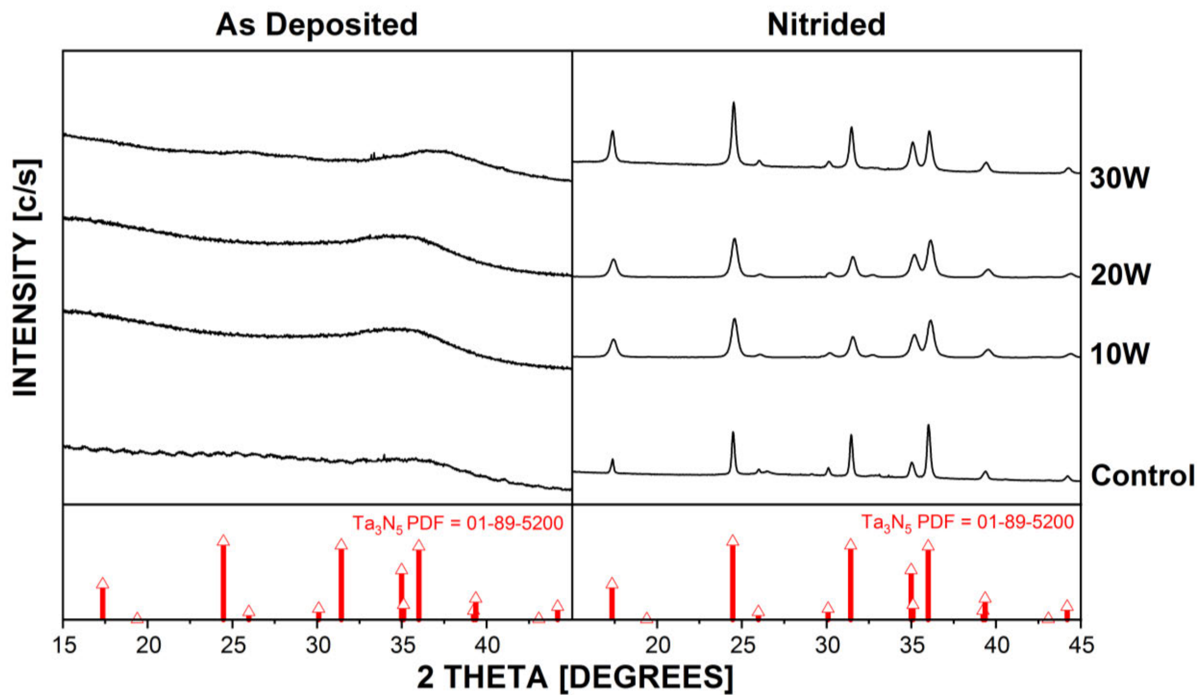

Figure 8-43. XRD diffractograms of TaAlO and TaO thin films deposited at 10W, 20W and 30W, before and after nitridation. Control sample was deposited without power applied to the Al target.

SIMS was used once again to corroborate the EDS elemental results, as seen in Table 8.14. The SIMS depth profile for the as-deposited films can be seen in **Figure 8-44** while the annealed film depth profile can be seen in **Figure 8-45**. Looking at Figure 8-44, relative tantalum intensities were consistent between the undoped and doped 10 W film, however the 20 W and 30 W films both showed lower tantalum counts relative to the undoped control.

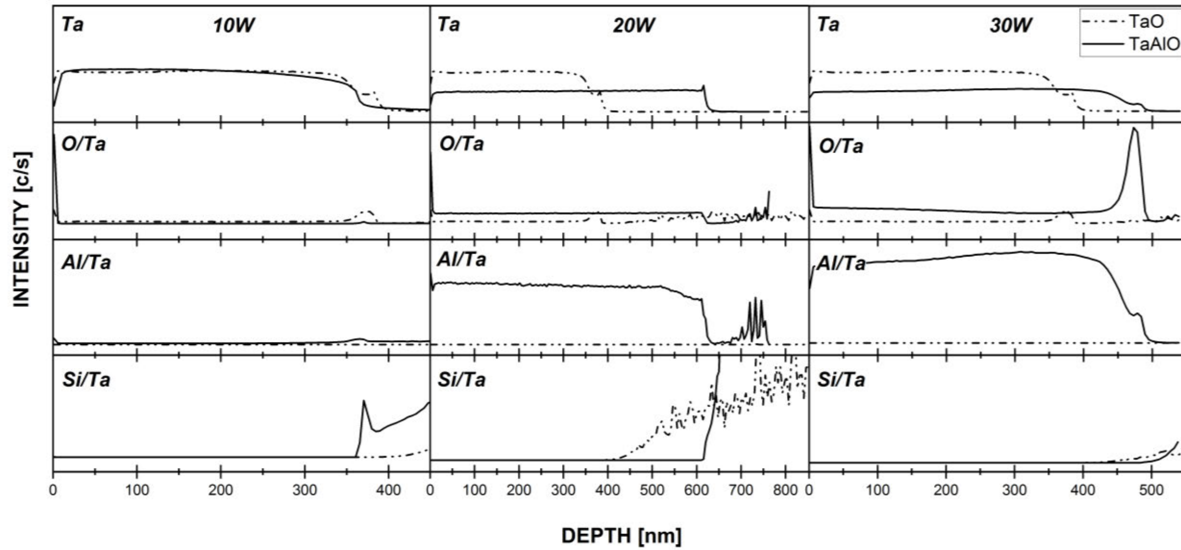

Figure 8-44. SIMS depth profile of 10 W, 20 W and 30 W TaAlO films before annealing, compared with the TaO control film deposited without an aluminium plasma.

This was also true in the case of the oxygen and aluminium intensities, which shared a proportional relationship, with counts for both elements increasing in the 20 W and 30 W films relative to the undoped control film. This seems to indicate that ejected aluminium could increase oxygen gettering, or eject as aluminium oxide species due to target poisoning, and displace tantalum species as a result (Depla, D. & De Gryse, R. 2004). Aluminium content was observed in all doped films, albeit a signal indistinguishable from the undoped baseline was observed in the 10 W doped film.

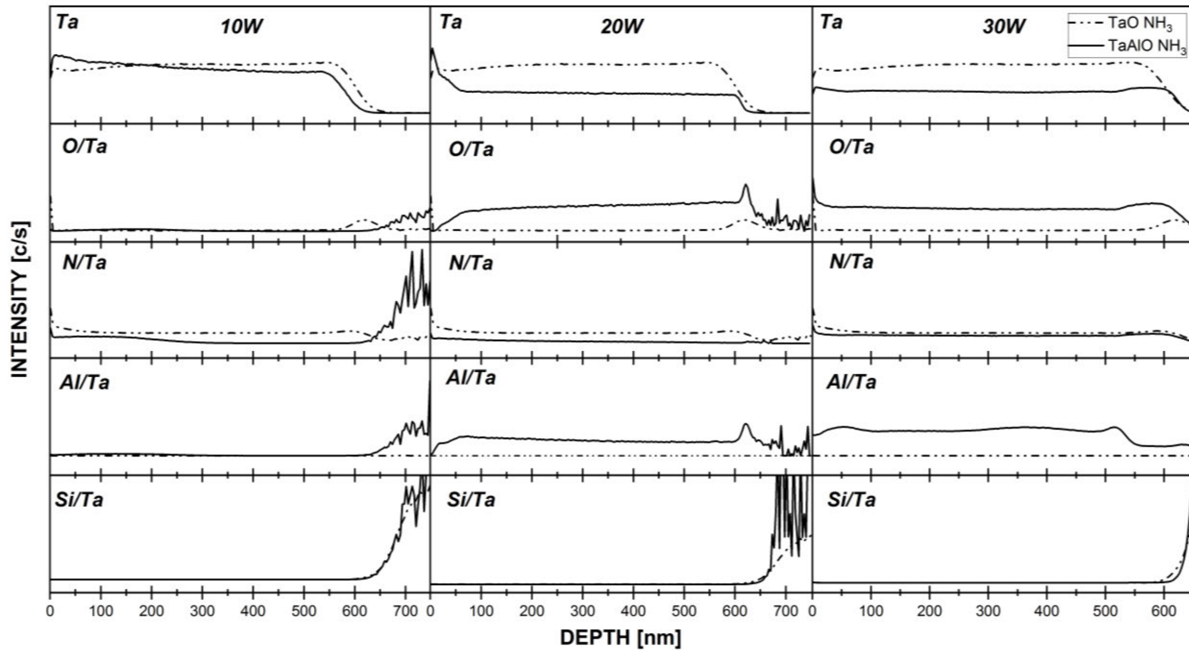

Figure 8-45. SIMS depth profile of 10W, 20W and 30W TaAlO films after annealing, compared with TaO film deposited with 0W on the Al target.

Similar results are seen after annealing as displayed in Figure 8-45. Tantalum presence was relatively lower in the 20 W and 30 W doped films than the undoped film, while the 10 W film shared a similar tantalum trace. This is expected, given the higher amount of aluminium in the 20 W and 30 W films. Oxygen intensity once again corresponded to aluminium presence, which shows that aluminium accumulates with oxygen during annealing. Oxygen appears to migrate to the film-substrate interface after annealing, along with aluminium, with some oxygen possibly migrating into the silicon substrate or forming an oxide layer at the interface. Both possibilities are far from ideal from a water splitting perspective, as an oxide layer at the interface would act to impinge the movement of electrons across the circuit.

8.3.3.3 Reaction Kinetics of Ta_3N_5 Evolution in Aluminium Doped Tantalum Oxide Films

Further investigation into the reaction kinetics of the doped and undoped films presented in this section was warranted to provide more information on the possible reaction trajectories of the films. This investigation was structured similarly to the subsection in the previous Cr-Ta_3N_5 section of this work, which was the annealing of doped and undoped films deposited with $p(O_2)$ = 10% and 20% for 2, 4 and 8 hours of dwell time. The XRD diffractograms for this series of films can be seen below in **Figure 8-46**.

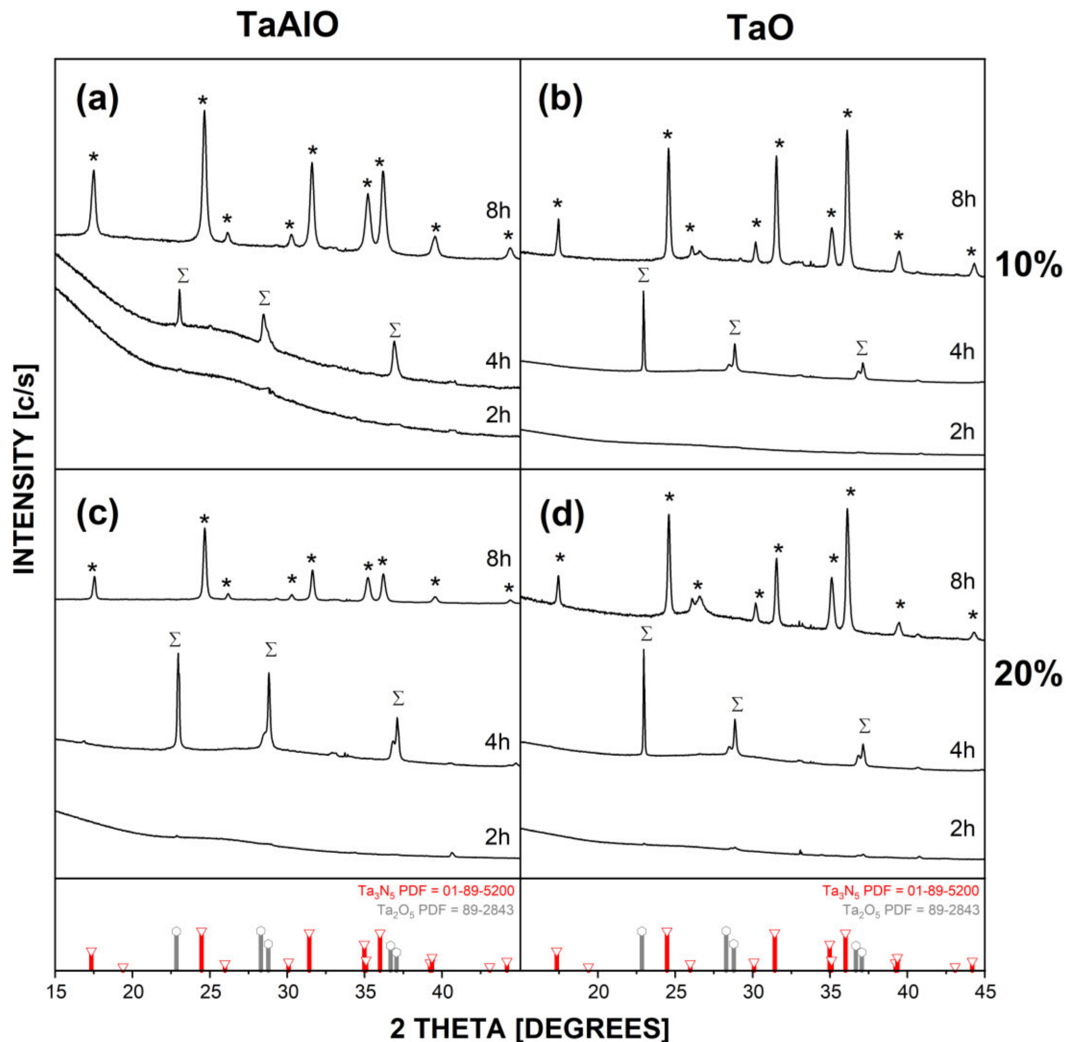

Figure 8-46. XRD diffractograms of TaAlO and TaO films annealed at 2, 4 and 8 hour dwell times, where a) TaAlO 10% pO_2, b) TaO 10% pO_2, c) TaAlO 20% pO_2 and d) TaO 20% pO_2. Where * denotes Ta_3N_5 peaks and Σ denotes Ta_2O_5 (tantite) peaks.

A notable difference between the XRD results in Figure 8-46 and those reported in the previous chromium doping study is the lack of an intermediate dopant phase, which in the previous study was $CrTaO_4$ in Ta_2O_5 after 4 h of annealing. This phase was observable after 4h of annealing but no analogous aluminium phase is observed in this study. This can be explained by the numerous oxidation states of Cr (commonly +6, +3 and +2 (Arévalo-López & Alario-Franco 2009)) facilitating the formation of $CrTaO_4$, relative to aluminium (+1, +2, +3). However, the Cr oxidation state in $CrTaO_4$ is +3 (Arévalo-López & Alario-Franco 2009), which instead points to the difference in atomic radii between the two dopants. It is noted that an amorphous peak below 15° 2theta can be seen in Figure 8-46a) in the 2h and 4h annealed films, but not in the 8h films. Otherwise, the films proceed in a similar trajectory to the previously reported chromium results, with TaO (amorphous) reacting into Ta_2O_5 after 4h, before full nitridation taking place between 4h and 8h.

There is a difference in relative peak intensity between the doped films and the undoped films, which can more easily be seen in Figure 8-46c) and d). It isn't clear what role aluminium would play in enforcing such preferred orientation, or if it is a result of strain brought on by the nitridation process. To gain a better understanding of the elemental content, SIMS was performed on the films displayed in Figure 8-46. The resulting SIMS depth profiles can be found in **Figure 8-47** and **Figure 8-48**.

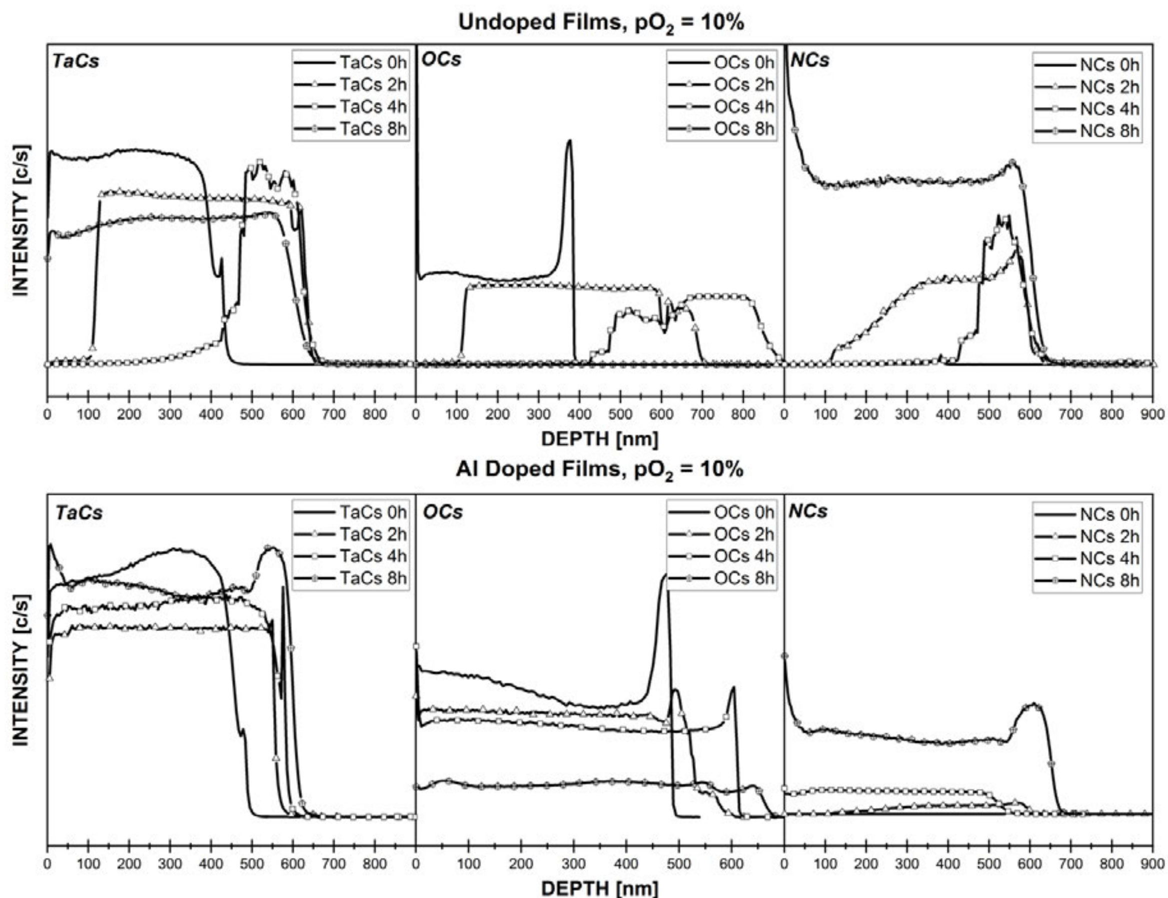

Figure 8-47. SIMS depth profiles of 2h, 4h and 8h thermally annealed undoped and Al doped films deposited with 10% pO_2.

The undoped films, as seen Figure 8-47, have been discussed in previous works, where it was concluded that the poor electrical conductivity of the Ta_2O_5 phase inhibits secondary ion yield (Balachandran & Eror 1982). The transitionary interface between Ta_2O_5 and the amorphous TaO phase can be inferred from the sharp steps seen in the 100 nm region for the 2 h film and between 450-500 nm in the 4 h film. The increase in thickness is seen in less than 2 h of annealing, as Ta counts begin at 450 nm for the 0 h film and 650 nm for the 2 h film, a result also attributed to the crystallisation of the Ta_2O_5 phase. The N yield follows the trends observed in Ta and O graphs, and worth noting is the lack of N yields at 0 h (prior to nitridation) as expected.

The aluminium doped films in Figure 8-47 exhibit elemental profiles that contrast with those of the undoped films, as the Ta traces are consistent with depth in 0, 2, 4 and 8 h films. Given the presence of the Ta_2O_5 phase in 4 h films, poor secondary ion yield was expected in line with the undoped films but not observed. Whether this is due to aluminium incorporation improving the conductivity is unknown, however previous SIMS results do indicate the presence of aluminium in these films. A hump in the Ta trace can be seen in the 8 h film between 500-600 nm, which indicates an accumulation of Ta in the surface region in the completed Ta_3N_5 films. The source of this hump cannot be seen in the XRD results in Figure 8-46, and given the similarity to the N trace but not the O trace for the 8 h film in the same region, is likely a tantalum oxy-nitride phase.

Looking at the O traces for the doped films in Figure 8-47 also shows peaks in the film/interface region indicative of either a substrate oxide formation or the migration of oxygen to this region during annealing. This was also observed in the chromium doping study but left as a compelling option for future works. Finally, the N profiles for the doped films show consistent counts throughout the depth profile in agreement with Ta and O traces, with N content increasing with annealing time. By 8 h of annealing, the N intensity increases significantly with a corresponding drop in the O intensity. This result is in agreement with previous EDS data indicating that some oxygen presence is maintained even after 8 h of annealing, however no residual oxide phase is noted in the XRD results.

Upon increasing of the $p(O_2)$ to 20% (as per Figure 8-48), Ta, O and N yields are generally consistent with those of the undoped film depth profiles in Figure 8-47. Focusing on the doped films in Figure 8-48, Ta yields are generally consistent throughout the films, and the increase in thickness as annealing proceeds from 2 h to 4 h, before reaching their thickest at ~500 nm after 8 h. O yields for the doped films show a repeat of the previously observed accumulation in the film/interface region between 400-600 nm in all films. It can also be observed that O yields are continuing past the point of Ta yields in the 8 h doped film, in agreement with previous results suggesting an oxide phase in the interfacial region. N yields in the doped films are broadly like those of the doped films shown in Figure 8-47, with increasing N yield as the anneal time increases, an expected result of the nitridation process.

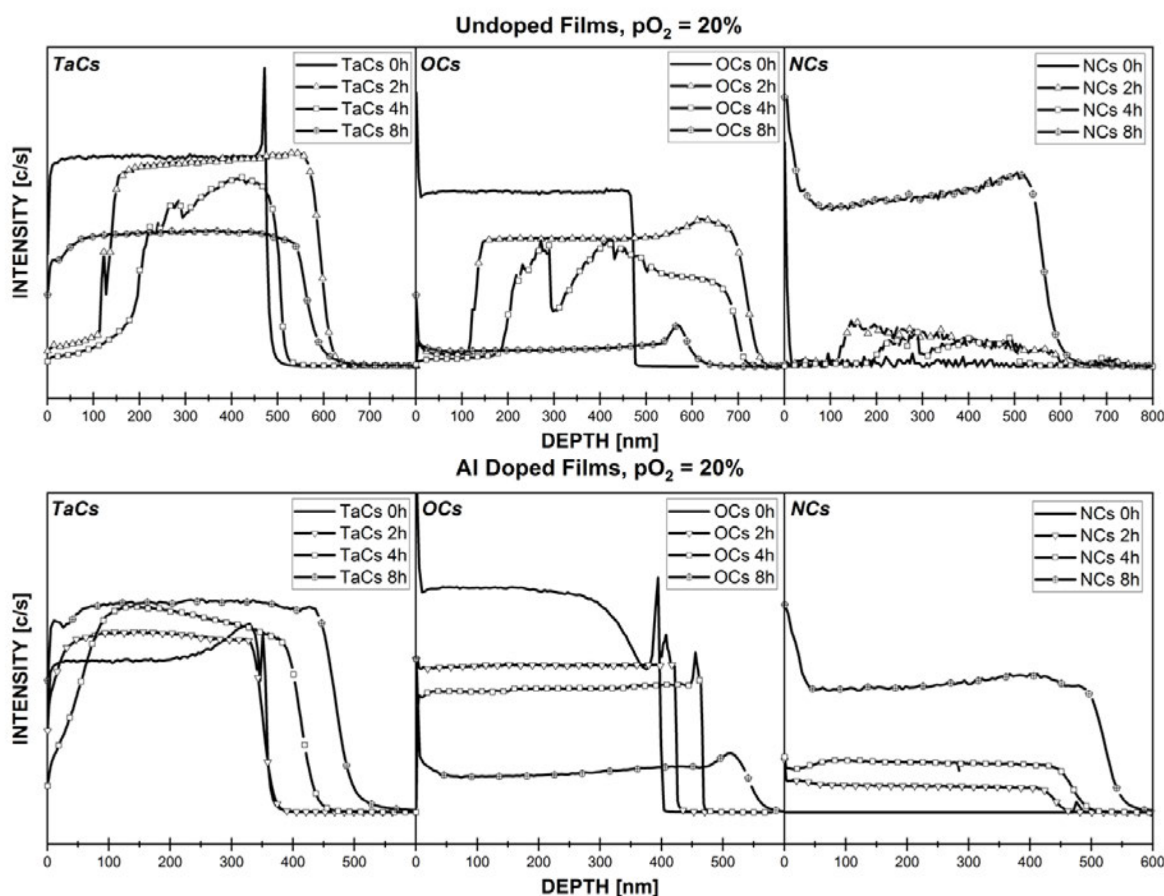

Figure 8-48. SIMS depth profiles of 2h, 4h and 8h thermally annealed undoped and Al doped films deposited with 20% pO_2.

These kinetic experiments have produced results broadly in agreement with those of the previously discussed chromium doping work 8.3.2), which is a) that the evolution of Ta_3N_5 from amorphous Ta-O proceeds through a slow crystallisation of the Ta_2O_5 phase before a rapid transformation into Ta_3N_5 between 4 h and 8 h of annealing and b) oxygen appears to accumulate at the film/substrate interface region, however the nature of this accumulation cannot be discerned from the obtained XRD and SIMS results. Investigations of the interplay between oxygen, nitrogen and the Si substrate during ammonolysis conditions presented here present future research opportunities.

Following the synthesis of chromium doped Ta_3N_5 films in this work, this section of the discussion presents novel aluminium doped Ta_3N_5 thin films produced via a multi-step synthetic method. Aluminium doped tantalum oxide precursor films were reliably deposited after a partial hysteresis experiment identified a suitable partial pressure range based on target poisoning dynamics. These films were then successfully reacted into crystalline Ta_3N_5 films with no secondary phases detected in XRD results.

Aluminium presence in the films was controlled with target power but not $p(O_2)$, the latter of which producing excessive target poisoning and inhibiting deposition of aluminium. Oxygen

impurities were again noted in all films, even after 8 h of annealing in NH_3. SIMS analysis revealed small amounts of aluminium in all doped films, however EDS only detected aluminium in the films deposited at 20 W and 30 W, with the 30 W Al-Ta_3N_5 film exhibiting 11% at. Al after annealing.

From the previous chromium doping study, chromium incorporation into Ta_3N_5 was speculated to be less than 6 at. %, due to the solubility limit of Cr in the precursor Ta_2O_5 phase. In contrast, the results of the present work indicate that aluminium solubility in Ta_3N_5 does not face the same limitations as with chromium, as no secondary aluminium phase emerged as aluminium doping increased. There was also no aluminium tantalum oxide intermediate phase seen in the kinetic investigation XRD results as there was with chromium. Assuming aluminium incorporates as per Equation 27, the results of this paper provide a potential synthetic route towards developing a p-type Ta_3N_5 electrode doped with aluminium. Future works aimed at characterising the opto-electronic properties and photo-electrochemical performance of Al-Ta_3N_5 films synthesized in this project are currently being carried out.

8.3.3.4 UV-Vis Characterisation of Al-Ta_3N_5

UV-Vis characterisation of the aluminium doped films was performed in an identical fashion to previously discussed chromium doped films. The UV-Vis instrumentation was setup with a DRA and utilised to determine the absorption edge in the films and verify the expected light absorption before proceeding with photo-electrochemical EIS evaluation.

As previously discussed for Cr-Ta_3N_5 standard films, a Ta_3N_5 standard film of ~800nm thickness was again used as a strongly absorbing standard of comparison for Al-Ta_3N_5 films. The standard Ta_3N_5 film exhibited a red lustre. Previously, Cr-Ta_3N_5 films began to exhibit a metallic colour as doping was increased, and this was reflected in the poorly absorbing highly doped Cr-Ta_3N_5 films. On the other hand, Al-Ta_3N_5 films exhibited the distinct Ta_3N_5 red tinge even as doping was increased up to the maximum doped 30 W Al films. The UV Vis spectra of the Ta_3N_5 and aluminium doped films can be seen below in Figure 8-49.

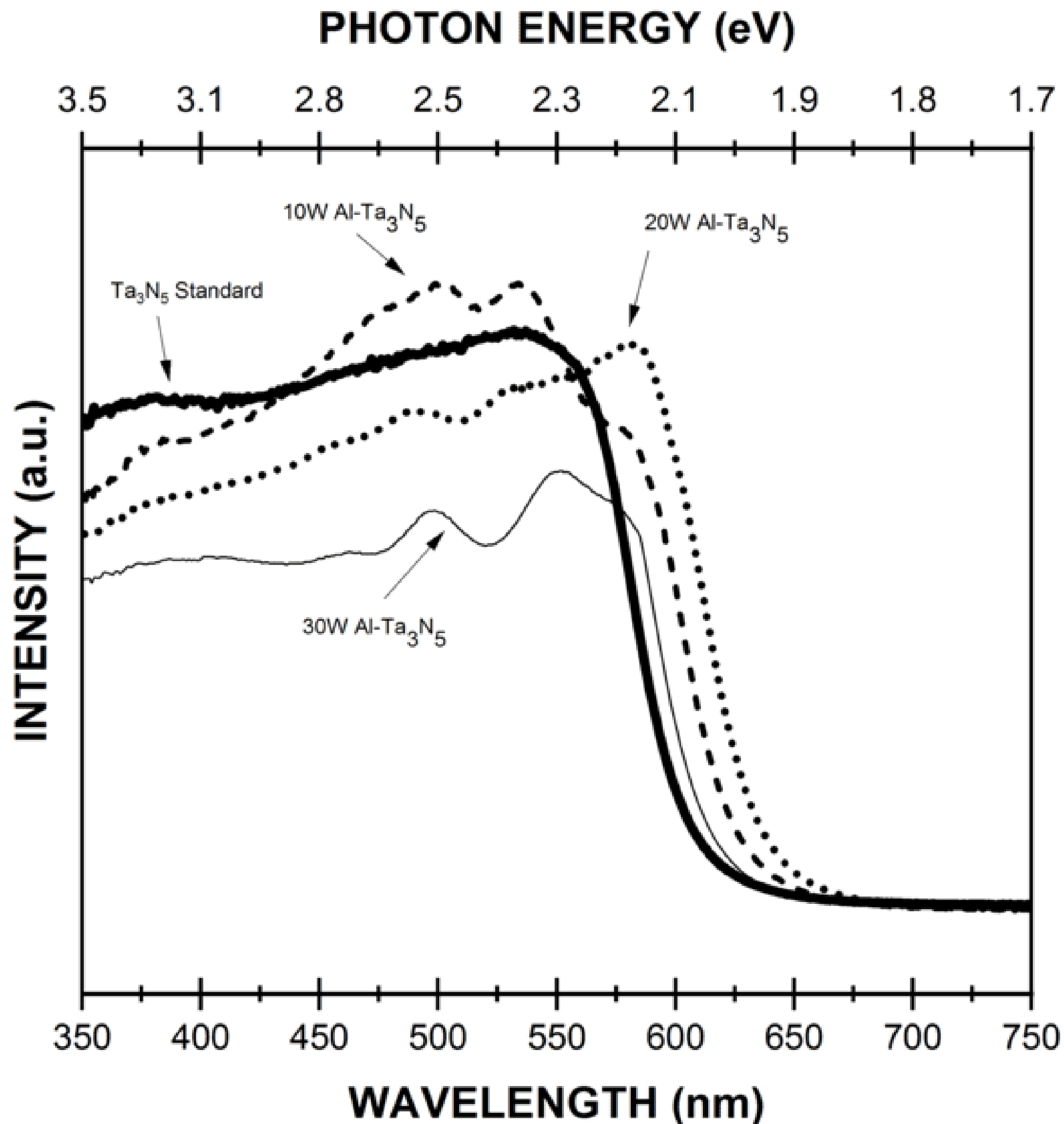

Figure 8-49. UV-Vis diffuse reflectance spectra of Ta_3N_5 standard film contrasted with 10W, 20W and 30W aluminium doped films, with wavelength (nm) and photon energy (eV) included. Arbitrary units are used for absorbance intensity.

As per Figure 8-49, the Ta_3N_5 standard film shows a clear absorption edge at ~600nm, whereas the absorption edge of all 3 Al doped films shifts between 620 to 650nm, with the 20 W doped film possessing the earliest absorption edge at 650nm. All 3 doped films show lower relative absorption intensity relative to the standard however, with the most highly doped film (30 W Al) exhibiting the lowest intensity of the 4 films tested, and the 10 W Al film closest to that of the Ta_3N_5 standard. All Al doped films show absorption in the visible range, in contrast to the Cr doped films. This result is attributed to the formation of the suspect CrN phase during annealing, which appears to disrupt light absorption in the Cr doped films. A similar phase is not observed in the Al doped films as per section 8.3.3.3.

8.4 Photo-electrochemical and Electronic Assessment

This section of the discussion will detail the measurements and data acquired in characterising the solar water splitting performance and notable electronic properties of the films in accordance with Project Aim 2.

8.4.1 Electronic Properties and PEC Performance Ta_3N_5 Films

The established literature indicates that the Ta_3N_5 phase is the most insulating phase in the tantalum nitride phase series, exhibiting n-type semiconductor properties and poor conductivity (Hitoki et al. 2002). As discussed in the literature review, many studies have cited the electronic anisotropic nature of Ta_3N_5 (Harb & Basset 2020) and its poor charge transport properties imposed by harsh synthetic methods, namely high temperature ammonia annealing (Harb & Basset 2020). Hall measurements were performed on films described in the section 8.2.1 to determine the majority charge carrier and the magnitude thereof.

Sheet resistivity and mobility are also provided by this equipment and can be found in the appendix section. The results from hall measurements of these films (post nitridation) can be seen in **Table 8.15**. To ensure results were representative of the deposited films and not the substrate, an insulating layer of aluminium nitride was deposited prior to deposition of the tantalum nitride precursor layer. This aluminium nitride layer was deposited to a thickness of 200nm and Hall measurements indicated a resistivity of $2x10^3$ Ωcm^{-1}, in contrast to those of the deposited films at approximately $5x10^{-2}$ Ωcm^{-1}.

Table 8.15. Carrier concentration as determined from Hall measurements of Ta_3N_5, deposited with $p(O_2)$ = 10%, 15% and 20%, after nitridation.

Oxygen Atmospheric % (%)	Thickness (nm)	Carrier Concentration (/cm^{-3})
10	650	-7.865E+19
15	580	-7.928E+19
20	459	-8.930E+19

These films were used as a standard of comparison for the measurements performed on subsequent doped films, in particular the $p(O_2)$ = 10% film, which has been discussed in previous chapters. The values were in the cited range of 10^{16} cm^{-3} to 10^{20} cm^{-3} as per literature values for similar films, both Ta_3N_5 specifically and other n-type semiconductors (e.g. $BiVO_4$) (Ziani et al. 2015). The results indicated an n-type semiconductor, with carrier concentration increasing as atmospheric oxygen was increased.

As per the discussion relating to these films in previous sections, the $p(O_2)$ = 10% film was selected for further experiments with dopants primarily due to the excess amount of oxygen

in films deposited at higher p(O_2) values. This film is also considered the standard Ta_3N_5 film in the proceeding section of this work.

In addition to Hall measurements, electrochemical techniques were utilised to generate CV and Mott-Schottky plots. CV plots were generated in the dark and under illumination to determine the light response in the films, while frequency response scans were performed in the dark and Mott-Schottky plots generated from the calculated capacitance to estimate the dopant density and flat band potential of the films. All electrochemical experiments were performed with a Pt counter electrode and Ag/AgCl reference electrode. Films were tested in two electrolyte solutions prior to scans to ensure stability, these were 0.5M H_2SO_4 (pH of 2) and 0.1M KOH (pH of 13). 10 scans were performed at a rate of 3mV/s, 5 in the dark and 5 under illumination (100mW/cm^2 or 1.5 AM), with 2 scans selected from each and plotted in **Figure 8-50**.

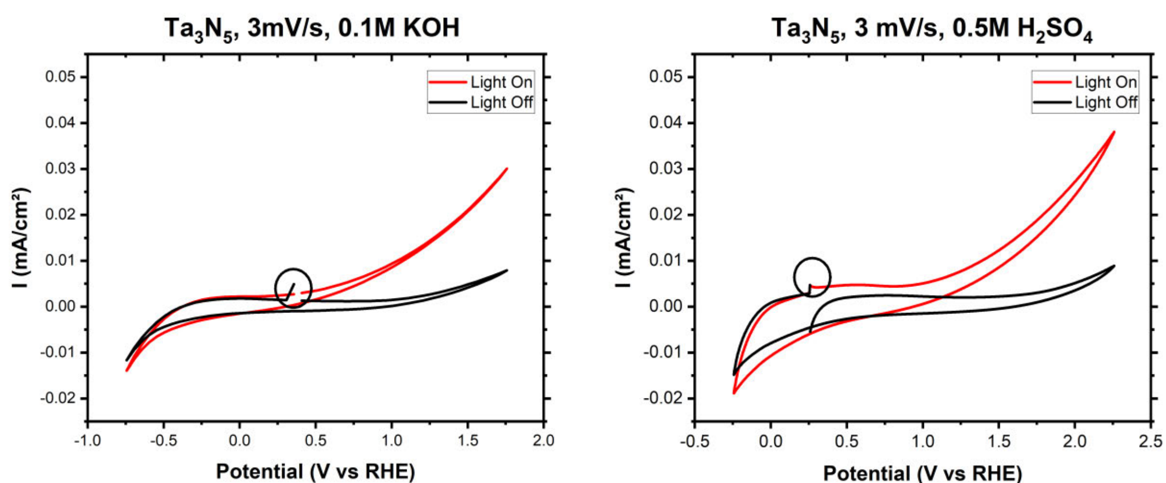

Figure 8-50. CV plots of Ta_3N_5 in 0.1M KOH and 0.5 H_2SO_4 electrolytes performed at 3mV/s and two different potential ranges relative to the electrolyte pH.

Electrodes showed clear photocurrents after exposure to simulated sunlight, with the observed anodic current rising from 0.005 mA/cm^{-2} in the dark, to 0.04 mA/cm^{-2} under illumination at 2.25 V vs RHE. While far from the performance of cutting edge Ta_3N_5 based materials, these values are broadly within the photocurrent range published in the literature pertaining to Ta_3N_5 electrodes of this type (Yokoyama et al. 2011). In both electrolytes the Ta_3N_5 electrodes were stable in dark and illuminated conditions. While the anodic and cathodic photocurrents were relatively larger in the H_2SO_4 electrolyte solution, a capacitance effect can be seen in the gap between cathodic and anodic traces from -0.5 V to 0.5 V in the H_2SO_4 electrolyte. This, along with concerns about the stability of the film in highly acidic solutions over multiple slow scans, prompted the selection of KOH as the standard electrolyte for future scans.

From the CV scans, an appropriate potential range in the double-layer capacitance region without Faradaic currents (typically 0.6 V to 1.0 V vs. RHE) was determined prior to performing impedance measurements (for Mott-Schottky plots).

Impedance scans were performed over a frequency range of 10-100,000Hz (amplitude of 5mV), scanned at 5 frequencies per decade across a potential range of -1 to 1.5V. Mott-Schottky plots generated from impedance scans can be seen in **Figure 8-51**.

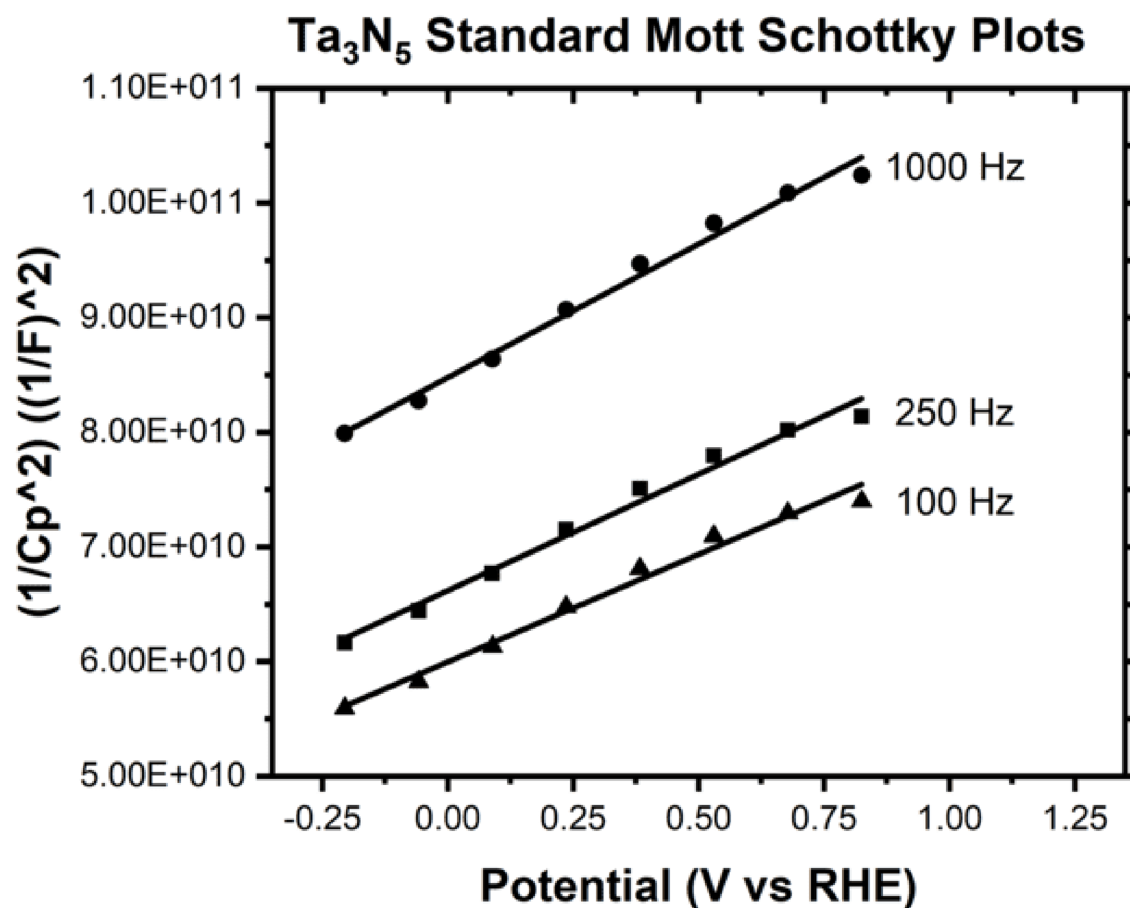

Figure 8-51. Mott-Schottky plot of Ta_3N_5 electrodes ($p(O_2)$ = 10%) performed in 0.1M KOH electrolyte solution at 100Hz, 250Hz and 1000Hz across an applied potential range of -1V to 1.5V.

The plots shown in Figure 8-51 indicate an n-type Ta_3N_5 electrode from the positive slopes (per Equation 4 and 5), with a flat band potential of approximately -0.8 V vs RHE and dopant density of ~2.829×10^{19} cm^{-3} (n-type doping per Hall measurements), which compares consistently to previously listed Hall values. The V_{FB} and carrier concentration are comparable to those reported in the literature when utilising similar experimental setups (Alishahi et al. 2016; Khan et al. 2015; Nurlaela, Ziani & Takanabe 2016). The V_{FB} of -0.8 V is reportedly close to the conduction band of Ta_3N_5, which is composed mostly of empty Ta d^0 orbitals (Li, F et al. 2020).

8.4.2 Electronic Properties and PEC Performance of Cr-Ta_3N_5 Films

As discussed in the previous chapter pertaining to synthesis of Cr-Ta_3N_5 films, a second phase was identified as Cr loading increased in the films. Despite the identification of the Ta_3N_5 phase in the presence of this secondary CrN phase, UV-Vis measurements showed poor absorbance relative to the Ta_3N_5 standards. Hall effect measurements were performed to evaluate the electronic properties of the films and can be seen in **Table 8.16**. An aluminium nitride insulative layer was also deposited on the substrate prior to film deposition for these films.

Table 8.16. Carrier concentration as determined from Hall measurements of the Ta_3N_5 standards and Cr-Ta_3N_5 films.

Film	Ta:Cr Power (W)	Thickness (nm)	Carrier Concentration ($/cm^{-3}$)
Ta_3N_5	100:0	650	-7.865E+19
Cr-Ta_3N_5	100:10	785	-5.569E+18
Cr-Ta_3N_5	100:20	817	-5.299E+17
Cr-Ta_3N_5	100:30	738	1.293E+17

The magnitude of the carrier concentration shifted from n-type to p-type as Cr loading was increased. Hall results therefore indicated the possibility of a p-type doped Ta_3N_5 material at highest Cr loading. Electrochemical techniques were again utilised to evaluate the effect of chromium doping relative to the Ta_3N_5 standard. The CV scans for the films can be seen below in **Figure 8-52**.

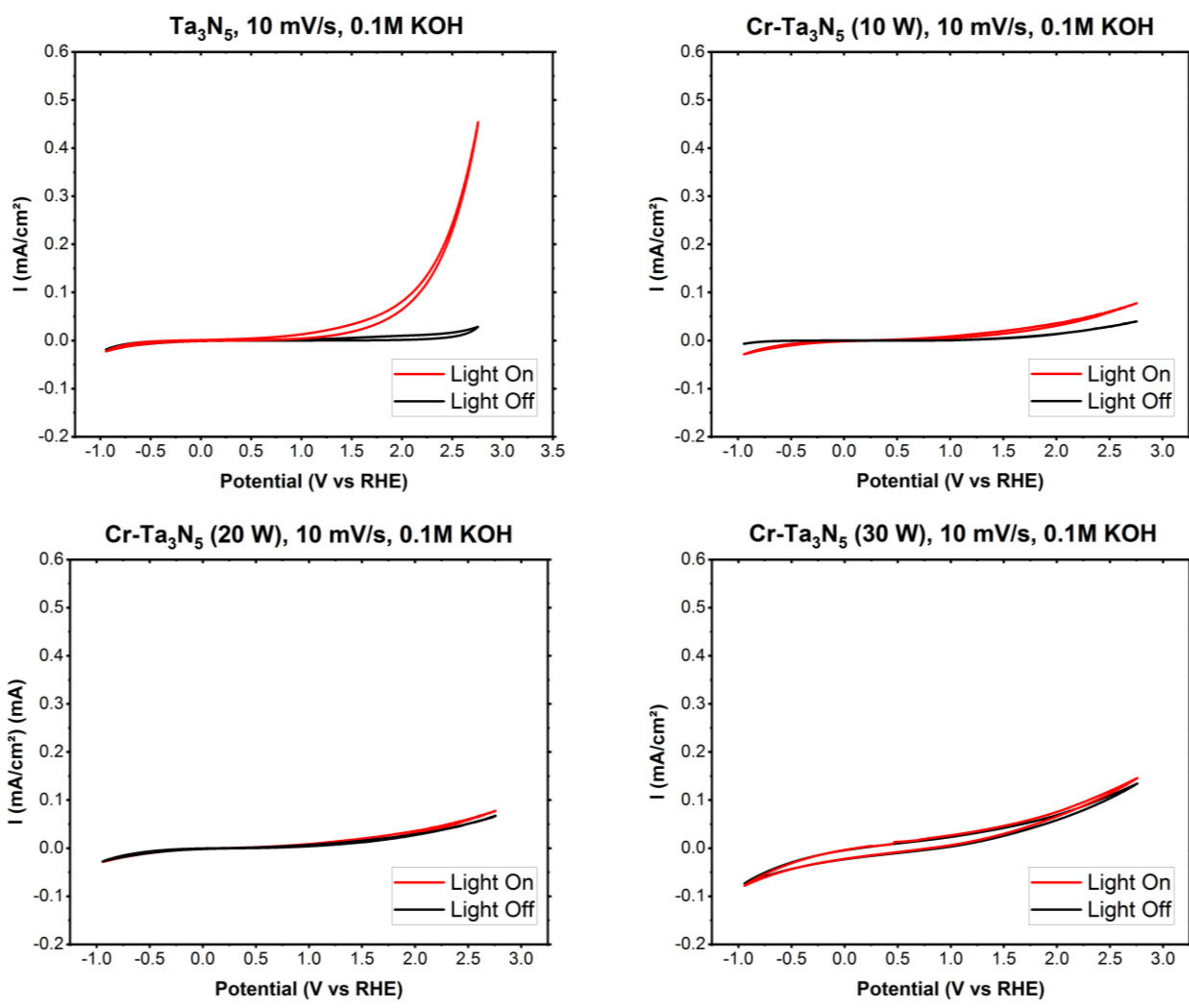

Figure 8-52. Cyclic Voltammetry scans of Cr-Ta_3N_5 films and Ta_3N_5 standard performed at 10mV/s under 100mW/cm^2 of illumination and in the dark.

Increased Cr loading suppressed the photocurrent, however even in the 10 W film which apparently showed no secondary CrN phase in XRD results and a similar absorption edge to the Ta_3N_5 standard in UV-Vis results, the magnitude of the anodic photocurrent was still significantly smaller relative to the standard Ta_3N_5 film, although the cathodic photocurrent is relatively larger. In the 20 W and 30 W films, no significant photocurrent is observed, with the most heavily doped film tested (30 W) showing relatively larger capacitance to all other films.

Impedance analysis was performed in the same fashion as with the Ta_3N_5 standard films, described in the previous subsection. The subsequent Mott-Schottky plots can be seen below in **Figure 8-53**.

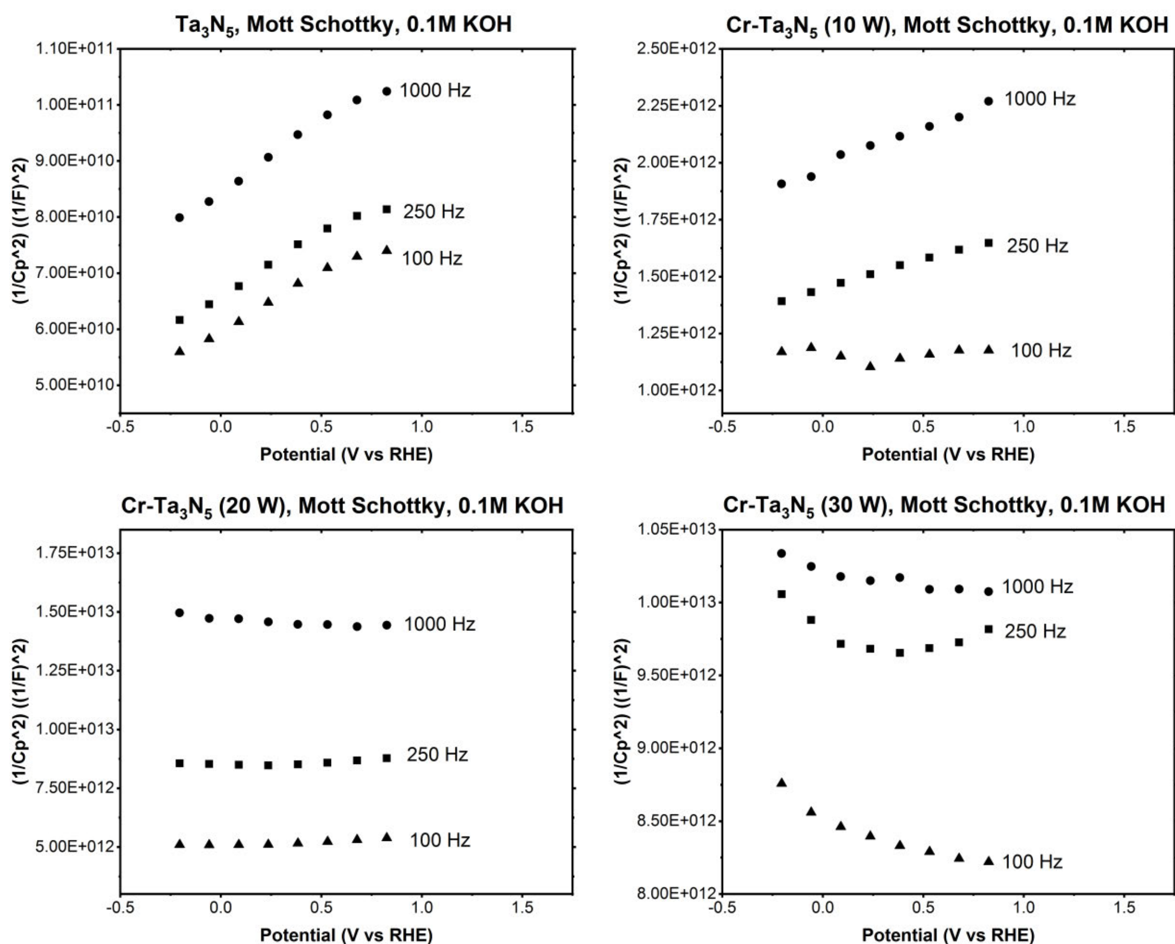

Figure 8-53. Mott-Schottky plot of Cr-Ta_3N_5 and Ta_3N_5 electrodes performed in 0.1M KOH electrolyte solution at 100Hz, 250Hz and 1000Hz across an applied potential range of -1V to 1.5V.

The CrN phase appears to disrupt impedance scans for the 20 W and 30 W doped films, as anomalous Mott-Schottky curves can be seen for these films in the above figure. The 10 W doped film produced a similar plot to the undoped Ta_3N_5 standard, indicating an n-type electrode in agreement with Hall measurement results. This is expected from the EDS, XRD and SIMS results pertaining to this film; the Cr loading was not enough to produce the exsolved CrN phase which here appears to disrupt the measurements. As a result, dopant density can only be accurately calculated for the 10W and standard samples, which were $N_D = 3.44 \times 10^{17}$ cm^{-3} and $N_D = 2.829 \times 10^{19}$ cm^{-3}, respectively. While very little Cr is present in the 10W film, the Cr present appears to reduce the carrier concentration substantially compared to the standard films.

8.4.3 Electronic Properties and PEC Performance of Al-Ta_3N_5 Films

Aluminium doped Ta_3N_5 films were evaluated using the same Hall measurement and electrochemical methodology as were described in sections 8.4.1 and 8.4.2. Hall measurements taken for the Al-Ta_3N_5 films can be seen below in **Table 8.17**. As with previous

films, an insulating aluminium nitride layer was deposited on the substrate prior to deposition and nitridation of the Al-Ta_3N_5 phase.

Table 8.17. Carrier concentration as determined from Hall measurements of the Ta_3N_5 standards and Al-Ta_3N_5 films.

Film	Ta:Al Power (W)	Thickness (nm)	Carrier Concentration (cm^{-3})
Ta_3N_5	100:0	650	-7.865E+19
Al-Ta_3N_5	100:10	753	-7.840E+18
Al-Ta_3N_5	100:20	747	4.978E+18
Al-Ta_3N_5	100:30	718	4.645E+20

The general trend observed with the carrier concentration in the Al-Ta_3N_5 films is like that of the Cr-Ta_3N_5 films, albeit the magnitude of the majority carrier shifts at Al 20 W and peaks with the 30 W film. Both results indicate the synthesis of a p-type film.

CV scans were performed to determine photo-response and Mott-Schottky plots were generated from impedance scans to calculate the carrier concentration. All electrochemical work was performed in the dark, with a 0.1M KOH solution as the electrolyte, a Pt counter electrode and Ag/AgCl reference electrode. The voltage range was shifted to favour a response in the cathodic region relative to the Cr-Ta_3N_5 scans, due to initial scans of the Al-Ta_3N_5 electrodes showing improved cathodic photocurrent relative to the Cr doped films. CV plots were generated and can be seen below in **Figure 8-54**.

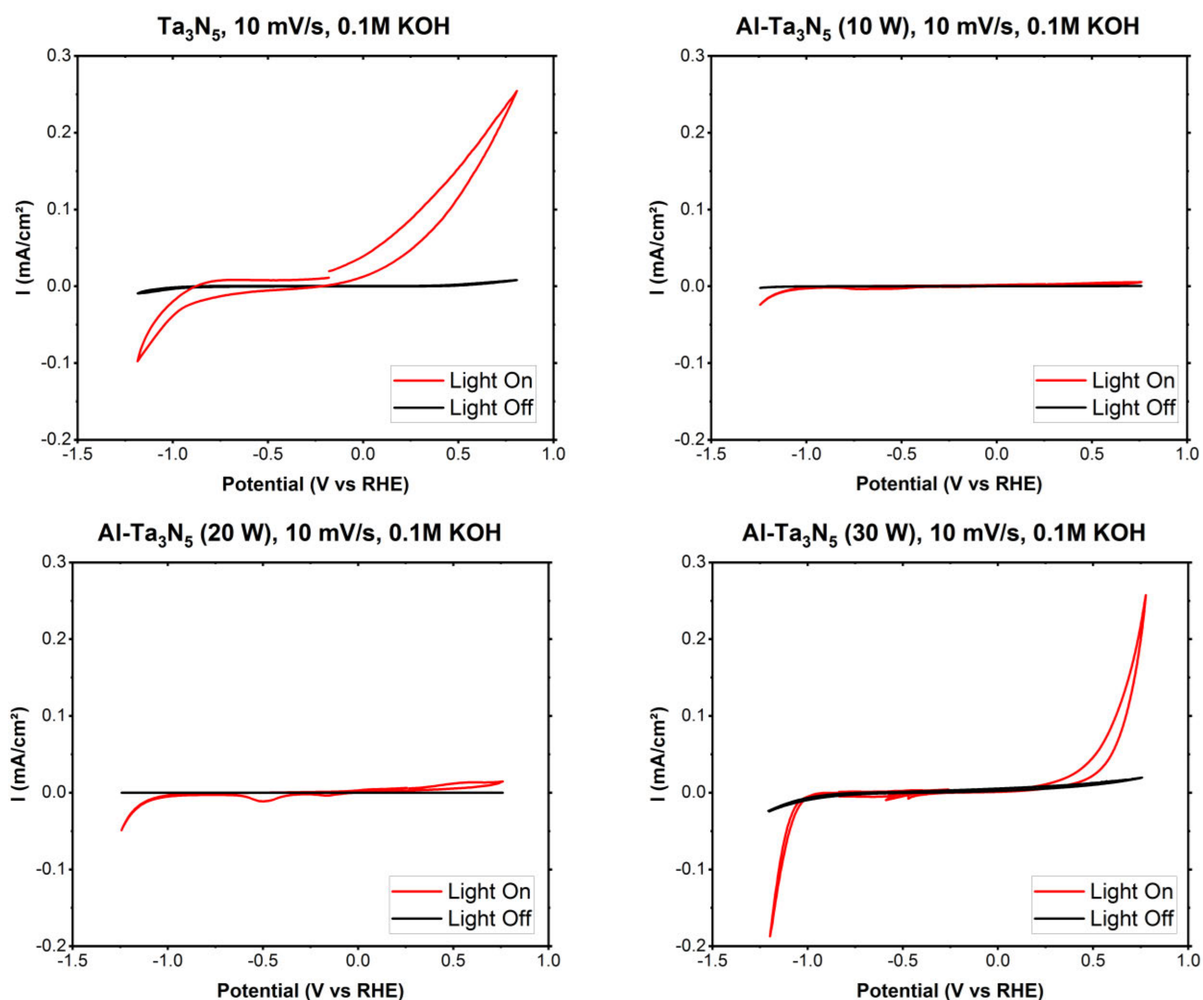

Figure 8-54. Cyclic Voltammetry scans of Al-Ta_3N_5 films and Ta_3N_5 standard performed at 10mV/s under 100mW/cm^2 of illumination and in the dark.

Looking at the 10W doped film first, a light response can be seen over the cathodic voltage range selected, however the photocurrents observed are negligible compared to the Ta_3N_5 standard. The photocurrent onset can be seen after 0 V vs RHE but is small within the voltage range used. The 10W film possessed very little aluminium as per EDS and SIMS results given in section 8.3.3, while XRD results presented in the same section agreed: only the Ta_3N_5 phase was identified in the 10W sample. Additionally, the UV-Vis results (Figure 8-49) for the 10W film exhibited a similar absorption edge to the Ta_3N_5 standard. As a result, the carrier concentration for the 10W film, shown in Table 8.17, is also comparable to the Ta_3N_5 standard, albeit is an order of magnitude lower.

A similar scan can be seen for the 20W doped film, although the carrier concentration indicates that holes are the majority charge carrier for this film. The formation of a thin surface Ta_2O_5 layer (He et al. 2016) could be blamed for the suppressed photocurrent, however this does not account for the photocurrent observed in the standard and 30W films. Nonetheless, as Al

loading is increased (20W and 30W films), an increased anodic and cathodic photocurrent is observed in comparison to the standard film, which exhibits a large anodic photocurrent of ~0.27 mA/cm^2 at 0.75 V vs RHE. Small current drops in the illuminated traces can be seen in the 20W and 30W scans, around -0.5 V vs RHE, which could be attributed to O_2 species adsorbed at the surface undergoing reduction. In conclusion, these results indicate that Al loading under the synthetic conditions presented improve the photocathodic response relative to the standard Ta_3N_5 film, although the observed photocurrents are low in comparison to cutting edge devices (Zhong et al. 2017).

Impedance analysis was performed for the Al doped samples and Mott-Schottky plots generated from the calculated capacitance and applied potential. This was done to provide a secondary measurement of the carrier concentration. These plots can be seen below in **Figure 8-55**.

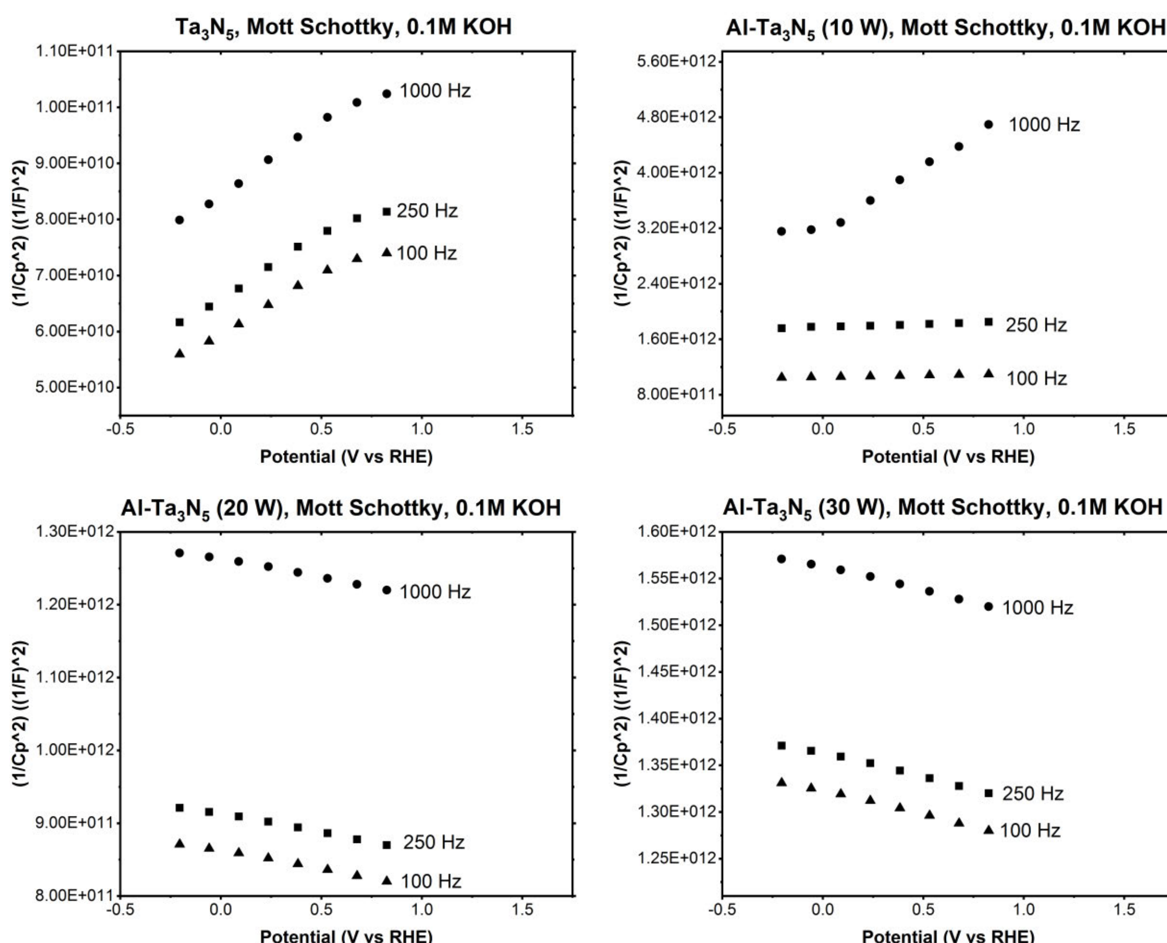

Figure 8-55. Mott-Schottky plot of Al-Ta_3N_5 and Ta_3N_5 electrodes performed in 0.1M KOH electrolyte solution at 100Hz, 250Hz and 1000Hz across an applied potential range of -1V to 1.5V.

Mott Schottky plots for the Al-Ta_3N_5 films exhibit a linear capacitance/V vs RHE relationship, relative to the Cr doped films, which enables determination of the carrier concentration. Plots

for the 20 W and 30 W films indicate a p-type material due to the negative slopes, relative to the positive slopes for the n-type Ta_3N_5 standard shown above (Bott 1998; Joshi & Maggard 2012; Kyle et al. 2015). The dopant density was calculated to be $N_D = 1.592\text{x}10^{17}$ cm^{-3} for the 10W film, $N_D = 5.240\text{x}10^{17}$ cm^{-3} for the 20W film and $N_D = 5.031\text{x}10^{19}$, for the 30W film, based on the slope of the 1000Hz scan. These results are broadly comparable to the Hall measurements given in Table 8.17. In conclusion, the aluminium doped films show promising results compared to the chromium doped films but further investigation is required to determine the role of aluminium in producing these results, especially the CV scans for the 10W and 20W films.

9 Conclusions

The primary aim of this thesis was to synthesize Ta_3N_5 thin films via magnetron sputtering with controlled performance related properties for use as a photo-electrode material. This chapter distils the main findings of this thesis as they pertain to the preparation of Ta_3N_5 prepared by sputtering in this project. Finally, a discussion of the possibilities for future work are provided.

9.1 Conclusions

The primary aim of this work was to synthesize Ta_3N_5 thin films via magnetron sputtering, and secondly to drive p-type conductivity via acceptor doping of the films for use in photo-electrochemical cells. The Ta_3N_5 phase is established as a compelling material for solar water-splitting research efforts. The reason for this is its convenient band gap which allows the absorption of a large part of the solar spectrum (~610nm), and band edge positions that straddle the redox potentials of water, enabling Ta_3N_5 to simultaneously perform the oxidation and reduction of water under visible light. However the phase is difficult to synthesize as it possesses both the highest at. % of nitrogen of all tantalum nitride phases, and the Ta species in the +5 oxidation state, as opposed to the majority of other phases in the tantalum nitride phase spectrum which possess Ta in the +3 oxidation state.

These two factors make deposition of the phase difficult; the conditions to synthesize the phase require high nitrogen partial pressures and a method of driving charge in the deposited Ta species from Ta^{3+} to Ta^{5+}. Regarding the former, when high nitrogen partial pressures were explored in this project, it did not drive formation of the phase, nor did adjustments to the total deposition pressure and substrate temperature. These parameters resulted in the deposition of various phases in the TaN phase spectrum, predominantly δ-TaN, but also preferred orientations of the phase. Predictably, increasing substrate temperature improved film crystallinity and altered the dominant plane in the films, but did not drive synthesis of the Ta_3N_5 phase.

It is demonstrated in the literature that incorporating oxygen during deposition is important in driving the formation of the Ta_3N_5 phase, however the inclusion of O_2 during sputtering did not promote synthesis of the phase and instead produced TaN films with poor crystallinity and oxygen impurities. The conclusion being that Ta is still sputtered in the +3 oxidation state even when oxygen is introduced with the deposition conditions presented. Further experimentation may determine the appropriate parameters to achieve the Ta_3N_5 phase directly with the equipment used, however this was not done for reasons of time constraints. Regardless, even in cases where the Ta_3N_5 is deposited with magnetron sputtering, post-deposition annealing in NH_3 is still required to purge excess residual oxygen in the lattice.

The Ta_3N_5 phase was instead synthesized via annealing tantalum oxide films in NH_3, mirroring the traditional synthetic route, which is less desirable because of the defects imparted by high temperature treatment and the use of sensitive and corrosive gas mixtures. Producing Ta_3N_5 films via this route proved reproducible and the dopants of chromium and aluminium were incorporated into the films during deposition. A mechanism for the conversion of Ta_2O_5 to Ta_3N_5 was provided to justify the importance of NH_3 in stabilising the Ta^{5+} species, and to fill the mechanistic gap that exists in the current literature pertaining to the synthesis of Ta_3N_5.

The amount of chromium in the films was effectively controlled using target power during the deposition of the precursor films. XRD analysis of films with low amounts of chromium showed the Ta_3N_5 phase with oxygen impurities, while films with higher amounts of chromium exhibited an exsolved phase that was determined to be a chromium nitride. The chromium solubility limit in Ta_3N_5 was concluded to be less than 6 at. %, it was shown that the limit of Cr solubility in Ta_3N_5 is limited by the Cr limit in Ta_2O_5 due to the specific approach applied in this investigation.

Hall and electrochemical analysis showed the disruptive effect of Cr on the electronic properties of the films; photo-response was suppressed as Cr loading increased, capacitance increased and Mott-Shottky results for highly doped films were questionable. These results were attributed to the CrN phase noted in XRD results.

Aluminium doped tantalum oxide films were successfully deposited and control over the aluminium content was achieved using the applied power to the aluminium target. These films were then successfully reacted into crystalline aluminium doped Ta_3N_5 films with no secondary phases detected in XRD results, in contrast to the chromium doped films. SIMS analysis revealed small amounts of aluminium in all doped films, however EDS only detected aluminium in the films deposited at 20 W and 30 W, with the 30 W Al-Ta3N5 film exhibiting 11% at. Al after annealing. Aluminium solubility in Ta_3N_5 does not appear to face the same limitations as with chromium, as no secondary aluminium phase emerged as aluminium doping increased. The aluminium solubility limit was not observed at the highest Al doping investigated in this work.

Finally, Hall and electrochemical characterisation pertaining to the Al-Ta_3N_5 films suggested p-type carrier concentrations, with improved photocathode response under illumination relative to the undoped standard observed in the film with highest aluminium loading (30W aluminium). Mott-Schottky plots for the aluminium doped films produced carrier concentration values in broad agreement with the Hall measurement results for the same films.

9.2 Future Work and Outlook

Opportunities for future work can be categorised either as expanding on the synthetic methodology, or further investigating the electrochemical characteristics of the films synthesized in this work.

First, the core challenge of this work was synthesizing Ta_3N_5 via sputter deposition, and failing that, explaining the difficulty in doing so and accounting for the reason why the phase could not be deposited directly. Answering this question could constitute a future study itself and would include plasma analysis techniques to evaluate characteristics of the in-situ deposition environment.

Additionally, there were multiple aspects of the synthetic work that received limited attention due to time and equipment constraints, these include:

- Substrate selection. Silicon substrates were almost exclusively used due to film adhesion under high temperature treatment. Investigations have determined the importance of substrate selection in terms of Ta_3N_5 epitaxial film growth (Rudolph, Martin 2017).
- The prevailing strategy for improving the solar water splitting efficacy of Ta_3N_5 in the literature is the inclusion of co-layers, which stabilise Ta_3N_5 against photocorrosion via hole-storage layers. This strategy was not examined in this work.
- There is also the prospect of evaluating more dopants in Ta_3N_5. Many of these potential metals are listed in Table 8.6.
- Future work may also expand on the tantalum oxide (doped and undoped) sintering kinetics, ideally with a method of in-situ analysis such as high temperature XRD.

Finally, there is the electrochemical work, which showed Cr to be detrimental to the optoelectronic properties of Ta_3N_5 but indicated Al as a potential acceptor dopant for future performance studies in driving p-type behaviour in Ta_3N_5 films. Future work could investigate the effect of Cr doping in more detail or look to determine the role of aluminium doping in driving p-type behaviour in Ta_3N_5.

10 References

Abe, R, Higashi, M & Domen, K 2010, 'Facile Fabrication of an Efficient Oxynitride TaON Photoanode for Overall Water Splitting into H_2 and O_2 under Visible Light Irradiation', *Journal of the American Chemical Society*, vol. 132, no. 34, pp. 11828-9, DOI 10.1021/ja1016552, <http://dx.doi.org/10.1021/ja1016552>.

Abe, R, Takata, T, Sugihara, H & Domen, K 2005, 'Photocatalytic overall water splitting under visible light by TaON and WO_3 with an IO_3^-/I^- shuttle redox mediator', *Chemical Communications*, no. 30, pp. 3829-31.

Ahmad, H, Kamarudin, SK, Minggu, LJ & Kassim, M 2015, 'Hydrogen from photo-catalytic water splitting process: A review', *Renewable and Sustainable Energy Reviews*, vol. 43, pp. 599-610, DOI http://dx.doi.org/10.1016/j.rser.2014.10.101, <http://www.sciencedirect.com/science/article/pii/S1364032114009265>.

Akiyama, S, Nakabayashi, M, Shibata, N, Minegishi, T, Asakura, Y, Abdulla-Al-Mamun, M et al. 2016, 'Highly Efficient Water Oxidation Photoanode Made of Surface Modified $LaTiO_2N$ Particles', *Small*, vol. 12, no. 39, pp. 5468-76, DOI 10.1002/smll.201601929, <http://dx.doi.org/10.1002/smll.201601929>.

Alishahi, M, Mahboubi, F, Khoie, SM, Aparicio, M, Lopez-Elvira, E, Méndez, J et al. 2016, 'Structural properties and corrosion resistance of tantalum nitride coatings produced by reactive DC magnetron sputtering', *RSC Advances*, vol. 6, no. 92, pp. 89061-72.

American Society for Testing Materials 2003, ASTM international, Committee G03 on Weathering Durability.

An, J & Zhang, Q 2007, 'Structure, hardness and tribological properties of nanolayered TiN/TaN multilayer coatings', *Materials characterization*, vol. 58, no. 5, pp. 439-46.

Arévalo-López, ÁM & Alario-Franco, MÁ 2009, 'Reliable Method for Determining the Oxidation State in Chromium Oxides', *Inorganic Chemistry*, vol. 48, no. 24, pp. 11843-6, DOI 10.1021/ic901887y, <https://doi.org/10.1021/ic901887y>.

Arshi, N, Lu, J, Lee, CG, Koo, BH & Ahmed, F 2014, 'Effects of Nitrogen Content on the Phase and Resistivity of TaN Thin Films Deposited by Electron Beam Evaporation', *JOM*, vol. 66, no. 9, pp. 1893-9, DOI 10.1007/s11837-014-1028-6, <https://doi.org/10.1007/s11837-014-1028-6>.

Baba, K & Hatada, R 1996, 'Synthesis and properties of tantalum nitride films formed by ion beam assisted deposition', *Surface and Coatings Technology*, vol. 84, no. 1, pp. 429-33, DOI http://dx.doi.org/10.1016/S0257-8972(95)02799-8, <http://www.sciencedirect.com/science/article/pii/S0257897295027998>.

Balachandran, U & Eror, NG 1982, 'Electrical conductivity in Ta_2O_5', *Materials Research Bulletin*, vol. 17, no. 2, pp. 151-60.

Bard, AJ & Fox, MA 1995, 'Artificial photosynthesis: solar splitting of water to hydrogen and oxygen', *Accounts of Chemical Research*, vol. 28, no. 3, pp. 141-5.

Bayrak Pehlivan, İ, Edoff, M, Stolt, L & Edvinsson, T 2019, 'Optimum Band Gap Energy of ((Ag),Cu)(InGa)Se2 Materials for Combination with NiMo–NiO Catalysts for Thermally Integrated Solar-Driven Water Splitting Applications', *Energies*, vol. 12, no. 21, p. 4064, <https://www.mdpi.com/1996-1073/12/21/4064>.

Belver, C, Bedia, J, Gómez-Avilés, A, Peñas-Garzón, M & Rodriguez, JJ 2019, 'Semiconductor Photocatalysis for water purification', in *Nanoscale Materials in Water Purification*, Elsevier, pp. 581-651.

Bithas, K & Kalimeris, P 2016, 'A Brief History of Energy Use in Human Societies', in *Revisiting the Energy-Development Link: Evidence from the 20th Century for Knowledge-based and Developing Economies*, Springer International Publishing, Cham, pp. 5-10.

Boden, TA, Marland, G & Andres, RJ 2009, 'Global, regional, and national fossil-fuel CO2 emissions', *Carbon Dioxide Information Analysis Center, Oak Ridge National Laboratory, US Department of Energy, Oak Ridge, Tenn., USA doi*, vol. 10.

Borovinskaya, IP 2017, 'Tantalum Nitride', in IP Borovinskaya, AA Gromov, EA Levashov, YM Maksimov, AS Mukasyan & AS Rogachev (eds), *Concise Encyclopedia of Self-Propagating High-Temperature Synthesis*, Elsevier, Amsterdam, pp. 370-1.

Bott, AW 1998, 'Electrochemistry of semiconductors', *Current Separations*, vol. 17, pp. 87-92.

Bousquet, A, Zoubian, F, Cellier, J, Sauvage, T & Tomasella, E 2013, 'Control the Composition of Tantalum Oxynitride Films by Sputtering a Tantalum Target in Ar/O2/N2 Radiofrequency Magnetron Plasmas', *Plasma Processes and Polymers*, vol. 10, no. 11, pp. 990-8, DOI 10.1002/ppap.201300036, <http://dx.doi.org/10.1002/ppap.201300036>.

Boyko, T, Hunt, A, Zerr, A & Moewes, A 2013, 'Electronic structure of spinel-type nitride compounds Si 3 N 4, Ge 3 N 4, and Sn 3 N 4 with tunable band gaps: application to light emitting diodes', *Physical Review Letters*, vol. 111, no. 9, p. 097402.

Bräuer, G, Szyszka, B, Vergöhl, M & Bandorf, R 2010, 'Magnetron sputtering–Milestones of 30 years', *Vacuum*, vol. 84, no. 12, pp. 1354-9.

Brauer, G & Weidlein, J 1965, 'Synthesis and properties of red tantalum nitride Ta3N5', *Angewandte Chemie International Edition*, vol. 4, no. 3, pp. 241-2.

Brese, NE, O'Keeffe, M, Rauch, P & DiSalvo, FJ 1991, 'Structure of Ta3N5 at 16 K by time-of-flight neutron diffraction', *Acta Crystallographica Section C: Crystal Structure Communications*, vol. 47, no. 11, pp. 2291-4.

Brownson, J 2020, *The Air Mass useed in Engineering Testing*, Pennsylvania State University, <https://www.e-education.psu.edu/eme810/node/469>.

Cao, S & Yu, J 2014, 'g-C3N4-Based Photocatalysts for Hydrogen Generation', *The Journal of Physical Chemistry Letters*, vol. 5, no. 12, pp. 2101-7, DOI 10.1021/jz500546b, <http://dx.doi.org/10.1021/jz500546b>.

Cardenas-Morcoso, D, Peiro-Franch, A, Herraiz-Cardona, I & Gimenez, S 2017, 'Chromium doped copper vanadate photoanodes for water splitting', *Catalysis today*, vol. 290, pp. 65-72.

Cardona, M & Peter, YY 2005, *Fundamentals of semiconductors*, Springer.

Chaneliere, C, Autran, J, Devine, R & Balland, B 1998, 'Tantalum pentoxide (Ta2O5) thin films for advanced dielectric applications', *Materials Science and Engineering: R: Reports*, vol. 22, no. 6, pp. 269-322.

Chang, J-C, Eriksson, F, Sortica, MA, Greczynski, G, Bakhit, B, Hu, Z et al. 2020, 'Orthorhombic Ta3-xN5-yOy thin films grown by unbalanced magnetron sputtering: The role of oxygen on structure, composition, and optical properties', *Surface and Coatings Technology*, p. 126665, DOI https://doi.org/10.1016/j.surfcoat.2020.126665, <http://www.sciencedirect.com/science/article/pii/S0257897220313359>.

Chanhoon, K, Gaeun, H, Ji-Won, J, Su-Ho, C, Young, CJ, Sunghee, S et al. 2017, 'Fast, Scalable Synthesis of Micronized Ge3N4@C with a High Tap Density for Excellent Lithium Storage', *Advanced Functional Materials*, vol. 27, no. 14, p. 1605975, DOI doi:10.1002/adfm.201605975, <https://onlinelibrary.wiley.com/doi/abs/10.1002/adfm.201605975>.

Chaoumead, A, Sung, Y-m & Kwak, D-J 2012, 'The effects of RF sputtering power and gas pressure on structural and electrical properties of ITiO thin film', *Advances in Condensed Matter Physics*, vol. 2012.

Chauhan, DB, Chauhan, KV, Sonera, AL, Makwana, NS, Dave, DP & Rawal, SK 2018, 'Study the effect of nitrogen flow rate on tribological properties of tantalum nitride based coatings', *AIP Publishing*, vol. 1953, no. 1, p. 030150.

Chen, S, Qi, Y, Hisatomi, T, Ding, Q, Asai, T, Li, Z et al. 2015, 'Efficient Visible-Light-Driven Z-Scheme Overall Water Splitting Using a MgTa2O6− xNy/TaON Heterostructure Photocatalyst for H2 Evolution', *Angewandte Chemie International Edition*, vol. 54, no. 29, pp. 8498-501.

Chen, S, Shen, S, Liu, G, Qi, Y, Zhang, F & Li, C 2015, 'Interface Engineering of a CoOx/Ta3N5 Photocatalyst for Unprecedented Water Oxidation Performance under Visible-Light-Irradiation', *Angewandte Chemie International Edition*, vol. 54, no. 10, pp. 3047-51.

Chun, W-J, Ishikawa, A, Fujisawa, H, Takata, T, Kondo, JN, Hara, M et al. 2003, 'Conduction and Valence Band Positions of Ta2O5, TaON, and Ta3N5 by UPS and Electrochemical Methods', *The Journal of Physical Chemistry B*, vol. 107, no. 8, pp. 1798-803, DOI 10.1021/jp027593f, <http://dx.doi.org/10.1021/jp027593f>.

Conroy, LE & Christensen, AN 1977, 'Preparation and crystal structure of β-Ta2N', *Journal of Solid State Chemistry*, vol. 20, no. 2, pp. 205-7, DOI https://doi.org/10.1016/0022-4596(77)90069-X, <http://www.sciencedirect.com/science/article/pii/002245967790069X>.

Constantin, C, Haider, MB, Ingram, D & Smith, AR 2004, 'Metal/semiconductor phase transition in chromium nitride (001) grown by rf-plasma-assisted molecular-beam epitaxy', *Applied Physics Letters*, vol. 85, no. 26, pp. 6371-3.

Contoux, G, Cosset, F, Celerier, A & Machet, J 1997, 'Deposition process study of chromium oxide thin filmsobtained by dc magnetron sputtering', *Thin Solid Films*, vol. 292, no. 1-2, pp. 75-84.

Cristea, D, Cunha, L, Gabor, C, Ghiuta, I, Croitoru, C, Marin, A et al. 2019, 'Tantalum Oxynitride Thin Films: Assessment of the Photocatalytic Efficiency and Antimicrobial Capacity', *Nanomaterials*, vol. 9, no. 3, p. 476.

Dabirian, A, Spijker, Hvt & van de Krol, R 2012, 'Wet ammonia Synthesis of Semiconducting N:Ta2O5, Ta3N5 and β-TaON Films for Photoanode Applications', *Energy Procedia*, vol. 22, pp. 15-22, DOI https://doi.org/10.1016/j.egypro.2012.05.222, <http://www.sciencedirect.com/science/article/pii/S1876610212010156>.

Dang, HX, Hahn, NT, Park, HS, Bard, AJ & Mullins, CB 2012, 'Nanostructured Ta3N5 Films as Visible-Light Active Photoanodes for Water Oxidation', *The Journal of Physical Chemistry C*, vol. 116, no. 36, pp. 19225-32, DOI 10.1021/jp307369z, <http://dx.doi.org/10.1021/jp307369z>.

Depla, D & De Gryse, R 2004, 'Target poisoning during reactive magnetron sputtering: Part I: the influence of ion implantation', *Surface and Coatings Technology*, vol. 183, no. 2-3, pp. 184-9.

Depla, D & De Gryse, R 2004, 'Target poisoning during reactive magnetron sputtering: Part II: the influence of chemisorption and gettering', *Surface and Coatings Technology*, vol. 183, no. 2, pp. 190-5, DOI https://doi.org/10.1016/j.surfcoat.2003.10.007, <https://www.sciencedirect.com/science/article/pii/S0257897203011368>.

Dial, S 2008, *Plot of selected energy densities (excluding oxidizers)*, viewed 08 August 2019.

Etourneau, J, Portier, J & Menil, F 1992, 'The role of the inductive effect in solid state chemistry: how the chemist can use it to modify both the structural and the physical properties of the materials', *Journal of Alloys and Compounds*, vol. 188, pp. 1-7.

Fan, G, Fang, T, Wang, X, Zhu, Y, Fu, H, Feng, J et al. 2019, 'Interfacial Effects on the Band Edges of Ta3N5 Photoanodes in an Aqueous Environment: A Theoretical View', *Iscience*, vol. 13, pp. 432-9.

Fang, C, Orhan, E, De Wijs, G, Hintzen, H, De Groot, R, Marchand, R et al. 2001, 'The electronic structure of tantalum (oxy) nitrides TaON and Ta3N5', *Journal of Materials Chemistry*, vol. 11, no. 4, pp. 1248-52.

Farrell, AE, Keith, DW & Corbett, JJ 2003, 'A strategy for introducing hydrogen into transportation', *Energy policy*, vol. 31, no. 13, pp. 1357-67.

Feiner, A-S & McEvoy, A 1994, 'The nernst equation', *Journal of chemical education*, vol. 71, no. 6, p. 493.

Feng, X, LaTempa, TJ, Basham, JI, Mor, GK, Varghese, OK & Grimes, CA 2010, 'Ta3N5 nanotube arrays for visible light water photoelectrolysis', *Nano letters*, vol. 10, no. 3, pp. 948-52.

Firouzabadi, S, Naderi, M, Dehghani, K & Mahboubi, F 2017, 'Effect of nitrogen flow ratio on nano-mechanical properties of tantalum nitride thin film', *Journal of Alloys and Compounds*, vol. 719, pp. 63-70.

Fix, R, Gordon, RG & Hoffman, DM 1993, 'Chemical vapor deposition of vanadium, niobium, and tantalum nitride thin films', *Chemistry of materials*, vol. 5, no. 5, pp. 614-9.

Fu, G, Yan, S, Yu, T & Zou, Z 2015, 'Oxygen related recombination defects in Ta3N5 water splitting photoanode', *Applied Physics Letters*, vol. 107, no. 17, p. 171902, DOI 10.1063/1.4934758, <http://aip.scitation.org/doi/abs/10.1063/1.4934758>.

Fujishima, A & Honda, K 1972, 'Photolysis-decomposition of water at the surface of an irradiated semiconductor', *Nature*, vol. 238, no. 5385, pp. 37-8.

Gates, DM 1966, 'Spectral Distribution of Solar Radiation at the Earth's Surface', *Science*, vol. 151, no. 3710, pp. 523-9, viewed 2020/05/31/, JSTOR, <www.jstor.org/stable/1717033>.

Gelderman, K, Lee, L & Donne, S 2007, 'Flat-band potential of a semiconductor: using the Mott–Schottky equation', *Journal of chemical education*, vol. 84, no. 4, p. 685.

Gladczuk, L, Patel, A, Demaree, JD & Sosnowski, M 2005, 'Sputter deposition of bcc tantalum films with TaN underlayers for protection of steel', *Thin Solid Films*, vol. 476, no. 2, pp. 295-302, DOI https://doi.org/10.1016/j.tsf.2004.10.020, <http://www.sciencedirect.com/science/article/pii/S0040609004014476>.

Goklany, IM 2007, *The improving state of the world: why we're living longer, healthier, more comfortable lives on a cleaner planet*, Cato Institute.

Goldschmidt, HJ 1967, *Interstitial Alloys*, 1 edn, vol. 1, Butterworth & Co., Great Britain.

Grigorescu, S, Bärhausen, B, Wang, L, Mazare, A, Yoo, JE, Hahn, R et al. 2015, 'Tungsten doping of Ta3N5-nanotubes for band gap narrowing and enhanced photoelectrochemical water splitting efficiency', *Electrochemistry communications*, vol. 51, pp. 85-8, DOI http://dx.doi.org/10.1016/j.elecom.2014.12.019, <http://www.sciencedirect.com/science/article/pii/S1388248114004007>.

Grosser, M, Seidel, H & Schmid, U 2017, 'Microstructure and mechanical properties of sputter deposited tantalum nitride thin films after high temperature loading', *Thin Solid Films*, vol. 629, pp. 69-78.

Gudmundsson, JT & Lundin, D 2020, '1 - Introduction to magnetron sputtering', in D Lundin, T Minea & JT Gudmundsson (eds), *High Power Impulse Magnetron Sputtering*, Elsevier, pp. 1-48.

Guglya, A & Lyubchenko, E 2018, 'Chapter 4 - Ion-beam-assisted deposition of thin films', in A Barhoum & ASH Makhlouf (eds), *Emerging Applications of Nanoparticles and Architecture Nanostructures*, Elsevier, pp. 95-119.

Hamann, T 2016, 'Photoelectrochemical Investigation of Ta3N5 Films on TCO Substrates Synthesized Via Atomic Layer Deposition for Photocatalytic Water Splitting', *The Electrochemical Society*, no. 38, pp. 1905-.

Hara, M, Chiba, E, Ishikawa, A, Takata, T, Kondo, JN & Domen, K 2003, 'Ta3N5 and TaON Thin Films on Ta Foil: Surface Composition and Stability', *The Journal of Physical Chemistry B*, vol. 107, no. 48, pp. 13441-5, DOI 10.1021/jp036189t, <http://dx.doi.org/10.1021/jp036189t>.

Hara, M, Takata, T, Kondo, JN & Domen, K 2004, 'Photocatalytic reduction of water by TaON under visible light irradiation', *Catalysis today*, vol. 90, no. 3, pp. 313-7, DOI

https://doi.org/10.1016/j.cattod.2004.04.040,
<http://www.sciencedirect.com/science/article/pii/S0920586104001609>.

Harb, M & Basset, J-M 2020, 'Predicting the Most Suitable Surface Candidates of Ta3N5 Photocatalysts for Water-Splitting Reactions Using Screened Coulomb Hybrid DFT Computations', *The Journal of Physical Chemistry C*, vol. 124, no. 4, pp. 2472-80, DOI 10.1021/acs.jpcc.9b09707, <https://doi.org/10.1021/acs.jpcc.9b09707>.

He, Y, Thorne, JE, Wu, CH, Ma, P, Du, C, Dong, Q et al. 2016, 'What Limits the Performance of Ta 3 N 5 for Solar Water Splitting?', *Chem*, vol. 1, no. 4, pp. 640-55.

Hieber, K 1974, 'Structural and electrical properties of Ta and Ta nitrides deposited by chemical vapour deposition', *Thin Solid Films*, vol. 24, no. 1, pp. 157-64, DOI http://dx.doi.org/10.1016/0040-6090(74)90261-2, <http://www.sciencedirect.com/science/article/pii/0040609074902612>.

Higashi, M, Abe, R, Ishikawa, A, Takata, T, Ohtani, B & Domen, K 2008, 'Z-scheme Overall Water Splitting on Modified-TaON Photocatalysts under Visible Light (λ < 500 nm)', *Chemistry letters*, vol. 37, no. 2, pp. 138-9.

Higashi, M, Domen, K & Abe, R 2011, 'Fabrication of efficient TaON and Ta3N5 photoanodes for water splitting under visible light irradiation', *Energy & Environmental Science*, vol. 4, no. 10, pp. 4138-47, DOI 10.1039/C1EE01878G, <http://dx.doi.org/10.1039/C1EE01878G>.

Higashi, M, Domen, K & Abe, R 2012, 'Highly stable water splitting on oxynitride TaON photoanode system under visible light irradiation', *Journal of the American Chemical Society*, vol. 134, no. 16, pp. 6968-71.

Hisatomi, T & Kazunari Domen, K 2009, 'Recent progress in photocatalysts for overall water splitting under visible light', *Proceedings of solar hydrogen and nanotechnology*, vol. 7408, pp. 740802-1.

Hitoki, G, Ishikawa, A, Takata, T, Kondo, JN, Hara, M & Domen, K 2002, 'Ta3N5 as a novel visible light-driven photocatalyst (λ< 600 nm)', *Chemistry letters*, vol. 31, no. 7, pp. 736-7.

Holl, MMB, Kersting, M, Pendley, BD & Wolczanski, PT 1990, 'Ammonolysis of tantalum alkyls: formation of cubic tantalum nitride and a trimeric nitride,[Cp* MeTaN] 3 tris [(. eta. 5-pentamethylcyclopentadienyl)(methyl) nitridotantalum]', *Inorganic Chemistry*, vol. 29, no. 8, pp. 1518-26.

Holladay, JD, Hu, J, King, DL & Wang, Y 2009, 'An overview of hydrogen production technologies', *Catalysis today*, vol. 139, no. 4, pp. 244-60.

Hones, P, Diserens, M & Lévy, F 1999, 'Characterization of sputter-deposited chromium oxide thin films', *Surface and Coatings Technology*, vol. 120-121, pp. 277-83, DOI https://doi.org/10.1016/S0257-8972(99)00384-9,
<http://www.sciencedirect.com/science/article/pii/S0257897299003849>.

Hou, J, Yang, C, Cheng, H, Jiao, S, Takeda, O & Zhu, H 2014, 'High-performance p-Cu 2 O/n-TaON heterojunction nanorod photoanodes passivated with an ultrathin carbon sheath for photoelectrochemical water splitting', *Energy & Environmental Science*, vol. 7, no. 11, pp. 3758-68.

Hsiang, S, Kopp, R, Jina, A, Rising, J, Delgado, M, Mohan, S et al. 2017, 'Estimating economic damage from climate change in the United States', *Science*, vol. 356, no. 6345, pp. 1362-9.

Hu, Y, Zhu, J, Zhang, C, Yang, W, Fu, L, Li, D et al. 2019, 'Understanding the Preferred Crystal Orientation of Sputtered Silver in Ar/N₂ Atmosphere: A Microstructure Investigation', *Advances in Materials Science and Engineering*, vol. 2019, p. 3079393, DOI 10.1155/2019/3079393, <https://doi.org/10.1155/2019/3079393>.

Huda, MN, Yan, Y, Wei, S-H & Al-Jassim, MM 2008, 'Electronic structure of ZnO:GaN compounds: Asymmetric bandgap engineering', *Physical Review B*, vol. 78, no. 19, p. 195204, <https://link.aps.org/doi/10.1103/PhysRevB.78.195204>.

Ishikawa, A, Takata, T, Kondo, JN, Hara, M & Domen, K 2004, 'Electrochemical Behavior of Thin Ta3N5 Semiconductor Film', *The Journal of Physical Chemistry B*, vol. 108, no. 30, pp. 11049-53, DOI 10.1021/jp048802u, <http://dx.doi.org/10.1021/jp048802u>.

Jenkins, T 2005, 'A brief history of... semiconductors', *Physics education*, vol. 40, no. 5, p. 430.

Jiang, Y, Jing, X, Zhu, K, Peng, Z, Zhang, J, Liu, Y et al. 2018, 'Ta 3 N 5 nanoparticles/TiO 2 hollow sphere (0D/3D) heterojunction: facile synthesis and enhanced photocatalytic activities of levofloxacin degradation and H 2 evolution', *Dalton Transactions*, vol. 47, no. 37, pp. 13113-25.

Johnston, B, Mayo, MC & Khare, A 2005, 'Hydrogen: the energy source for the 21st century', *Technovation*, vol. 25, no. 6, pp. 569-85.

Jones, DR, Gomez, V, Bear, JC, Rome, B, Mazzali, F, McGettrick, JD et al. 2017, 'Active removal of waste dye pollutants using Ta 3 N 5/W 18 O 49 nanocomposite fibres', *Scientific reports*, vol. 7, no. 1, p. 4090.

Joshi, UA & Maggard, PA 2012, 'CuNb3O8: A p-Type Semiconducting Metal Oxide Photoelectrode', *The Journal of Physical Chemistry Letters*, vol. 3, no. 11, pp. 1577-81, DOI 10.1021/jz300477r, <https://doi.org/10.1021/jz300477r>.

Kado, Y, Hahn, R, Lee, C-Y & Schmuki, P 2012, 'Strongly enhanced photocurrent response for Na doped Ta3N5-nano porous structure', *Electrochemistry communications*, vol. 17, pp. 67-70, DOI http://dx.doi.org/10.1016/j.elecom.2012.01.028, <http://www.sciencedirect.com/science/article/pii/S1388248112000331>.

Kado, Y, Lee, C-Y, Lee, K, Müller, J, Moll, M, Spiecker, E et al. 2012, 'Enhanced water splitting activity of M-doped Ta 3 N 5 (M= Na, K, Rb, Cs)', *Chemical Communications*, vol. 48, no. 69, pp. 8685-7.

Kamimura, J, Bogdanoff, P, Abdi, FF, Lähnemann, J, van de Krol, R, Riechert, H et al. 2017, 'Photoelectrochemical Properties of GaN Photoanodes with Cobalt Phosphate Catalyst for Solar Water Splitting in Neutral Electrolyte', *The Journal of Physical Chemistry C*, vol. 121, no. 23, pp. 12540-5, DOI 10.1021/acs.jpcc.7b02253, <https://doi.org/10.1021/acs.jpcc.7b02253>.

Kang, CS, Cho, H-J, Kim, Y, Choi, R, Onishi, K, Shahriar, A et al. 2003, 'Characterization of resistivity and work function of sputtered-TaN film for gate electrode applications', *Journal of Vacuum Science & Technology B: Microelectronics and Nanometer Structures Processing, Measurement, and Phenomena*, vol. 21, no. 5, pp. 2026-8.

Kasahara, A, Nukumizu, K, Hitoki, G, Takata, T, Kondo, JN, Hara, M et al. 2002, 'Photoreactions on LaTiO2N under Visible Light Irradiation', *The Journal of Physical Chemistry A*, vol. 106, no. 29, pp. 6750-3, DOI 10.1021/jp025961+, <http://dx.doi.org/10.1021/jp025961+>.

Kasahara, A, Nukumizu, K, Takata, T, Kondo, JN, Hara, M, Kobayashi, H et al. 2003, 'LaTiO2N as a Visible-Light (≤600 nm)-Driven Photocatalyst (2)', *The Journal of Physical Chemistry B*, vol. 107, no. 3, pp. 791-7, DOI 10.1021/jp026767q, <http://dx.doi.org/10.1021/jp026767q>.

Katsushi, F, Takeshi, K & Kazuhiro, O 2005, 'Hydrogen Gas Generation by Splitting Aqueous Water Using n-Type GaN Photoelectrode with Anodic Oxidation', *Japanese Journal of Applied Physics*, vol. 44, no. 4L, p. L543, <http://stacks.iop.org/1347-4065/44/i=4L/a=L543>.

Kawashima, K, Hojamberdiev, M, Wagata, H, Yubuta, K, Oishi, S & Teshima, K 2015, 'Chloride Flux Growth of La2TiO5 Crystals and Nontopotactic Solid-State Transformation to LaTiO2N Crystals by Nitridation Using NH3', *Crystal Growth & Design*, vol. 15, no. 1, pp. 333-9, DOI 10.1021/cg501397x, <http://dx.doi.org/10.1021/cg501397x>.

Kawashima, K, Hojamberdiev, M, Wagata, H, Yubuta, K, Vequizo, JJM, Yamakata, A et al. 2015, 'NH3-Assisted Flux-Mediated Direct Growth of LaTiO2N Crystallites for Visible-Light-Induced Water Splitting', *The Journal of Physical Chemistry C*, vol. 119, no. 28, pp. 15896-904, DOI 10.1021/acs.jpcc.5b03718, <http://dx.doi.org/10.1021/acs.jpcc.5b03718>.

Kazuhiko, M & Kazunari, D 2016, 'Development of Novel Photocatalyst and Cocatalyst Materials for Water Splitting under Visible Light', *Bulletin of the Chemical Society of Japan*, vol. 89, no. 6, pp. 627-48, DOI 10.1246/bcsj.20150441, <http://www.journal.csj.jp/doi/abs/10.1246/bcsj.20150441>.

Kelly, PJ, Zhou, Y & Postill, A 2003, 'A novel technique for the deposition of aluminium-doped zinc oxide films', *Thin Solid Films*, vol. 426, no. 1, pp. 111-6, DOI https://doi.org/10.1016/S0040-6090(02)01332-9, <http://www.sciencedirect.com/science/article/pii/S0040609002013329>.

Kerlau, M, Merdrignac-Conanec, O, Guilloux-Viry, M & Perrin, A 2004, 'Synthesis of crystallized TaON and Ta3N5 by nitridation of Ta2O5 thin films grown by pulsed laser deposition', *Solid State Sciences*, vol. 6, no. 1, pp. 101-7.

Khan, S, Zapata, MJ, Pereira, MB, Gonçalves, RV, Strizik, L, Dupont, J et al. 2015, 'Structural, optical and photoelectrochemical characterizations of monoclinic Ta 3 N 5 thin films', *Physical Chemistry Chemical Physics*, vol. 17, no. 37, pp. 23952-62.

Khandelwal, B, Karakurt, A, Sekaran, PR, Sethi, V & Singh, R 2013, 'Hydrogen powered aircraft: The future of air transport', *Progress in Aerospace Sciences*, vol. 60, pp. 45-59.

Kibria, M, Zhao, S, Chowdhury, F, Wang, Q, Nguyen, H, Trudeau, M et al. 2014, 'Tuning the surface Fermi level on p-type gallium nitride nanowires for efficient overall water splitting', *Nature communications*, vol. 5, p. 3825.

Kibria, MG, Qiao, R, Yang, W, Boukahil, I, Kong, X, Chowdhury, FA et al. 2016, 'Atomic-Scale Origin of Long-Term Stability and High Performance of p-GaN Nanowire Arrays for Photocatalytic Overall Pure Water Splitting', *Advanced Materials*, vol. 28, no. 38, pp. 8388-97.

Kim, I-S, Cho, M-Y, Lee, D-W, Ko, P-J, Shin, WH, Park, C et al. 2020, 'Degradation behaviors and failure of magnetron sputter deposited tantalum nitride', *Thin Solid Films*, vol. 697, p. 137821.

Kim, S & Cha, B 2005, 'Deposition of tantalum nitride thin films by DC magnetron sputtering', *Thin Solid Films*, vol. 475, no. 1, pp. 202-7.

Kim, SK & Cha, BC 2005, 'Deposition of tantalum nitride thin films by D.C. magnetron sputtering', *Thin Solid Films*, vol. 475, no. 1, pp. 202-7, DOI http://dx.doi.org/10.1016/j.tsf.2004.08.059, <http://www.sciencedirect.com/science/article/pii/S004060900401171X>.

Kissinger, PT & Heineman, WR 1983, 'Cyclic voltammetry', *Journal of chemical education*, vol. 60, no. 9, p. 702.

Kofstad, P 1995, 'Defects and transport properties of metal oxides', *Oxidation of Metals*, vol. 44, no. 1, pp. 3-27, DOI 10.1007/BF01046721, <https://doi.org/10.1007/BF01046721>.

Koller, CM, Marihart, H, Bolvardi, H, Kolozsvári, S & Mayrhofer, PH 2018, 'Structure, phase evolution, and mechanical properties of DC, pulsed DC, and high power impulse magnetron sputtered Ta–N films', *Surface and Coatings Technology*, vol. 347, pp. 304-12, DOI https://doi.org/10.1016/j.surfcoat.2018.05.003, <http://www.sciencedirect.com/science/article/pii/S0257897218304705>.

Kyle, EC, Kaun, SW, Young, EC & Speck, JS 2015, 'Increased p-type conductivity through use of an indium surfactant in the growth of Mg-doped GaN', *Applied Physics Letters*, vol. 106, no. 22, p. 222103.

Laboratory, NRE 2018, *Hydrogen Production Pathways*, National Renewable Energy Laboratory, https://www.energy.gov/eere/fuelcells/hydrogen-production, viewed 3 July, 2018, <https://www.nrel.gov/docs/fy19osti/72776.pdf>.

Lee, Y, Watanabe, T, Takata, T, Hara, M, Yoshimura, M & Domen, K 2006, 'Effect of High-Pressure Ammonia Treatment on the Activity of Ge3N4 Photocatalyst for Overall Water Splitting', *The Journal of Physical Chemistry B*, vol. 110, no. 35, pp. 17563-9, DOI 10.1021/jp063068v, <http://dx.doi.org/10.1021/jp063068v>.

Léonard, F & Tersoff, J 2000, 'Role of Fermi-Level Pinning in Nanotube Schottky Diodes', *Physical Review Letters*, vol. 84, no. 20, pp. 4693-6, <https://link.aps.org/doi/10.1103/PhysRevLett.84.4693>.

Leroy, C, Sanjines, R, Sivula, K, Cornuz, M, Xanthopoulos, N, Laporte, V et al. 2012, 'TaOxNy sputtered photoanodes for solar water splitting', *Energy Procedia*, vol. 22, pp. 119-26.

Li, F, Jian, J, Xu, Y, Liu, W, Ye, Q, Feng, F et al. 2020, 'Surface defect passivation of Ta3N5 photoanode via pyridine grafting for enhanced photoelectrochemical performance', *The Journal of Chemical Physics*, vol. 153, no. 2, p. 024705, DOI 10.1063/5.0012873, <https://aip.scitation.org/doi/abs/10.1063/5.0012873>.

Li, Q, Li, X & Yu, J 2020, 'Chapter 10 - Surface and interface modification strategies of CdS-based photocatalysts', in J Yu, M Jaroniec & C Jiang (eds), *Interface Science and Technology*, vol. 31, Elsevier, pp. 313-48.

Li, W, Zhan, F, Li, J, Liu, C, Yang, Y, Li, Y et al. 2015, 'Enhancing photoelectrochemical water splitting by aluminum-doped plate-like WO3 electrodes', *Electrochimica Acta*, vol. 160, pp. 57-63, DOI

https://doi.org/10.1016/j.electacta.2015.01.095,
<http://www.sciencedirect.com/science/article/pii/S0013468615001152>.

Li, X 2007, 'Chapter One - Thermodynamic Performance of Fuel Cells and Comparison with Heat Engines', in TS Zhao, KD Kreuer & T Van Nguyen (eds), *Advances in Fuel Cells*, vol. 1, Elsevier Science, pp. 1-46.

Li, Y, Takata, T, Cha, D, Takanabe, K, Minegishi, T, Kubota, J et al. 2013, 'Vertically Aligned Ta3N5 Nanorod Arrays for Solar-Driven Photoelectrochemical Water Splitting', *Advanced Materials*, vol. 25, no. 1, pp. 125-31.

Li, Y, Zhang, L, Torres-Pardo, A, González-Calbet, JM, Ma, Y, Oleynikov, P et al. 2013, 'Cobalt phosphate-modified barium-doped tantalum nitride nanorod photoanode with 1.5% solar energy conversion efficiency', *Nature communications*, vol. 4, p. 2566.

Li, Z, Kong, C & Lu, G 2015, 'Visible photocatalytic water splitting and photocatalytic two-electron oxygen formation over Cu-and Fe-doped g-C3N4', *The Journal of Physical Chemistry C*, vol. 120, no. 1, pp. 56-63.

Ling, SJ, Sanny, J & Moebs, W 2016, *Semiconductors and Doping*,
<https://opentextbc.ca/universityphysicsv3openstax/chapter/semiconductors-and-doping/>.

Liu, D, Wang, C, Yu, Y, Zhao, B-H, Wang, W, Du, Y et al. 2019, 'Understanding the nature of ammonia treatment to synthesize oxygen vacancy-enriched transition metal oxides', *Chem*, vol. 5, no. 2, pp. 376-89.

Liu, G, Niu, P, Sun, C, Smith, SC, Chen, Z, Lu, GQ et al. 2010, 'Unique Electronic Structure Induced High Photoreactivity of Sulfur-Doped Graphitic C3N4', *Journal of the American Chemical Society*, vol. 132, no. 33, pp. 11642-8, DOI 10.1021/ja103798k, <http://dx.doi.org/10.1021/ja103798k>.

Liu, G, Shi, J, Zhang, F, Chen, Z, Han, J, Ding, C et al. 2014, 'A Tantalum Nitride Photoanode Modified with a Hole-Storage Layer for Highly Stable Solar Water Splitting', *Angewandte Chemie International Edition*, vol. 53, no. 28, pp. 7295-9.

Liu, G, Ye, S, Yan, P, Xiong, F, Fu, P, Wang, Z et al. 2016, 'Enabling an integrated tantalum nitride photoanode to approach the theoretical photocurrent limit for solar water splitting', *Energy & Environmental Science*, DOI 10.1039/C5EE03802B, <http://dx.doi.org/10.1039/C5EE03802B>.

Liu, J, Chen, G, Li, Z & Zhang, Z 2006, 'Electronic structure and visible light photocatalysis water splitting property of chromium-doped SrTiO3', *Journal of Solid State Chemistry*, vol. 179, no. 12, pp. 3704-8.

Liu, Z & Shen, Y 2005, 'Temperature effect on surface roughening of thin films', *Surface Science - SURFACE SCI*, vol. 595, pp. 20-9, DOI 10.1016/j.susc.2005.07.032.

Luo, J, Im, J-H, Mayer, MT, Schreier, M, Nazeeruddin, MK, Park, N-G et al. 2014, 'Water photolysis at 12.3% efficiency via perovskite photovoltaics and Earth-abundant catalysts', *Science*, vol. 345, no. 6204, pp. 1593-6.

Ma, SSK, Hisatomi, T, Maeda, K, Moriya, Y & Domen, K 2012, 'Enhanced water oxidation on Ta3N5 photocatalysts by modification with alkaline metal salts', *Journal of the American Chemical Society*, vol. 134, no. 49, pp. 19993-6.

Macartney, S, Liu, R, Wuhrer, R & Sheppard, LR 2020, 'Chromium Doping of Ta3N5 Thin Films via Thermal Nitridation of Sputtered Tantalum Oxide Films', *Materials Chemistry and Physics*, p. 123838.

Maeda, K & Domen, K 2007, 'New Non-Oxide Photocatalysts Designed for Overall Water Splitting under Visible Light', *The Journal of Physical Chemistry C*, vol. 111, no. 22, pp. 7851-61, DOI 10.1021/jp070911w, <http://dx.doi.org/10.1021/jp070911w>.

Maeda, K, Saito, N, Lu, D, Inoue, Y & Domen, K 2007, 'Photocatalytic Properties of RuO2-Loaded β-Ge3N4 for Overall Water Splitting', *The Journal of Physical Chemistry C*, vol. 111, no. 12, pp. 4749-55, DOI 10.1021/jp067254c, <http://dx.doi.org/10.1021/jp067254c>.

Maeda, K, Takata, T, Hara, M, Saito, N, Inoue, Y, Kobayashi, H et al. 2005, 'GaN: ZnO solid solution as a photocatalyst for visible-light-driven overall water splitting', *Journal of the American Chemical Society*, vol. 127, no. 23, pp. 8286-7.

Mallinson, CF, Gray, BM, Hector, AL, McLachlan, MA & Owen, JR 2013, 'Templated Non-Oxide Sol-Gel Preparation of Well-Ordered Macroporous (inverse opal) Ta3N5 Films', *Inorganic Chemistry*, vol. 52, no. 17, pp. 9994-9, DOI 10.1021/ic4012718, <http://dx.doi.org/10.1021/ic4012718>.

Manna, MV, Sabia, P, Ragucci, R & de Joannon, M 2020, 'Oxidation and pyrolysis of ammonia mixtures in model reactors', *Fuel*, vol. 264, p. 116768.

Marbán, G & Valdés-Solís, T 2007, 'Towards the hydrogen economy?', *International Journal of Hydrogen Energy*, vol. 32, no. 12, pp. 1625-37.

Matsuoka, M, Kitano, M, Takeuchi, M, Tsujimaru, K, Anpo, M & Thomas, JM 2007, 'Photocatalysis for new energy production: Recent advances in photocatalytic water splitting reactions for hydrogen production', *Catalysis today*, vol. 122, no. 1–2, pp. 51-61, DOI http://dx.doi.org/10.1016/j.cattod.2007.01.042, <http://www.sciencedirect.com/science/article/pii/S0920586107000570>.

McCarty, JP 2001, 'Ecological consequences of recent climate change', *Conservation biology*, vol. 15, no. 2, pp. 320-31.

McDermott, EJ, Kurmaev, EZ, Boyko, TD, Finkelstein, LD, Green, RJ, Maeda, K et al. 2012, 'Structural and Band Gap Investigation of GaN:ZnO Heterojunction Solid Solution Photocatalyst Probed by Soft X-ray Spectroscopy', *The Journal of Physical Chemistry C*, vol. 116, no. 14, pp. 7694-700, DOI 10.1021/jp301231p, <http://dx.doi.org/10.1021/jp301231p>.

Min, KH, Chun, KC & Kim, KB 1996, 'Comparative study of tantalum and tantalum nitrides (Ta2N and TaN) as a diffusion barrier for Cu metallization', *Journal of Vacuum Science & Technology B: Microelectronics and Nanometer Structures Processing, Measurement, and Phenomena*, vol. 14, no. 5, pp. 3263-9, DOI 10.1116/1.588818, <http://avs.scitation.org/doi/abs/10.1116/1.588818>.

Minegishi, T, Nishimura, N, Kubota, J & Domen, K 2013, 'Photoelectrochemical properties of LaTiO 2 N electrodes prepared by particle transfer for sunlight-driven water splitting', *Chemical Science*, vol. 4, no. 3, pp. 1120-4.

Morbec, JM, Narkeviciute, I, Jaramillo, TF & Galli, G 2014, 'Optoelectronic properties of Ta3N5: A joint theoretical and experimental study', *Physical Review B*, vol. 90, no. 15, p. 155204, <https://link.aps.org/doi/10.1103/PhysRevB.90.155204>.

Morosanu, C, Dumitru, V, Cimpoiasu, E & Nenu, C 1997, 'Comparison Between DC and RF Magnetron Sputtered Aluminum Nitride Films', in MA Prelas, A Benedictus, L-TS Lin, G Popovici & P Gielisse (eds), *Diamond Based Composites: and Related Materials*, Springer Netherlands, Dordrecht, pp. 127-32.

Muhl, S, Zapien, JA, Mendez, JM & Andrade, E 1997, 'Aluminium nitride films prepared by reactive magnetron sputtering', *Journal of Physics D: Applied Physics*, vol. 30, no. 15, pp. 2147-55, DOI 10.1088/0022-3727/30/15/005, <http://dx.doi.org/10.1088/0022-3727/30/15/005>.

Murphy, A, Barnes, P, Randeniya, L, Plumb, I, Grey, I, Horne, M et al. 2006, 'Efficiency of solar water splitting using semiconductor electrodes', *International Journal of Hydrogen Energy*, vol. 31, no. 14, pp. 1999-2017.

Narkeviciute, I, Chakthranont, P, Hahn, C, Mackus, A, Bent, SF & Jaramillo, TF 2016, 'Core-Shell Si-Ta3N5 Heterostructures As Photoanodes for Photoelectrochemical Water Splitting', *The Electrochemical Society*, no. 46, pp. 3375-.

Narkeviciute, I, Chakthranont, P, Mackus, AJ, Hahn, C, Pinaud, BA, Bent, SF et al. 2016, 'Tandem core–shell Si–Ta3N5 photoanodes for photoelectrochemical water splitting', *Nano letters*, vol. 16, no. 12, pp. 7565-72.

Narkeviciute, I & Jaramillo, TF 2017, 'Impact of Nanostructuring on the Photoelectrochemical Performance of Si/Ta3N5 Nanowire Photoanodes', *The Journal of Physical Chemistry C*, vol. 121, no. 49, pp. 27295-302, DOI 10.1021/acs.jpcc.7b08690, <https://doi.org/10.1021/acs.jpcc.7b08690>.

Nave, DCR 2007, *The Doping of Semiconductors.*, Georgia State University, <http://hyperphysics.phy-astr.gsu.edu/hbase/Solids/dope.html#c3>.

Nelson, JA 2003, *The physics of solar cells*, World Scientific Publishing Company.

Ni, M, Leung, MK, Leung, DY & Sumathy, K 2007, 'A review and recent developments in photocatalytic water-splitting using TiO2 for hydrogen production', *Renewable and Sustainable Energy Reviews*, vol. 11, no. 3, pp. 401-25.

Nie, HB, Xu, SY, Wang, SJ, You, LP, Yang, Z, Ong, CK et al. 2001, 'Structural and electrical properties of tantalum nitride thin films fabricated by using reactive radio-frequency magnetron sputtering', *Applied Physics A*, vol. 73, no. 2, pp. 229-36, DOI 10.1007/s003390000691, <https://doi.org/10.1007/s003390000691>.

Niu, B & Xu, Z 2019, 'A stable Ta3N5@PANI core-shell photocatalyst: Shell thickness effect, high-efficient photocatalytic performance and enhanced mechanism', *Journal of Catalysis*, vol. 371, pp. 175-84.

Nnamchi, PS & Obayi, CS 2018, 'Chapter 4 - Electrochemical Characterization of Nanomaterials', in S Mohan Bhagyaraj, OS Oluwafemi, N Kalarikkal & S Thomas (eds), *Characterization of Nanomaterials*, Woodhead Publishing, pp. 103-27.

Nobuzo, T 1971, 'Structure of Tantalum Nitrides', *Japanese Journal of Applied Physics*, vol. 10, no. 2, p. 248, <http://stacks.iop.org/1347-4065/10/i=2/a=248>.

Noda, S, Tepsanongsuk, K, Tsuji, Y, Kajikawa, Y, Ogawa, Y & Komiyama, H 2004, 'Preferred orientation and film structure of TaN films deposited by reactive magnetron sputtering', *Journal of Vacuum Science & Technology A: Vacuum, Surfaces, and Films*, vol. 22, no. 2, pp. 332-8.

Nordin, M, Larsson, M & Hogmark, S 1999, 'Wear resistance of multilayered PVD TiN/TaN on HSS', *Surface and Coatings Technology*, vol. 120, pp. 528-34.

Nowotny, J, Bak, T, Nowotny, M & Sheppard, L 2007, 'Titanium dioxide for solar-hydrogen I. Functional properties', *International Journal of Hydrogen Energy*, vol. 32, no. 14, pp. 2609-29.

Nowotny, MK, Sheppard, LR, Bak, T & Nowotny, J 2008, 'Defect chemistry of titanium dioxide. Application of defect engineering in processing of TiO2-based photocatalysts', *The Journal of Physical Chemistry C*, vol. 112, no. 14, pp. 5275-300.

Nurlaela, E, Ziani, A & Takanabe, K 2016, 'Tantalum nitride for photocatalytic water splitting: concept and applications', *Materials for Renewable and Sustainable Energy*.

Ogden, JM 1999, 'PROSPECTS FOR BUILDING A HYDROGEN ENERGY INFRASTRUCTURE', *Annual Review of Energy and the Environment*, vol. 24, no. 1, pp. 227-79, DOI 10.1146/annurev.energy.24.1.227, <https://www.annualreviews.org/doi/abs/10.1146/annurev.energy.24.1.227>.

Oku, T, Kawakami, E, Uekubo, M, Takahiro, K, Yamaguchi, S & Murakami, M 1996, 'Diffusion barrier property of TaN between Si and Cu', *Applied Surface Science*, vol. 99, no. 4, pp. 265-72, DOI http://dx.doi.org/10.1016/0169-4332(96)00464-3, <http://www.sciencedirect.com/science/article/pii/0169433296004643>.

Oreskes, N 2004, 'The scientific consensus on climate change', *Science*, vol. 306, no. 5702, pp. 1686-.

Ottone, C, Laurenti, M, Bejtka, K, Sanginario, A & Valentina, C 2014, 'The Effects of the Film Thickness and Roughness in the Anodization Process of Very Thin Aluminum Films', *Journal of Materials Science & Nanotechnology*, vol. 1, p. S107, DOI 10.15744/2348-9812.1.S107.

Paskov, PP & Monemar, B 2018, '2 - Point defects in group-III nitrides', in J Stehr, I Buyanova & W Chen (eds), *Defects in Advanced Electronic Materials and Novel Low Dimensional Structures*, Woodhead Publishing, pp. 27-61.

Pei, L, Wang, HX, Wang, X, Yan, SC & Zou, Z 2018, 'Nanostructured TaON/Ta3N5 as highly efficient type-II heterojunction photoanode for photoelectrochemical water splitting', *Dalton Transactions*.

Peng, Y-H, Huang, G-F & Huang, W-Q 2012, 'Visible-light absorption and photocatalytic activity of Cr-doped TiO2 nanocrystal films', *Advanced Powder Technology*, vol. 23, no. 1, pp. 8-12.

Perng, D-C, Yeh, J-B & Hsu, K-C 2008, 'Phosphorous doped Ru film for advanced Cu diffusion barriers', *Applied Surface Science*, vol. 254, no. 19, pp. 6059-62.

Philips'Gloeilampenfabrieken, O 1958, 'A method of measuring specific resistivity and Hall effect of discs of arbitrary shape', *Philips Res. Rep*, vol. 13, no. 1, pp. 1-9.

Pinaud, BA, Vailionis, A & Jaramillo, TF 2014, 'Controlling the Structural and Optical Properties of Ta3N5 Films through Nitridation Temperature and the Nature of the Ta Metal', *Chemistry of materials*, vol. 26, no. 4, pp. 1576-82, DOI 10.1021/cm403482s, <http://dx.doi.org/10.1021/cm403482s>.

Premkartikkumar, D & Pradeepkumar, D 2015, 'Effect of using hydrogen mixed gases as a fuel in internal Combustion engines–A Review', *International Journal of Innovative Research in Advanced Engineering (IJIRAE) ISSN: 23492163 Issue*, vol. 9.

Radhakrishnan, K, Geok Ing, N & Gopalakrishnan, R 1999, 'Reactive sputter deposition and characterization of tantalum nitride thin films', *Materials Science and Engineering: B*, vol. 57, no. 3, pp. 224-7, DOI http://dx.doi.org/10.1016/S0921-5107(98)00417-6, <http://www.sciencedirect.com/science/article/pii/S0921510798004176>.

Raftery, AE, Zimmer, A, Frierson, DMW, Startz, R & Liu, P 2017, 'Less than 2 °C warming by 2100 unlikely', *Nature Climate Change*, vol. 7, p. 637, DOI 10.1038/nclimate3352 https://www.nature.com/articles/nclimate3352#supplementary-information, <https://doi.org/10.1038/nclimate3352>.

Rajaambal, S, Mapa, M & Gopinath, CS 2014, 'In 1− x Ga x N@ ZnO: a rationally designed and quantum dot integrated material for water splitting and solar harvesting applications', *Dalton Transactions*, vol. 43, no. 33, pp. 12546-54.

Rao, GV, Kumar, M, Rajesh, T, Reddy, DRK, Anjaneyulu, D, Sainath, B et al. 2016, 'Investigations on the Nitride Interface Engineering at HfO2/Ge stacks for MOS devices'.

Rebenne, HE & Bhat, DG 1994, 'Review of CVD TiN coatings for wear-resistant applications: deposition processes, properties and performance', *Surface and Coatings Technology*, vol. 63, no. 1-2, pp. 1-13.

Riekkinen, T, Molarius, J, Laurila, T, Nurmela, A, Suni, I & Kivilahti, JK 2002, 'Reactive sputter deposition and properties of TaxN thin films', *Microelectronic Engineering*, vol. 64, no. 1, pp. 289-97, DOI http://dx.doi.org/10.1016/S0167-9317(02)00801-8, <http://www.sciencedirect.com/science/article/pii/S0167931702008018>.

Rietveld, G, Koijmans, CV, Henderson, L, Hall, M, Harmon, S, Warnecke, P et al. 2003, 'DC conductivity measurements in the Van Der Pauw geometry', *Instrumentation and Measurement, IEEE Transactions on*, vol. 52, pp. 449-53, DOI 10.1109/TIM.2003.809917.

Rioult, M 2015, *Hematite-based epitaxial thin films as photoanodes for solar water splitting*.

Ritala, M, Kalsi, P, Riihelä, D, Kukli, K, Leskelä, M & Jokinen, J 1999, 'Controlled Growth of TaN, Ta3N5, and TaOxNy Thin Films by Atomic Layer Deposition', *Chemistry of materials*, vol. 11, no. 7, pp. 1712-8, DOI 10.1021/cm980760x, <http://dx.doi.org/10.1021/cm980760x>.

Ritchie, H & Roser, M 2020, *Energy*, ourworldindata, viewed 10/06/2021 2021.

Rudolph, M 2017, *Synthesis and characterization of magnetron-sputtered Ta_3N_5 thin films for the photoelectrolysis of water*, Université Paris-Saclay (ComUE).

Rudolph, M, Stanescu, D, Alvarez, J, Foy, E, Kleider, JP, Magnan, H et al. 2016, 'The role of oxygen in magnetron-sputtered Ta3N5 thin films for the photoelectrolysis of water', *Surface and Coatings Technology*, DOI https://doi.org/10.1016/j.surfcoat.2016.09.007, <http://www.sciencedirect.com/science/article/pii/S0257897216308787>.

Rudolph, M, Vickridge, I, Foy, E, Alvarez, J, Kleider, J-P, Stanescu, D et al. 2019, 'Oxygen incorporated during film growth determines the crystallinity of magnetron-sputtered Ta3N5 films', *Thin Solid Films*.

Salamon, K, Radić, N, Radović, IB & Očko, M 2016, 'Phase map, composition and resistivity of reactively magnetron sputtered and annealed Ta–N films', *Journal of Physics D: Applied Physics*, vol. 49, no. 19, p. 195301.

Sato, J, Saito, N, Yamada, Y, Maeda, K, Takata, T, Kondo, JN et al. 2005, 'RuO2-Loaded β-Ge3N4 as a Non-Oxide Photocatalyst for Overall Water Splitting', *Journal of the American Chemical Society*, vol. 127, no. 12, pp. 4150-1, DOI 10.1021/ja042973v, <http://dx.doi.org/10.1021/ja042973v>.

Scandurra, A, Indelli, GF, Pignataro, B, Di Marco, S, Di Stefano, MA, Ravesi, S et al. 2008, 'Tantalum nitride thin film resistors by low temperature reactive sputtering for plastic electronics', *Surface and Interface Analysis: An International Journal devoted to the development and application of techniques for the analysis of surfaces, interfaces and thin films*, vol. 40, no. 3-4, pp. 758-62.

Schonberg, N, Overend, W, Munthe-Kaas, A & Sörensen, N 1954, 'An X-ray study of the tantalum-nitrogen system', *Acta Chem. Scand*, vol. 8, no. 2, pp. 199-203.

Schubert, EF 2015, *Doping in III-V semiconductors*, E. Fred Schubert.

Schwarz, SA 2001, 'Secondary Ion Mass Spectroscopy', in KHJ Buschow, RW Cahn, MC Flemings, B Ilschner, EJ Kramer, S Mahajan & P Veyssière (eds), *Encyclopedia of Materials: Science and Technology*, Elsevier, Oxford, pp. 8283-90.

Schwinghammer, K, Mesch, MB, Duppel, V, Ziegler, C, Senker, J & Lotsch, BV 2014, 'Crystalline Carbon Nitride Nanosheets for Improved Visible-Light Hydrogen Evolution', *Journal of the American Chemical Society*, vol. 136, no. 5, pp. 1730-3, DOI 10.1021/ja411321s, <http://dx.doi.org/10.1021/ja411321s>.

Seo, J, Takata, T, Nakabayashi, M, Hisatomi, T, Shibata, N, Minegishi, T et al. 2015, 'Mg–Zr Cosubstituted Ta3N5 Photoanode for Lower-Onset-Potential Solar-Driven Photoelectrochemical Water Splitting', *Journal of the American Chemical Society*, vol. 137, no. 40, pp. 12780-3, DOI 10.1021/jacs.5b08329, <http://dx.doi.org/10.1021/jacs.5b08329>.

Shafarman, WN, Siebentritt, S & Stolt, L 2011, 'Cu(InGa)Se2 Solar Cells', in *Handbook of Photovoltaic Science and Engineering*, John Wiley & Sons, Ltd, pp. 546-99.

Shafiee, S & Topal, E 2009, 'When will fossil fuel reserves be diminished?', *Energy policy*, vol. 37, no. 1, pp. 181-9.

Shannon, RD 1976, 'Revised effective ionic radii and systematic studies of interatomic distances in halides and chalcogenides', *Acta crystallographica section A: crystal physics, diffraction, theoretical and general crystallography*, vol. 32, no. 5, pp. 751-67.

Sharifi, T, Ghayeb, Y, Mohammadi, T & Momeni, MM 2018, 'Enhanced photoelectrochemical water splitting of CrTiO 2 nanotube photoanodes by the decoration of their surface via the photodeposition of Ag and Au', *Dalton Transactions*, vol. 47, no. 33, pp. 11593-604.

She, X, Wu, J, Xu, H, Zhong, J, Wang, Y, Song, Y et al. 2017, 'High Efficiency Photocatalytic Water Splitting Using 2D α-Fe2O3/g-C3N4 Z-Scheme Catalysts', *Advanced Energy Materials*, vol. 7, no. 17, pp. 1700025-n/a, DOI 10.1002/aenm.201700025, <http://dx.doi.org/10.1002/aenm.201700025>.

Shet, S, Ahn, K-S, Deutsch, T, Wang, H, Ravindra, N, Yan, Y et al. 2011, 'Synthesis and characterization of band gap-reduced ZnO:N and ZnO:(Al,N) films for photoelectrochemical water splitting', *Journal of Materials Research*, vol. 25, no. 1, pp. 69-75, Cambridge Core, Cambridge University Press, DOI 10.1557/JMR.2010.0017, <https://www.cambridge.org/core/article/synthesis-and-characterization-of-band-gapreduced-znon-and-znoaln-films-for-photoelectrochemical-water-splitting/14E917255BE1EA9D10598D34AD44BBE5>.

Shin, C-J, Yoo, H-I & Lee, C-E 2007, 'Al-doped SrTiO3: Part I, anomalous oxygen nonstoichiometry', *Solid State Ionics*, vol. 178, no. 15-18, pp. 1081-7.

Shin, CS, Kim, YW, Gall, D, Greene, JE & Petrov, I 2002, 'Phase composition and microstructure of polycrystalline and epitaxial TaNx layers grown on oxidized Si(001) and MgO(001) by reactive magnetron sputter deposition', *Thin Solid Films*, vol. 402, no. 1, pp. 172-82, DOI http://dx.doi.org/10.1016/S0040-6090(01)01618-2, <http://www.sciencedirect.com/science/article/pii/S0040609001016182>.

Shirley, R, Kraft, M & Inderwildi, OR 2010, 'Electronic and optical properties of aluminium-doped anatase and rutile TiO 2 from ab initio calculations', *Physical Review B*, vol. 81, no. 7, p. 075111.

Simon, AH 2012, '4 - Sputter Processing', in K Seshan (ed.), *Handbook of Thin Film Deposition (Third Edition)*, William Andrew Publishing, Oxford, pp. 55-88.

Singh, R & Dutta, S 2021, '18 - Integrated photocatalytic hydrogen production and pollutants or wastes treatment: prospects and challenges', in S Dutta & C Mustansar Hussain (eds), *Sustainable Fuel Technologies Handbook*, Academic Press, pp. 541-9.

Solomon, S 2007, 'IPCC (2007): Climate change the physical science basis'.

Soprano, P 2013, 'International Green Growth Forum-the EU Approach to Green Economy within the International Framework'.

Sputtering Yield Rates 2019, SEMICORE Equipment, Inc., viewed 28 August, 2019 2019, <http://www.semicore.com/reference/sputtering-yields-reference>.

Stampfl, C & Freeman, AJ 2005, 'Stable and metastable structures of the multiphase tantalum nitride system', *Physical Review B*, vol. 71, no. 2, p. 024111, <https://link.aps.org/doi/10.1103/PhysRevB.71.024111>.

Su, Z, Grigorescu, S, Wang, L, Lee, K & Schmuki, P 2015, 'Fast fabrication of Ta2O5 nanotube arrays and their conversion to Ta3N5 for efficient solar driven water splitting', *Electrochemistry communications*, vol. 50, pp. 15-9.

Su, Z, Wang, L, Grigorescu, S, Lee, K & Schmuki, P 2014, 'Hydrothermal growth of highly oriented single crystalline Ta 2 O 5 nanorod arrays and their conversion to Ta 3 N 5 for efficient solar driven water splitting', *Chemical Communications*, vol. 50, no. 98, pp. 15561-4.

Sun, Q, Cortie, D, Zhang, S, Frankcombe, TJ, She, G, Gao, J et al. 2017, 'The Formation of Defect-Pairs for Highly Efficient Visible-Light Catalysts', *Advanced Materials*, vol. 29, no. 11, p. 1605123.

Sun, W, Holder, A, Orvananos, B, Arca, E, Zakutayev, A, Lany, S et al. 2017, 'Thermodynamic Routes to Novel Metastable Nitrogen-Rich Nitrides', *Chemistry of materials*, DOI 10.1021/acs.chemmater.7b02399, <http://dx.doi.org/10.1021/acs.chemmater.7b02399>.

Suzuki, T, Nomura, T, Kuroha, T, Miyata, N, Tamura, S, Tokuhiro, K et al. 2015, 'Niobium nitride and method for producing same, niobium nitride-containing film and method for producing same, semiconductor, semiconductor device, photocatalyst, hydrogen generation device, and energy system', Google Patents.

Swann, S 1988, 'Magnetron sputtering', *Physics in Technology*, vol. 19, no. 2, pp. 67-75, DOI 10.1088/0305-4624/19/2/304, <http://dx.doi.org/10.1088/0305-4624/19/2/304>.

Swisher, J & Read, M 1972, 'Thermodynamic properties and electrical conductivity of Ta3N5 and TaON', *Metallurgical Transactions*, vol. 3, no. 2, pp. 493-8.

Szaleniec, M, Drzewiecka-Matuszek, A, Witko, M & Hejduk, P 2013, 'Ammonium adsorption on Brønsted acidic centers on low-index vanadium pentoxide surfaces', *Journal of molecular modeling*, vol. 19, no. 10, pp. 4487-501.

Tabata, M, Maeda, K, Higashi, M, Lu, D, Takata, T, Abe, R et al. 2010, 'Modified Ta3N5 powder as a photocatalyst for O2 evolution in a two-step water splitting system with an iodate/iodide shuttle redox mediator under visible light', *Langmuir*, vol. 26, no. 12, pp. 9161-5.

Thiede, T, Parala, H, Reuter, K, Passing, G, Kirchmeyer, S, Hinz, J et al. 2008, 'Evaluation of MOCVD grown Niobium nitride films as gate electrode for advanced CMOS technology', *ECS Transactions*, vol. 16, no. 5, pp. 229-34.

Thiede, TB, Parala, H, Reuter, K, Passing, G, Kirchmeyer, S, Hinz, J et al. 2009, 'Deposition of Niobium Nitride Thin Films from Tert-Butylamido-Tris-(Diethylamido)-Niobium by a Modified Industrial MOCVD Reactor', *Chemical Vapor Deposition*, vol. 15, no. 10-12, pp. 334-41, DOI 10.1002/cvde.200906810, <http://dx.doi.org/10.1002/cvde.200906810>.

Tudose, IV, Comanescu, F, Pascariu, P, Bucur, S, Rusen, L, Iacomi, F et al. 2019, 'Chapter 2 - Chemical and physical methods for multifunctional nanostructured interface fabrication', in V Dinca & MP Suchea (eds), *Functional Nanostructured Interfaces for Environmental and Biomedical Applications*, Elsevier, pp. 15-26.

Van Hoornick, N, De Witte, H, Witters, T, Zhao, C, Conard, T, Huotari, H et al. 2006, 'Evaluation of atomic layer deposited NbN and NbSiN as metal gate materials', *Journal of The Electrochemical Society*, vol. 153, no. 5, pp. G437-G42.

Vlachogianni, T & Valavanidis, A 2013, 'Energy and Environmental Impact on the Biosphere Energy Flow, Storage and Conversion in Human Civilization', *American Journal of Educational Research*, vol. 1, no. 3, pp. 68-78, <http://pubs.sciepub.com/education/1/3/2>.

Walter, MG, Warren, EL, McKone, JR, Boettcher, SW, Mi, Q, Santori, EA et al. 2010, 'Solar water splitting cells', *Chemical Reviews*, vol. 110, no. 11, pp. 6446-73.

Wang, C, Hisatomi, T, Minegishi, T, Nakabayashi, M, Shibata, N, Katayama, M et al. 2016, 'Effects of interfacial layers on the photoelectrochemical properties of tantalum nitride photoanodes for solar water splitting', *Journal of Materials Chemistry A*, vol. 4, no. 36, pp. 13837-43.

Wang, C, Yin, L, Zhang, L, Xiang, D & Gao, R 2010, 'Metal oxide gas sensors: sensitivity and influencing factors', *Sensors*, vol. 10, no. 3, pp. 2088-106.

Wang, D, Pierre, A, Kibria, MG, Cui, K, Han, X, Bevan, KH et al. 2011, 'Wafer-level photocatalytic water splitting on GaN nanowire arrays grown by molecular beam epitaxy', *Nano letters*, vol. 11, no. 6, pp. 2353-7.

Wang, J, Fang, T, Zhang, L, Feng, J, Li, Z & Zou, Z 2014, 'Effects of oxygen doping on optical band gap and band edge positions of Ta3N5 photocatalyst: A GGA+U calculation', *Journal of Catalysis*, vol. 309, pp. 291-9, DOI https://doi.org/10.1016/j.jcat.2013.10.014, <http://www.sciencedirect.com/science/article/pii/S0021951713003655>.

Wang, J, Ma, A, Li, Z, Jiang, J, Feng, J & Zou, Z 2014, 'Effects of Ba-O codoping on the photocatalytic activities of Ta3N5 photocatalyst: a DFT study', *RSC Advances*, vol. 4, no. 98, pp. 55615-21, DOI 10.1039/C4RA11053F, <http://dx.doi.org/10.1039/C4RA11053F>.

Wang, L, Dionigi, F, Nguyen, NT, Kirchgeorg, R, Gliech, M, Grigorescu, S et al. 2015, 'Tantalum Nitride Nanorod Arrays: Introducing Ni–Fe Layered Double Hydroxides as a Cocatalyst Strongly Stabilizing Photoanodes in Water Splitting', *Chemistry of materials*, vol. 27, no. 7, pp. 2360-6, DOI 10.1021/cm503887t, <http://dx.doi.org/10.1021/cm503887t>.

Wang, L, Mazare, A, Hwang, I & Schmuki, P 2016, 'Tantalum nitride nanotube photoanodes: establishing a beneficial back-contact by lift-off and transfer to titanium nitride layer', *Electrochemistry communications*, vol. 72, pp. 27-31.

Wang, L, Zhou, X, Nguyen, NT, Hwang, I & Schmuki, P 2016, 'Strongly Enhanced Water Splitting Performance of Ta3N5 Nanotube Photoanodes with Subnitrides', *Advanced Materials*, vol. 28, no. 12, pp. 2432-8, DOI 10.1002/adma.201505312, <http://dx.doi.org/10.1002/adma.201505312>.

Wang, X, Maeda, K, Thomas, A, Takanabe, K, Xin, G, Carlsson, JM et al. 2009, 'A metal-free polymeric photocatalyst for hydrogen production from water under visible light', *Nature materials*, vol. 8, no. 1, pp. 76-80.

Wang, Y, Wang, X & Antonietti, M 2012, 'Polymeric graphitic carbon nitride as a heterogeneous organocatalyst: from photochemistry to multipurpose catalysis to sustainable chemistry', *Angewandte Chemie International Edition*, vol. 51, no. 1, pp. 68-89.

Wang, Y, Zhu, D & Xu, X 2016, 'Zr-Doped Mesoporous Ta3N5 Microspheres for Efficient Photocatalytic Water Oxidation', *ACS Applied Materials & Interfaces*, vol. 8, no. 51, pp. 35407-18, DOI 10.1021/acsami.6b14230, <https://doi.org/10.1021/acsami.6b14230>.

Wasa, K 2012, '2 - Sputtering Phenomena', in K Wasa, I Kanno & H Kotera (eds), *Handbook of Sputtering Technology (Second Edition)*, William Andrew Publishing, Oxford, pp. 41-75.

Wilson, AH 1931, 'The theory of electronic semi-conductors', *Proceedings of the Royal Society of London. Series A, Containing Papers of a Mathematical and Physical Character*, vol. 133, no. 822, pp. 458-91.

Xie, Y, Wang, Y, Chen, Z & Xu, X 2016, 'Role of Oxygen Defects on the Photocatalytic Properties of Mg-Doped Mesoporous Ta3N5', *ChemSusChem*, vol. 9, no. 12, pp. 1403-12.

Yan, S, Lv, S, Li, Z & Zou, Z 2010, 'Organic–inorganic composite photocatalyst of gC 3 N 4 and TaON with improved visible light photocatalytic activities', *Dalton Transactions*, vol. 39, no. 6, pp. 1488-91.

Yang, JF, Prakash, B, Yuan, ZG, Jiang, Y, Wang, XP & Fang, QF 2012, 'Influence of Sputtering Target Power on Microstructure and Mechanical Properties of W-N and Ta-N Coatings', *Nanoscience and Nanotechnology Letters*, vol. 4, no. 6, pp. 604-8, DOI 10.1166/nnl.2012.1372, <https://www.ingentaconnect.com/content/asp/nnl/2012/00000004/00000006/art00005 https://doi.org/10.1166/nnl.2012.1372>.

Yang, JF, Yuan, ZG, Wang, XP & Fang, QF 2011, 'Comparative Study of Ta-N and W-N Films Deposited by Reactive Magnetron Sputtering', *Nanoscience and Nanotechnology Letters*, vol. 3, no. 2, pp. 280-4, DOI 10.1166/nnl.2011.1153, <https://www.ingentaconnect.com/content/asp/nnl/2011/00000003/00000002/art00034 https://doi.org/10.1166/nnl.2011.1153>.

Yin, W-J, Tang, H, Wei, S-H, Al-Jassim, MM, Turner, J & Yan, Y 2010, 'Band structure engineering of semiconductors for enhanced photoelectrochemical water splitting: the case of TiO 2', *Physical Review B*, vol. 82, no. 4, p. 045106.

Yokoyama, D, Hashiguchi, H, Maeda, K, Minegishi, T, Takata, T, Abe, R et al. 2011, 'Ta3N5 photoanodes for water splitting prepared by sputtering', *Thin Solid Films*, vol. 519, no. 7, pp. 2087-92, DOI http://dx.doi.org/10.1016/j.tsf.2010.10.055, <http://www.sciencedirect.com/science/article/pii/S0040609010014884>.

Yu, H, Yan, S, Li, Z, Yu, T & Zou, Z 2012, 'Efficient visible-light-driven photocatalytic H2 production over Cr/N-codoped SrTiO3', *International Journal of Hydrogen Energy*, vol. 37, no. 17, pp. 12120-7.

Yu, L, Stampfl, C, Marshall, D, Eshrich, T, Narayanan, V, Rowell, JM et al. 2002, 'Mechanism and control of the metal-to-insulator transition in rocksalt tantalum nitride', *Physical Review B*, vol. 65, no. 24, p. 245110, DOI 10.1103/PhysRevB.65.245110, <https://link.aps.org/doi/10.1103/PhysRevB.65.245110>.

Zaman, A & Meletis, EI 2017, 'Microstructure and Mechanical Properties of TaN Thin Films Prepared by Reactive Magnetron Sputtering', *Coatings*, vol. 7, no. 12, p. 209, <http://www.mdpi.com/2079-6412/7/12/209>.

Zhang, J, Zhang, G, Chen, X, Lin, S, Möhlmann, L, Dołęga, G et al. 2012, 'Co-Monomer Control of Carbon Nitride Semiconductors to Optimize Hydrogen Evolution with Visible Light', *Angewandte Chemie*, vol. 124, no. 13, pp. 3237-41, DOI 10.1002/ange.201106656, <http://dx.doi.org/10.1002/ange.201106656>.

Zhang, Q & Gao, L 2004, 'Ta3N5 nanoparticles with enhanced photocatalytic efficiency under visible light irradiation', *Langmuir*, vol. 20, no. 22, pp. 9821-7.

Zhang, Z & Yates, JT 2012, 'Band Bending in Semiconductors: Chemical and Physical Consequences at Surfaces and Interfaces', *Chemical Reviews*, vol. 112, no. 10, pp. 5520-51, DOI 10.1021/cr3000626, <http://dx.doi.org/10.1021/cr3000626>.

Zhong, M, Hisatomi, T, Sasaki, Y, Suzuki, S, Teshima, K, Nakabayashi, M et al. 2017, 'Highly Active GaN-Stabilized Ta3N5 Thin-Film Photoanode for Solar Water Oxidation', *Angewandte Chemie International Edition*, vol. 56, no. 17, pp. 4739-43.

Zhu, Y-P, Ren, T-Z & Yuan, Z-Y 2015, 'Mesoporous phosphorus-doped g-C3N4 nanostructured flowers with superior photocatalytic hydrogen evolution performance', *ACS Applied Materials & Interfaces*, vol. 7, no. 30, pp. 16850-6.

Ziani, A, Nurlaela, E, Dhawale, DS, Silva, DA, Alarousu, E, Mohammed, OF et al. 2015, 'Carrier dynamics of a visible-light-responsive Ta 3 N 5 photoanode for water oxidation', *Physical Chemistry Chemical Physics*, vol. 17, no. 4, pp. 2670-7.

Ziolli, RL & Jardim, WF 2002, 'Photocatalytic decomposition of seawater-soluble crude-oil fractions using high surface area colloid nanoparticles of TiO2', *Journal of photochemistry and photobiology A: Chemistry*, vol. 147, no. 3, pp. 205-12.

Zou, J-P, Wang, L-C, Luo, J, Nie, Y-C, Xing, Q-J, Luo, X-B et al. 2016, 'Synthesis and efficient visible light photocatalytic H2 evolution of a metal-free g-C3N4/graphene quantum dots hybrid photocatalyst', *Applied Catalysis B: Environmental*, vol. 193, pp. 103-9, DOI https://doi.org/10.1016/j.apcatb.2016.04.017, <http://www.sciencedirect.com/science/article/pii/S0926337316302831>.

11 Appendices

11.1 Doped Film Capacitance Results

Scans were performed to check the capacitance of the films. Capacitance is a difficult value to calculate but can be visually gauged by plotting the current from a selected applied voltage value at different scan rates, as per **Figure 11-1** (for the chromium doped films).

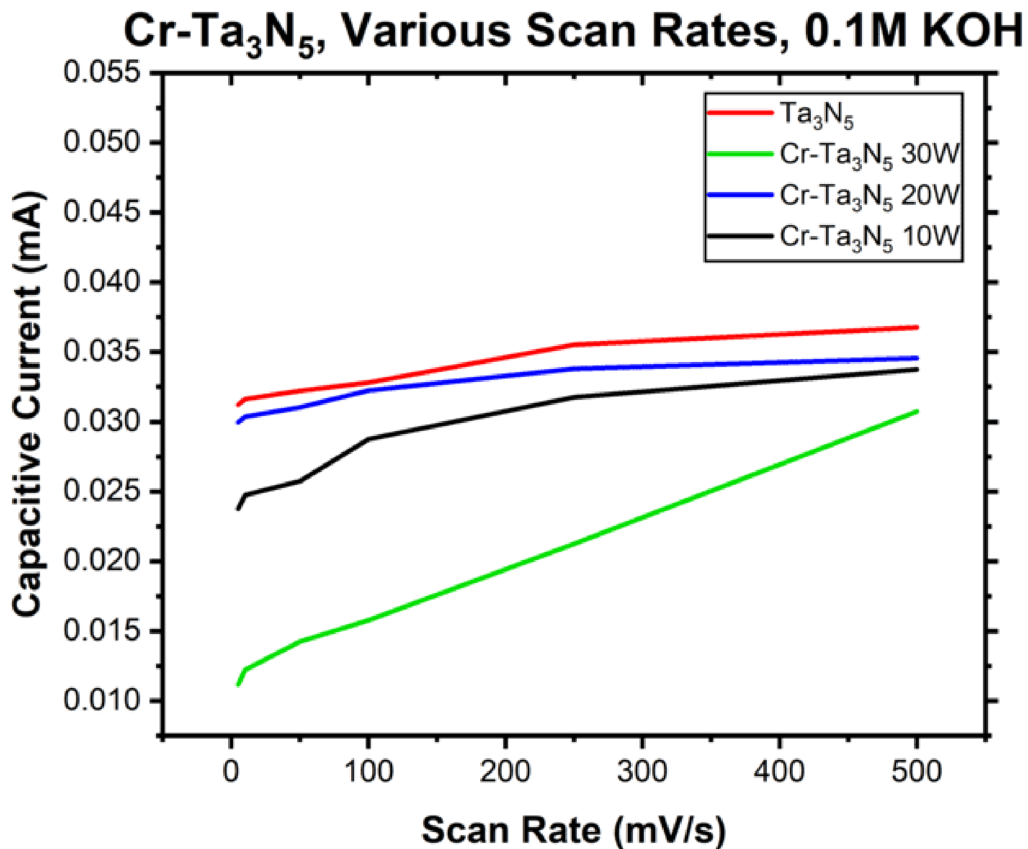

Figure 11-1. Plot showing the linear relationship between the capacitive current and different scan rates for Cr-Ta_3N_5 and Ta_3N_5 films. Scan rates of 5mV/s, 10mV/s, 100mV/s, 250mV/s and 500mV/s are shown for the selected voltage of 0.5V.

The 10 W and 20 W doped films exhibit relatively similar linear plots as the Ta_3N_5 standard, however the 30 W film exhibits greater relative capacitance to all other films. The capacitance plots for the aluminium doped films can be seen below in **Figure 11-2**.

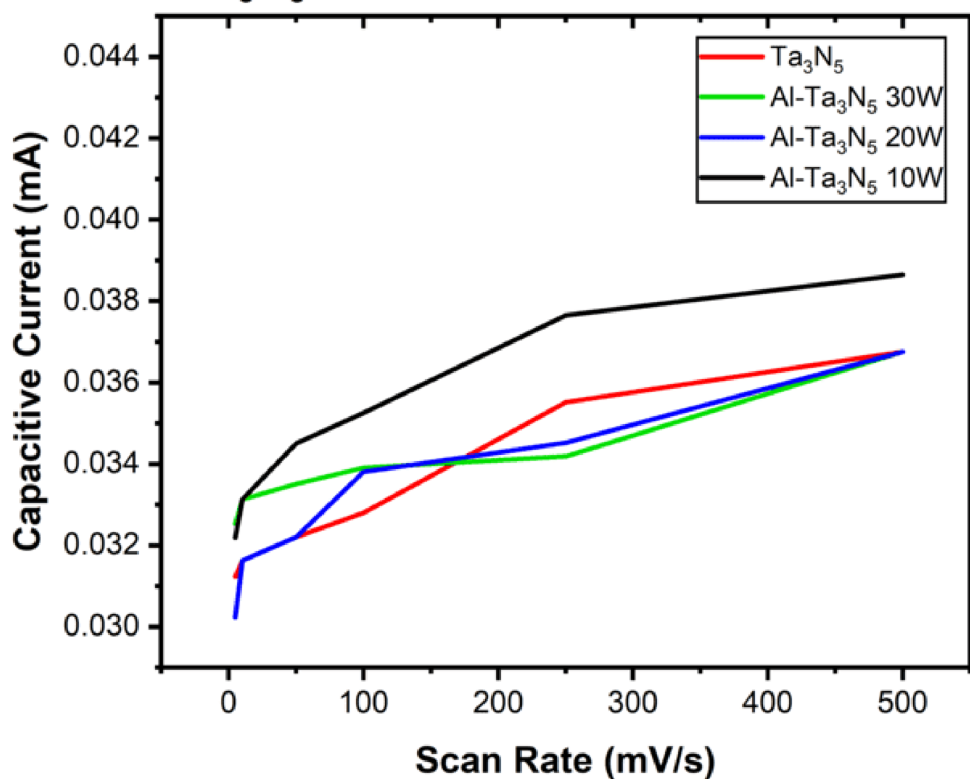

Figure 11-2. Plot showing the linear relationship between the capacitive current and different scan rates for Al-Ta_3N_5 and Ta_3N_5 films. Scan rates of 5mV/s, 10mV/s, 100mV/s, 250mV/s and 500mV/s are shown for the selected voltage of 0.5V.

Linear capacitance, i.e increasing capacitive current with scan speed, can be seen in all films, both Al-Ta_3N_5 and Ta_3N_5, per Figure 11-2.